School of Civil and Mechanical Engineering
Department of Mechanical Engineering

A Numerical Study of the Behaviour of Flexible Inserts in Laminar Channel Flow

Lawrence Shien Hui Lai

This thesis is presented for the degree of
Doctor of Philosophy
of
Curtin University

April 2017

Declaration

To the best of my knowledge and belief this thesis contains no material previously published by any other person except where due acknowledgement has been made. This thesis contains no material which has been accepted for the award of any other degree or diploma in any university.

All investigations presented in this thesis are my own except where specific reference has been made to the work of others. Some of the work presented in this thesis has been published in the following:

L. Lai, N. S. J. Elliott, A. D. Lucey, and M. W. Pitman. Numerical two-dimensional flexible channel model fixed at both ends for flow-induced instability analysis. In *6th Australasian Congress on Applied Mechanics, ACAM 6, Perth, Western Australia: Engineers Australia*, 2010.

L. Lai, A. D. Lucey, N. S. J. Elliott, and M. W. Pitman. Computational modelling of a fluid-conveying flexible channel using oomph-lib. In *Proc. 19th International Congress on Modelling and Simulation*, 2011.

L. Lai, A. D. Lucey, and N. S. J. Elliott. Computational stability analysis of a channel flow with a large deformation compliant insert. In *The 18th Australasian Fluid Mechanics Conference, Launceston, Australia: Australasian Fluid Mechanics Society*, 2012.

L. Lai, A. D. Lucey, and N. S. J. Elliott. Flow-induced deformations of a compliant insert in channel flow: from small to large amplitudes. In *ASME 2012 International Design Engineering Technical Conferences and Computers and Information in Engineering Conference, IDETC/CIE 2012, Chicago, IL, USA*, 2012.

L. Lai, J. Cisonni and A. D. Lucey. Stability of flexible inserts in laminar channel flow. In *The 20th Australasian Fluid Mechanics Conference, Perth, Australia: Australasian Fluid Mechanics Society*, 2016.

Signature:

Date: 14/04/2017

Acknowledgements

I would like to acknowledge the contribution of all the people, without which this work would not have been possible.

The first is my supervisor Professor Tony Lucey for his vision, support and encouragement throughout this journey. A huge thank you to my co-supervisors throughout my PhD.; Dr. Mark Pitman, Dr. Novak Elliott and Dr. Julien Cisonni who have each contributed their own views and expertise to this work. I would also like to thank all the members of the Fluid Dynamics Research Group (FDRG) at Curtin University for creating a healthy and productive research environment.

A very special thank you to my wife Yu Ling Sii for her infinite patience, support and care in encouraging me to finish this PhD. Lastly, to my parents and sisters for their guidance throughout my life. Thank you.

Abstract

The fluid-structure interaction (FSI) mechanics of a fluid-conveying two-dimensional channel that has one or two flexible insert sections is studied. This is achieved by applying numerical Finite Element Modelling (FEM) using the Object-Oriented Multi-Physics Finite-Element Library (`oomph-lib`). The computational model accounts for unsteady laminar flow interacting with large-amplitude (nonlinear) deformations of a thin flexible wall. The fluid loading on the wall comprises of both pressure and viscous stresses while the wall mechanics includes flexural and tension forces.

The current `oomph-lib` model was used to replicate the FSI behaviour presented in previous independent numerical studies as well as validate the present modelling and its implementation. With the validated model, it was found instability can occur under certain parameter combinations. This instability is characterised by the flexible wall oscillating with a fixed, saturated amplitude that continues indefinitely. This instability is mainly driven by the FSI of large wall deformations and the evolution (growth, decay and shedding) of recirculation zones behind the flexible insert. The magnitude of flexible wall movement depends on the downstream location and magnitude of the vortex shedding.

A non-dimensional scheme consisting of three parameters to characterise the FSI system behaviour and its stability bounds for large wall deformations was developed. These three parameters are the effective pressure, the effective Cauchy number and Reynolds number product, and ratio of the effective Cauchy number and Reynolds number. The non-dimensional scheme was tested to ensure it satisfied variations of its internal parameters while maintaining similar system mean state and dynamic behaviour. A parameter sensitivity analysis was also performed to test the relative importance of each parameter.

The relationship for static or steady-state FSI relating to the system effective pressure and ratio of the effective Cauchy number and Reynolds number was developed. The steady-state FSI behaviour is only weakly related to the effective Cauchy number and Reynolds number product. Curve fitting on the simulation data provides a simple expression allowing predictions of the maximum wall deflection from the dimensional system properties. All three parameters are important to characterise the dynamic FSI system behaviour. The dynamic simulation data was used to generate a plot consisting of the three parameters to predict system stability. Comparison with previously published

numerical and experimental studies was shown to be qualitatively consistent and within reasonable quantitative bounds.

The stability of flow in a channel with flexble inserts on opposing walls was studied. It was found that instability occurs in this system with mechanisms similar to the single insert configuration but with two stages of saturated instability forms. The first of this is with both walls having symmetric motion (symmetric state) and the second where the recirculation vortex is larger downstream of one of the flexible inserts (non-symmetric state). The system then maintains the non-symmetric state indefinitely. This second state could be triggered by any numerical imbalance in the fluid domain or differences in initial perturbation conditions applied on the flexible walls. It was shown that the same non-dimensional scheme proposed for the single wall case can be used for the dual wall to develop a new set of parametric conditions for predicting maximum wall deformation and system stability.

Contents

List of Figures **ix**

List of Tables **xvi**

Nomenclature **xviii**

1 Introduction **1**
1.1 Motivations 1
1.1.1 Industrial Engineering 2
1.1.2 Biomechanical Engineering 3
1.2 Objectives and Methodology 4
1.3 Thesis Outline 5

2 Literature Review **7**
2.1 Experimental Studies 7
2.2 Numerical Model Development 9
2.3 2-Dimensional Bounded Flow 11
2.4 Summary 13

3 Numerical Model and Study Methodology **15**
3.1 General 15
3.2 Model Description 15
3.3 Governing Equations 16
3.3.1 Fluid Flow 16
3.3.2 Flexible Wall 17
3.3.3 Fluid-Structure Interaction (FSI) 18
3.3.4 Energy Budget 18
3.3.5 Numerical Implementation 20
3.3.6 Start-up Procedure 22
3.4 Summary 23

4 Model Validation **24**
4.1 Validation Overview 24

4.2 Transient Small Deformation Flexible Insert Validation 25
4.3 Steady Large Deformation Flexible Insert Validation 26
4.4 Steady and Transient Large Deformation Flexible Insert Validation . . 32
4.5 Summary 40

5 Detailed Study of Single Flexible Wall Behaviour 43
5.1 General 43
5.1.1 Flexible Insert Normalising and Characterisation Parameters . 43
5.1.2 Instability Mechanism 44
5.2 Effects of Perturbation Pressure 47
5.3 Energy Budget 47
5.3.1 Channel Fluid 49
5.3.2 Flexible Insert 51
5.4 Summary 53

6 Static Single Flexible Insert Non-Dimensional Scheme and Parameterisation 54
6.1 General 54
6.2 Static Scheme Validation 55
6.3 Scheme Sensitivity 59
6.4 Scheme Parameterisation 63
6.5 Parameterisation Sensitivity 64
6.6 Summary 67

7 Dynamic Single Wall Parameterisation Scheme 68
7.1 Dynamic Scheme Validation 68
7.2 Single Flexible Insert Dynamic Parameterisation 69
7.3 Dynamic Behaviour across P_{eff} Values 73
7.4 Stability Surface Dynamic Behaviour Analysis 83
7.5 Stability Surface Energy Budget Analysis 95
7.6 Alternative Non-Dimensional Formulation 105
7.7 Experimental Comparison 106
7.8 Summary 109

8 Dual Flexible Insert Configuration Study 110
8.1 General 110
8.2 Instability Study 110
8.3 Energy Budget 117
8.4 Dual Flexible Insert Non-Dimensional Scheme 122
8.4.1 Dual Flexible Insert Static Non-Dimensional Verification . . . 122
8.4.2 Dual Flexible Insert Dynamic Non-Dimensional Verification . 130

8.5 Summary 136

9 Conclusions **138**
9.1 General 138
9.2 Original Contributions 138
9.3 Single Wall Study 139
9.4 Dual Wall Study 140
9.5 Limitations 140
9.6 Future Research Direction 141

References **143**

Appendix A Fluid Domain Streamlines with No Dimensional Scaling **151**

Appendix B Dynamic Flexible Insert Parameterisation Detailed Study **153**

Appendix C Mesh and Time Independence Study **157**
C.1 Mesh Independence 157
C.2 Time Independence 163

List of Figures

1.1 Schematics of the fluid-structure interaction systems studied with 2-d internal channel flow and flexible insert sections. 2

2.1 Typical experimental setup of the Starling Resistor that represents most theoretical models. The flexible tube cross section is circular at A-A and B-B shows the development of non-circular cross section collapse due to large external pressure wall deformation (Heil and Jensen 2003). 8

2.2 Neutral stability curve in the (C_λ, Re)-space. Branch M-2 goes through points n_5 to n_{11}, branch M-3 goes through n_2 to n_4, and branch M-4 goes through n_1. The system is stable on the left of the branches and the top of M-2, and on the right of branches (below M-2), it is unstable (Luo et al. 2008). 14

3.1 Diagram of the positional history values assignment for newly-created nodes in the FSI problems used in `oomph-lib`. The positional history values of the newly-created nodes (shown in red) are given by the positions they would have had if they had already existed at previous timesteps (oomph-lib 2016). 21

4.1 `oomph-lib` model flexible insert x' and y' positions for small transient deformations from initial condition (red line) and the following decaying oscillations (black lines). 26

4.2 Flexible wall midpoint vertical displacement y'_{mid} vs. time t with oscillations about the mean position with numerical simulations from (a) present `oomph-lib` model, and (b) Heil and Jensen (2003). 27

4.3 Displacement of flexible wall under different case parameters for (a) the Luo et al. (2008) study, and (b) the present `oomph-lib` model. . . 30

4.4 Flexible wall transmural pressure distribution for (a) the Luo et al. (2008) study, and (b) the present `oomph-lib` model. Pressure non-dimensionalisation scheme based on Luo et al. (2008) with $p' = p^*/(\rho^* U^*_{\text{mean}})$. 31

4.5 Fluid flow comparison for (a) the Luo et al. (2008) study streamlines (thin lines) and vorticity contours (thick lines), and (b) the current oomph-lib model streamlines and pressure contours (red-high, blue-low). 32
4.6 oomph-lib large amplitude non-dimensional flexible wall shape comparison with Liu et al. (2009). 36
4.7 oomph-lib large amplitude non-dimensional pressure along the flexible wall comparison with Liu et al. (2009). Pressure non-dimensionalisation scheme based on Liu et al. (2009) with $p' = p^*/(\rho^* U^*_{\text{mean}})$. 37
4.8 Large amplitude non-dimensional flexible wall midpoint y-displacement vs. non-dimensional time comparison with Liu et al. (2009). 38
4.9 Case A mean streamline and pressure contours (red-high, blue-low) comparison between numerical models from Liu et al. (2009) and oomph-lib. The streamlines are clipped at horizontal lengths of 3 and 16 to magnify the streamlines around the deformed wall. 41

5.1 oomph-lib flexible insert midpoint vertical displacement y'_{mid} and maximum vertical displacement y'_{max} time history based on Case A of Liu et al. (2009) study showing the system settling into the unstable saturated oscillation state. 45
5.2 oomph-lib flexible insert results under steady-state conditions (black line) and over one oscillation cycle (red lines) based on Case A of Liu et al. (2009). 46
5.3 Time history of the flexible insert maximum vertical displacement y'_{max} with corresponding fluid streamlines (white), vorticity contour (black) lines and pressure (colour) contours over one instability oscillation cycle based on Case A from the study by Liu et al. (2009). The fluid domain is scaled with a ratio of 1:5 (channel length to height). 48
5.4 oomph-lib system sensitivity to 0.5 and 2.0 times P_{pturb} only affecting initial transient behaviour with no impact on final instability behaviour. 49
5.5 Rate of work/energy plots for the channel fluid domain and its individual components. 50
5.6 oomph-lib rate of work/energy plots for the flexible insert and its individual components. 52

6.1 Static non-dimensional scheme variation testing flexible insert steady-state results overlaid on each other. 58
6.2 Steady-state streamlines (white) and vorticity contour (black) lines with the non-dimensional pressure (colour) contours for select cases looking at static non-dimensional scheme variation validation. The fluid domain is scaled with a ratio of 1:5 (channel length to height). 59

6.3 P_{eff} (case S-1, S-2) and $\text{Ca}_{\text{eff}}/\text{Re}$ (case S-3, S-4) sensitivity tests steady-state flexible insert behaviour results. 61
6.4 Ca_{eff}.Re (case S-5 to S-8) sensitivity tests steady-state flexible insert behaviour results. 62
6.5 Maximum vertical displacement y'_{max} results with $\ln(\text{Ca}_{\text{eff}}/\text{Re})$ and P_{eff} variation. 64
6.6 Maximum vertical displacement $y'_{\text{max}} - 0.1P_{\text{eff}}$ results quadratic best fit line for $\ln(\text{Ca}_{\text{eff}}/\text{Re})$ parameter-space tested. 65
6.7 Maximum vertical displacement $y'_{\text{max}} - 0.1P_{\text{eff}}$ best fit line for $\ln(\text{Ca}_{\text{eff}}.\text{Re})$ parameter space tested. 66
6.8 Maximum vertical displacement $y'_{\text{max}} - 0.1P_{\text{eff}}$ results with sensitivities at $\ln(\text{Ca}_{\text{eff}}/\text{Re})$=-10.1 to -6. 66

7.1 Time history for y' at the steady-state maximum deformation point from simulation start-up showing the system settling into constant oscillations. 69
7.2 Truncated time history for the maximum vertical displacement y'_{max} for various internal parameter variation cases showing the saturated oscillation form. 70
7.3 Flexible insert deformation shape under steady-state conditions (black) and over one oscillation period (red). 71
7.4 Pressure p along the flexible insert under steady-state conditions (black) and over one oscillation period (red). 72
7.5 Contour plot of critical stability for the single flexible insert configuration. 74
7.6 Contour plot of the single flexible insert steady-state maximum deformation. 74
7.7 Critical stability surface with effective pressure P_{eff} variation lines. Solid lines and dashed lines denote the unstable and stable regions of the parameter-space respectively. 76
7.8 Maximum vertical displacement y'_{max} time history for set α effective pressure P_{eff} variation tests. 77
7.9 Maximum vertical displacement y'_{max} time history for set β effective pressure P_{eff} variation tests. 78
7.10 Flexible insert shape over one oscillation for effective pressure P_{eff} variation set α. 79
7.11 Fluid pressure p along flexible insert over one oscillation for effective pressure P_{eff} variation set α. 80
7.12 Flexible insert shape over one oscillation for effective pressure P_{eff} variation set β. 81
7.13 Fluid pressure p along flexible insert over one oscillation for effective pressure P_{eff} variation set β. 82

7.14 Dynamic critical stability lines for test points A to D and Case A of Liu et al. (2009) from Chapter 5. 83
7.15 Flexible insert deformation shape in steady-state (black) and over one saturated oscillation period (red) for critical stability test points A to D. 85
7.16 Flexible insert maximum deformation point location in steady-state (black) and over one saturated oscillation period (red) for critical stability test points A to D. 86
7.17 Pressure p along the flexible insert in steady-state (black) and over one saturated oscillation period (red) for critical stability test points A to D. 88
7.18 Truncated time history of maximum vertical displacement $y'_{\max}$ at the steady-state maximum deformation point for critical stability test points A to D. 89
7.19 Maximum vertical displacement $y'_{\max}$ time history over one saturated oscillation cycle with corresponding streamlines (white), vorticity contours (black) and non-dimensional pressure (colour) contours at various timesteps for critical stability test point A. The fluid domain is scaled with a ratio of 1:5 (channel length to height). 90
7.20 Maximum vertical displacement $y'_{\max}$ time history over one saturated oscillation cycle with corresponding streamlines (white), vorticity contours (black) and non-dimensional pressure (colour) contours at various timesteps for critical stability test point B. The fluid domain is scaled with a ratio of 1:5 (channel length to height). 91
7.21 Maximum vertical displacement $y'_{\max}$ time history over one saturated oscillation cycle with corresponding streamlines (white), vorticity contours (black) and non-dimensional pressure (colour) contours at various timesteps for critical stability test point C. The fluid domain is scaled with a ratio of 1:5 (channel length to height). 93
7.22 Maximum vertical displacement $y'_{\max}$ time history over one saturated oscillation cycle with corresponding streamlines (white), vorticity contours (black) and non-dimensional pressure (colour) contours at various timesteps for critical stability test point D. The fluid domain is scaled with a ratio of 1:5 (channel length to height). 94
7.23 Test point A rate of work/energy plots for the channel fluid domain and its individual components. 96
7.24 Test point B rate of work/energy plots for the channel fluid domain and its individual components. 97
7.25 Test point C rate of work/energy plots for the channel fluid domain and its individual components. 98
7.26 Test point D rate of work/energy plots for the channel fluid domain and its individual components. 99

7.27 Test point A rate of work/energy plots for the flexible insert and its individual components. 100
7.28 Test point B rate of work/energy plots for the flexible insert and its individual components. 101
7.29 Test point C rate of work/energy plots for the flexible insert and its individual components. 102
7.30 Test point D rate of work/energy plots for the flexible insert and its individual components. 103
7.31 Alternative formulation for critical stability lines using C_λ and Re based on the approach by Luo et al. (2008). 105
7.32 Current numerical study critical stability surface (red lines) and experimental data points denoting unstable cases (blue dots). 108
7.33 Experimental data points denoting unstable cases (blue dots) and dynamic critical stability lines for $P_{\text{eff}} = 0.23$ & 0.25. The P_{eff} lines are shown to compare with the respective experimental case points. 108

8.1 Flexible insert y'_{max} vs. time t for the top and bottom flexible insert showing two stages of saturated oscillation states. 112
8.2 Stage 1 (symmetric state) top flexible insert behaviour under steady-state conditions (black line) and over one unstable oscillation cycle (red lines) for a dual flexible wall configuration unstable case at $\text{Ca}_{\text{eff}}.\text{Re} = 1.0$, $\text{Ca}_{\text{eff}}/\text{Re} = 10^{-4}$ and $P_{\text{eff}} = 0.05$. 114
8.3 Stage 2 (non-symmetric state) flexible wall comparison between the top and bottom wall. The steady-state conditions (black line) and over one unstable oscillation cycle (red lines) for a dual flexible wall configuration unstable case at $\text{Ca}_{\text{eff}}.\text{Re} = 1.0$, $\text{Ca}_{\text{eff}}/\text{Re} = 10^{-4}$ and $P_{\text{eff}} = 0.05$. 115
8.4 Stage 2 (non-symmetric state) pressure along the flexible inserts comparison between the top and bottom wall. The steady-state conditions (black line) and over one unstable oscillation cycle (red lines) for a dual flexible wall configuration unstable case at $\text{Ca}_{\text{eff}}.\text{Re} = 1.0$, $\text{Ca}_{\text{eff}}/\text{Re} = 10^{-4}$ and $P_{\text{eff}} = 0.05$. 116
8.5 Stage 1 (symmetric state) bottom wall variation of the maximum vertical displacement y'_{max} over one unstable oscillation cycle at effective pressure $P_{\text{eff}} = 0.05$. Marked with crosses 'x' are the time steps when snapshots of the fluid domain are shown with the streamlines (white), vorticity contour (black) lines and the non-dimensional pressure (colour) contours. The fluid domain is scaled with a ratio of 1:5 (channel length to height). 118

8.6 Stage 2 (non-symmetric state) upper and lower wall variation of y' over one unstable oscillation cycle for the steady-state maximum deformation point at $P_{\text{eff}} = 0.05$. Marked with crosses 'x' are the time steps when snapshots of the fluid domain are shown with the streamlines (white), vorticity contour (black) lines and the non-dimensional pressure (colour) contours. The fluid domain is scaled with a ratio of 1:5 (channel length to height). 119
8.7 `oomph-lib` rate of work/energy plots for the channel fluid domain and its individual components. 121
8.8 Rate of work/energy plots for the dual flexible insert and its individual components. 123
8.9 Flexible insert rate of work comparison between top and bottom wall. 124
8.10 Flexible insert behaviour for non-dimensional scheme verification keeping parameters $\text{Ca}_{\text{eff}}.\text{Re} = 1.0$, $\text{Ca}_{\text{eff}}/\text{Re} = 10^{-4}$ and $P_{\text{eff}} = 0.05$ constant while varying internal dimensional parameters. The base case and variations V-1 to V-6 are overlaid on each other. 125
8.11 Dual wall flexible insert channel fluid streamlines (white) and vorticity contour (black) lines and non-dimensional pressure colour contours for steady-state (static) non-dimensional scheme verification comparing the base case and variation test cases V-3 and V-6. The fluid domain is scaled with a ratio of 1:5 (channel length to height). 126
8.12 Flexible insert deformation and pressure behaviour for non-dimensional scheme sensitivity test cases S-1 to S-4 comparison with base case. . . 128
8.13 Flexible insert deformation and pressure behaviour for non-dimensional scheme sensitivity test cases S-5 to S-8 comparison with base case. . . 129
8.14 Flexible insert top wall maximum vertical displacement y'_{max} time history for non-dimensional scheme verification keeping parameters $\text{Ca}_{\text{eff}}.\text{Re} = 1.0$, $\text{Ca}_{\text{eff}}/\text{Re} = 10^{-4}$ and effective prssure $P_{\text{eff}} = 0.05$ constant while varying internal dimensional parameters. The base case and variation cases V-1 to V-6 are overlaid on each other. 131
8.15 Dual wall flexible insert deformation shape during steady-state (black line) and dynamic instability over one oscillation period (red lines) comparing the base case and sample variation test cases V-3 and V-6. . 132
8.16 Pressure p along the dual wall flexible insert during steady-state (black line) and dynamic instability over one oscillation period (red lines) comparing the base case and sample variation test cases V-3 and V-6. . 133
8.17 Transient oscillations of the flexible insert maximum vertical displacement y'_{max} vs. time t for the base case (unstable) and cases S-7 (stable) and S-8 (unstable). 134

8.18 Dual wall flexible insert deformation shape during steady-state (black line) and dynamic instability over one oscillation period (red lines) comparing the base case and unstable sensitivity test case S-8. 134
8.19 Pressure p along the dual wall flexible insert during steady-state (black and dynamic instability over one oscillation period (red lines) comparing the base case and unstable sensitivity test case S-8. 135

A.1 Time history of the flexible insert maximum vertical displacement $y'_{\max}$ with corresponding fluid streamlines (white lines), vorticity lines (black lines) and pressure contours over one instability oscillation cycle based on Case A from the study by Liu et al. (2009) with no scaling of the fluid domain dimensions. 152

B.1 Dynamic single flexible insert stability at effective pressure $P_{\text{eff}} = 0.20$. 154
B.2 Dynamic single flexible insert stability at effective pressure $P_{\text{eff}} = 0.24$. 154
B.3 Dynamic single flexible insert stability at effective pressure $P_{\text{eff}} = 0.30$. 155
B.4 Dynamic single flexible insert stability at effective pressure $P_{\text{eff}} = 0.40$. 155
B.5 Dynamic critical stability lines. 156

C.1 Undeformed channel with various levels of mesh densities for testing mesh independence. The fluid domain is scaled with a ratio of 1:5 (channel length to height) for visualisation purposes. 158
C.2 Steady-state deformed channel with velocity vector colour contours with various levels of mesh densities for testing mesh independence. The fluid domain is scaled with a ratio of 1:5 (channel length to height). 160
C.3 Flexible insert results under steady-state conditions comparison for different mesh densities. 161
C.4 Maximum vertical displacement point $y'_{\max}$ time history based on Case A of Liu et al. (2009) for the mesh independence study. 162
C.5 Dynamic simulation results for different timestep sizes based on the $y'_{\max}$ time history of Case A from Liu et al. (2009) for the time independence study. 164
C.6 Dynamic simulation flexible insert results at the minimum (trough) $y'_{\max}$ position for different analysis timestep sizes. 165

List of Tables

3.1 Scaling quantities for non-dimensionalisation. 16
3.2 Non-dimensional quantities. 16

4.1 Dimensional and non-dimensional parameters for `oomph-lib` model small-amplitude deformation validation against Heil and Jensen (2003). 25
4.2 Steady state solution flexible deformation validation - dimensional and non-dimensional parameters for Luo et al. (2008) study comparison. . 28
4.3 Selected test points with C_λ parameter variation from Luo et al. (2008). 28
4.4 Numerical model details for steady and transient large deformation study by Liu et al. (2009) and `oomph-lib`. 33
4.5 Dimensional and non-dimensional parameters for large deformation transient validation against Liu et al. (2009). 34
4.6 Liu et al. (2009) flexible wall midpoint y-displacement comparison with `oomph-lib`. 39
4.7 Liu et al. (2009) frequency comparison with `oomph-lib`. 39

5.1 Non-dimensional average rates of energy and work for overall flexible insert and channel fluid over one oscillation cycle. 51
5.2 Non-dimensional average rates of energy and work for the flexible insert. 53

6.1 Static non-dimensional scheme validation base case parameters. . . . 56
6.2 Static non-dimensional scheme variations test parameters. 57
6.3 Static non-dimensional scheme variation test results. 57
6.4 Static non-dimensional scheme sensitivity test parameter variations. . 60
6.5 Static non-dimensional scheme test results for sensitivity cases S-5 to S-8. 63
6.6 Parameter variations for static non-dimensional scheme sensitivity test. 65

7.1 Dynamic non-dimensional scheme validation variation results. 69
7.2 Dynamic non-dimensional scheme parameter test limits. 70
7.3 Dynamic test parameters for effective pressure P_{eff} variation. 75
7.4 Dynamic simulation test results for effective pressure P_{eff} variation sets α and β while keeping $\text{Ca}_{\text{eff}}/\text{Re}$ and $\text{Ca}_{\text{eff}}.\text{Re}$ constant. 76
7.5 Detailed dynamic analysis test point non-dimensional parameters. . . 84

7.6 Detailed dynamic analysis oscillation results for test points A to D. . . 87
7.7 Average rates of work and energy for overall flexible insert and channel fluid for test points A to D. 104
7.8 Average rates of potential energy for flexible insert for test points A to D. 104
7.9 Average rates of work for flexible insert for test points A to D. 104
7.10 Dimensional and non-dimensional parameters for experimental studies showing oscillatory instability onset. 107

8.1 Base case dimensional and non-dimensional validation parameters for dual flexible wall system stability testing. 111
8.2 Dual wall dynamic stability test results with variation of effective pressure P_{eff} and external pressure P^*_{ext}. 111
8.3 Average rates of work and energy for the overall flexible insert and channel fluid for the symmetric and non-symmetric unstable oscillation stages. 120
8.4 Average rates of potential energy for the dual flexible inserts. 122
8.5 Average rates of work and energy for the dual flexible inserts. 122
8.6 Dual wall configuration non-dimensional scheme validation variations. 124
8.7 Maximum deformation and percentage difference results for dual wall configuration static non-dimensional scheme verification. 126
8.8 Non-dimensional scheme sensitivity variations for the dual wall configuration. 127
8.9 Non-dimensional scheme sensitivity results for the dual wall configuration. 130
8.10 Dual wall dynamic non-dimensional scheme validation results. 130
8.11 Dual wall configuration dynamic behaviour results for Ca_{eff}.Re sensitivity. 136

B.1 Critical stability line formulae for various effective pressure P_{eff} values. 154

C.1 Mesh density (number of cells) along channel length dimensions for various mesh densities. 157
C.2 Dynamic simulation results comparison based on y'_{max} for testing sensitivity of different timestep sizes. 163

Nomenclature

Roman Symbols

Ca	Cauchy number
$\mathrm{Ca}_{\mathrm{eff}}$	Effective Cauchy number
A	Beam centerline position after deformation
a	Beam centerline position before deformation
A_{peak}	Peak-to-peak amplitude at flexible insert maximum deformation point
B	Flexural rigidity
C	Beam centerline curvature after deformation
c	Beam centerline curvature before deformation
C_λ	Non-dimensional wall stiffness
D_{fluid}	Fluid dissipation
E	Young's modulus
E_{eff}	Effective Young's modulus
f	Flexible insert oscillation frequency
H	Channel height
h	Flexible insert thickness
KE_{fluid}	Fluid domain kinetic energy
KE_{IO}	Channel boundary (inlet and outlet) kinetic energy
KE_{wall}	Flexible insert kinetic energy
L_{down}	Channel downstream section length
L_{flex}	Channel flexible insert section length

L_{total} Total channel longitudinal length

L_{up} Channel upstream section length

N Eulerian components of outer unit normal on the fluid domain boundary

p Pressure

P'_{ext} Non-dimensional external pressure as defined in Luo et al. (2008)

p' Alternative pressure normalisation based on $p^*/(\rho^* U^*_{\text{mean}})$

P_{down} Flexible insert downstream-end pressure

P_{eff} Effective pressure acting on the flexible insert

P_{entry} Channel entry (inlet) pressure

P_{exit} Channel exit (outlet) pressure

P_{ext} Applied uniform external pressure on flexible insert

P_{pturb} Temporary external pressure to generate system perturbation

P_{temp} Temporary applied external pressure to negate mean fluid pressure

P_{up} Flexible insert upstream-end pressure

PE_{axial} Axial potential energy

PE_{bend} Bending potential energy

Q Fluid pressure scale ratio

R Flexible insert cross-sectional area

s Infinitesimal flexible insert section

T Flexible insert pre-tension

t Time

T_{natural} Time scale

U_{mean} Fluid mean velocity

W_{IO} Work at boundary (inlet and outlet)

W_{Pext} Work by external pressure P_{ext}

$W_{\text{wall,n}}$ Normal fluid traction component of work on flexible insert

$W_{\text{wall,p}}$ Pressure component of work on flexible insert

$W_{\text{wall,t}}$ Tangential fluid traction component of work on flexible insert

W_{wall} Work on flexible insert

x x-coordinate

x'_{max} Local x-coordinate relating to maximum deformation point location

x' Local x-coordinate along flexible insert

y y-coordinate

y' Local y-coordinate of flexible insert displacement

y'_{max} Local y-coordinate of flexible insert maximum displacement point η_{max}

y'_{mid} Flexible wall midpoint vertical displacement

1-d One-dimensional

2-d Two-dimensional

3-d Three-dimensional

$\mathbf{e}$ Unit vector

$\mathbf{f}$ Applied traction along length of flexible insert

$\mathbf{N}$ Beam centerline

$\mathbf{R}_{\text{w}}$ Flexible wall displaced position

$\mathbf{r}_{\text{w}}$ Flexible wall undeformed position

$\mathbf{V}$ Velocity vector

Re Reynolds number

St Strouhal Number

Roman Dimensional Symbols

B^* Flexural rigidity (N.m)

E^* Young's modulus (Pa)

E^*_{eff} Effective Young's modulus (Pa)

H^* Channel height (m)

h^* Flexible insert thickness (m)

L^*_{down} Channel downstream section length (m)

L^*_{flex} Channel flexible insert section length (m)

L^*_{total} Total channel longitudinal length (m)

L^*_{up} Channel upstream section length (m)

p^* Pressure (Pa)

P^*_{mean} Mean fluid pressure acting on the flexible insert

P^*_{entry} Channel entry (inlet) pressure (Pa)

P^*_{ext} Applied uniform external pressure on flexible insert (Pa)

P^*_{pturb} Temporary external pressure to generate system perturbation (Pa)

R^* Flexible insert cross-sectional area (m^2)

t^* Time (s)

T^*_{natural} Time scale (s)

U^*_{mean} Fluid mean velocity (m/s)

Greek Symbols

η_{max} Flexible insert maximum deformation point

Γ Inlet and outlet boundaries

γ Strain tensor

κ Bending tensor

Λ^2 Non-dimensional wall density

μ Fluid dynamic viscosity

ν Poisson's ratio

Ω Fluid domain

$\rho^*_{\text{s}}/\rho^*_{\text{f}}$ Solid-to-fluid density ratio

ρ_{f} Fluid density

ρ_{s} Solid (flexible insert) density

σ_0 Flexible insert pre-stress

ξ Flexible insert undeformed Lagrangian coordinate

Greek Dimensional Symbols

μ^* Fluid dynamic viscosity (Pa.s)

ρ_f^* Fluid density (kg/m^3)

ρ_s^* Solid (flexible insert) density (kg/m^3)

σ_0^* Flexible insert pre-stress (Pa)

Superscripts

$\dot{N}$ Rate of 'N'quantity (work or energy)

$\overline{\dot{N}}$ Average rate of 'N'quantity (work or energy)

Subscripts

$_1$ Horizontal component

$_2$ Vertical component

$_{i,j}$ Vector components

Acronyms / Abbreviations

`oomph-lib` Object-oriented multi-physics finite-element library

ADINA Automatic Dynamic Incremental Nonlinear Analysis

BDF Backward differentiation formulae

FBM Fluid-beam model

FSI Fluid-structure interaction

NASA National Aeronautics and Space Administration

Chapter 1

Introduction

Fluid-structure interaction (FSI) is prevalent throughout Nature. FSI is of great interest to engineers because the combination of solid and fluid mechanics results in rich and interesting system dynamics. This is particularly true for the case of fluid flow in flexible tubes or pipes. The flexible pipe is a structure which conveys fluid. It may be strong and stiff when subjected to tension but compliant when subjected to bending or compression. This seemingly simple system has deep underlying complexities in terms of the interactions between the fluid and a highly elastic structure. A schematic of the main study configuration is illustrated in Figure 1.1a showing velocity-driven 2-d channel flow with a flexible wall section along one of the rigid channel walls. The aim of this work is to characterise this FSI behaviour when subjected to large wall deformations through the action of an external pressure applied on the flexible insert. It is of particular interest to understand the FSI behaviour when the system is unstable, where the flexible insert experiences self-sustaining cyclic oscillations. A study is also performed for a second configuration with the addition of another geometrically independent flexible insert on the opposing channel wall as shown in Figure 1.1b. The purpose of this is to see if the FSI behaviour observed for the single flexible insert configuration also occurs in this dual flexible insert configuration.

1.1 Motivations

This system configuration of fluid flowing through pipes or tubes is generic. There are many examples of such configurations observable in real-world situations. Two areas identified to be of practical use for engineering research at present are industrial and biomechanical engineering. Better understanding of this system will add to the body of fundamental engineering knowledge in these areas.

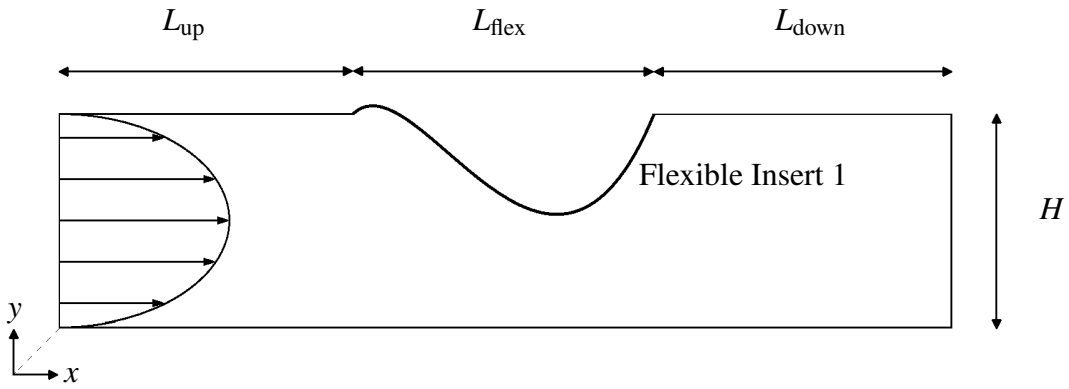

(a) Single flexible insert

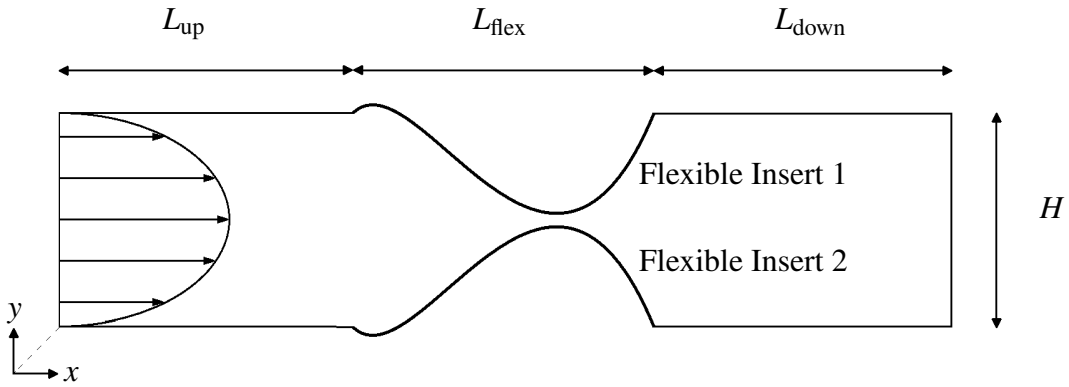

(b) Dual flexible insert

Figure 1.1 Schematics of the fluid-structure interaction systems studied with 2-d internal channel flow and flexible insert sections.

1.1.1 Industrial Engineering

The use of pipes as a delivery mechanism is widespread in industrial applications for fluid transport such as water, oil and gas. It is noted, however, that the majority of industrial pipes are rigid and made of either steel, aluminium or polymer composites (Hollaway 1993). A straight line is simply the most efficient method of transport between two points and high levels of pipe flexibility is not desirable. Initial work on fluid flow through pipes was driven by vibration problems in the transport of crude oil using pipelines. One of the earliest studies was by Dodds and Runyan (1965) for the National Aeronautics and Space Administration (NASA). These systems have varying degrees of flexibility depending on the lengths between pipe supports. Generally in these applications, the requirement is to determine the possibility of instability, and if present, understand its mechanisms and mitigate them.

Notable early works in this area looked at simply supported thin cylindrical shells under conditions of pulsatile flow, resonant harmonic motion and nonlinear axisymmet-

ric free vibration (Ginsberg 1973a, 1973b, 1974). These studies showed the possibility of static and dynamic instabilities. The study by Ting and Hosseinipour (1983) also showed dynamic instability occurring for both a simply supported and hanging cantilever pipe. The study by Holmes (1978) arrived at the contrary conclusion that flutter motion was impossible with the configuration of pipes supported at both ends. Arguments for both sides have followed with significant insights being produced through the series of studies by Païdoussis et al. since 1972 (Païdoussis and Denise 1972). A comprehensive set of studies was conducted for the simply supported configuration showing the possibility of non-linear dynamic instability occurring by Amabili et al. (1999a, 1999b, 2000a, 2000b, 2010). Recent studies of dynamic motions of a cantilevered pipe have been conducted by looking at three-dimensional motion with various boundary conditions, as well as spring and mass attachments (Wadham-Gagnon et al. 2007a, Païdoussis et al. 2007b, Modarres-Sadeghi et al. 2007c, Ghayesh et al. 2013).

There are instances where flexible pipes or tubes are necessary. Short flexible pipe sections are called jumpers and function to transfer fluid between separate pieces of equipments over short distances (Bai and Bai 2012). The pipe flexibility allows for relative equipment movement. This is for engineering design purposes to account for required equipment placement, manufacturing tolerances and installation misalignment. It could also be to accommodate operational equipment deformation due to thermal expansion and vibrations.

1.1.2 Biomechanical Engineering

In recent decades, investigation of flexible tubes has garnered increasing interest in the field of biomechanical engineering due to its relevance to physiological applications. All macroscopic organisms use flexible conduit systems to transport biofluids internally. This is also true of the human body where flexible conduit systems are universal. The study of large deformation flexible tubes are of particular interest as they are responsible for many biological functions. Examples of these are the arterial, venous, lymphatic, pulmonary airway and urinary systems. A comprehensive description of these biomechanical applications was undertaken by Wootton and Ku (1999).

Flexibility has a particular benefit in these sytems through its ability to accomodate skeletal bending and assist in the function of blood distribution by a beating heart (Bertram 2009). Normal arterial flow is laminar but under certain circumstances artherosclerotic disease causes localised narrowing of the artery lumen, resulting in turbulence (Ku 1997). Hemodynamics through the inferior vena cava which returns blood to the heart from the lower parts of the body was studied by Gardner et al. (1977). Venous fluid flow regimes were described using a mathematical model by Griffiths (1971c). It has been found that spontaneous collapse of veins above the heart can occur due to hydrostatic reduction of blood pressure (Bertram 2009). Studies have also been

extended to animals to characterise blood flow in jugular veins of upright giraffes with specific consideration of gravity-driven flows (Brook et al. 1999, 2002).

A study of the micturition for both sexes was undertaken by performing experiments to measure flow characteristics as the basis for developing theoretical models of the urethra (Griffiths 1969a, 1969b, 1971a,1971b).

It is found that limitation of expiratory flow is controlled by flow-induced collapse of the pulmonary airways. Wheezing during forced expiration and production of Korotkoff sounds during sphygmomanometry are believed to be generated by self-excited oscillations of the vessel walls and their interaction with the fluid flow (Heil and Waters 2008).

Research on the FSI in these systems can help in developing better understanding of human physiology and generating potential solutions to ailments.

1.2 Objectives and Methodology

The overall objective of this work is to characterise the FSI behaviour of the system configuration with fluid flowing through a two-dimensional (2-d) channel with a large deformation flexible insert (as illustrated in Figure 1.1a). This study was conducted using numerical methods with the software package `oomph-lib` (Object-oriented multi-physics finite-element library). The main objective can be divided into several sub-objectives which are:

1. Validation of the `oomph-lib` single flexible insert model by reproducing published steady-state and transient FSI numerical results.

2. Formulation based on a reduced set of non-dimensional parameters to uniquely characterise the FSI mean-state (static) and dynamic behaviour.

3. Derivation of simple expressions to predict the static maximum wall deflection and the occurance of dynamic instability.

4. Detailed analysis of particular cases to describe the different underlying instability mechanisms.

5. A second configuration is analysed with an additional flexible wall, with identical properties, inserted on the opposing channel wall as illustrated in Figure 1.1b. The purpose of this is to analyse the FSI behaviour and compare between the single and dual insert cases.

1.3 Thesis Outline

This thesis consists of nine chapters which address the objectives based on the methodology described above. The chapters are summarised as follows.

Chapter 1 - The current chapter provides a broad overview on the FSI area of flexible insert channel flow, the motivation behind the work, objectives of the work and an outline of the thesis.

Chapter 2 - A literature review covering previous investigations of the FSI of internal channel or pipe flow with a focus on tubes with flexible sections and their instability mechanisms is presented. The review looks at experimental, analytical and numerical studies. Particular attention is directed at 2-d formulations and the instability behaviours observed and related theories. This will be the basis of further investigation and developing further system understanding.

Chapter 3 - The system governing equations are presented for the flexible insert, internal fluid and FSI. The numerical implementation and various inputs within `oomph-lib` are discussed.

Chapter 4 - The various validations performed on the single flexible insert `oomph-lib` model are explained. The steady (static) and transient (dynamic) behaviour of the flexible insert and channel fluid flow is compared to published data. This includes validation against a small deformation transient study and large deformation steady and transient studies.

Chapter 5 - A case with large deformation transient unstable oscillation is analysed in detail from the previous validation section and the simulations extended to the long-term evolution of the oscillations. The system energetics are also analysed by characterising the energy transfer between the flexible insert and fluid flow.

Chapter 6 - A comprehensive parametric study of the static system is performed with variations of the three main system components; the internal fluid flow, flexible insert and external pressure applied. A non-dimensional scheme is proposed and tested to satisfy variations in all three parameters. The main metrics for measurement is the static flexible insert shape.

Chapter 7 - The system parameters study is extended to transient behaviour. The same non-dimensional scheme is applied to the variation of the three system components. This is the basis for developing a stability surface plot that predicts system

stability for variation of system parameters within the laminar flow region for large wall deformations. Comparison is performed with previously published parametric study and experimental works.

Chapter 8 - The symmetric dual flexible wall configuration is analysed, subjected to the same steady and transient behaviour tests. The purpose is to compare instability types between the single and dual wall cases and test whether the non-dimensional scheme is still applicable. This is limited to relatively large wall deformation cases.

Chapter 9 - A summary of the overall work is provided along with key conclusions. Limitations of the current work and potential avenues of future work are also discussed.

Chapter 2

Literature Review

A literature review is performed on previous studies of flows through collapsible tubes. This includes both experimental testing and development of numerical models of this system. Particular attention is given to system behaviours and current theories of system stability for 2-d internal flows which is the focus of this thesis. A comprehensive review of knowledge on this subject has been undertaken by Grotberg and Jensen (2004), Heil and Hazel (2011) and Jensen (2013).

2.1 Experimental Studies

One of the earlier experimental investigations on pipe instabilities was by Dodds and Runyan (1965) who observed static divergence when a critical fluid velocity is achieved in a simply supported pipe setup. With increasing interest in biomechanical applications, experimental studies then gravitated towards more flexible tubes collapsing to non-circular cross-sectional shapes. This was of interest as it more closely replicated biological conduits. The large deformations were achieved with the external pressure exceeding the internal tube pressure. Under such conditions, phenomena such as flow rate limitation and self-excited oscillations are observed. These phenomena have been shown experimentally for both thin-walled and thick-walled tubes studies.

The classical Starling Resistor experiment was first introduced by Knowlton and Starling (1912). A schematic of the Starling Resistor is shown in Figure 2.1 (Heil and Jensen 2003). In this experimental setup, a thin-walled elastic tube is mounted between two rigid tubes inside a pressure chamber. This elastic tube is typically made of latex rubber. Fluid is then driven through the tube, usually water or air. There are two methods to control this system. The first is by controlling the pressure drop ($P_{\text{entry}} - P_{\text{exit}}$) between the rigid tube ends. The second is by controlling the flow rate through the tube. These consitute the two different driving mechanisms; pressure-driven or flow/velocity-driven. The external pressure P_{ext} can be controlled independently. The elastic tube buckles non-axisymmetrically if P_{ext} is sufficiently larger than the

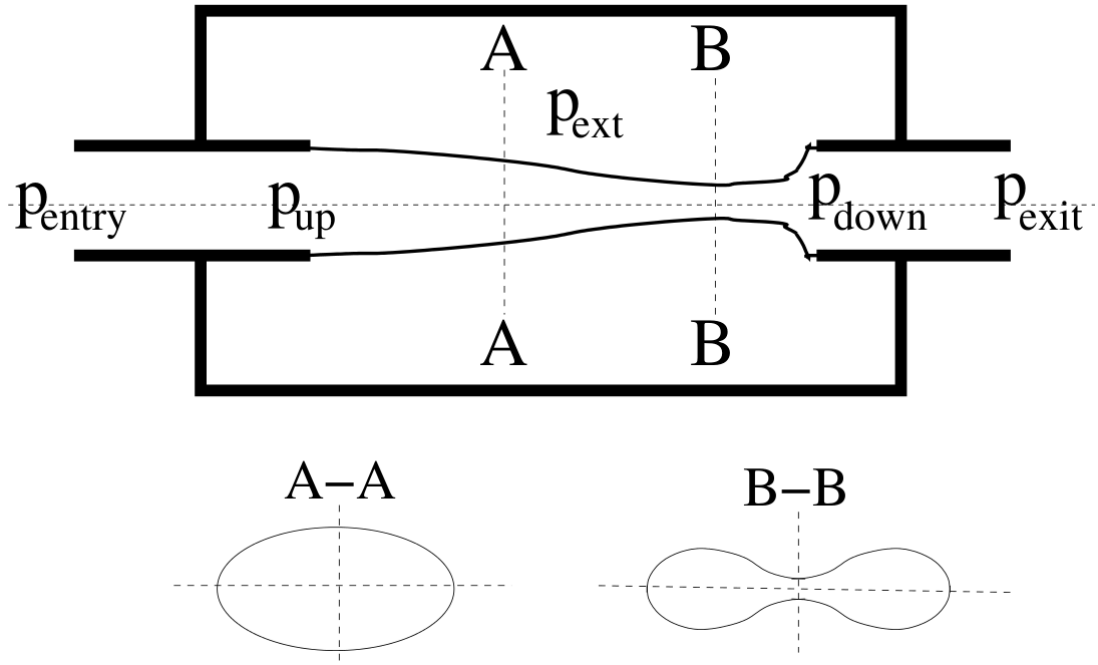

Figure 2.1 Typical experimental setup of the Starling Resistor that represents most theoretical models. The flexible tube cross section is circular at A-A and B-B shows the development of non-circular cross section collapse due to large external pressure wall deformation (Heil and Jensen 2003).

internal tube fluid pressure. In this state and at sufficiently large Reynolds numbers Re, the fluid-structure interaction (FSI) then leads to the elastic tube fluttering (Heil and Jensen 2003).

The phenomena of flexible tube collapse and oscillations was reported by Conrad (1969) with a steady flow setup. Experiments were performed by Kececioglu et al. (1981) using a thin-walled compliant tube under a partially collapsed state due to negative transmural pressure at steady, supercritical flow. With logitudinal tension applied, it was shown that a train of standing waves appear upstream of the local disturbance created by the collapsed tube section. In the absence of longitudinal tension and bending stiffness, variations in streamwise velocity is still observed due to the action of gravity, friction and external pressure gradients (Shapiro 1977). Flutter in collapsible thick-walled latex and silastic tubes were reported by Gavriely et al. (1989) with a setup of high-impedance vacuum pump connected at the downstream end. Tube oscillations with loud honking sounds was observed when the tubes were buckled and flow-limiting. Flow rate limitation and flow-induced oscillations were also shown using the Starling Resistor in the work by Bertram (1982, 1986). Variation in tube length showed longer tubes had a higher tendency of displaying dynamic oscillatory behaviour whereas shorter length tubes are more likely to be divergently unstable (Bertram et al. 1990). The effects of controlling the upstream transmural pressure was investigated in Bertram and Castles (1999) and the downstream outlet pressure

by Wang et al. (2009) showed the conditions of flow limitation and oscillation onset. The work by Truong and Bertram (2009) showed the flow-field downstream of the collapsed section could be measured with a higher degree of resolution using high-speed particule image velocimetry. A wall thickness comparison showed that thick and thin wall cases exhibited flow rate limitation but the thin wall case experienced larger amplitude self-excited oscillation (Bertram and Elliott 2003). In Bertram and Tscherry (2006), the role of fluid viscosity variation through a mixture of water and glycerine was investigated showing oscillation amplitudes gradually descreased to zero by increasing fluid viscosity. Through this extensive body of experimental work, it is clear that a compressed flexible tube which conveys fluid is susceptible to flow-induced instabilities, and it is therefore of interest to represent this system theoretically and better understand its driving mechanisms.

2.2 Numerical Model Development

The experimental work described in the previous section is complemented by the development of theoretical models in attempts to describe the physical phenomena with the earliest being lumped parameter models. The work by Katz et al. (1969) highlighted the importance of the role of transmural pressure in the flexible tube collapse and attempted to link the relationship between cross-sectional area, transmural pressure and the energy loss coefficient. The numerical results were confirmed against the experimental results for both steady and transient flow conditions. Progress was also made in using lumped parameter models for the study of human physiology by creating a cardiovascular model and comparing against measured clinical data (Li et al. 2002, Shim et al. 2004). These models successfully captured many important flow characteristics, for instance, the fluid flow behaviour in the rigid wall sections of the flexible insert channel system (refer to Figure 1.1a). However these models fail to capture key behaviours like wave propagation and dissipation (Bertram and Pedley 1982, Heil and Jensen 2003).

This resulted in the development of more sophisticated 1-dimensional models which added more mechanical considerations in the modelling. The work by Mcclurken et al. (1981) attempted to approximate the tube mechanics with longitudinal bending and tension considered, and is the accompaniment to the experimental in Kececioglu et al. (1981). Effects of fluid viscosity was accounted for in the work by Bonsignori and Salvini (1985) and logitudinal wall tension and downstream flow separation energy by Cancelli and Pedley (1985). Small, time-dependent perturbations were then introduced to steady flows by Jensen (1990), which identified three distinct instability modes with strong correlation with the separation point motion. Study of unsteady flow showed the possibility of rolling waves occuring (Brook et al. 1999). The master thesis work by Ghomeshi (2003) demonstrated static divergence when coupled with consideration of

the wall inertia predicted infinite wave speed. The approximate analytical solution for locating the points of flow separation and re-attachment for low Reynolds number is provided in Wijeratne and Hoo (2007). The flexible wall sections experiencing unstable oscillation behaviour could be amplified from wave reflections of the rigid sections. This behaviour involved the interaction of travelling wave flutter and static-divergent modes (Stewart et al. 2009). Using the approach of the Lie group method, a complete symmetry classification was performed by Molati and Mahomed 2012 considering logitudinal tension and tube wall curvature. Different mechanisms of flexible insert oscillation instability driven by divergence and resonance were introduced in Xu et al. (2013) and Xu et al. (2014) respectively. The experimental measurements from giraffe arteries and veins were compared with a 1-d model and showed qualitatively consistent results (Pedley and Pihler-Puzović 2015). The 1-d model uses partial differential equations to describe the mass and momentum conservation with coupling through a local pressure and area relationship (Grotberg and Jensen 2004). 1-d models capture the wave propagation behaviours and dissipation due to internal flow separation. These are aspects critical to the generation of self-excited oscillations or flutter (Heil and Jensen 2003). The 1-d models, however, are limited by the need for some *ad hoc* assumptions. Improvement on these models is therefore limited.

2-d models are free of this limitation and have seen great success in providing insights into more complex FSI behaviours. An example is the model developed by Heil and Jensen (2003) which consists of solving the 2-d Navier-Stokes equation for fluid flow and is fully coupled with the solid solver. The solid can be modelled as a compliant panel or membrane for characterising small or large wall deformations respectively. The 2-d model is a useful and suitable model to capture the rich FSI dynamics observed experimentally. There is also still much more to understand regarding the 2-d system as evidenced by significant developments by Luo and Pedley in their series of investigations from 1995 onwards (discussed in more detail in the following sub-section); Luo and Pedley (1995a), Pedley and Luo (1998a), Luo and Pedley (1998b), Luo and Pedley (2000), Luo et al. (2008), Liu et al. (2009), and Heil and Jensen (2003).

A fully coupled 3-d model is necessary to more accurately replicate the Starling resistor experiment findings. One of the earliest attempts was by Rosar (1994) where partial tube collapse was observed but not instability oscillations. There have been some recent successes in development of 3-d models. The study by Hazel and Heil (2003) used finite-element methods to couple the FSI system. The flexible wall is characterised by geometrically nonlinear Kirchoff-Love shell theory to capture large deformations and small strains and the internal fluid flow is described using the 3-d Navier-Stokes equation. The work by Scroggs et al. (2004) found that it was necessary to simulate the physical experiment startup loading sequence to achieve the final collapsed tube shape. Wall thickness was investigated by Marzo et al. (2005) with good agreement shown between the modelling of the flexible tube using solid elements and thin-shell elements. A

model capable of accommodating large strain and displacement for the incompressible isotropic neo-Hookean material of the thick-walled flexible tube was used by Zhu et al. (2013) to model tube collapse. Self-excited oscillations were simulated by Heil and Waters (2008) and the critical Re determined where energy is extracted from the fluid by the flexible tube. Then in the work by Heil and Boyle (2010) it was shown that self-excited oscillations tend to arise from steady equilibrium configurations in which the flexiblte tube is buckled non-axisymmetrically. Though these studies are important and insightful in their own right, they are limited to steady flow, small deformation instabilities or buckling analysis. The limitation is due to very high computational costs. However it is noted that with the ongoing improvement in computational power they will follow the trend of the current increase in 2-d studies and be more feasible in the near future.

For the present, the ability to generate meaningful parameter-space relationships and system understanding comes at a more reasonable computation cost in the 2-d space than a fully-coupled 3-d formulation. Therefore, the 2-d model is the subject of the current study. The following section describes specific developments in the bounded flow category of 2-d models.

2.3 2-Dimensional Bounded Flow

The term bounded flow relates to a finite or bounded system where the flexible insert has a finite extent that can in principle undergo large-amplitude deformation of which the previously discussed Starling Resistor qualifies. The 2-dimensional collapsible channel model shown in Figure 1.1a was developed by Pedley (1992) to replicate the instabilities observed through the Starling resistor experiments. It consists of a 2-dimensional (2-d) channel with one segment of the wall replaced by a membrane under longitudinal tension. There are practical difficulties in producing the 2-d flow experimentally. However it still has considerable theoretical advantages as it avoids the complications of fully 3-d flows found in the Starling Resistor while exhibiting flow limitation and self-excited oscillations (Heil and Jensen 2003). A review of research findings of this flow configuration is discussed in Pedley and Luo (1998a).

A significant number of studies have been performed on the configuration with small compliant insert deformation relative to channel height. Davies and Carpenter (1997) replaced the membrane with a compliant panel. The compliant panel is spring-backed and constrained to move only in the vertical direction whereas the membrane does not have this restriction. Through their computational formulation of linearised Navier-Stokes equations they were able to show the interaction between Tollmien–Schlichting and Travelling Wave Flutter instability modes.

Guneratne (1999, 2006) studied a membrane flexible insert in high Reynolds-number flow with external pressure $P_{\text{ext}} = 0$ and membrane tension T, but without bending

stiffness, in steady flows using interactive boundary-layer theory. This work identified static eigenmodes occuring due to static divergence instability (Grotberg and Jensen 2004). It was also found that instability occured with the growth rate increasing with T as the problem was ill-posed. By fixing the pressure difference downstream at zero, the problem is well-posed and this produced all stable solutions (Kudenatti et al. 2012).

Huang (2001) applied a P_{ext} value that maintains steady flow over a low tensioned membrane with inertia and damping. In this study, eigenmodes representing both static divergence and flutter instabilities were found. Heil and Jensen (2003) applied large tensions to the membrane to essentially hold it flat. Asymptotic and computational methods were used to characterise self-excited oscillations which is a global mode of the entire system, independent of local hydrodynamics (as are Tollmien-Schlichting or Travelling Wave Flutter instability modes). It however, requires Stokes-layer dissipation to avoid static divergence (Grotberg and Jensen 2004).

A number of these studies have employed finite-element schemes with fully coupled fluid and solid solvers. There has been a series of investigations spanning the last two decades by Luo and / or Pedley et al. It was found that steady solutions became unstable with flexible insert tension below a certain value, with this threshold decreasing with increasing Re. As a consequence, steady flow gives way to self-excited oscillations, which become increasingly complicated as tension is decreased (Luo and Pedley 1995a). Lowe and Pedley (1995b) studied the effects of reducing wall tension and found steeper slopes of the flexible insert at the downstream of the flexible wall. Though at a certain magnitude of tension reduction, numerical convergence was no longer achievable in this instance. The effects of wall inertia is discussed in Luo and Pedley (1998b) where the critical tension magnitude below which flexibile insert oscillations occur is found to increase as the wall inertia is increased.

There has also been many other notable studies performed. A symmetric channel was modelled by Rothmayer (1989) and tube collapse was seen to be possible over a wide range of flexible section lengths. Rast (1994) investigated the energy loss during flow separation for a flexible insert under longitudinal tension. A more accurate representation of human physiological processes was modelled by Pedrizzetti (1996, 1998) using suitable governing parameters and geometries as well as applying pulsatile flow. Wall thickness with a linear taper was investigated by Shim and Kamm (2002) showing changes in the location of the constriction and therefore the pressure distribution. Djordjevic and Vukobratovic (2003) studied different flows regimes for low Re lubrication type flow and moderately high Re boundary layer flow. The work by Tang et al. (2015) utilised a 2-d model to model flow through blood vessel and was able to simulate self-excited oscillations.

A rich body of knowledge has been created through all these studies on 2-d bounded flows. There has also been significant studies of laminar flow systems with Re of up to a few hundred. This has culminated in idenfitification of a more holistic system

understanding of the instability types and required conditions. This line of investigation is seen in Luo and Pedley (2000) through a categorisation of steady and unsteady cases. A more comprehensive parametric-space investigation was then performed to study instability behaviour using a fluid-beam model (Luo et al. 2008). First an eigenvalue approach was applied to solve the beam-modified Orr-Sommerfeld equations. They looked at the range of $\mathrm{Re} = 200 - 600$ and discovered the cascade stability structure reproduced in Figure 2.2. For the same Re, the system varies between stable and unstable states as it passes through a succession of unstable zones with increase in instability mode number as the wall stiffness C_λ is decreased. This trend results in 'tongue' shaped zones giving the overall cascade structure. Numerical simulations were performed solving the nonlinear fully coupled FSI system to identify this cascade stability structure. The letter designation (in Figure 2.2) of the various test cases are categorised based on the outcome of their transient behaviour; stable *s* cases mean the oscillation due to an impulse damps out, neutral *n* cases mean the system settles into saturated oscillation state, and unstable *u* cases denote a system that will oscillate with a growing displacement until computational system failure. Three cases were presented in Liu et al. 2009 to exhibit the mechanisms behind the behaviour of stability and instability through sustained flexible insert oscillations.

An explanation for the oscillatory behaviour of neutral stability systems was attempted based on the energy budget of both a pressure-driven and flow-driven systems in Liu et al. (2012). It was found that the cascade instability structure is not present for a pressure-driven system. Furthermore the relative dominance of mode-1 and mode-2 instabilities are different depending on the pressure and velocity-driven systems. In some instances, the energy budget analysis showed oscillations are sustained by extracting kinetic energy from the mean flow with two-thirds of kinetic energy dissipated by oscillations and the remainder dissipated by the mean flow. This however was found not to be true for cases of larger wall deformations. This work also analysed only a single flexible insert length and limited variations of external pressures. These limitations are addressed in the current work for the flow-driven system.

2.4 Summary

Instability has been observed to occur in collapsible tubes with rigid ends both experimentally and theoretically. Development of numerical models has progressed from lumped systems to 1-d, 2-d and, most recently 3-d. Though 3-d models are most representative of physical experiment conditions, they are numerically expensive. The 2-d numerical model is at present the most computationally efficient whilst still capturing key instability behaviour such as flow limitation and self-excited oscillations.

The current understanding of 2-d bounded flow with finite flexible insert lengths has significantly improved in the past decade with the proposal of a cascade of instability

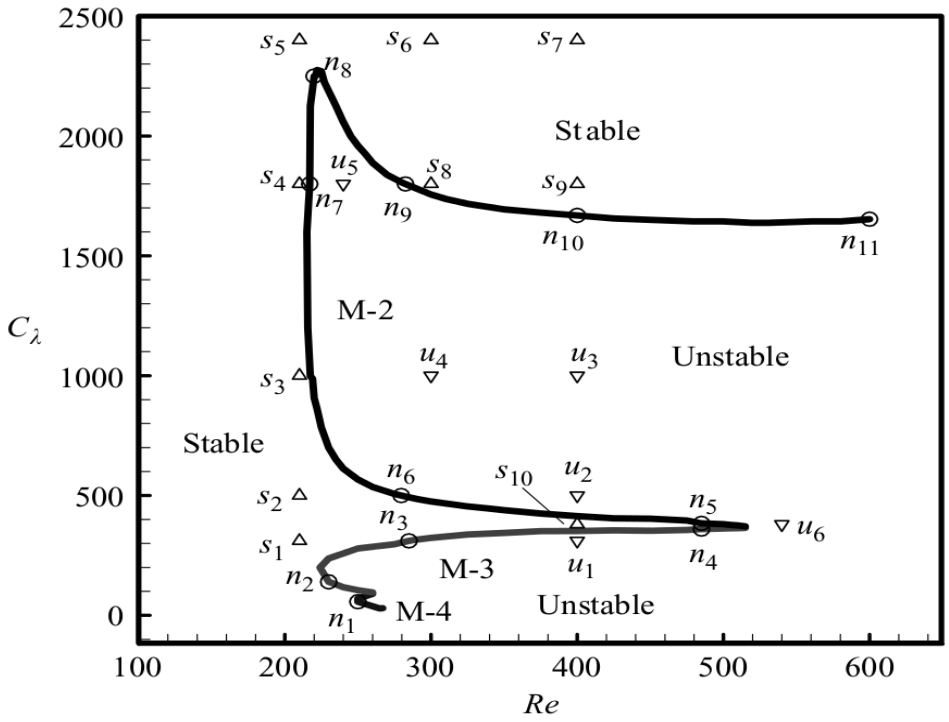

Figure 2.2 Neutral stability curve in the (C_λ, Re)-space. Branch M-2 goes through points n_5 to n_{11}, branch M-3 goes through n_2 to n_4, and branch M-4 goes through n_1. The system is stable on the left of the branches and the top of M-2, and on the right of branches (below M-2), it is unstable (Luo et al. 2008).

types and its elucidation through energy budget analysis. The current work looks to build on the understanding of 2-d bounded flow. The first step is to replicate the results of past studies then extend the work to investigate a wider range of system parameters such as the variation of external pressure P_{ext} and the flexible insert length L_{flex}. From this, a more comprehensive characterisation of the 2-d bounded flow system can be developed. Furthermore past investigations have focussed on a single flexible insert configuration with the bottom channel wall completely rigid. A second model is introduced with a dual flexible insert configuration to test whether current understanding of the single flexible insert configuration is still applicable.

Chapter 3

Numerical Model and Study Methodology

3.1 General

The study of fluid-structure interaction (FSI) problems using numerical methods has become increasingly popular due to advances in computational power. The object-oriented multiphysics finite element library `oomph-lib`, an open-source library, suits the objectives of this study (Heil and Hazel 2006). Described in this section is the system governing equations, numerical model and the numerical simulation startup procedures for performing simulations. The work in this chapter has been previously published by Lai et al. (2010).

3.2 Model Description

The `oomph-lib` model is created based on the system introduced by Pedley (1992). Figure 1.1a shows the major geometrical parameters of the model. Variables identified without asterisks are non-dimensional. Fluid flow is driven by a prescribed Poiseuille velocity profile, with an average velocity U_{mean}, at the inlet of the 2-d channel of height H and total length L_{total}. The total length is the summation of the upstream length L_{up}, flexible section length L_{flex}, and downstream length L_{down}. The upstream and downstream sections are rigid, while the central section is a flexible insert on the top wall and rigid bottom wall. The terms wall or insert are used interchangeably throughout this work. The insert is loaded by an external pressure P_{ext} and the traction that the fluid exerts on it. Figure 1.1a is not drawn to scale. Typically L_{down} is significantly longer to capture the ensuing fluid flow disturbance behaviour following the flexible wall.

Table 3.1 Scaling quantities for non-dimensionalisation.

Variable	Non-Dimensionalisation Quantity
Length	H^*
Velocity	U^*_{mean}
Time	$T^*_{\text{natural}} = H^*/U^*_{\text{mean}}$
Pressure	$\mu^* U^*_{\text{mean}}/H^*$
Stresses and Traction	$E^*_{\text{eff}} = E^*/\left(1-\nu^2\right)$

Table 3.2 Non-dimensional quantities.

Variable	Mathematical Representation
Reynolds Number	$\text{Re} = \rho^* U^*_{\text{mean}} H^*/\mu^*$
Strouhal Number	$\text{St} = (H^*/U^*_{\text{mean}})/T^*_{\text{natural}} = 1$
Fluid pressure scale ratio	$Q = \mu^* U^*/E^*_{\text{eff}} H^*$
Solid-to-fluid density ratio	$\rho^*_{\text{s}}/\rho^*_{\text{f}}$

3.3 Governing Equations

The governing equations are described for the viscous fluid flow and flexible wall components of the `oomph-lib` model. Some manipulation of these equations is performed to normalise the numerical problem so that it is numerically better-conditioned. Table 3.1 lists the quantities used for non-dimensionalisation. The parameters identified with asterisks are dimensional. Quantities used here include the channel height H^*, the dynamic viscosity μ^*, Young's modulus E^* and Poisson's ratio ν.

Table 3.2 lists the four non-dimensional quantities that govern the solution space; Reynolds Number Re, Strouhal Number St, fluid pressure scale ratio Q and the solid-to-fluid density ratio $(\rho^*_{\text{s}}/\rho^*_{\text{f}})$. Note Q is the ratio of the viscous pressure scale $\mu^* U^*/H^*$ used to non-dimensionalise the Navier-Stokes equations to the effective elastic modulus of the flexible wall $(E^*_{\text{eff}} = E^*/(1-\nu^2))$ (Elliott et al. 2010). For all instances in this work, the flexible wall is treated as massless and therefore $\rho^*_{\text{s}}/\rho^*_{\text{f}}$ is always zero.

The following sub-sections describe the governing equations of the fluid, flexible wall and fluid-structure interaction (FSI).

3.3.1 Fluid Flow

The Newtonian fluid is governed by the non-dimensional incompressible Navier-Stokes equation using the entries of Table 3.1

$$\text{Re}\left(\frac{\partial u_{\text{i}}}{\partial t} + u_{\text{j}}\frac{\partial u_{\text{i}}}{\partial x_{\text{j}}}\right) = -\frac{\partial p}{\partial x_{\text{i}}} + \frac{\partial u_{\text{i}}}{\partial x_{\text{j}}}\left(\frac{\partial u_{\text{i}}}{\partial x_{\text{j}}} + \frac{\partial u_{\text{j}}}{\partial x_{\text{i}}}\right) \tag{3.1}$$

and continuity equation

$$\frac{\partial u_{\mathrm{i}}}{\partial x_{\mathrm{i}}} = 0, \tag{3.2}$$

with velocity u, spatial coordinate x and time t. Subscripts $i, j = 1, 2$ respectively denote the horizontal and vertical components.

The velocity vector is

$$\mathbf{V} = u_1 \mathbf{e}_1 + u_2 \mathbf{e}_2 \tag{3.3}$$

where u_{i} is the velocity component and $\mathbf{e}_{\mathrm{i}}$ the unit vector.

The fluid flow is subject to the following boundary conditions:

- Inflow is prescribed to be a plane Poiseuille velocity profile

$$\mathbf{V}(x_1 = 0, x_2) = 6 x_2 (1 - x_1) \mathbf{e}_1 \tag{3.4}$$

- Exit pressure is fixed at zero

$$P_{\mathrm{exit}} = 0 \tag{3.5}$$

- No slip on rigid walls

$$\mathbf{V} = 0 \tag{3.6}$$

- No slip on flexible walls

$$\mathbf{V} = \frac{\partial \mathbf{R}_{\mathrm{w}}}{\partial t} \tag{3.7}$$

  where $\mathbf{R}_{\mathrm{w}}$ is the flexible wall displaced position.

3.3.2 Flexible Wall

The beam elements in `oomph-lib` are based on geometrically-nonlinear Kirchoff-Love beam theory with incrementally linear constitutive equations (Hjelmstad 2007).

The beam's undeformed shape is parametrised by a non-dimensional Lagrangian coordinate ξ and the non-dimensional position vector to a material particle on the beam's centerline in the undeformed configuration is given by $\mathbf{r}_{\mathrm{w}}(\xi)$. The unit normal to the beam's undeformed centerline is denoted by $\mathbf{n}$. The applied traction $\mathbf{f} = \mathbf{f}^* / E_{\mathrm{eff}}$ (a force per unit deformed length of the beam) which deforms the beam causes its material particle to be displaced to the new position $\mathbf{R}_{\mathrm{w}}(\xi)$, and the unit normal to the beam's centerline is $\mathbf{N}(\xi)$ (Elliott et al. 2010).

The non-dimensional form of the principle of virtual displacements that governs the beam deformation is then given by

$$\int_0^{L_{\mathrm{flex}}} \left[(\gamma^2) \cdot \delta\gamma + \frac{h^2}{12} (\kappa^2) \cdot \delta\kappa - \left(\frac{1}{h} \sqrt{\frac{A}{a}}\, \mathbf{f} - \frac{1}{2} \Lambda^2 \frac{\partial^2 \mathbf{R}_{\mathrm{w}}}{\partial t^2} \right) \cdot \delta \mathbf{R}_{\mathrm{w}} \right] \mathrm{d}s = 0, \tag{3.8}$$

where

$$a = \frac{\partial \mathbf{r}_\mathrm{w}}{\partial \xi} \cdot \frac{\partial \mathbf{r}_\mathrm{w}}{\partial \xi} \qquad \text{and} \qquad A = \frac{\partial \mathbf{R}_\mathrm{w}}{\partial \xi} \cdot \frac{\partial \mathbf{R}_\mathrm{w}}{\partial \xi} \tag{3.9}$$

represent the squares of the lengths of infinitesimal material line elements in the undeformed and deformed configurations, respectively. These may also be interpreted as the '1×1 metric tensors' of the beam's centerline in the respective configurations. The quantity $\sqrt{A/a}$ represents the 'extension ratio' of the beam's centerline, and $\mathrm{d}s = \sqrt{a}\,\mathrm{d}\xi$.

The curvature or the beam's centerline before and after deformation is represented by

$$c = \mathbf{n} \cdot \frac{\partial^2 \mathbf{r}_\mathrm{w}}{\partial \xi^2} \qquad \text{and} \qquad C = \mathbf{N} \cdot \frac{\partial^2 \mathbf{R}_\mathrm{w}}{\partial \xi^2} \tag{3.10}$$

The strain and bending 'tensors' γ and κ are then given by

$$\gamma = \frac{1}{2}(A - a) \qquad \text{and} \qquad \kappa = -\frac{1}{2}(C - c) \tag{3.11}$$

Next, the ratio of the natural timescale of the beam's in-plane extensional oscillations is

$$\Lambda^2 = \frac{H^*}{T^*_\mathrm{natural}} \sqrt{\frac{\rho^*_\mathrm{s}}{E^*_\mathrm{eff}}} \qquad \text{where} \qquad T^*_\mathrm{natural} = \frac{H^*}{U^*} \tag{3.12}$$

Λ^2 may be interpreted as the non-dimensional wall density, thus it is set as equal to zero corresponding to the massless wall with zero wall inertia.

3.3.3 Fluid-Structure Interaction (FSI)

The wall is loaded by an external pressure P_ext and the traction that the fluid exerts on it. The components of load vector $\mathbf{f}$ that act on the wall are given by

$$\mathbf{f} = -P_\mathrm{ext} N_\mathrm{i} + Q\left(pN_\mathrm{i} - \left(\frac{\partial u_\mathrm{i}}{\partial x_\mathrm{j}} + \frac{\partial u_\mathrm{j}}{\partial x_\mathrm{i}}\right) N_\mathrm{j}\right) \tag{3.13}$$

for $i, j = 1, 2$, where N_i are the Eulerian components of the outer unit normal on the boundary of the fluid domain.

This FSI term is the same for both single and dual insert cases because the system is symmetric.

3.3.4 Energy Budget

The energy budget can be considered in terms of the rate of energy transfer between the flexible insert and the fluid. The flexible rate of work is based on equation 3.8 and is integrated over the entire length of the flexible insert (L_flex), given by

$$\int_0^{L_{\text{flex}}} \left[\left(\frac{\partial \gamma^2}{\partial t} \right) \cdot \delta\gamma + \frac{h^2}{12} \left(\frac{\partial \kappa^2}{\partial t} \right) \cdot \delta\kappa - \left(\frac{1}{h} \sqrt{\frac{A}{a}}\, \mathbf{f} \partial u_{\text{i}} - \frac{1}{2} \Lambda^2 \frac{\partial^2 \mathbf{R}_{\text{w}}}{\partial t^2} \right) \cdot \delta \mathbf{R}_{\text{w}} \right] \mathrm{d}s = 0, \tag{3.14}$$

This considers the rate of wall potential energy (axial and bending strain energy) $\dot{PE}$, rate of work on the wall $\dot{W}_{\text{wall}}$, and wall kinetic energy $\dot{KE}_{\text{wall}}$. Equation 3.14 can be re-arranged and be represented by

$$\dot{PE}_{\text{axial}} + \dot{PE}_{\text{bend}} = \dot{W}_{\text{wall}} + \dot{W}_{P\text{ext}} - \dot{KE}_{\text{wall}} \tag{3.15}$$

where

$$\dot{PE}_{\text{axial}} = \int_0^{L_{\text{flex}}} \left(\frac{\partial \gamma^2}{\partial t} \right) \cdot \delta\gamma \, \mathrm{d}s \tag{3.16a}$$

$$\dot{PE}_{\text{bend}} = \int_0^{L_{\text{flex}}} \frac{h^2}{12} \left(\frac{\partial \kappa^2}{\partial t} \right) \cdot \delta\kappa \, \mathrm{d}s \tag{3.16b}$$

$$\dot{W}_{\text{wall}} = \frac{Q}{h} \int_0^{L_{\text{flex}}} \left[\sqrt{\frac{A}{a}} \left(pN_{\text{i}} - \left(\frac{\partial u_{\text{i}}}{\partial x_{\text{j}}} + \frac{\partial u_{\text{j}}}{\partial x_{\text{i}}} \right) N_{\text{j}} \right) \partial u_{\text{i}} \right] \cdot \delta \mathbf{R}_{\text{w}} \, \mathrm{d}s \tag{3.16c}$$

$$\dot{W}_{P\text{ext}} = \frac{-P_{\text{ext}}}{h} \int_0^{L_{\text{flex}}} \left(\sqrt{\frac{A}{a}}\, N_{\text{i}} \partial u_{\text{i}} \right) \cdot \delta \mathbf{R}_{\text{w}} \, \mathrm{d}s \tag{3.16d}$$

$$\dot{KE}_{\text{wall}} = \int_0^{L_{\text{flex}}} \left(\frac{1}{2} \Lambda^2 \frac{\partial^2 \mathbf{R}_{\text{w}}}{\partial t^2} \right) \cdot \delta \mathbf{R}_{\text{w}} \, \mathrm{d}s = 0 \tag{3.16e}$$

The $\dot{W}_{\text{wall}}$ term consists of the normal and tangential fluid traction as well as fluid pressure loading as shown in equation 3.13. The $\dot{W}_{P\text{ext}}$ term is the rate of work by the uniform external pressure P_{ext}. Note that $\dot{KE}_{\text{wall}}$ is zero due to the flexible insert being massless.

The rate of energy interaction within the channel considers the rates of fluid kinetic energy $\dot{KE}_{\text{fluid}}$ and dissipation $\dot{D}_{\text{fluid}}$ in the fluid domain Ω, kinetic energy $\dot{KE}_{\text{IO}}$ and work $\dot{W}_{\text{IO}}$ along the inlet and outlet boundaries Γ and $\dot{W}_{\text{wall}}$ on L_{flex}. This is given by

$$\int_0^{\Omega} \left[u_{\text{i}} \frac{\partial u_{\text{i}}}{\partial t} + \frac{1}{4} \left(\frac{\partial u_{\text{i}}}{\partial x_{\text{j}}} + \frac{\partial u_{\text{j}}}{\partial x_{\text{i}}} \right)^2 \right] \mathrm{d}\Omega - \int_0^{\Gamma} \left[\left(\frac{1}{2} u_{\text{i}}^3 + p \right) N_{\text{i}} - \left(\frac{\partial u_{\text{i}}}{\partial x_{\text{j}}} + \frac{\partial u_{\text{j}}}{\partial x_{\text{i}}} \right) N_{\text{j}} \right] \mathrm{d}\Gamma - \int_0^{L_{\text{flex}}} \left[pN_{\text{i}} - \left(\frac{\partial u_{\text{i}}}{\partial x_{\text{j}}} + \frac{\partial u_{\text{j}}}{\partial x_{\text{i}}} \right) N_{\text{j}} \right] \mathrm{d}s = 0 \tag{3.17}$$

and can be simplified and re-arranged to

$$\dot{KE}_{\text{fluid}} = \dot{KE}_{\text{IO}} + \dot{W}_{\text{IO}} + \dot{W}_{\text{wall}} - \dot{D}_{\text{fluid}} \tag{3.18}$$

where

$$\dot{KE}_{\text{fluid}} = \int_0^{\Omega} u_{\text{i}} \frac{\partial u_{\text{i}}}{\partial t} \, \mathrm{d}\Omega \tag{3.19a}$$

$$\dot{KE}_{\text{IO}} = \int_0^{\Gamma} \frac{1}{2} u_{\text{i}}^3 N_{\text{i}} \, \mathrm{d}\Gamma \tag{3.19b}$$

$$\dot{W}_{\text{IO}} = \int_0^{\Gamma} pN_{\text{i}} - \left(\frac{\partial u_{\text{i}}}{\partial x_{\text{j}}} + \frac{\partial u_{\text{j}}}{\partial x_{\text{i}}} \right) N_{\text{j}} \, \mathrm{d}\Gamma \tag{3.19c}$$

$$\dot{W}_{\text{wall}} = \int_0^{L_{\text{flex}}} pN_{\text{i}} - \left(\frac{\partial u_{\text{i}}}{\partial x_{\text{j}}} + \frac{\partial u_{\text{j}}}{\partial x_{\text{i}}} \right) N_{\text{j}} \, \mathrm{d}s \tag{3.19d}$$

$$\dot{D}_{\text{fluid}} = \int_0^{\Omega} \frac{1}{4} \left(\frac{\partial u_{\text{i}}}{\partial x_{\text{j}}} + \frac{\partial u_{\text{j}}}{\partial x_{\text{i}}} \right)^2 \, \mathrm{d}\Omega \tag{3.19e}$$

The $\dot{W}_{\text{IO}}$ term is similar to the $\dot{W}_{\text{wall}}$ term as it contains the normal and tangential fluid traction, and fluid pressure loading.

Study of the energy budget allows analysis of the magnitude contribution of rate of energy/work to the system and their relative importance in an unstable system. In the case of two flexible inserts, all terms involving the flexible insert are simply duplicated with the magnitude contributions being similar (essentially $\times 2$) as they are assumed to be symmetric about the channel centre-line.

3.3.5 Numerical Implementation

The problem is formulated using `oomph-lib`. Two-node Hermite beam elements are used for the 1-d beam (Szabó and Babuška 2011, Bathe 2006). Nine-node quadrilateral Taylor-Hood elements are used for the fluid (Reddy and Gartling 2010, Braess 2007). The fluid domain Navier-Stokes elements are based on the Arbitrary-Lagrangian-Eulerian (ALE) formulation to permit computation of the flexible wall moving domain.

The highly deformed flexible insert configuration leads to significant deformation in the underlying fluid domain mesh. Mesh adaptation is required to adequately capture this behaviour. In `oomph-lib`, this is done using the quadtree-based refinement technique for refining the quadrilateral elements shown in Figure 3.1.

Assuming the initial mesh is sufficiently fine to resolve the solution at $t = t_0$ and $t = t_0 + \Delta t$, at $t = t_0 + 2\Delta t$ the automatic mesh adaptation splits the fluid elements,

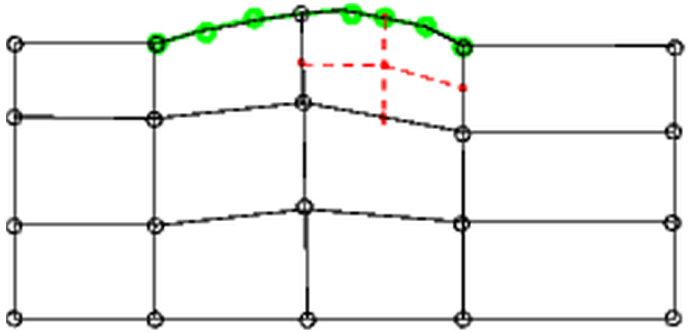

(a) t_0

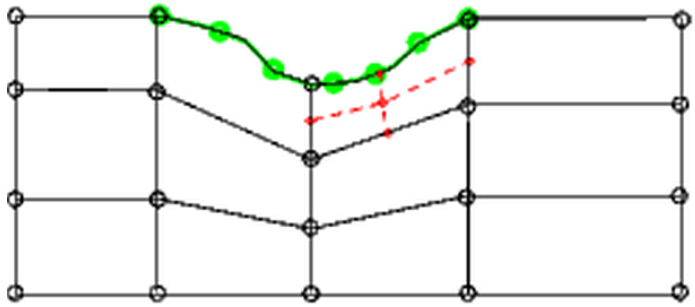

(b) $t_0 + \Delta t$

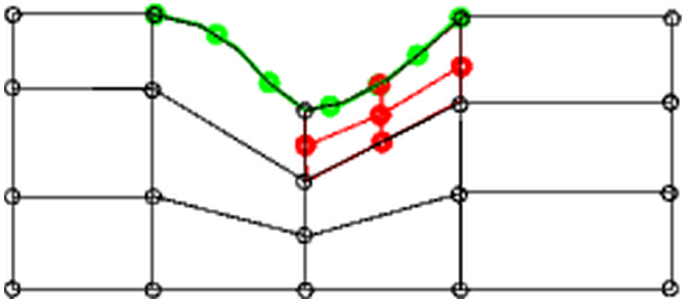

(c) $t_0 + 2\Delta t$

Figure 3.1 Diagram of the positional history values assignment for newly-created nodes in the FSI problems used in `oomph-lib`. The positional history values of the newly-created nodes (shown in red) are given by the positions they would have had if they had already existed at previous timesteps (oomph-lib 2016).

creating five new 'son' nodes, shown in red. Their position is determined by the 'father' element's current position, obtained from the interpolation between the flexible insert nodal positions (shown as green circles).

Initial position values have to be assigned to these newly-created nodes. Using the backward differentiation formulae (BDF2) timestepper, two history values of the nodal positions is required to evaluate the time-derivative $\partial u_i/\partial t$ in the momentum equations. A dummy (steady) timestepper is employed to produce these two initialisation history values with its time-derivative set to zero. The new 'son' nodes will then take on non-zero values at $t = t_0 + 2\Delta t$.

Timestepping is performed using a Steady scheme for the massless flexible wall (Shampine 1994). The FSI problem is discretised monolithically and the Newton-Raphson method is used to solve the nonlinear system of equations (specified by the global Jacobian matrix and the global residual vectors), employing the SuperLU direct linear solver within the Newton iteration (Langtangen 2013, Burden and Faires 1993, Khaitan and Gupta 2013).

The numerical algorithm is the same for all simulations in the current work. The difference in steady (static) and unsteady (dynamic) simulations is achieved through the start-up procedure employed, described in the following section.

3.3.6 Start-up Procedure

All simulations performed in this work have the same start-up procedure. A fully-developed viscous flow is passing through the channel with the Poiseuille velocity profile specified at the inlet. This is characterised by specifying either the entry pressure P_{entry} or inlet mean velocity U_{mean}.

At this point, a temporary external pressure P_{temp} is applied on the flexible wall to negate the opposing pressure due to the fluid flow. P_{temp} is defined as

$$P_{\text{temp}} = 12(\xi + L_{\text{down}}) \tag{3.20}$$

This is of equal value to the undeformed channel fluid pressure, varying across the flexible insert length. Application of P_{temp} is required to ensure numerical convergence at startup.

For a static simulation, P_{temp} is then gradually removed whilst at the same time the external pressure P_{ext} is applied. P_{ext} is a uniform, constant pressure applied across the entire flexible panel. Upon full aplication of P_{ext}, P_{temp} is completely removed. No variation in fluid or flexible wall motion occurs thereafter, resulting in the static solution. The purpose of this is to produce the flexible wall static or mean shape.

For a dynamic simulation, an additional perturbation pressure P_{pturb} is applied in addition to P_{ext}. P_{pturb} is also uniform across the flexible panel. P_{temp} is completely removed upon full application of P_{ext} and P_{pturb}. Several timesteps later P_{pturb} is then

completely removed in a single timestep to generate the perturbation. Only P_{ext} remains to the end of the simulation. This creates a step change in the external pressure and a perturbation is generated.

The following system dynamic response observed involves disturbance in the fluid flow and flexible insert oscillations. The two typical outcomes are either the flexible wall oscillations damp out (stable system) or settle into a persistent oscillation pattern (unstable system). It is also possible that the system becomes highly unstable and does not converge to a final steady state solution.

3.4 Summary

The FSI system governing equations have been described in terms of the fluid domain and flexible insert as well as the FSI relationship. The rate of energy and work relation is also established for a deeper understanding of the system and its instability behaviour. The numerical schemes for applying these governing equation and the numerical simulation startup procedures have also been described. These governing equations and methodology is applied in subsequent sections for numerical studies using `oomph-lib`.

Chapter 4

Model Validation

4.1 Validation Overview

This chapter presents the validations performed to ensure that the model is implemented correctly prior to its use for investigation of large flexible wall deformation instabilities. Three studies have been identified as suitable for validation: Heil and Jensen (2003), Luo et al. (2008) and Liu et al. (2009). Validation studies have been previously published by Lai et al. (2011) and Lai et al. (2012).

The first study by Heil and Jensen (2003) was selected because it is a preceding study in the development and use of `oomph-lib`. Therefore, it forms the basis to ensure the `oomph-lib` model set-up is correct through replication of results. For this purpose, a transient case was selected with the flexible insert oscillating in the linear (small) deformation range.

The second study by Luo et al. (2008) is important because it is a study of large flexible insert deformations which is of interest in the present study. This study is validated mainly in terms of its static (steady) flexible insert shape under the action of a mean fluid flow and uniform external pressure. This paper also categorised the associated instabilities into a cascade structure (Luo et al. 2008).

A more comprehensive dynamic large deformation validation effort is performed with Liu et al. (2009). In this, the dynamic behaviour with the introduction of a perturbation is analysed. This paper is suitable for dynamic comparison because it compares several numerical solution methods. It also highlights differences between cases exhibiting stable and unstable conditions.

It is to be noted that a consistent set of parameters for testing is not possible as comparison between the various journal papers require the use of different set of test parameters in each. These also include some differences in system set up. In Heil and Jensen (2003), the system is pressure-driven and there is a flexible insert with pre-tension applied whereas in the Luo et al. (2008) study it is velocity-driven and there is no pre-tension. This approach is still valid as they are simply testing different regions of the parameter space.

Table 4.1 Dimensional and non-dimensional parameters for `oomph-lib` model small-amplitude deformation validation against Heil and Jensen (2003).

Parameter	Value	Description
L^*_{up} (mm)	50	Upstream length of channel
L^*_{flex} (mm)	100	Collapsible length of channel
L^*_{down} (mm)	300	Downstream length of channel
H^* (mm)	10	Height of channel
h^* (mm)	0.1	Thickness of flexible wall
ρ^*_{f} ($\times 10^3$ kg.m^{-3})	1	Density of fluid
μ^* ($\times 10^{-3}$ Pa.s)	1	Dynamic viscosity of fluid
P^*_{entry} (Pa)	2.7	Fluid inlet pressure
B^* ($\times 10^{-9}$ N.m)	2.08333	Flexural rigidity of flexible wall
E^*_{eff} ($\times 10^6$ Pa)	0.025	Young's modulus of flexible insert
σ^*_0 ($\times 10^7$ Pa)	2.5	Flexible wall pre-stress
P^*_{ext} (Pa)	-3.5033	External pressure
P^*_{pturb} (Pa)	22.30	Perturbation pressure
Re	500	Reynolds Number
St	1	Strouhal Number
Q ($\times 10^{-7}$)	2	FSI parameter
$\rho^*_{\text{s}}/\rho^*_{\text{f}}$	0	Solid-to-fluid density ratio

4.2 Transient Small Deformation Flexible Insert Validation

The small-amplitude flexible wall deformation validation is performed by comparing with results from Heil and Jensen (2003). Dimensional parameters used in this model are shown in Table 4.1. The fluid is water and the flexible wall is massless. As this is a pressure-driven system, the inlet or entry pressure P^*_{entry} is specified. P^*_{entry} relates to the mean inlet velocity U^*_{mean} using the pressure scaling parameter ($\mu^* U^*_{\text{mean}}/H^*$) listed in Table 3.1. A pre-stress σ^*_0 and external pressure P^*_{ext} is applied on the flexible wall. This ensures that the mean position of the flexible wall is aligned with the upper channel wall. The specific perturbation pressure P^*_{pturb} value is selected to replicate the startup conditions as in Heil and Jensen (2003).

The dynamic behaviour of the flexible wall produced by `oomph-lib` can be seen in Figure 4.1. This plot shows the deformation profile at successive time steps. The flexible insert oscillates about the undeformed position along $y' = 1.0$ (prime '$'$' denotes length dimensions normalised with channel height H^*). However, there is an uneven distribution of black lines with a greater concentration approaching the undeformed flexible wall position. This is because in this case, the oscillations are actually decaying.

This decay can be more clearly seen by plotting the flexible wall midpoint vertical displacement y'_{mid} variation with time t in Figure 4.2. The upper plot is the present results from `oomph-lib`. The lower is from the original study by Heil and Jensen (2003)

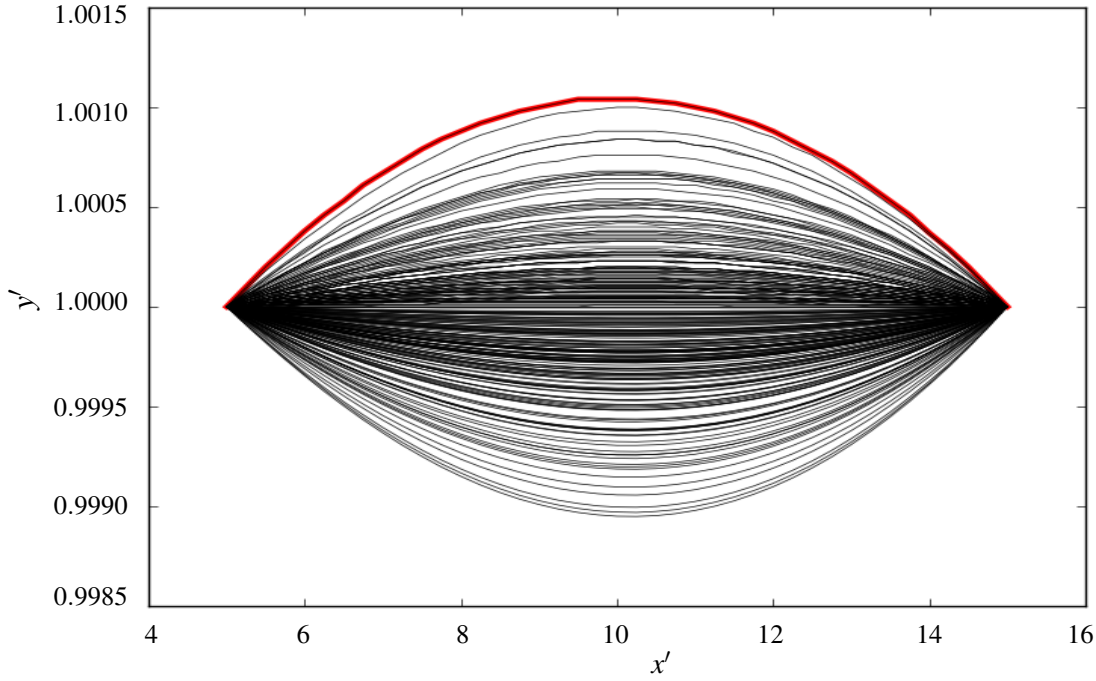

Figure 4.1 `oomph-lib` model flexible insert x' and y' positions for small transient deformations from initial condition (red line) and the following decaying oscillations (black lines).

with the red line the computational data and the green dashed line a best fit line based on the Levenberg-Marquardt algorithm (Heil and Jensen 2003). Between the `oomph-lib` and Heil and Jensen (2003) study results, it can be seen that the form, amplitude and rate of decay are similar. Comparing the oscilation frequency, the original case gives a non-dimensional frequency of 2.129 whereas the current study produced a result of 2.136, a difference of only 0.3%. As can be seen, the maximum peak-to-peak amplitude at the start of the simulation is only approximately 0.002. This validation shows the numerical model is setup correctly to achieve similar flexible wall deformation and transient behaviour.

4.3 Steady Large Deformation Flexible Insert Validation

The next stage of validation is for large flexible wall deformations cases in steady flow. A comparison is made against results from Luo et al. (2008), in which a parametric approach consists of holding the fluid properties (*i.e.* Reynolds number Re) constant and varying the wall property (*i.e.* stiffness ratio), resulting in changes in the flexible insert deformation size and shape. The large-deformation case is particularly interesting to confirm that the effects of the uniform external pressure and of the fluid-induced stresses on the wall deformation are both correctly captured by the present model.

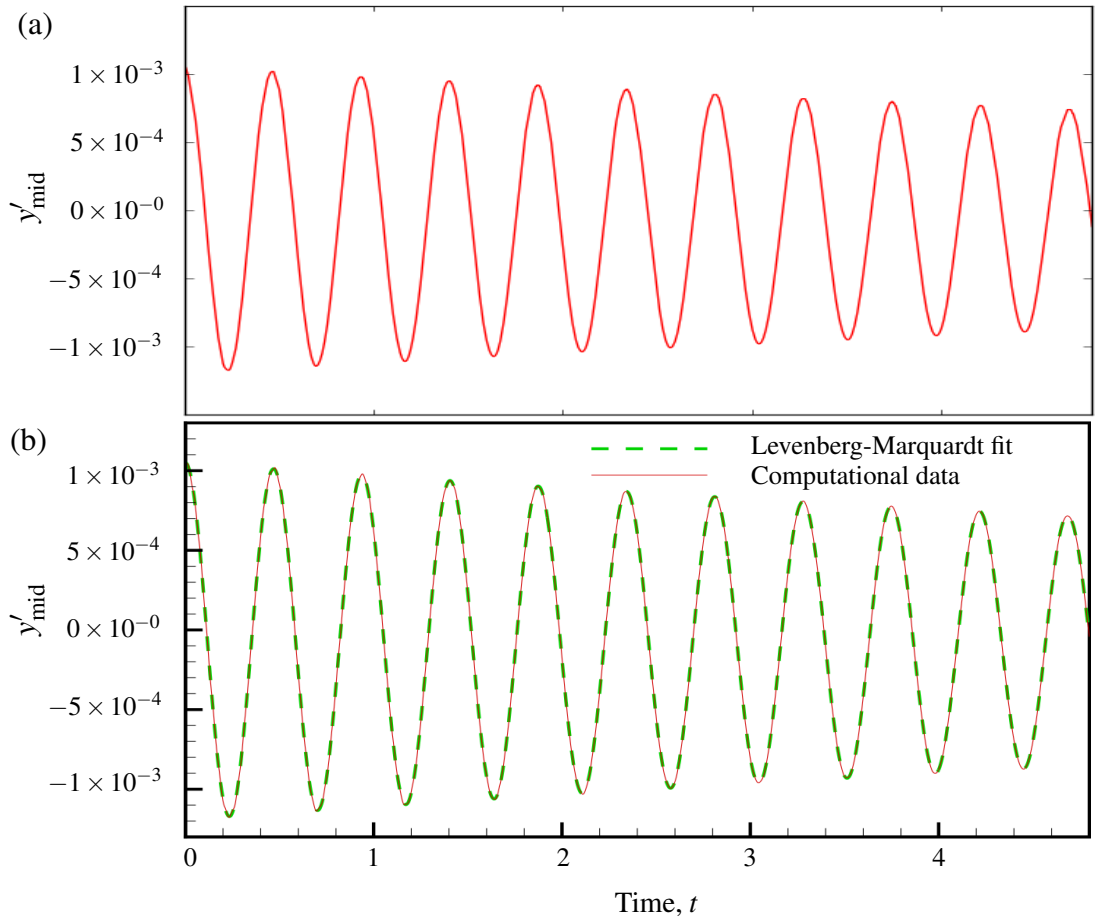

Figure 4.2 Flexible wall midpoint vertical displacement y'_{mid} vs. time t with oscillations about the mean position with numerical simulations from (a) present `oomph-lib` model, and (b) Heil and Jensen (2003).

Table 4.2 Steady state solution flexible deformation validation - dimensional and non-dimensional parameters for Luo et al. (2008) study comparison.

Parameter	Value	Description
L^*_{up} (mm)	50	Upstream length of channel
L^*_{flex} (mm)	50	Collapsible length of channel
L^*_{down} (mm)	300	Downstream length of channel
H^* (mm)	10	Height of channel
h^* (mm)	0.1095	Thickness of flexible wall
ρ^*_{f} ($\times 10^3$ kg.m^{-3})	1	Density of fluid
μ^* ($\times 10^{-3}$ Pa.s)	1	Dynamic viscosity of fluid
U^*_{mean}($\times 10^{-2}$ m/s)	4	Inlet mean velocity
ν	0.5	Poisson's ratio of solid
$\rho^*_{\text{s}} h^*$	0	Mass per unit area of solid
B^*($\times 10^{-9}$ N.m)	7.2	Flexural rigidity of flexible wall
E^*_{eff} ($\times 10^6$ Pa)	0.065	Young's modulus of flexible insert
P^*_{ext} (Pa)	-3.120	External pressure
Re	400	Reynolds number
St	1	Strouhal number
$Q(\times 10^{-8})$	3.0429	FSI parameter
$\rho^*_{\text{s}}/\rho^*_{\text{f}}$	0	Solid-to-fluid density ratio

Table 4.3 Selected test points with C_λ parameter variation from Luo et al. (2008).

Case	n_{10}	s_7	s_9	s_{10}	u_1	u_2	u_3
Wall stiffness C_λ	1668.75	2400	1800	380	310.94	500	1000

Table 4.2 shows the base parameters used in `oomph-lib` for comparison with Case u_3 in Luo et al. (2008). The uniform external pressure P_{ext} and Reynolds number Re remain the same for all cases. The only parameter changing in the cases other than Case u_3 is the wall stiffness value C_λ which is defined as

$$C_\lambda = \frac{E^* R^*}{\rho^*_{\text{f}} U^{*2}_{\text{mean}} H^*} \tag{4.1}$$

where $R^* = h^* \times 1$; the flexible wall thickness multiplied by unit width.

Table 4.3 shows the C_λ value for the different cases considered. Changes to C_λ are implemented in `oomph-lib` by modifying the flexural rigidity B^*. The various letter designations for the cases are consistent with the cascade stability structure as defined in Luo et al. (2008), where *s* is stable and oscillations damp out to static deformation, *n* is neutral with constant amplitude oscillations occuring indefinitely, and *u* is unstable with growing oscillation size (Luo et al. 2008).

Figure 4.3a shows flexible wall shapes for the various cases comparing the results from the original study by Luo et al. (2008) and the present `oomph-lib` model. The stable cases are plotted with dotted lines and the neutral and unstable cases with solid lines. The flexible insert deformations created in `oomph-lib` are very similar to the original study. On the y-axis, 0 denotes the channel bottom and 1.0 the channel top. Therefore these cases actually represent a range of small to large deformations (smaller and larger than channel midheight). The `oomph-lib` model is consistent with Luo et al. (2008) for small as well as large deformations. The flexible wall deformation is dependent on C_λ because this alters the ratio between the wall stiffness, fluid pressure force and external pressure force. With increasing C_λ, the wall stiffness dominates and this reduces wall deformation and a more parabolic wall shape is produced. The reverse is true with smaller C_λ resulting in larger flexible insert deformation and the maximum deformation point skewed increasingly to the right (downstream).

Figure 4.4 shows the fluid pressure p variation along the flexible wall comparing results between Luo et al. (2008) and the present `oomph-lib` model. Note the pressure normalisation is based on the method by Luo et al. (2008) using $p' = p^*/(\rho^* U^*_{\text{mean}})$ as opposed to that listed in Table 3.1. There are some differences in magnitude but the overall form of the plots are similar. Comparing the pressure at the start (upstream) of the flexible insert, cases u_1 and s_{10} are 0.514 and 0.211 respectively in the original Luo et al. (2008) study whereas the present `oomph-lib` model yields 0.463 and 0.229 respectively. The differences between the original and present models are 0.05 (9.9%) and 0.018 (8.5%) for cases u_1 and s_{10} respectively. The stable cases are again shown with dotted lines and the neutral and unstable cases with solid lines. The pressure magnitudes are consistent with the size of flexible insert deformation. Larger wall deformations result in a larger pressure change between the start and end of the insert. The minimum pressure is also smaller with larger deformations. This is as expected as larger wall deformation would cause a larger change in fluid pressure. It can also be seen the minima points shift increasingly to the right with increasing C_λ. This is consistent with the maximum deformation x-position.

The fluid flow behaviour is compared for case u_3 in Figure 4.5. The u_3 case is unsteady with growing oscillations. Figure 4.5a is a single time step capture during its oscillation period when the flexible wall is approximately at its mean position. It can be seen fluid streamline disturbances occurring in the channel downstream section in Figure 4.5a whereas the streamlines are steady in Figure 4.5b. The `oomph-lib` case actually settles into its mean position and exhibits no instability. The `oomph-lib` results are consistent with the discussion in Luo et al. (2008) which had predicted the oscillation frequency of the Heil and Jensen (2003) model to be significantly lower. In this instance it is not a lower oscillation frequency but simply a damped system. However there are still some similarities in the fluid flow behaviour as there is recirculation occuring just after the flexible wall section in both models.

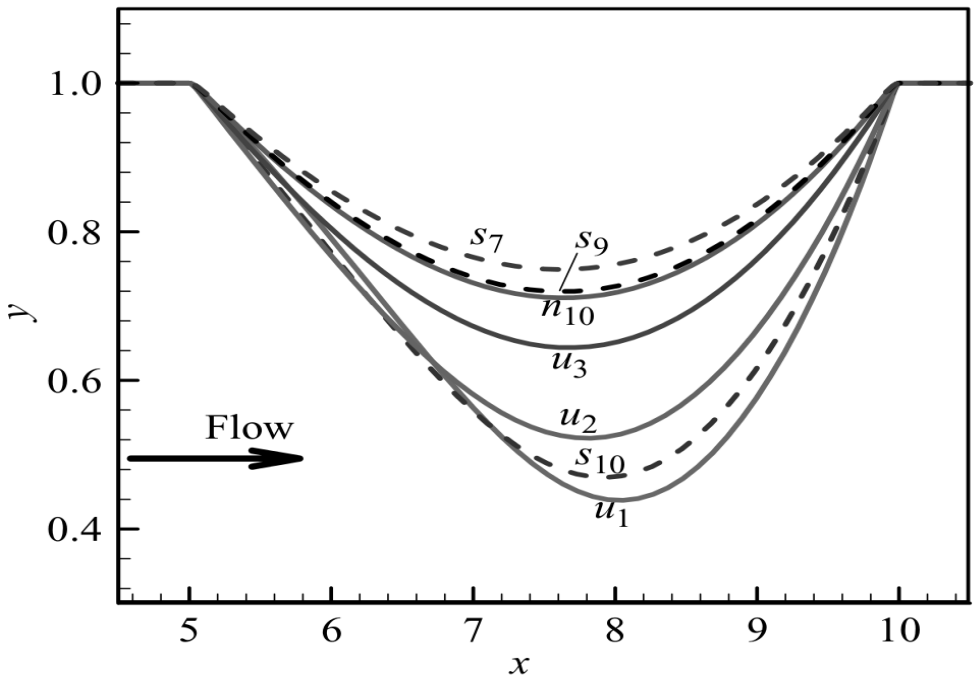

(a) Luo *et al.* 2008

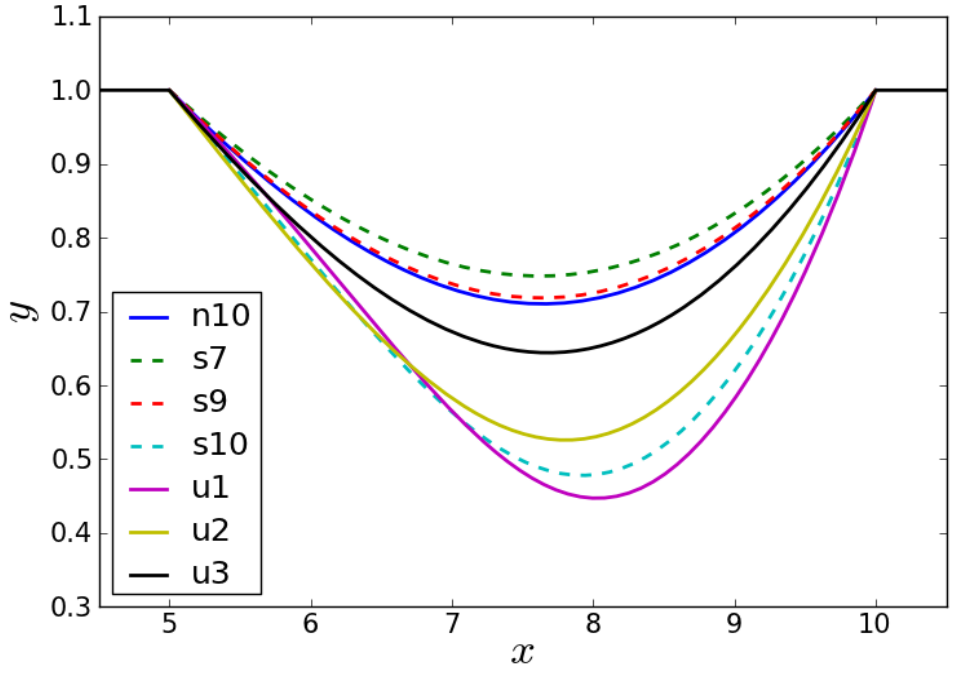

(b) `oomph-lib`

Figure 4.3 Displacement of flexible wall under different case parameters for (a) the Luo et al. (2008) study, and (b) the present `oomph-lib` model.

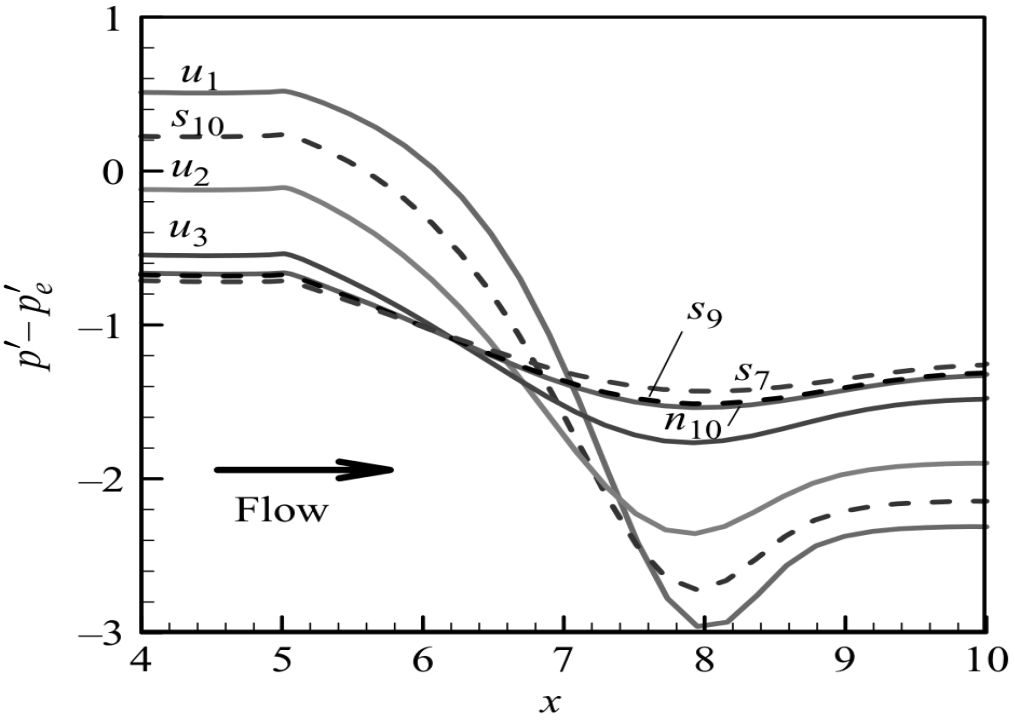

(a) Luo et al. (2008)

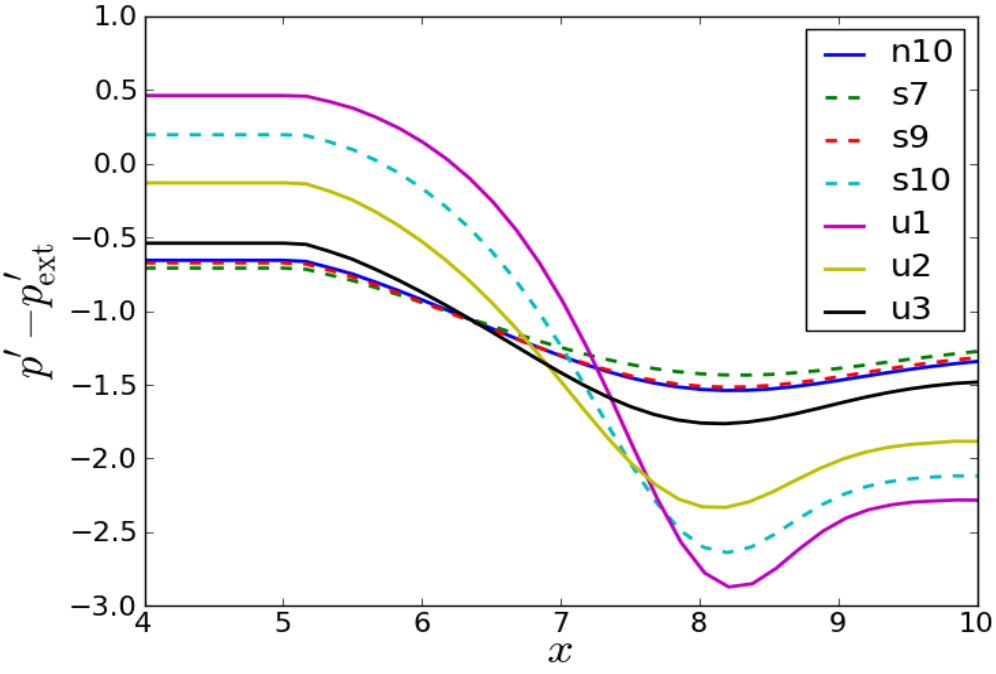

(b) `oomph-lib`

Figure 4.4 Flexible wall transmural pressure distribution for (a) the Luo et al. (2008) study, and (b) the present `oomph-lib` model. Pressure non-dimensionalisation scheme based on Luo et al. (2008) with $p' = p^*/(\rho^* U^*_{\text{mean}})$.

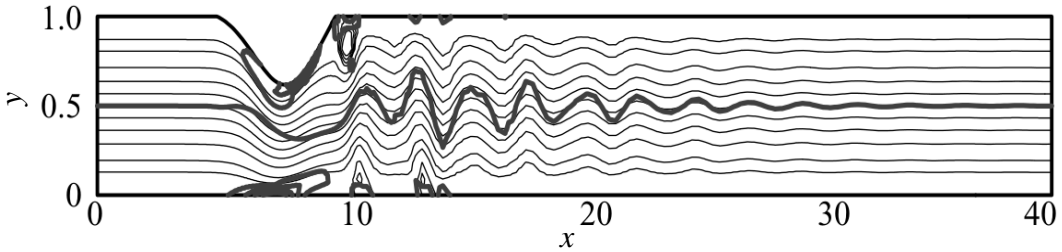

(a) Luo *et al.* 2008

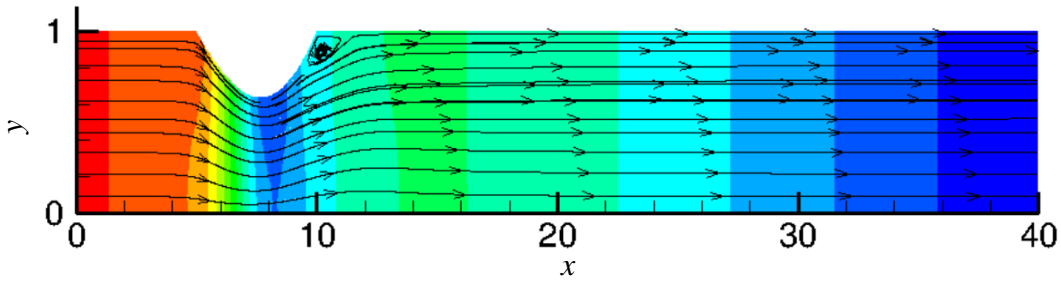

(b) `oomph-lib`

Figure 4.5 Fluid flow comparison for (a) the Luo et al. (2008) study streamlines (thin lines) and vorticity contours (thick lines), and (b) the current `oomph-lib` model streamlines and pressure contours (red-high, blue-low).

In this comparison, the models have been shown to produce similar steady solutions but the following transient behaviour is different between the two models. This difference in dynamic behaviour is analysed in a later study by Liu et al. (2009) and is the subject of discussion in the following section.

4.4 Steady and Transient Large Deformation Flexible Insert Validation

Following the successful comparison of steady solutions with the in-house fluid-beam model (FBM) from Luo et al. (2008), the transient behaviour comparison produced different dynamic behaviours as seen above in Section 4.3. The dynamic instability behaviour could not be replicated with `oomph-lib`. In general, the FBM has a greater tendency to instability where the corresponding `oomph-lib` equivalent case still remained stable. In the subsequent study by Liu et al. (2009), this difference in transient behaviour is studied by comparing their FBM with the commercial code ADINA (Automatic Dynamic Incremental Nonlinear Analysis). The ADINA code formulation has several solver options. Liu et al. (2009) opted to create three models with ADINA; 2D-solid large strain, 2D-solid small strain and iso-beam. Details of the numerical model formulation are listed in Table 4.4. This section discusses the comparison between the `oomph-lib` model with this study by Liu et al. (2009). This consists firstly of the steady solution validation and then the transient analysis. The steady solution validation method is similar to the previous section but it is a worthwhile exercise to ensure results

Table 4.4 Numerical model details for steady and transient large deformation study by Liu et al. (2009) and `oomph-lib`.

Numerical Description	Code			
	FBM	ADINA	ADINA	`oomph-lib`
Flexible Insert Element	3-node beam	9-node 2D solid	4-node iso-beam	2-node beam
Fluid Element	6-node triangle	9-node quadrilateral	9-node quadrilateral	9-node quadrilateral
Structural Assumptions	Large strain, large deformation, without shear strain, with coupling terms	Large/small strain, large deformation, without shear strain	Small strain, large deformation, with shear strain, without coupling terms	Small strain, large deformation, with shear strain, with coupling terms
Time Integration	First/second-order variable timestep	First/second-order fixed timestep	First/second-order fixed timestep	First/second-order fixed timestep
Fluid solver	Second order, adaptive mesh	First-order upwind	First-order upwind	Second order, adaptive mesh
Solid solver	Second order	Second order	Second order	Second order

are still similar with the ADINA models which are using a different formulation and are independently developed of the FBM and `oomph-lib` models. The transient simulation stage is also compared.

The study by Liu et al. (2009) presented three case studies to highlight the possibilty of stable/unstable behaviour differences when comparing their in-house FBM model and the ADINA numerical models. These cases are termed Case A, B and C. The dimensional and non-dimensional parameters for these cases are listed in Table 4.5. All three cases have a water-like fluid density and a massless flexible wall. No pre-stress is applied on the flexible wall which could cause the fluid pressure on the wall to dominate. This is also the major factor for causing the system to experience large wall deformations. The P_{pturb} values are selected to replicate the flexible wall transient displacements as in Liu et al. (2009). Case A is also used as the sample case for a mesh and timestep independence study to ensure the mesh density and timestep selection is suitable. This is discussed in Appendix C.

The steady-state flexible wall shape for Case A, B and C produced by `oomph-lib` compared to those generated by FBM and ADINA models from Liu et al. (2009) can be seen in Figure 4.6. The overall forms of the flexible inserts are similar between the models, although there are slight differences. It is noted that Case A wall shape is skewed to the right significantly whereas Case B and C are gradually more parabolic.

Table 4.5 Dimensional and non-dimensional parameters for large deformation transient validation against Liu et al. (2009).

Parameter	Value		
	Case A	Case B	Case C
L^*_{up} (mm)	50	50	50
L^*_{flex} (mm)	50	50	50
L^*_{down} (mm)	300	300	300
H^* (mm)	10	10	10
h^* (mm)	0.1250	0.125	0.1254
ρ^*_f ($\times 10^3$ kg/m^3)	1	1	1
μ^* ($\times 10^{-3}$ Pa.s)	1	1	1
U^*_{mean} ($\times 10^{-2}$ m/s)	3	3	5
P^*_{entry} ($\times 10^{-2}$ m/s)	N/A	N/A	N/A
B^* ($\times 10^{-9}$N.m)	1.629	2.930	7.862
E^*_{eff} ($\times 10^6$ Pa)	0.01	0.018	0.4785
σ^*_0 ($\times 10^7$ Pa)	0	0	0
P^*_{ext} (Pa)	-4.255	-1.755	-4.875
P^*_{pturb} ($\times 10^{-2}$ Pa)	-50	-1.755	-15.8
Re	300	300	500
St	1	1	1
Q ($\times 10^{-7}$)	2.9986	1.6667	0.1045
$\rho^*_{\text{s}}/\rho^*_{\text{f}}$	0	0	0
Λ^2	1	1	1
C_λ	139	250	2400

This can be attributed to the flexural rigidity B^* where Case A has the largest value and gradually decreases in case B then case C.

The corresponding pressure distributions along the flexible insert are shown in Figure 4.7. Note the pressure normalisation is based on the method by Liu et al. (2009) using $p' = p^*/(\rho^* U^*_{\text{mean}})$ as opposed to that listed in Table 3.1. These pressure values are the fluid pressure component with the uniform external pressure P_{ext} subtracted. The pressure variation magnitude is consistent with the size of wall deformation. Case A has the largest wall deformation and also the largest pressure variation along the flexible wall followed by Case B and C. It is also noted that the location of minimum pressure is positioned with the largest wall deformation point. For instance, Case A has the largest wall deformation and its minimum point is skewed more to the right of flexible insert mid-length. Case C which has the most parabolic wall shape has its pressure minimum point closest to channel mid-length.

Overall, the `oomph-lib` steady solution behaviour is most similar with the 2D-solid small strain and large strain models, and still reasonably similar to the FBM model. The flexible wall shape similarities are expected as they also compare well with the Luo et al. (2008) study discussed in the previous section 4.3 which also used the FBM model.

The transient behaviour of these three cases is now discussed. The transient case setup for `oomph-lib` is as discussed in Section 3.3.6. The transient behaviour is shown primarily through selecting the flexible insert mid-length point y-displacement and plotting its time history. Figure 4.8 show the results for Cases A to C.

For Case A, the `oomph-lib` results conform with the behaviour of the ADINA models by oscillating indefinitely with a saturated oscillation whereas the FBM model is more unstable and becomes dominated by a higher frequency oscillation. Thus there is a difference in the overall behaviour between the FBM model and the other models. Using the system dynamics definitions of Liu et al. (2009), the FBM model is more likely to have unstable results. It is difficult to be certain unless a longer time period of the simulation is known beyond $t = 85$. The ADINA small strain and iso-beam models as well as `oomph-lib` models settle into saturated oscillations of similar amplitude. The ADINA large strain model also settles into saturated non-linear oscillations but with a larger oscillation amplitude. Although their dynamic behaviours are different, the mean streamline behaviour are similar as shown in Figure 4.9. Therefore the mean streamline state is not a good predictor of instability form.

Figure 4.8b shows the results for Case B. The `oomph-lib` results do not show much oscillatory behaviour and damp out to a stable steady deformation quickly. It can be seen the general trend of the `oomph-lib` results are similar to the other solvers except for the FBM model which again is oscillating with an increasingly large amplitude. It seems that this simulation set occurs at some critical stability point, as the `oomph-lib` and ADINA models decay to a stable state while the FBM model becomes unstable.

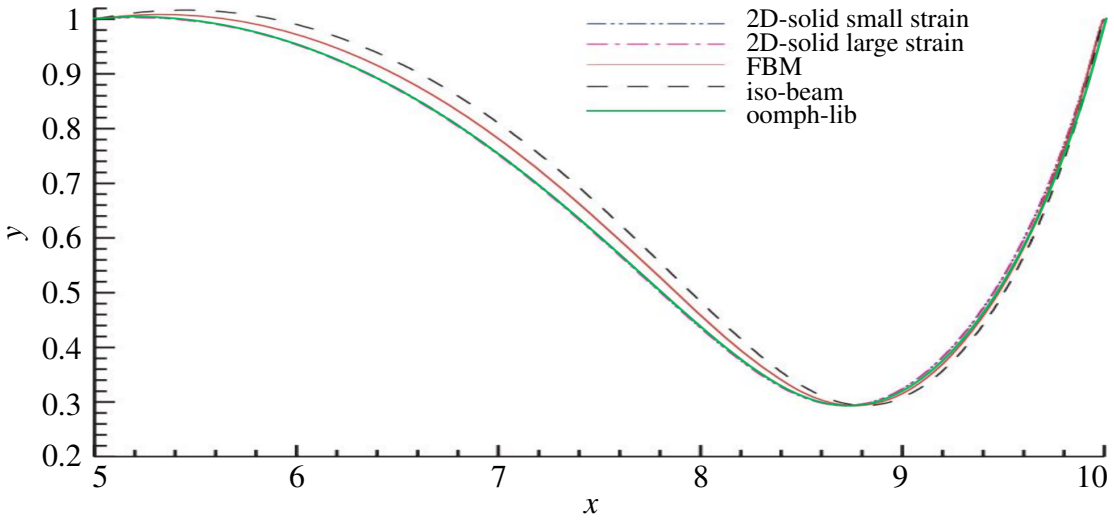

(a) Case A

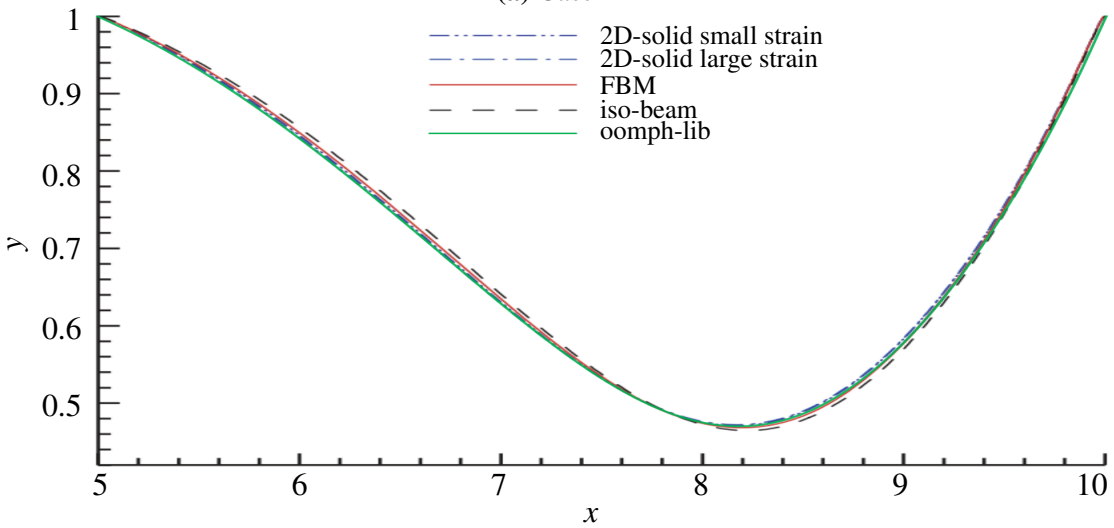

(b) Case B

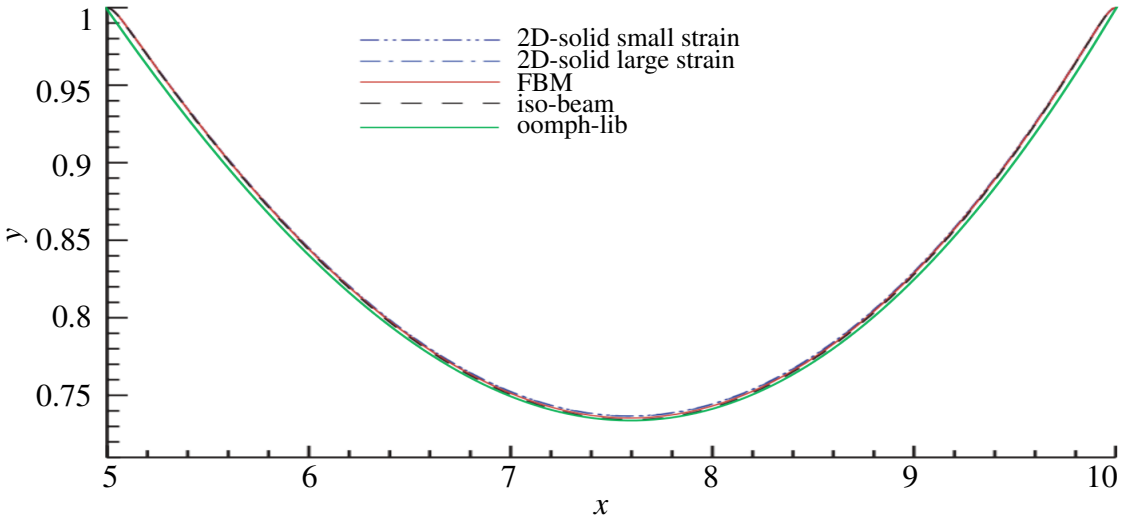

(c) Case C

Figure 4.6 `oomph-lib` large amplitude non-dimensional flexible wall shape comparison with Liu et al. (2009).

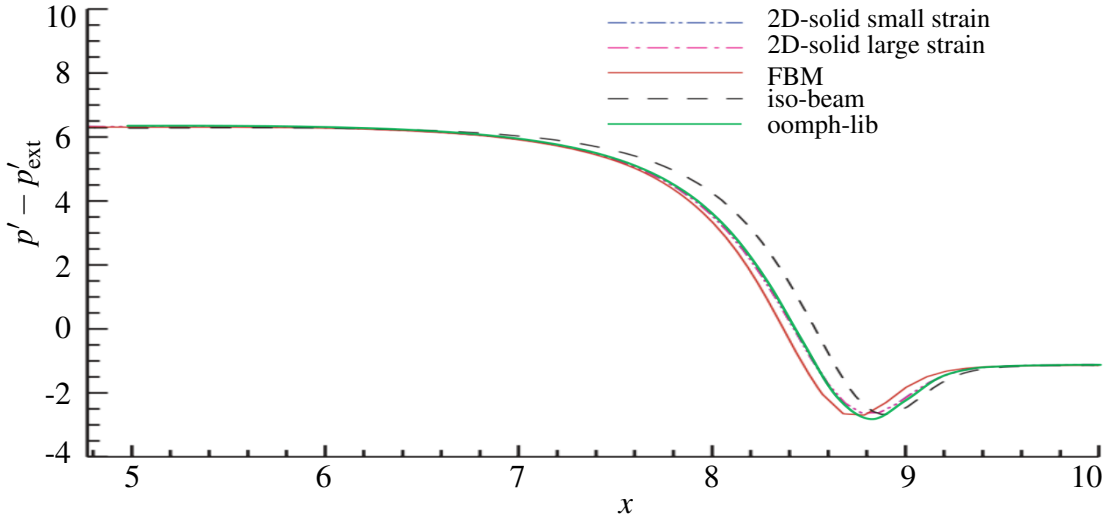

(a) Case A

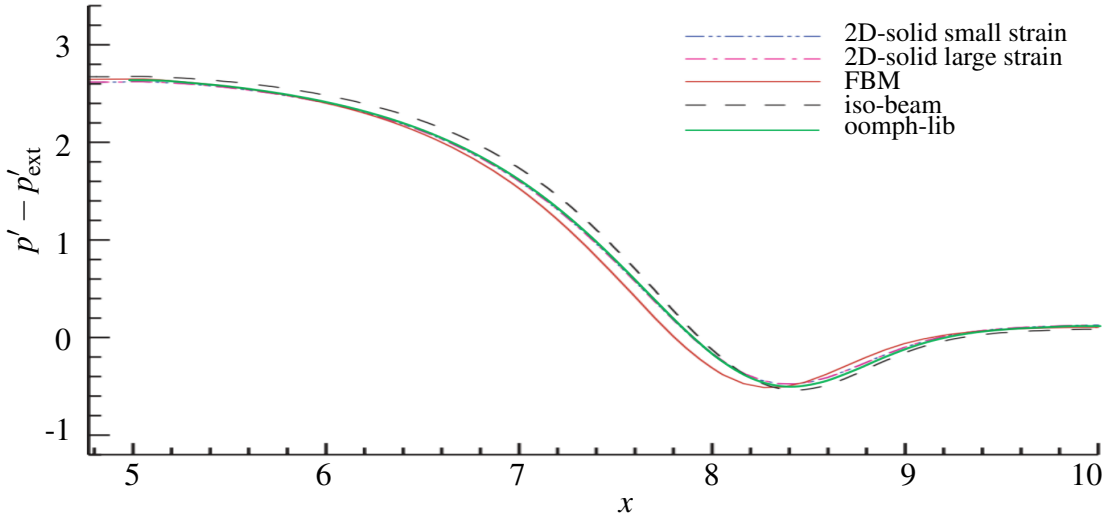

(b) Case B

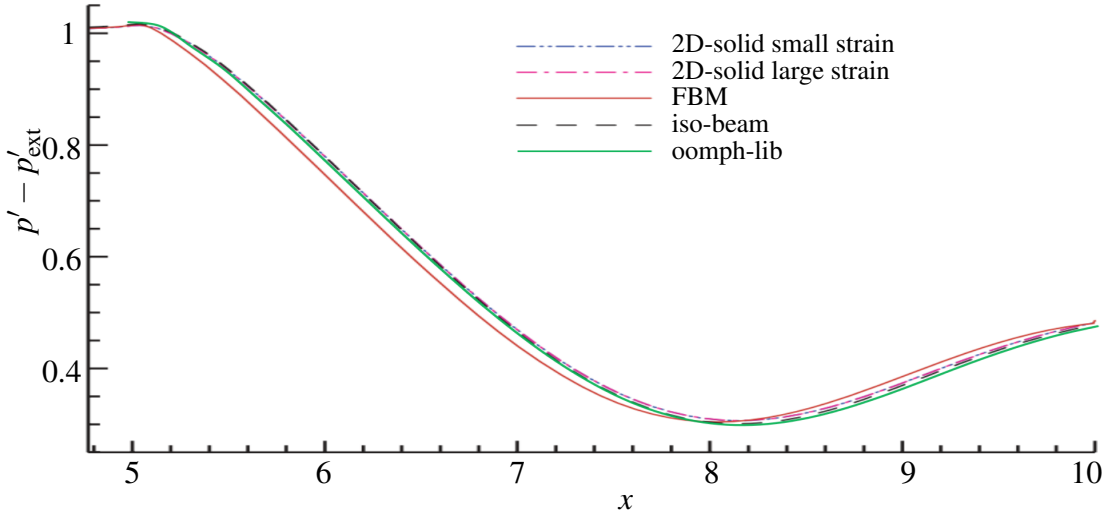

(c) Case C

Figure 4.7 `oomph-lib` large amplitude non-dimensional pressure along the flexible wall comparison with Liu et al. (2009). Pressure non-dimensionalisation scheme based on Liu et al. (2009) with $p' = p^*/(\rho^* U^*_{\text{mean}})$.

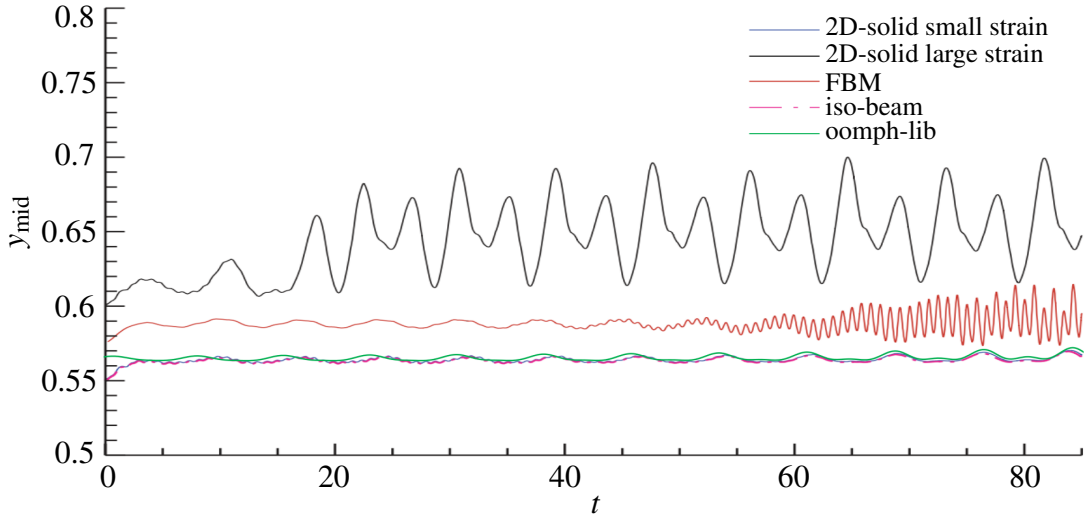

(a) Case A

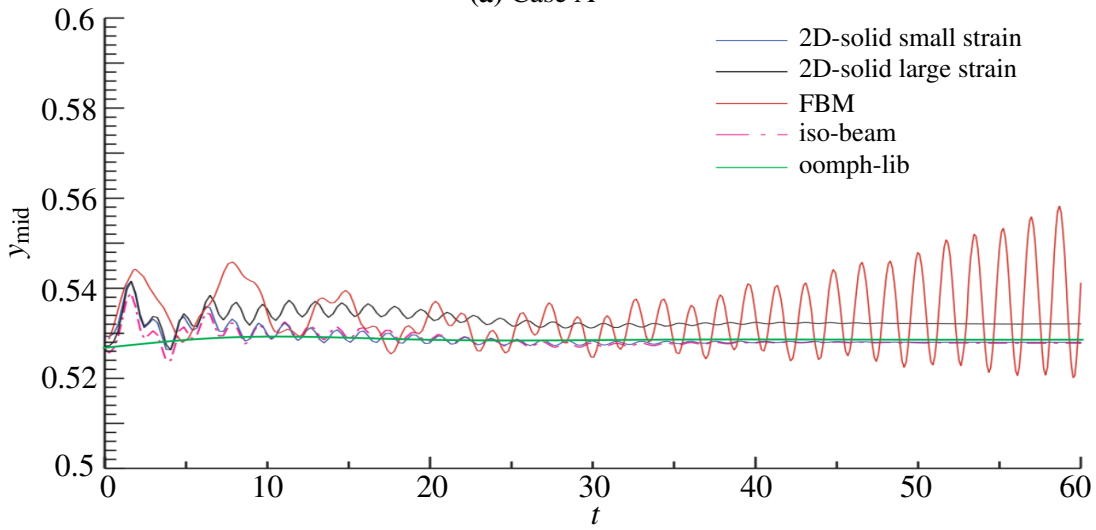

(b) Case B

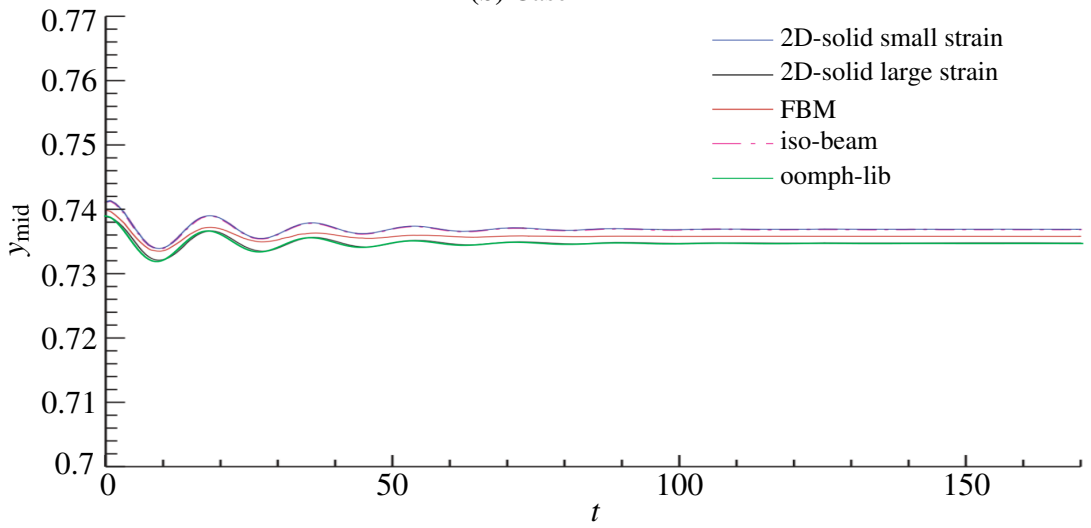

(c) Case C

Figure 4.8 Large amplitude non-dimensional flexible wall midpoint y-displacement vs. non-dimensional time comparison with Liu et al. (2009).

Table 4.6 Liu et al. (2009) flexible wall midpoint y-displacement comparison with `oomph-lib`.

Solver	Displacement Difference (%)		
	Case A	Case B	Case C
FBM	7.7	2.2	0.5
ADINA iso-beam/2D-solid small strain	1.2	0.1	0.8
ADINA 2D-solid large strain	28.6	0.8	0.1

Table 4.7 Liu et al. (2009) frequency comparison with `oomph-lib`.

Solver	Frequency Difference (%)		
	Case A	Case B	Case C
FBM	7.4	N/A	1.0
ADINA iso-beam/2D-solid small strain	1.2	N/A	1.0
ADINA 2D-solid large strain	44.4	N/A	1.0

Figure 4.8c shows the third case, Case C. All models exhibit the same oscillatory behaviour with only small differences in the mean displacement of the flexible wall.

The differences between the results of the `oomph-lib` model, ADINA models and FBM are characterised using two quantities. First is the steady-state y-displacement of the flexible wall midpoint. Second is the oscillation frequency of the system. These can be seen in Table 4.6 and Table 4.7 respectively. Note that in the Case A FBM results, there is a secondary (higher) frequency increasingly dominating the system. This frequency is not compared with the rest of the models as it does not exist in the others. Furthermore it is not comparable as this system seems to become unstable whereas the other solutions settle into saturated oscillations.

Comparing the initial flexible wall midpoint y-displacement results, `oomph-lib` results are most similar to that of the ADINA iso-beam and 2D-solid small strain models. The only exception is Case C where `oomph-lib` results most closely matches the 2D-solid large strain model. However, it can be seen that the displacement values of all models are very similar for Case C, thus all differences in this case are within acceptable bounds. It is also noted that for the highly dynamic Case A, the 2D-solid large strain model flexible insert midpoint y-displacement is significantly different from `oomph-lib` by 28.6%.

Frequency differences are most obvious in Case A where all models have distinct solutions. The `oomph-lib` results are most similar to the ADINA iso-beam/2D-solid small strain model results. The frequency for Case B is not applicable as the `oomph-lib` result damps out very quickly. The other ADINA models although having different startup wall dynamics eventually damp out and maintain a stationary state as well. The FBM model however experiences growing-amplitude oscillation. The frequency for

Case C is similar for all models. Thus the FBM and ADINA models are assumed to have the same frequency for comparison purposes. Although there are differences in the unstable oscillation frequencies, it is noted that the general behaviour of the ADINA models and `oomph-lib` are similar on the basis of whether the system remains stable or becomes unstable. The FBM however seems to be much more sensitive and tends to enter an unstable state when the other models remain stable.

Taking these two comparison sets into account, it is concluded that `oomph-lib` results are most similar to that of iso-beam/2D-solid small strain, followed by FBM and 2D-solid large strain quantitatively. Even though this is the case, the general behaviour of `oomph-lib` and the ADINA models are similar whereas the FBM model has a greater tendency to be unstable.

It is also noted that none of the ADINA model and `oomph-lib` systems exhibit 'unstable' behaviour as defined by having oscillations continuously growing in amplitude with time. Therefore in subsequent sections the system behaviour is re-defined to simply be stable or unstable. A stable system is defined as a perturbed system that settles into a static deformation of the mean state. An unstable system is defined as a perturbed system settling into sustained finite-amplitude self-excited oscillations.

The difference in unsteady results between the ADINA 2D-solid models and FBM was attributed to the inclusion of coupling terms. The FBM does include coupling terms whereas the ADINA iso-beam model does not include them (Liu et al. 2009). Non-inclusion of coupling would respresent a Timoshenko beam without longitudinal stretch (Carrera et al. 2011). It is unclear whether the 2D-solid beam models include these terms. It is suggested in Liu et al. (2009) that coupling is absent in the 2D-solid beam elements as the results from the 2D-solid small strain elements agree with the iso-beam model (Liu et al. 2009). To add to this discussion, the `oomph-lib` model is fully-coupled and exhibits the same behaviour as the ADINA iso-beam and 2D-solid small strain models rather than the FBM. Thus it appears the inclusion of coupling may not have a great effect to this aspect.

Another consideration is that the FBM model neglects the shear strain contribution to shear stress whereas ADINA and `oomph-lib` do take this into account (Liu et al. 2009). The difference of the 2D-large strain model with all other results perhaps is due to it overpredicting the effects of bending strain in this model as the flexible wall is 1D.

4.5 Summary

The `oomph-lib` model validation was performed in incremental steps by comparing its predictions with those of several published studies. First a dynamic or transient comparison was performed for small wall deformations with the numerical method that preceded the development of `oomph-lib`. The focus was then on comparison with large flexible insert deformation cases. Both steady and transient behaviour were validated

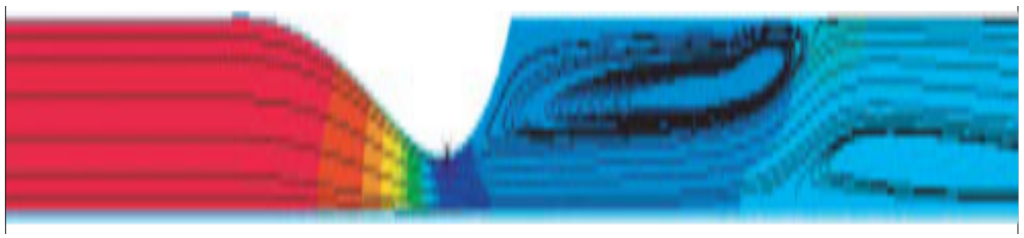

(a) ADINA 2D large strain

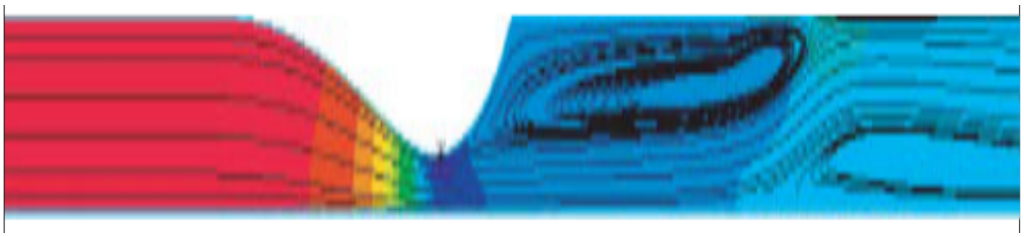

(b) ADINA 2D small strain

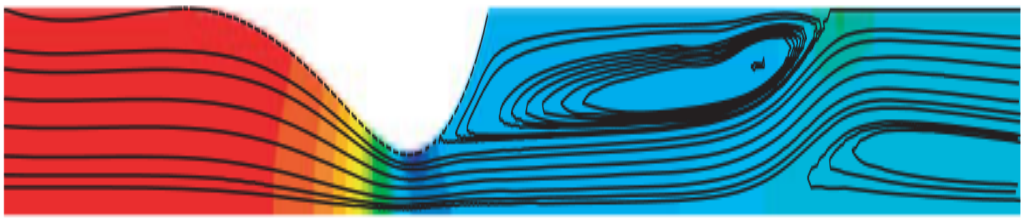

(c) Finite Beam Model by Liu et al. (2009)

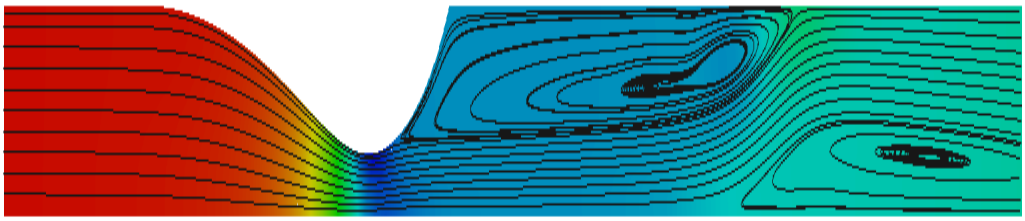

(d) `oomph-lib`

Figure 4.9 Case A mean streamline and pressure contours (red-high, blue-low) comparison between numerical models from Liu et al. (2009) and `oomph-lib`. The streamlines are clipped at horizontal lengths of 3 and 16 to magnify the streamlines around the deformed wall.

for large deformations against the independent FBM and ADINA models (2D-solid small and large strain, iso-beam). It was shown that the `oomph-lib` model conforms to the steady-state behaviours of these numerical models based on the static flexible insert shape and the fluid pressure distribution along the flexible insert. However, there are differences in the dynamic behaviour between the FBM compared to the other numerical methods. The FBM has a greater tendency to produce unstable behaviour whereas the `oomph-lib` and ADINA models remain stable. The only 'instability'in the `oomph-lib` and ADINA models see the flexible insert oscillate indefinitely with constant amplitude (re-defined as unstable in the current study), as opposed to some instances of growing amplitude oscillations in the FBM model. Overall, the validation is successful in ensuring that the `oomph-lib` model is appropriately comparable to other numerical models.

Chapter 5

Detailed Study of Single Flexible Wall Behaviour

5.1 General

It has been shown the instability behaviour captured with `oomph-lib` is consistent with that of previous studies. Case A from Liu et al. (2009) is further investigated because it is unstable and a better understanding of the instability mechanism is required. Presented in this chapter is a detailed account of the flexible insert and fluid behaviour as well as analysis of the energy interaction within the system. The work in this chapter has been previously published in Lai et al. (2012).

5.1.1 Flexible Insert Normalising and Characterisation Parameters

The validation in Chapter 4 of the flexible insert shape was based on its $x-$ and $y-$ coordinates (see Figure 4.6) and the flexible insert motion characterised by the y-displacement at the wall mid-length $x = 7.5$ (see Figures 4.8). All dimensional quantities in Chapter 4 were normalised with the channel height H^*. This method of representation was used to be consistent with the works of Luo et al. (2008) and Liu et al. (2009). Several alterations are made to the results presentation to better depict the flexible insert behaviour considering all parametric sensitivities and system configurations analysed in later chapters.

The first change is to characterise the flexible wall shape in terms of the vertical distance from the wall flush position y' rather than the vertical coordinate y. This means for the single (upper) wall case, the wall flush position is denoted by $y' = 0$ rather than $y = 1$. Using this method, it is simpler to see how much the flexible wall has deflected vertically (inwards of the channel as positive) from its flush position. The horizontal coordinate is also modified with $x' = 0$ being the upstream end of the flexible wall. This makes the coordinate system independent of the upstream length. When looking at the

dual wall case in Chapter 8.1, it also enables the upper and lower wall to have the same measurement metric, *i.e.*. no difference in coordinate system to compare wall vertical deflections.

The second change is in selecting the normalisation length to be the flexible insert length L^*_{flex}. This means $x' = 1$ is the flexible wall downstream end. In the previous works of Luo et al. (2008) and Liu et al. (2009), L^*_{flex} was fixed. In the current study however variation of L^*_{flex} is investigated. L^*_{flex} is used in all subsequent results as the normalisation length unless it is explicitly specified that H^* is used.

For the characterisation of wall movement, using the $y-$displacement at flexible wall midpoint is suitable for parabolic wall shapes. However with the wall shape skewed to the right, the y-displacement at wall mid-length y'_{mid} may be small and experiences similar magnitudes of vertical and lateral movement at this location. A more appropriate point to represent wall deformation is at the maximum vertical point y'_{max}. Use of y'_{mid} can be misleading as it captures the maximum vertical deformation of a parabolic wall shape but not the right-skewed wall shape (see Figure 4.6a). The only possible disadvantage is the loss of consistency in the horizontal position. This however is deemed a reasonable trade-off to capture the appropriate maximum deformation.

5.1.2 Instability Mechanism

The unstable case (Case A) in the study by Liu et al. (2009) is revisited to better understand the instability mechanism. The flexible insert mid-length $y-$displacement in Figure 4.8a show the oscillations still evolving at $t = 80$. Therefore the simulation is extended to a longer time to ascertain the later behaviour of this system after $t = 80$ with `oomph-lib`. This is shown in Figure 5.1. It can be seen the system eventually settles into a saturated oscillation pattern. This condition of saturated oscillations is termed 'neutral stability' in Luo et al. (2008) with 'unstable' defined as cases with continuously amplifying oscillations until numerical failure. Case A is 'unstable' using the FBM model whereas `oomph-lib` is 'neutrally stable'. This is perhaps due to the order of time integration between the models with a higher order formulation in the FBM model (used by Luo et al. (2008) and Liu et al. (2009)) compared to both ADINA and `oomph-lib`. The 'unstable' cases as defined by Luo et al. (2008) are never encountered in the `oomph-lib` model. For the remainder of this thesis, all cases in `oomph-lib` of 'neutral stability' are termed 'unstable' as they correspond to 'unstable' cases in Luo et al. (2008) and Liu et al. (2009).

The steady-state and transient flexible wall deformation over one oscillation cycle is shown in Figure 5.2a. The largest extent the flexible insert can deform is the location of the opposing rigid channel wall and is given by $y'^*/L^*_{\text{flex}} = y' = 0.2$. The black line is the steady-state form of the flexible wall. The red lines show flexible wall shapes over one saturated oscillatory cycle beginning at $t = 209$ of Figure 5.1. The flexible wall shape is skewed to the right due to uneven fluid pressure distribution along the

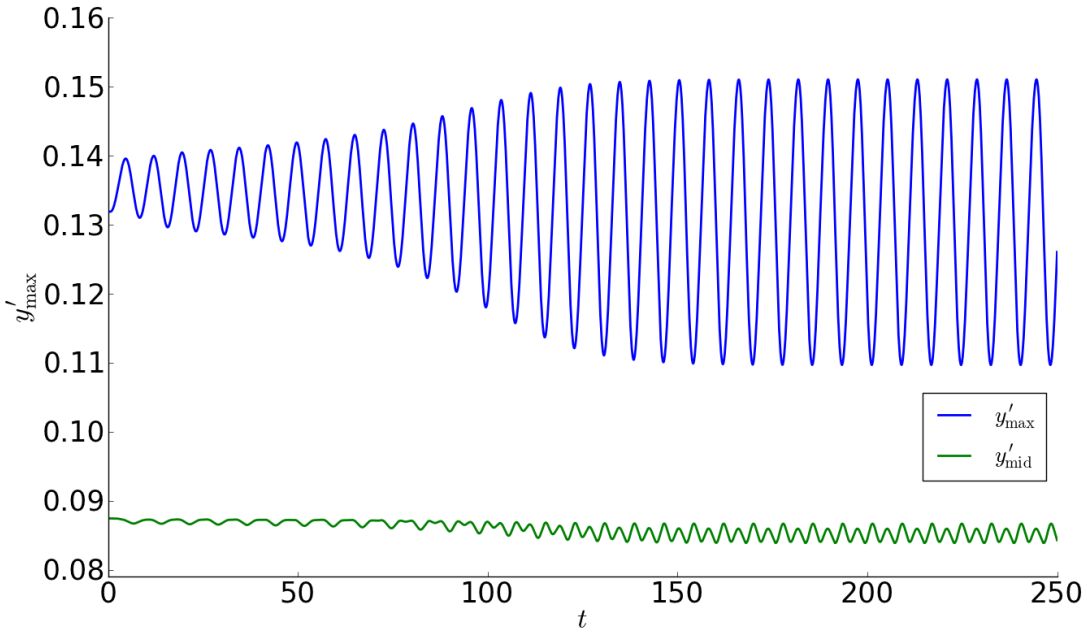

Figure 5.1 `oomph-lib` flexible insert midpoint vertical displacement y'_{mid} and maximum vertical displacement y'_{max} time history based on Case A of Liu et al. (2009) study showing the system settling into the unstable saturated oscillation state.

flexible insert and the fluid viscous forces pulling the flexible wall in the direction of fluid flow (left to right). The presence of vertical movement is obvious with the range the minimum point is moving. The vertical component can be explained to be due to the internal axial strain of the flexible wall, similar to that of a taut string being stretched and relaxed. However, it can be seen that the flexible wall movement is not purely vertical. There is also a lateral component. This is more clearly seen in Figure 5.2b where the x' and y' movement of η_{max} moves in a counter-clockwise orbital around the steady-state η_{max} position. The aspect ratio is 7:20 for the $y'-$axis to $x'-$axis and this is maintained for all plots in this thesis. The pressure p along the flexible insert is shown in Figure 5.2c. The pressure variation is consistent with the size of local insert deformation change. Upstream of the flexible insert has relatively small deformation changes compared to the downstream. Similarly, the pressure variation at the upstream is relatively smaller than the downstream which significantly varies between positive and negative pressure values.

Figure 5.3 shows the fluid flow behaviour within one period of the saturated oscillation cycle. Shown in the fluid domain plots are the vorticity contour lines (black), streamlines (white) and non-dimensional pressure colour contours. This is the colour convention used for all subsequent fluid domain plots. The time steps are adjusted to start from t =0 and end at approximately t =7.5 to represent one oscillation. The fluid domain has also been scaled with the channel height being five times the channel length to magnify the recirculation vortices in the system. For the original perspective, the

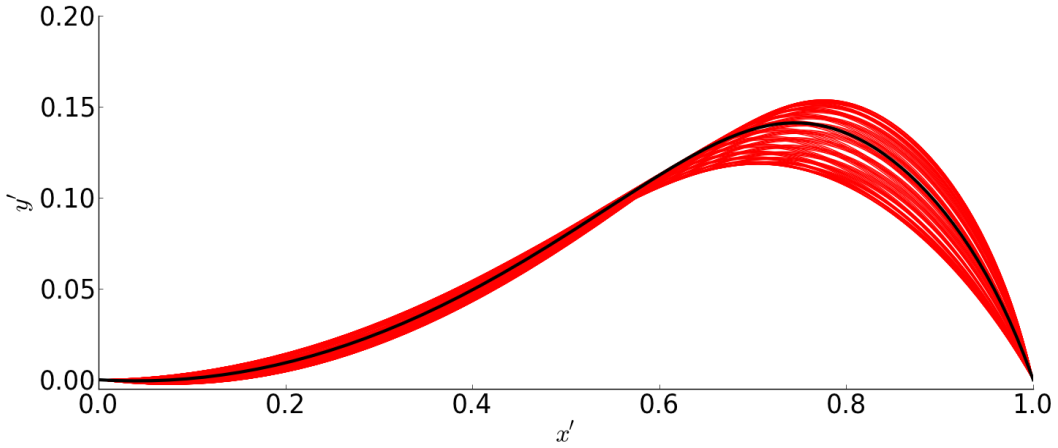

(a) Flexible insert deformation shape.

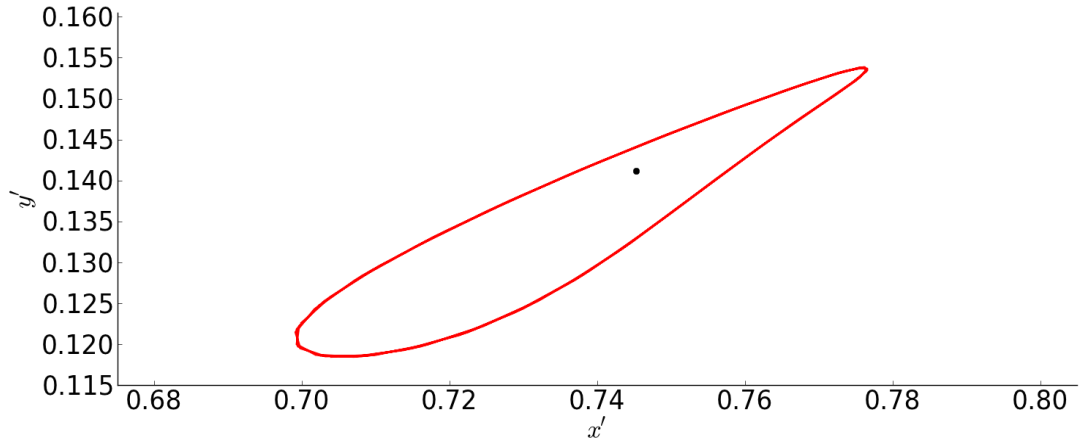

(b) Maximum deformation point $\eta_{\max}$ location.

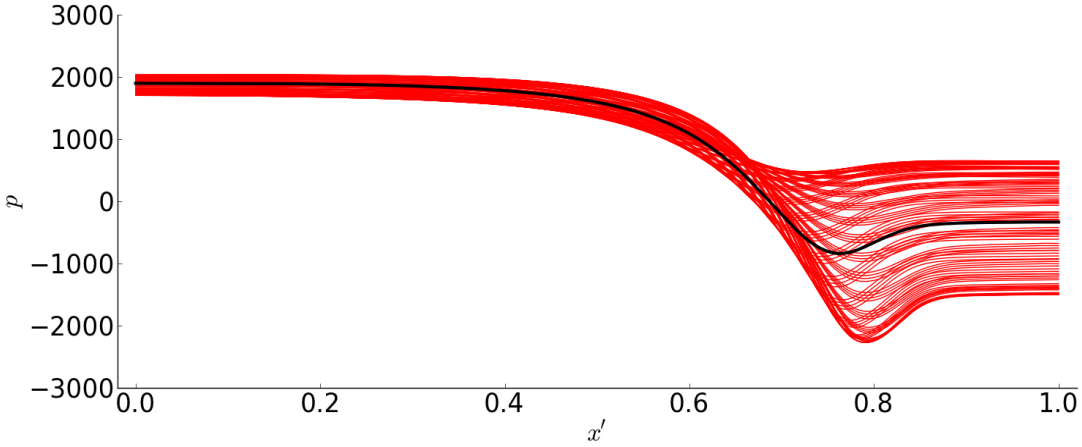

(c) Pressure along flexible insert.

Figure 5.2 `oomph-lib` flexible insert results under steady-state conditions (black line) and over one oscillation cycle (red lines) based on Case A of Liu et al. (2009).

unscaled fluid domain is shown in Appendix A. The peak-to-peak amplitude $A_{\max}$ and oscillation frequency f are 0.041 and 0.13 respectively.

In Figure 5.3 at t =0, the flexible insert is at its smallest deformation. There are multiple vortices downstream of the flexible insert on the upper wall and two on the lower wall. The recirculation vortex attached to the flexible insert (further downstream of the $\eta_{\max}$ location) grows at $t = 2.1$ while the other recirculation vortices continue to dissipate and move downstream. The flexible wall deformation continues to grow to $t = 3.9$ to its largest deformation. This coincides with the growth of the recirculation zone directly downstream of the flexible insert. A recirculation zone has also formed at the bottom wall slightly further downstream. The large recirculation vortex is not sustainable and collapses at $t = 5.7$ while the wall deformation reduces. The recirculation vortex at the bottom wall has grown further at this point. The oscillation cycle is complete at $t = 7.5$ with the recirculation vortex forming again downstream of the $\eta_{\max}$ location and the bottom wall recirculation vortex now reducing in size and moving downstream. The fluid flow is characterised by small separating vortices forming, growing and dissipating on the top and bottom walls.

5.2 Effects of Perturbation Pressure

The perturbation pressure P_{pturb} value used in Case A was selected to obtain similar flexible insert oscillation growth rates as the other numerical models used in Liu et al. (2009). Therefore a test is performed to determine whether instability behaviour is dependent on P_{pturb} by increasing and halving it by 2 from the original selected value (0.5 Pa), while keeping all other parameters the same.

The time histories of $y'_{\max}$ for the P_{pturb} changes and base case are shown in Figure 5.4. The starting point of the three cases are different as different P_{pturb} values are applied with $2P_{\text{pturb}}$ having the largest $y'_{\max}$ and $0.5P_{\text{pturb}}$ the smallest. The main difference is the time taken to reach the final saturated oscillation state. The smaller perturbation $0.5P_{\text{pturb}}$ takes a longer time to reach the saturated oscillation state, whereas the larger perturbation $2P_{\text{pturb}}$ takes a shorter amount of time. This is quantified based on the first peak or trough that shows no variation to the subsquent peak or trough. The $y'_{\max}$ peak-to-peak amplitude A_{peak} and saturated oscillation frequency f is similar in all instances. These results show that P_{pturb} only affects the initial transient behaviour and not the final state of system instability.

5.3 Energy Budget

The system energy budget is discussed in this section. The energy budget is analysed in terms of the overall channel flow as well as the individual flexible insert section and fluid domain contributions.

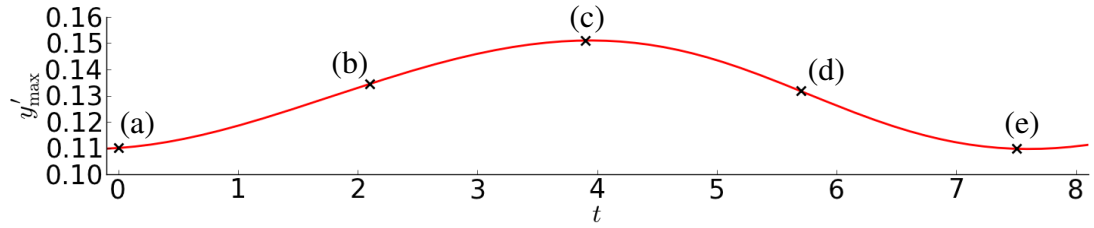

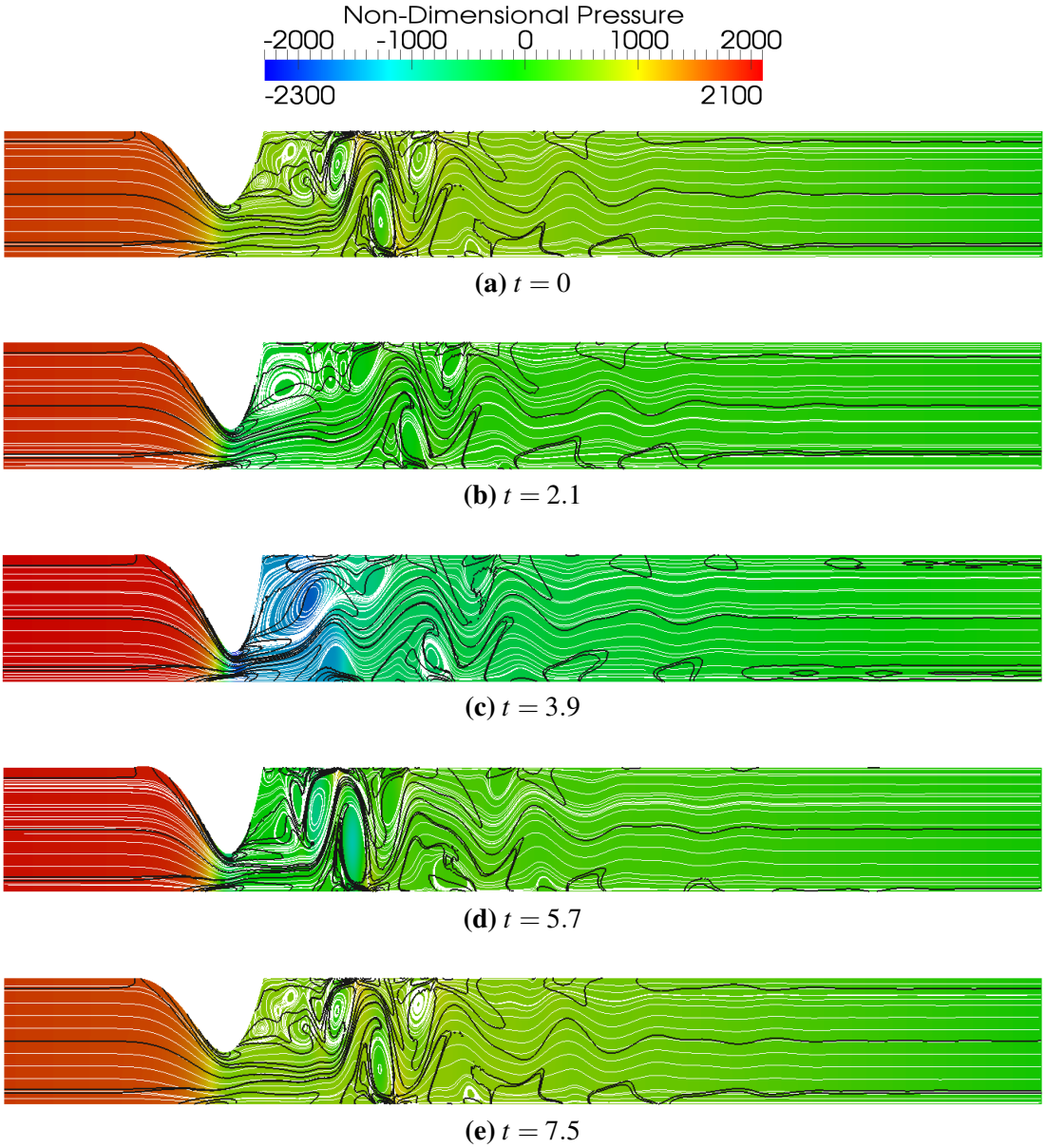

(a) $t = 0$

(b) $t = 2.1$

(c) $t = 3.9$

(d) $t = 5.7$

(e) $t = 7.5$

Figure 5.3 Time history of the flexible insert maximum vertical displacement y'_{max} with corresponding fluid streamlines (white), vorticity contour (black) lines and pressure (colour) contours over one instability oscillation cycle based on Case A from the study by Liu et al. (2009). The fluid domain is scaled with a ratio of 1:5 (channel length to height).

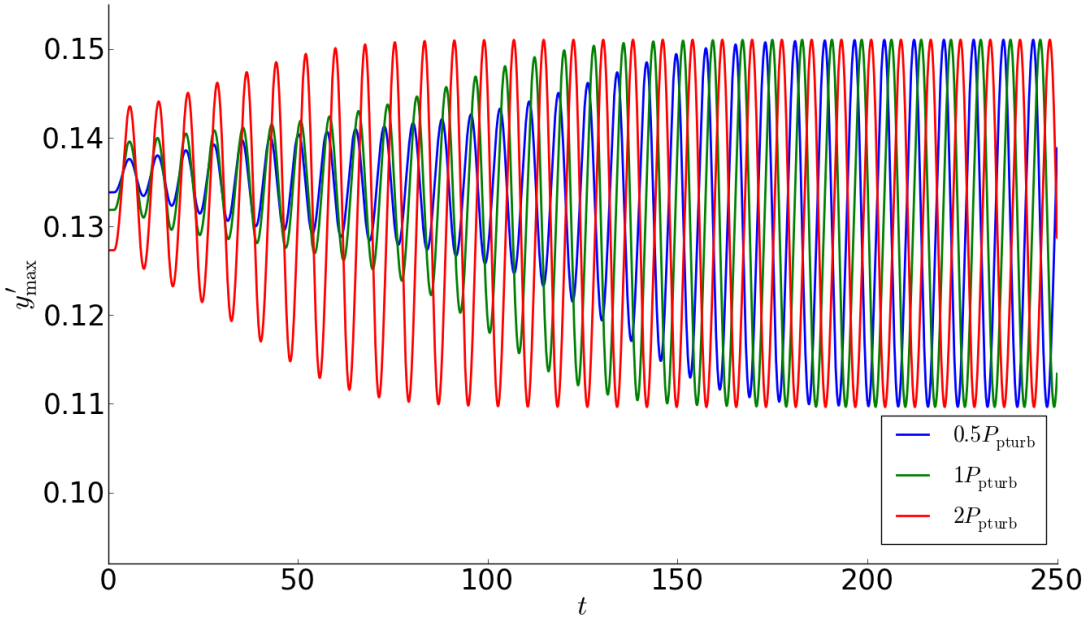

Figure 5.4 `oomph-lib` system sensitivity to 0.5 and 2.0 times P_{pturb} only affecting initial transient behaviour with no impact on final instability behaviour.

5.3.1 Channel Fluid

The fluid rate of energy has five main components as described in Equation 3.18 and is shown in Figure 5.5. The overall channel fluid flow rate of energy balance is shown in Figure 5.5a. The system net rate of boundary energy flux and fluid domain losses (dashed red line) equate to the fluid domain rate of kinetic energy $\dot{KE}_{\text{fluid}}$ (solid blue line). The dashed red line has been inverted to show the quantitative and phase match between the two lines and the energy budget balance within the system.

The individual boundary components for rates of energy flux and domain loss is displayed in Figure 5.5b. The main system driver is the velocity-driven fluid at the inlet through $\dot{W}_{\text{IO}}$. System losses are through $\dot{D}_{\text{fluid}}$ in the fluid domain. The components $\dot{KE}_{\text{IO}}$ and $\dot{W}_{\text{wall}}$ are small in comparison within the energy budget. The relative magnitudes of these components are consistent with the results by Liu et al. (2012).

For the current case mode-2 instability, the average rates of work/energy (denoted by overlines) are listed in Table 5.1. A positive value denotes a source of work/energy input into the channel fluid whilst a negative value denote a loss or retarding energy/work on the channel fluid. The $\overline{\dot{KE}}_{\text{fluid}}$ and $\overline{\dot{KE}}_{\text{IO}}$ approximate zero and the minute non-zero value can be attributed to numerical error. The dominating average values are the rate of work at the inlet and outlet which is mainly counteracted by $\overline{\dot{D}}_{\text{fluid}}$. The contribution of $\overline{\dot{W}}_{\text{wall}}$ is negligible. These magnitudes of the averages also conform to the Liu et al. (2012) study for mode-2 velocity-driven instabilities where $\overline{\dot{W}}_{\text{IO}}$ and $\overline{\dot{D}}_{\text{fluid}}$ dominate.

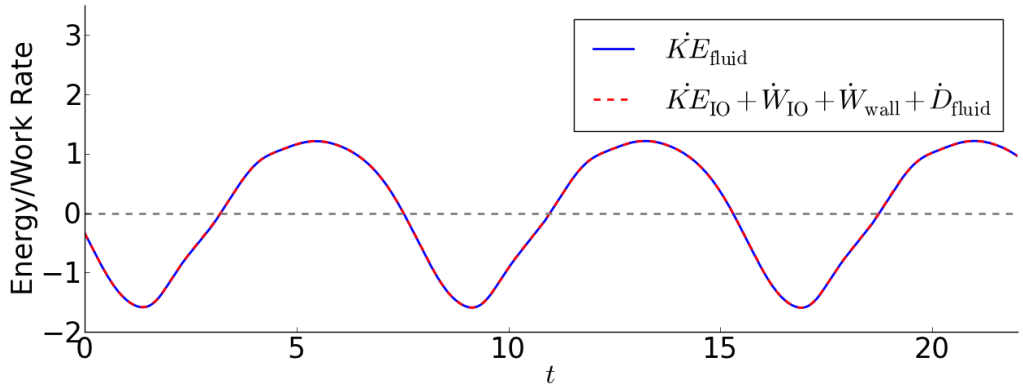

(a) Channel fluid domain kinetic energy rate $\dot{KE}_{\text{fluid}}$ matching with sum of other constituent components.

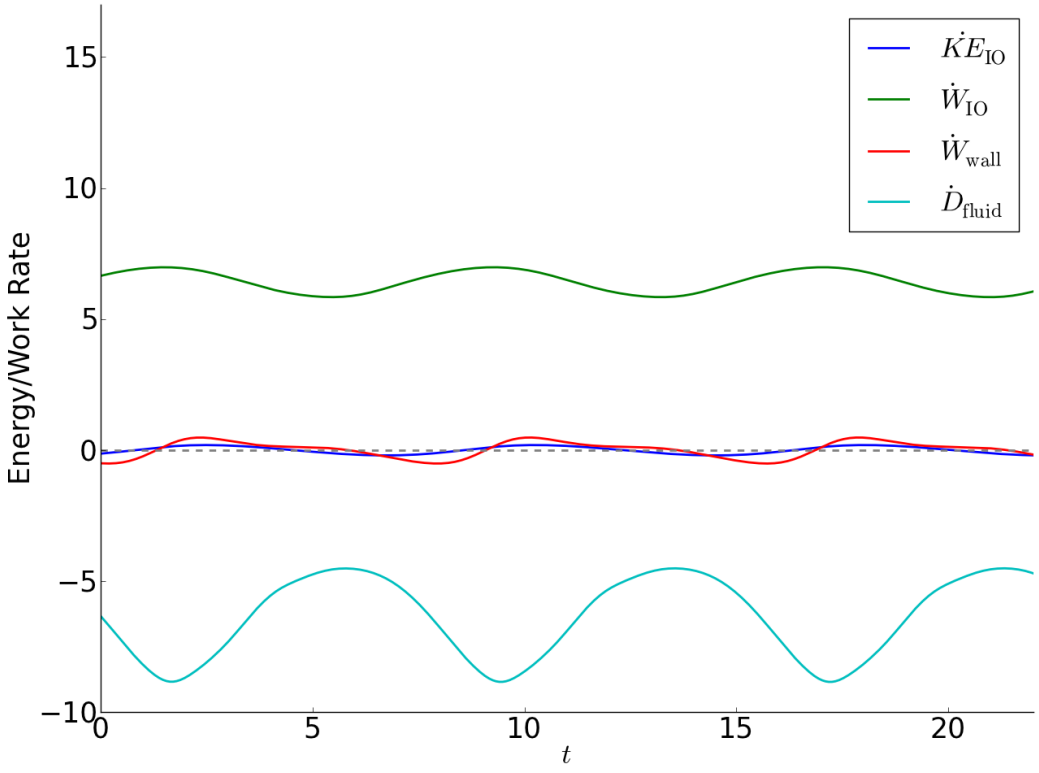

(b) Channel fluid components rate of energy vs. time.

Figure 5.5 Rate of work/energy plots for the channel fluid domain and its individual components.

Table 5.1 Non-dimensional average rates of energy and work for overall flexible insert and channel fluid over one oscillation cycle.

Parameter	$\overline{\dot{KE}}_{\text{fluid}}$	$\overline{\dot{KE}}_{\text{IO}}$	$\overline{\dot{W}}_{\text{IO}}$	$\overline{\dot{D}}_{\text{fluid}}$	$\overline{\dot{W}}_{\text{wall}}$
Value	5.38×10^{-3}	-1.23×10^{-3}	6.41	-6.34	0.024

5.3.2 Flexible Insert

The rates of work and energy pertaining to the flexible insert is described in this section and shown in Figure 5.6. Figure 5.6a shows the overall flexible insert rates of work, summation of the flexible insert internal components is shown in Figure 5.6b and the external components acting on the flexible insert shown in Figure 5.6c. They form the energy balance equation of the flexible wall (see equation 3.15). $\dot{W}_{\text{wall}}$ is the same term as in the previous sub-section and is the rate of work due to the fluid forcing. $\dot{W}_{P\text{ext}}$ is the rate of work done by the uniform external pressure on the flexible insert, and $\dot{PE}$ is the flexible insert potential energy. The $\dot{W}_{\text{wall}}$ and $\dot{W}_{P\text{ext}}$ quantities have been inverted to show the quantitative and phase match between the two lines.

Figure 5.6b show $\dot{PE}$ components which are the rates of flexible wall axial strain energy $\dot{PE}_{\text{axial}}$ and bending potential energy $\dot{PE}_{\text{bend}}$. The left axis is for the axial component (blue line) and the right axis for the bending component (red line). This shows the dominant potential energy component is the axial component. This is consistent with the inherent properties of the flexible insert which has very low bending stiffness. Thus the largest rate of energy variations originate from the magnitude change of the flexible wall stretching.

Figure 5.6c shows the external flexible wall rate of work/energies acting on the flexible wall. These include $\dot{W}_{P\text{ext}}$ and the individual components of $\dot{W}_{\text{wall}}$ which are the fluid pressure from the channel flow $\dot{W}_{\text{wall,p}}$ and channel viscous effects (normal $\dot{W}_{\text{wall,n}}$ and tangential $\dot{W}_{\text{wall,t}}$). The left y-axis is for the external pressure and fluid pressure components. The right y-axis are for the viscous effect components. The viscous effects are one order of magnitude smaller than the other two components.

The average rates of work and energy are listed in Table 5.2. The sign convention is with respect to the flexible insert. A positive sign denotes a work or energy source acting on the flexible insert, whereas a negative sign denotes work/energy counteracting this. The individual $\overline{\dot{W}}_{\text{wall}}$ components (pressure, normal and tangential traction) sum to 0.024 as was seen in the overall system averages in Table 5.1. The overall summation of $\overline{\dot{PE}}$ and $\overline{\dot{W}}_{\text{wall}} + \overline{\dot{W}}_{P\text{ext}}$ should balance. The difference between them is 6.5×10^{-4} and is attributed to numerical error.

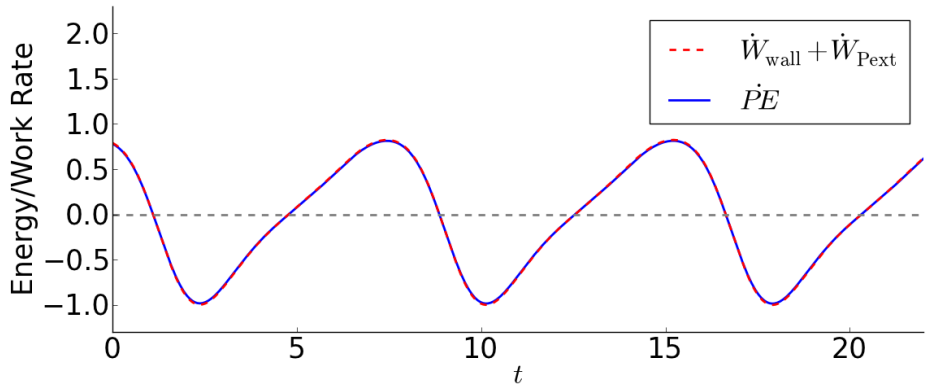

(a) Flexible wall overall rate of work vs. time.

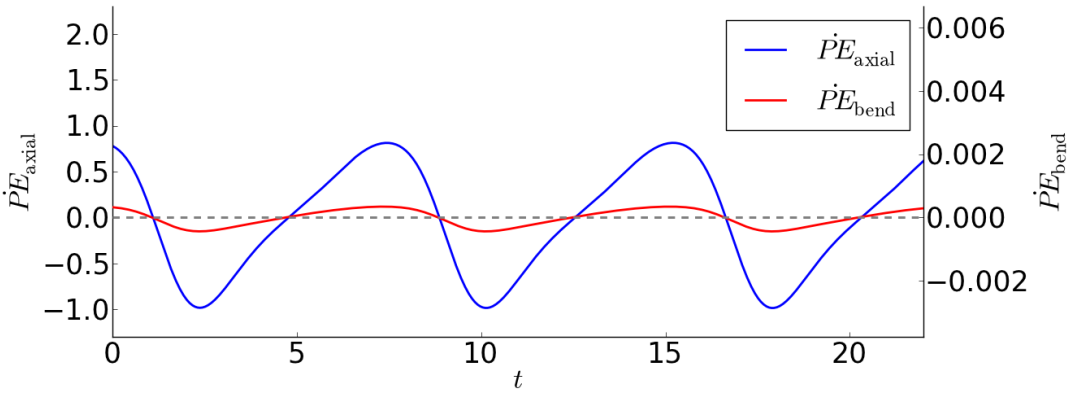

(b) Flexible wall rate of potential energy vs. time.

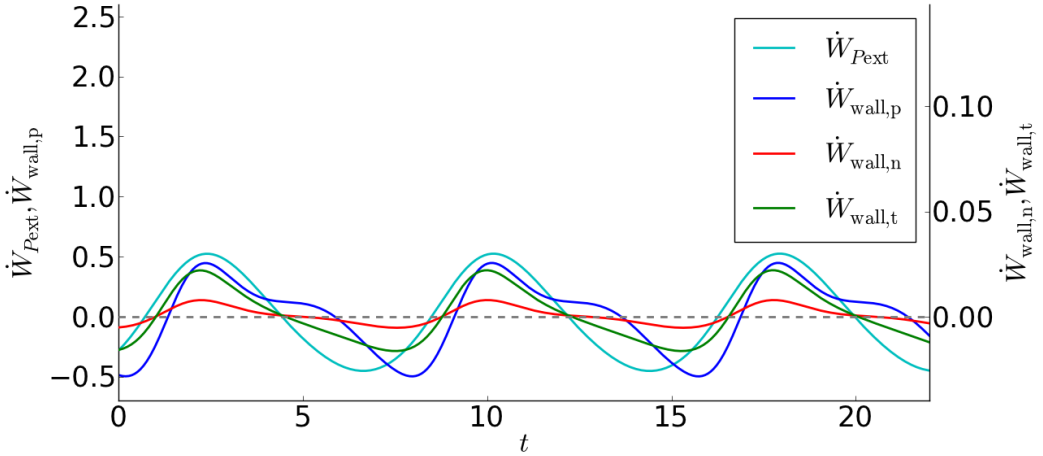

(c) Flexible wall rate of external work categorised into the external pressure, fluid pressure, and normal and tangential traction components.

Figure 5.6 `oomph-lib` rate of work/energy plots for the flexible insert and its individual components.

Table 5.2 Non-dimensional average rates of energy and work for the flexible insert.

Parameter	$\overline{\dot{P}\dot{E}}_{\text{axial}}$	$\overline{\dot{P}\dot{E}}_{\text{bend}}$	$\overline{\dot{W}}_{\text{wall,p}}$	$\overline{\dot{W}}_{\text{wall,n}}$	$\overline{\dot{W}}_{\text{wall,t}}$	$\overline{\dot{W}}_{P\text{ext}}$
Value	-0.049	-2.6×10^{-5}	0.023	6.9×10^{-4}	8.4×10^{-4}	0.025

5.4 Summary

Case A from the study by Liu et al. (2009) was selected for further analysis to better understand the instability behaviour. A standardised method for analysing the system and instability was utilised. This includes observation of the flexible insert shape, tracking of the flexible insert y-displacement in time (typically at the maximum deformation location), pressure along the flexible insert, channel fluid streamlines and the energy balance. In this case study, it was shown the flexible insert oscillates indefinitely with the growth and decay of vortices downstream of the flexible insert. The energy budget shows the dominant rates of work and energy components driving instability. A consistent rate of work input at the inlet (velocity-driven) is dissipated within the fluid domain with minor contributions by the flexible insert. The flexible insert is dominated by the axial potential energy, pressure and normal traction along the flexible wall and the work done by the uniform external pressure. The analysis tools employed for the particular case in this chapter is used in the system parametric study to characterise different steady-state systems in Chapter 6 and highlight the differences in dynamic instability mechanism types in Chapter 7.

Chapter 6

Static Single Flexible Insert Non-Dimensional Scheme and Parameterisation

6.1 General

In this section the non-dimensional scheme developed is discussed which characterises the single flexible insert steady-state behaviour (when not subjected to any perturbations to induce instability). The purpose of this is to determine system parameters that affect the flexible insert shape and their relative importance. The proposed non-dimensional formulation consists of three parameters; $\mathrm{Ca}_{\mathrm{eff}}$.Re, $\mathrm{Ca}_{\mathrm{eff}}/\mathrm{Re}$ and P_{eff}. The first two parameters are based on the effective Cauchy number $\mathrm{Ca}_{\mathrm{eff}}$ and Reynolds number Re which are defined as

$$\mathrm{Ca}_{\mathrm{eff}} = \frac{\rho^* U^{*2}}{E^*_{\mathrm{eff}}} \times \frac{2L^*_{\mathrm{flex}}}{h^*} \tag{6.1}$$

$$\mathrm{Re} = \frac{\rho^* U^* H^*}{\mu^*} \tag{6.2}$$

The term $\mathrm{Ca}_{\mathrm{eff}}$ is the ratio of flow stiffness to flexible wall stiffness. It is an effective form of the Cauchy number Ca that is applicable for this specific flexible insert configuration. The original Ca form is given by

$$\mathrm{Ca} = \frac{\rho^* U^{*2}}{E^*_{\mathrm{eff}}} \tag{6.3}$$

The proposed $\mathrm{Ca}_{\mathrm{eff}}$ term differs from the original Ca with the additional consideration of flexible insert thickness h^* and flexible insert length L^*_{flex}, both of which affect the insert stiffness. $\mathrm{Ca}_{\mathrm{eff}}$ is comparable to the inverse of the C_λ term in the formulation by Luo et al. (2008) (see equation 4.1).

The term Re is the Reynolds number which characterises the fluid flow behaviour. It is the ratio of the fluid inertial force to the fluid viscous force.

The first two characterising parameters are then defined as

$$\mathrm{Ca_{eff}}.\mathrm{Re} = \frac{\rho^* U^{*2}}{E^*_{\mathrm{eff}}} \times \frac{2L^*_{\mathrm{flex}}}{h^*} \times \frac{\rho^* U^* H^*}{\mu^*} \tag{6.4}$$

$$\frac{\mathrm{Ca_{eff}}}{\mathrm{Re}} = Q_{\mathrm{eff}} = \frac{\mu^* U^*}{E^*_{\mathrm{eff}} H^*} \times \frac{2L^*_{\mathrm{flex}}}{h^*} \tag{6.5}$$

The first parameter $\mathrm{Ca_{eff}}.\mathrm{Re}$ is the product of the $\mathrm{Ca_{eff}}$ and Re. This parameter represents the FSI product of the ratio of normal fluid stress to structural stress, and the ratio of inertial to viscous force. The second parameter is $\mathrm{Ca_{eff}}/\mathrm{Re}$. This term represents the FSI ratio of the fluid viscous stress scale to the structural stress scale.

The third parameter P_{eff} is defined as

$$P_{\mathrm{eff}} = \frac{(P^*_{\mathrm{ext}} - P^*_{\mathrm{mean}})L^*_{\mathrm{flex}}}{E^*_{\mathrm{eff}} h^*/2} \tag{6.6}$$

with

$$P^*_{\mathrm{mean}} = \frac{12\mu^* U^* (\frac{L^*_{\mathrm{flex}}}{2} + L^*_{\mathrm{down}})}{H^{*2}} \tag{6.7}$$

The P_{eff} term is the ratio of net flexible insert pressure loading to insert stiffness. Three main pressure load components act on the flexible insert. The first component is the external applied uniform pressure P^*_{ext}. The second is the undeformed flexible insert mean fluid pressure P^*_{mean} relative to the zero pressure boundary outlet. By selecting the pressure at the flexible insert midpoint as P^*_{mean}, it is assumed this is representative of the average pressure loading across the entire flexible insert. The sign convention is positive for pressure acting inwards; *i.e.* P^*_{ext} acting inwards is positive and P^*_{mean} acting outwards of the channel is negative. The third component is the flexible insert stiffness $E^*_{\mathrm{eff}} h^*/2L^*_{\mathrm{flex}}$ which considers the flexible insert thickness, length and stiffness.

This non-dimensional scheme differs from that used by Luo et al. (2008) with the purpose of incorporating the various parametrical variations (especially L^*_{flex}), as explained in the subsequent section. It also serves to 'unfold' the cascade structure shown in Figure 2.2 and is explained in more detail in Section 7.6.

6.2 Static Scheme Validation

Presented in this section are the validation tests for the non-dimensional parameters selected; P_{eff}, $\mathrm{Ca_{eff}}.\mathrm{Re}$ and $\mathrm{Ca_{eff}}/\mathrm{Re}$. A base case for testing is selected, with the dimensional and non-dimensional test parameters listed in Table 6.1. Internal dimensional parameter variations are applied as per Table 6.2. This involves applying different combinations of physical properties; fluid properties and speed, uniform external pressure

Table 6.1 Static non-dimensional scheme validation base case parameters.

Parameter	Value	Description
L^*_{up} (mm)	50	Upstream length of channel
L^*_{flex} (mm)	50	Collapsible length of channel
L^*_{down} (mm)	300	Downstream length of channel
H^* (mm)	10	Height of channel
h^* (mm)	0.1251	Thickness of flexible insert
ρ^*_{f} ($\times 10^3$ kg.m^{-3})	1	Density of fluid
μ^* ($\times 10^{-3}$ Pa.s)	1	Dynamic viscosity of fluid
ν	0.5	Poisson's ratio of solid
$\rho^*_{\text{s}} h^*$	0	Mass per unit area of solid
B^*($\times 10^{-9}$ N.m)	1.6315	Flexural rigidity of flexible insert
E^*_{eff}($\times 10^4$ Pa)	1	Young's modulus of flexible insert
U^*_{mean}($\times 10^{-2}$ m/s)	1	Inlet mean velocity
P^*_{ext} (Pa)	3.3	Uniform external pressure
P^*_{mean}	0.39	Mean pressure
Ca_{eff} ($\times 10^{-3}$)	8	Effective Cauchy number Ca_{eff}
Re	100	Reynolds number Re
Ca_{eff}.Re	0.8	FSI product
$\text{Ca}_{\text{eff}}/\text{Re}$ ($\times 10^{-5}$)	8	FSI ratio
P_{eff}	0.295	Effective pressure

magnitude, and flexible insert dimensions and material properties while maintaining parameters P_{eff}, Ca_{eff}.Re and $\text{Ca}_{\text{eff}}/\text{Re}$ constant.

The overlaid results for the base case and variation cases V-1 through V-6 are shown in Figure 6.1. The flexible insert shapes are shown in Figure 6.1a showing similar deformation shapes (if not the same) in all instances. The maximum vertical deflection y'_{max} values and the associated horizontal position x'_{max} are listed in Table 6.3. The maximum channel height in all instances is 0.2. These test cases are considered to have large deflections with $y'_{\text{max}} = 0.1608$ (larger than channel mid-height $y' = 0.1$). The largest errors from base case for y'_{max} and x'_{max} are 0.0004% and 0.02% respectively, which is essentially negligible.

The normal pressure along the flexible insert is shown in Figure 6.1b and it can be seen the results are similar for all variations, along with the system fluid domain behaviour shown in Figure 6.2. This is not plotted to scale with channel height scaled $5H$ for clearer illustration of the recirculation vortices. The fluid flow behaviour for all cases is also similar, proving the flexible insert and fluid flow behaviour are similar with all variations performed. Thus, the non-dimensional scheme is suitable to characterise the mean-state (static) FSI interaction between the flexible insert and fluid flow through the channel.

Table 6.2 Static non-dimensional scheme variations test parameters.

Variation Number	Dimensional Parameters							
	$L^*_{flex}+L^*_{down}$ (m)	H^* (m)	h^* (m)	ρ^* (kg/m^3)	μ^* (Pa.s)	E^*_{eff} (MPa)	U^* (m/s)	P^*_{ext} (Pa)
V-1	-	-	0.1	-	-	100	-	-
V-2	-	-	-	10	-	1	0.1	0.1
V-3	5	5	-	-	-	-	2	0.2
V-4	-	-	-	100	10	-	10	-
V-5	2	2	-	0.125	-	40	4	2
V-6	2	-	-	-	2	20	-	-

Table 6.3 Static non-dimensional scheme variation test results.

Variation Number	y'_{max}	x'_{max}	y'_{max} Error (%)	x'_{max} Error (%)
Base case	0.295	0.624	N/A	N/A
V-1	0.298	0.624	0.0000	0.016
V-2	0.295	0.624	0.0004	0.001
V-3	0.295	0.624	0.0001	0.006
V-4	0.295	0.624	0.0000	0.000
V-5	0.295	0.624	0.0001	0.004
V-6	0.295	0.624	0.0000	0.000

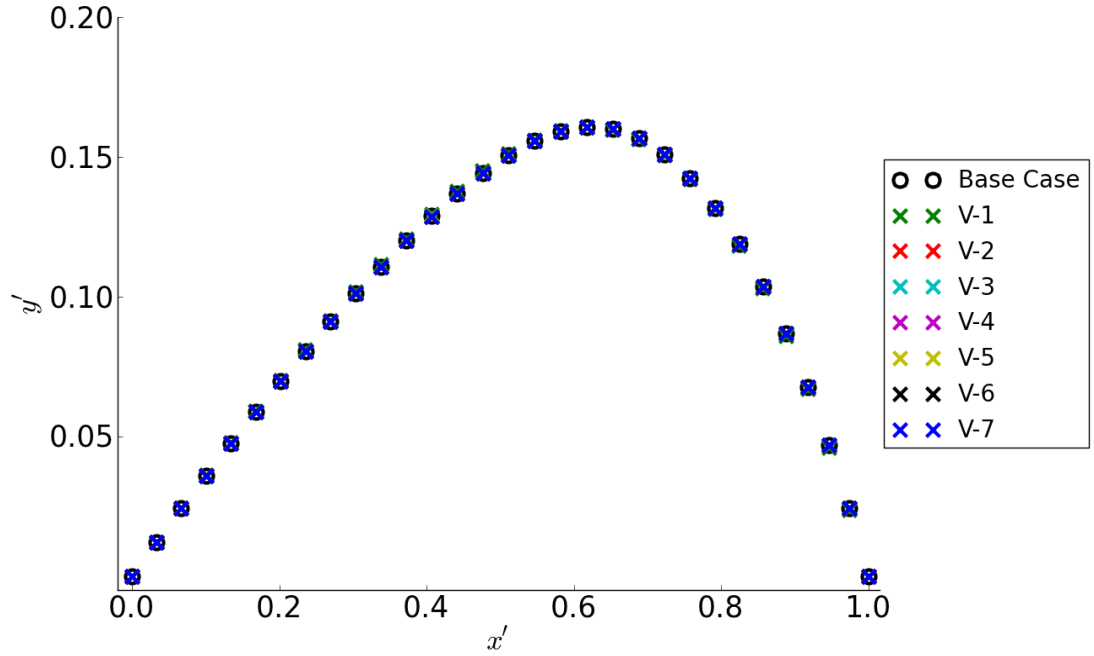

(a) Flexible insert deformation shape.

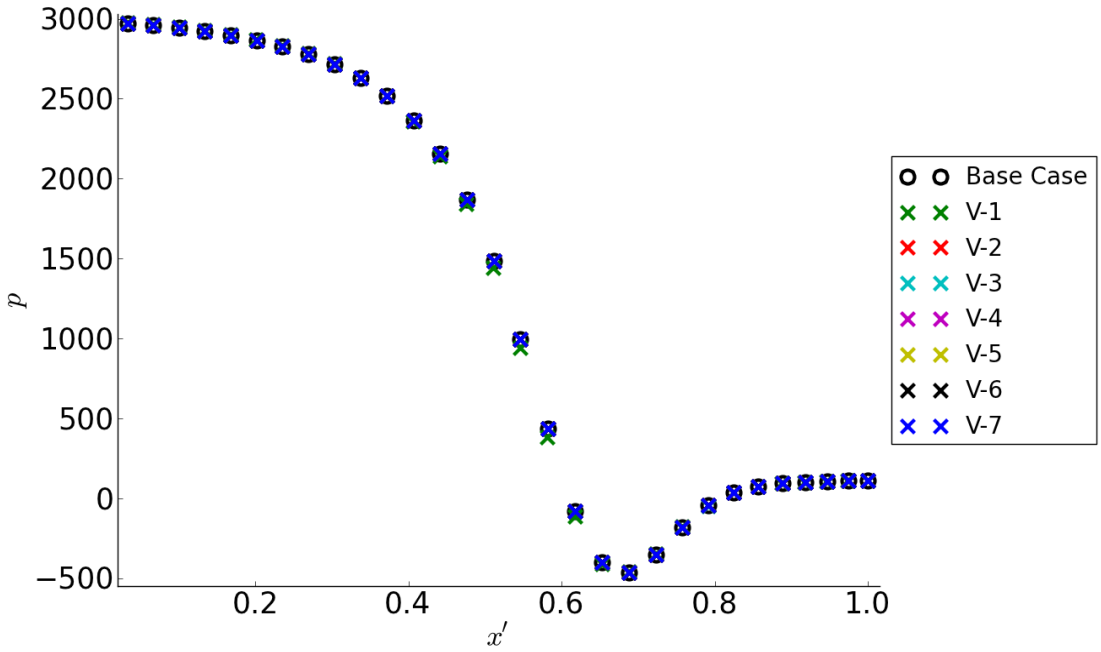

(b) Pressure along flexible insert.

Figure 6.1 Static non-dimensional scheme variation testing flexible insert steady-state results overlaid on each other.

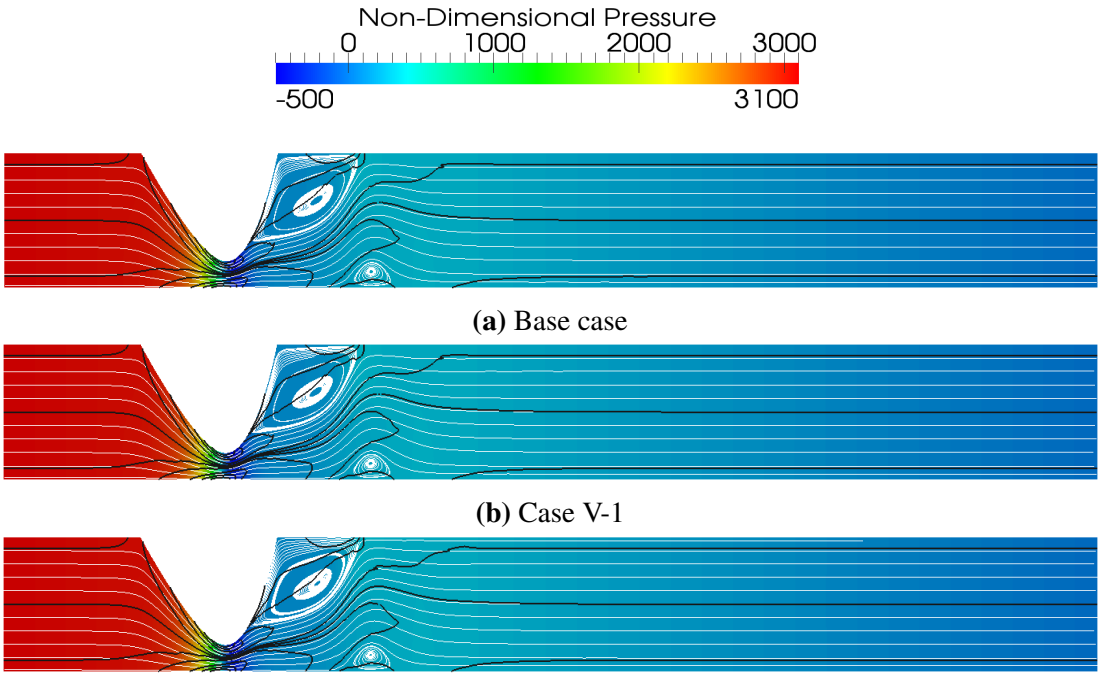

(a) Base case

(b) Case V-1

(c) Case V-4

Figure 6.2 Steady-state streamlines (white) and vorticity contour (black) lines with the non-dimensional pressure (colour) contours for select cases looking at static non-dimensional scheme variation validation. The fluid domain is scaled with a ratio of 1:5 (channel length to height).

6.3 Scheme Sensitivity

In the previous section it was established that the flexible insert shape can be characterised with the three non-dimensional parameters P_{eff}, $\text{Ca}_{\text{eff}}.\text{Re}$ and $\text{Ca}_{\text{eff}}/\text{Re}$. These three parameters are required to fully characterise the flexible insert shape. Sensitivity testing is performed on these non-dimensional parameters to determine the relative importance between all three terms and whether simplification of the system is possible. For each sensitivity testing instance, two parameters are kept constant and the third altered to determine its effect on the flexible insert shape. The altered parameter is doubled and halved in the first pass. If no significant changes occur, the term is then multiplied and divided by 10. Sensitivity testing parameter changes are listed in Table 6.4. These are presented in terms of multiplication factors on the base case parameters in Table 6.1.

Flexible insert behaviour results for test S-1 and S-2 (P_{eff} sensitivity), and S-3 and S-4 ($\text{Ca}_{\text{eff}}/\text{Re}$ sensitivity) are shown in Figure 6.3. The flexible insert shape can be seen in Figure 6.3a. For this particular instance to capture the sensitivity testing on the channel height, H^* is used as the y'^* normalisation length instead of L^*_{flex}. L^*_{flex} is kept as the x'^* normalisation length because there is also sensitivity testing involving L^*_{flex}. There are significant differences in insert shape between the base case and the P_{eff} and

Table 6.4 Static non-dimensional scheme sensitivity test parameter variations.

Sensitivity Number	Parameter Tested	Dimensional Parameter Ratio ($\times$ Base case)					
		$L^*_{flex}+L^*_{down}$ (m)	H^* (m)	ρ^* (kg/m^3)	E^*_{eff} (MPa)	U^* (m/s)	P^*_{ext} (Pa)
S-1	$0.5P_{eff}$	0.5	-	-	5	-	0.5
S-2	$2P_{eff}$	2	-	-	20	-	2
S-3	$0.5Ca_{eff}/Re$	2	-	$\sqrt{2}$	40	-	2
S-4	$2Ca_{eff}/Re$	0.5	-	$\sqrt{0.5}$	2.5	-	0.5
S-5	$0.5Ca_{eff}.Re$	2	2	$\sqrt{128}$	40	4	2
S-6	$2Ca_{eff}.Re$	2	2	$\sqrt{32}$	40	4	2
S-7	$0.1Ca_{eff}.Re$	2	2	$\sqrt{640}$	40	4	2
S-8	$10Ca_{eff}.Re$	2	2	$\sqrt{6.4}$	40	4	2

Ca_{eff}/Re sensitivity cases. The fluid pressure acting on the flexible insert for cases S-1 through S-4 is also shown in Figure 6.3b.

Cases S-1 and S-4 have similar flexible insert shapes that are more parabolic and have smaller y'_{max} than the base case. This is however due to different reasons in both instances. The smaller P_{eff} value in case S-1 results in a smaller inward deformation which reduces the flexible insert exposure to a larger shearing force from the fluid flow action. Case S-4 differs from this by having the same P_{eff} as the base case and a larger Ca_{eff}/Re value. A larger Ca_{eff}/Re value means the insert stiffness dominates over the fluid stiffness, which results in a more parabolic insert as well and reduced y'_{max}. This is confirmed by the relatively lower pressure loading on the flexible insert shown in Figure 6.3b for cases S-1 and S-4.

Cases S-2 and S-3 also have similar flexible insert shapes with x'_{max} skewed further to the right and larger y'_{max} than the base case. For case S-1, a larger P_{eff} results in larger insert deformation. The exposure to fluid shear forces and uneven fluid pressure distribution along the flexible insert push x'_{max} further to the right. For case S-4, a smaller Ca_{eff}/Re value means the flow stiffness and fluid viscous force is smaller compared to the flexible wall stiffness and fluid inertial force, resulting in the flexible insert having a more parabolic form. The large y'_{max} is due to the relatively higher pressure loading on the flexible insert as shown in Figure 6.3b. This signifies that P_{eff} and Ca_{eff}/Re are important parameters that have to be considered independently to adequately characterise the static flexible insert shape.

Flexible insert shape results for test cases S-5 through S-8 for $Ca_{eff}.Re$ sensitivity is shown in Figure 6.4a and the fluid pressure along the flexible insert in Figure 6.4b. The metrics for determining the difference between the base case and cases S-5 to S-8 are listed in Table 6.5.

The flexible insert shapes are similar for all $Ca_{eff}.Re$ instances tested. This shows the $Ca_{eff}.Re$ variation effect is not as critical to the flexible insert shape, as long as

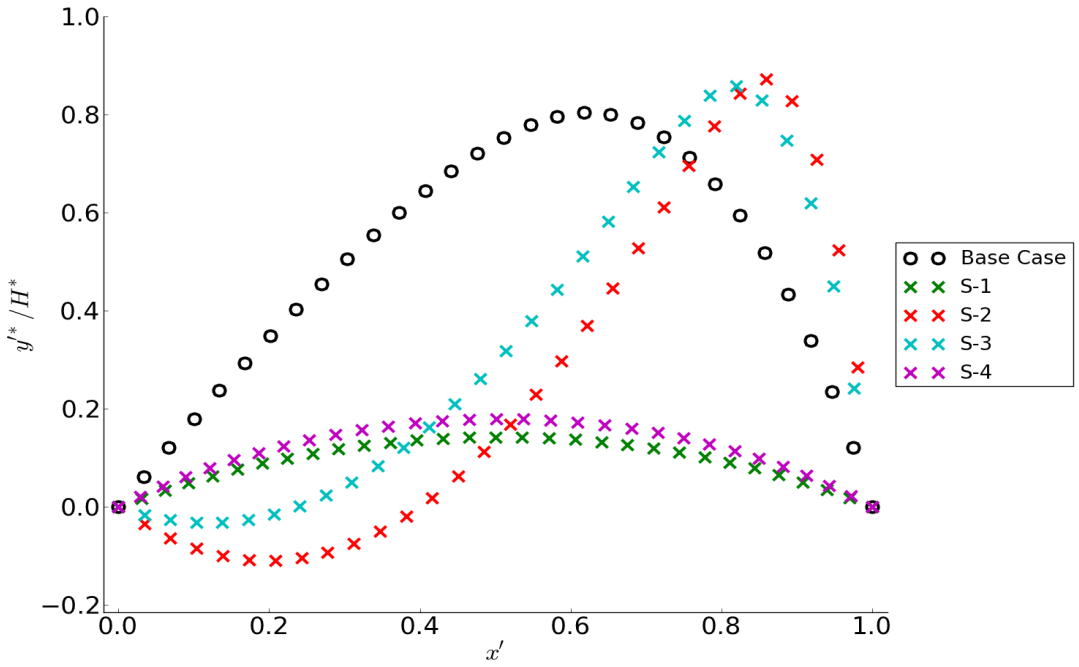

(a) Flexible insert deformation with y'/H^*.

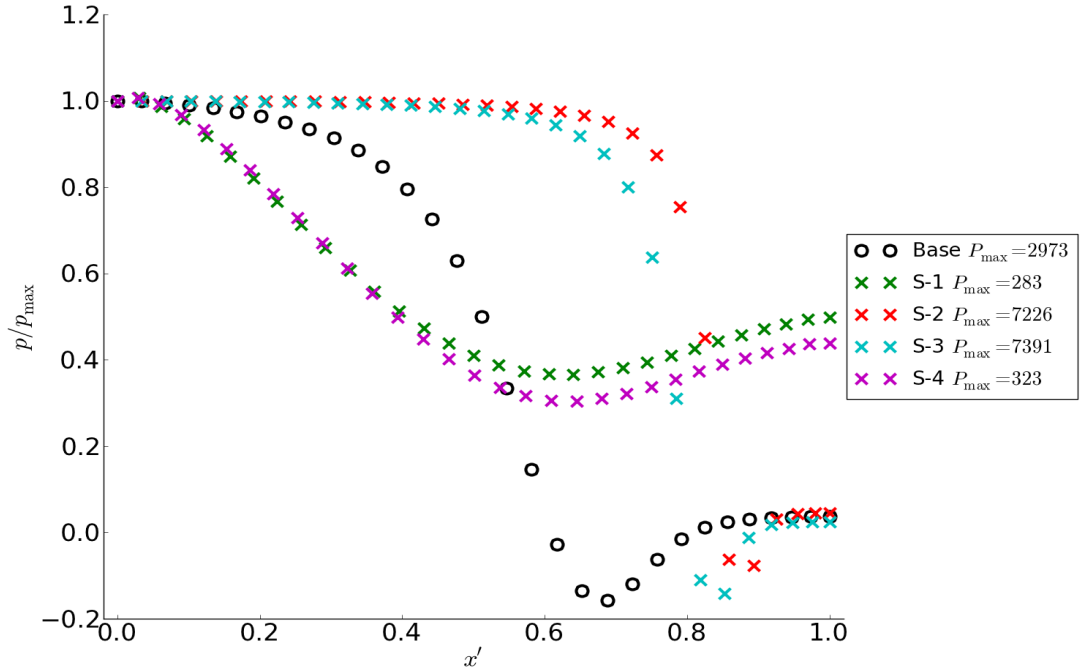

(b) Pressure along flexible insert.

Figure 6.3 P_{eff} (case S-1, S-2) and $\text{Ca}_{\text{eff}}/\text{Re}$ (case S-3, S-4) sensitivity tests steady-state flexible insert behaviour results.

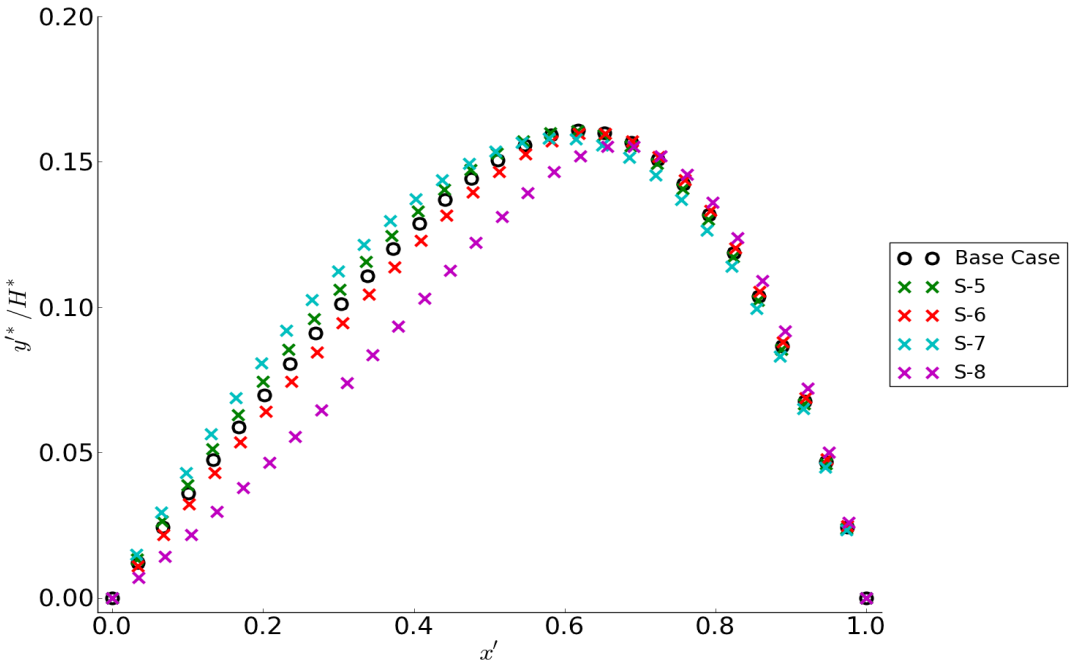

(a) Flexible insert deformation.

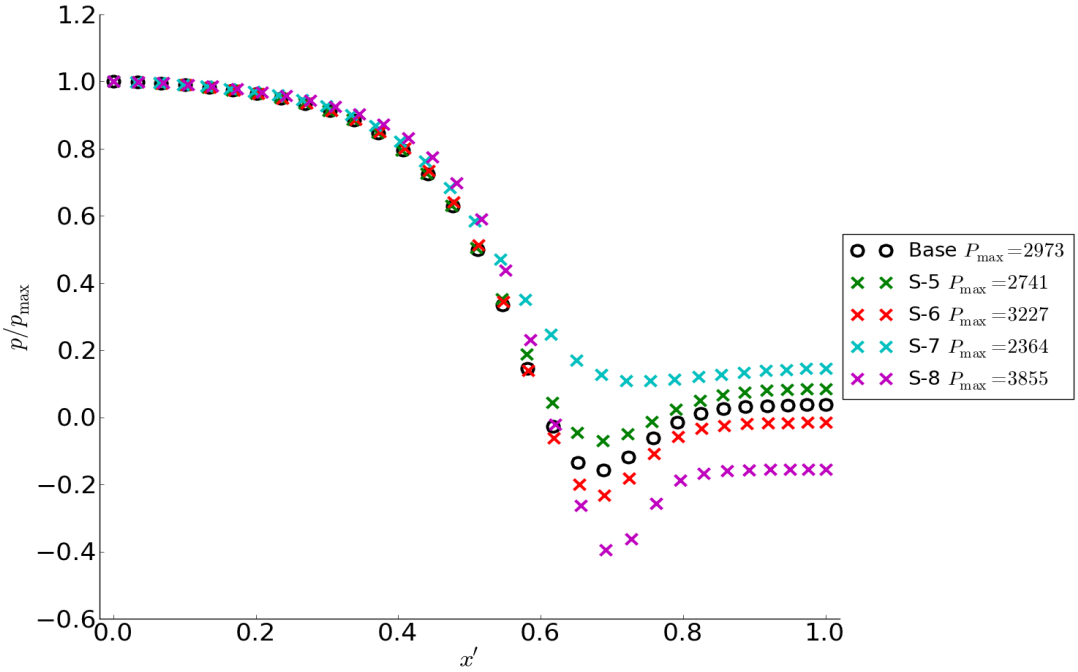

(b) Pressure along flexible insert.

Figure 6.4 Ca_{eff}.Re (case S-5 to S-8) sensitivity tests steady-state flexible insert behaviour results.

Table 6.5 Static non-dimensional scheme test results for sensitivity cases S-5 to S-8.

Variation Number	y'_{max}	x'_{max}	y'_{max} Error (%)	x'_{max} Error (%)
Base case	0.1608	0.6173	N/A	N/A
S-5	0.1607	0.6163	0.09	0.17
S-6	0.1598	0.6538	0.62	5.93
S-7	0.1582	0.5788	1.63	6.23
S-8	0.1553	0.6561	3.45	6.30

the ratio between the fluid and flexible insert stiffness (Ca_{eff}/Re) and the effective loading on the flexible insert (P_{eff}) is constant. For the purposes of selecting a metric to characterise the flexible insert deflection, y'_{max} is suitable as it is a good measure of how deformed the flexible insert is and more easily discernible than variations in x'_{max}. Furthermore, it is largely insensitive to changes in $Ca_{eff}.Re$. Variation of $Ca_{eff}.Re$ by 0.1 and 10 times of base case only produced differences of 1.6% and 3.5% respectively.

As shown in Figure 6.4b, the fluid pressure along the flexible insert can show significant differences. Case S-7 results in the smallest variation in non-dimensional pressure (2364 max, 256 min). Case S-8 results in the largest variation in non-dimensional pressure (3855 max, -1524 min). This is consistent with the magnitude of the $Ca_{eff}.Re$ values which is smaller for case S-7 (0.1$\times$ base case) and larger for case S-8 (10$\times$ base case). This however seems to only slightly change the flexible insert shape from being more parabolic in case S-7 to having y'_{max} skewed to the right in case S-8. Although that is the case, it is still useful to utilise the independence of y'_{max} (as the flexible insert defining characteristic) from the term $Ca_{eff}.Re$. Therefore the flexible insert shape can be characterised with just the two terms; Ca_{eff}/Re and P_{eff} in terms of its y'_{max} value.

6.4 Scheme Parameterisation

It has been shown that the two non-dimensional parameters Ca_{eff}/Re and P_{eff} are the primary parameters controlling the flexible insert shape in terms of y'_{max}. The effect of $Ca_{eff}.Re$ on y'_{max} is minimal and can be neglected. To establish the steady-state (static) parameterisation of this system, variation across a range of P_{eff} (0.2, 0.3, 0.4) and Ca_{eff}/Re (1×10^{-5} to 1×10^{-2}) was performed. The $Ca_{eff}.Re$ value is fixed at 0.1. The parameterisation results are shown in Figure 6.5 with variation of P_{eff} and Ca_{eff}/Re, and y'_{max} as the measurement metric. The possible y'_{max} range is from 0 (undeformed wall) to 0.2 (opposing rigid wall). The cases of interest are with large wall deformations only and this is deemed to be any deformation larger than half the channel height ($y' = 0.1$). The specification of the P_{eff} and Ca_{eff}/Re analysis range are based on an iterative process to meet this large deformation y'_{max} criterion. At $Ca_{eff}/Re = 1 \times 10^{-2}$, $y'_{max} = 0.0625$ at $P_{eff} = 0.2$ and $y'_{max} = 0.0787$ at $P_{eff} = 0.4$, less

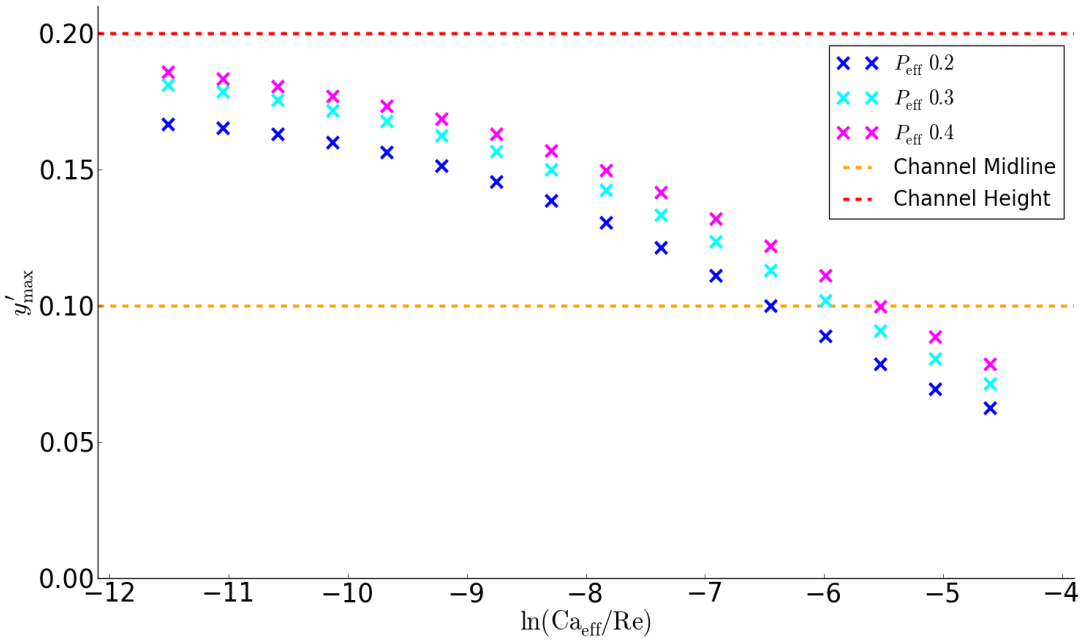

Figure 6.5 Maximum vertical displacement y'_{max} results with ln(Ca$_{eff}$/Re) and P_{eff} variation.

than channel mid-height. At Ca$_{eff}$/Re $= 1 \times 10^{-5}$, $y'_{max} = 0.167$ at $P_{eff} = 0.2$ and $y'_{max} = 0.186$ at $P_{eff} = 0.4$, approaching the opposing rigid wall. This range of P_{eff} and Ca$_{eff}$/Re therefore covers the range considered for large wall deformations.

The three sets of P_{eff} variations show a common trend across the Ca$_{eff}$/Re range analysed with application of an offset in y'_{max}. It was found that using the relationship y'_{max}-0.1P_{eff} provides a suitable collapse of all three P_{eff} sets to a single line as shown in Figure 6.6. The Ca$_{eff}$/Re and P_{eff} variation can then be characterised with the quadratic equation

$$y'_{max} = -0.00175[\ln(\text{Ca}_{eff}/\text{Re})]^2 - 0.0443\ln(\text{Ca}_{eff}/\text{Re}) - 0.13 + 0.1P_{eff} \qquad (6.8)$$

6.5 Parameterisation Sensitivity

Further system sensitivity testing is performed to confirm the independence from Ca$_{eff}$/Re variation (as was done in Section 6.3 at ln(Ca$_{eff}$/Re) $= -9.4$). To test the overall ln(Ca$_{eff}$/Re) range, an upper (-6.0) and lower (-10.1) value is selected. The variation of ln(Ca$_{eff}$.Re) is -9 to 0 as per Table 6.6. This range is limited by system numerical convergence.

The collapsed ($y'_{max} - 0.1P_{eff}$) results are shown in Figure 6.7 along with the calculated best-fit (green and blue) lines based on Equation 6.8. As can be seen, the results

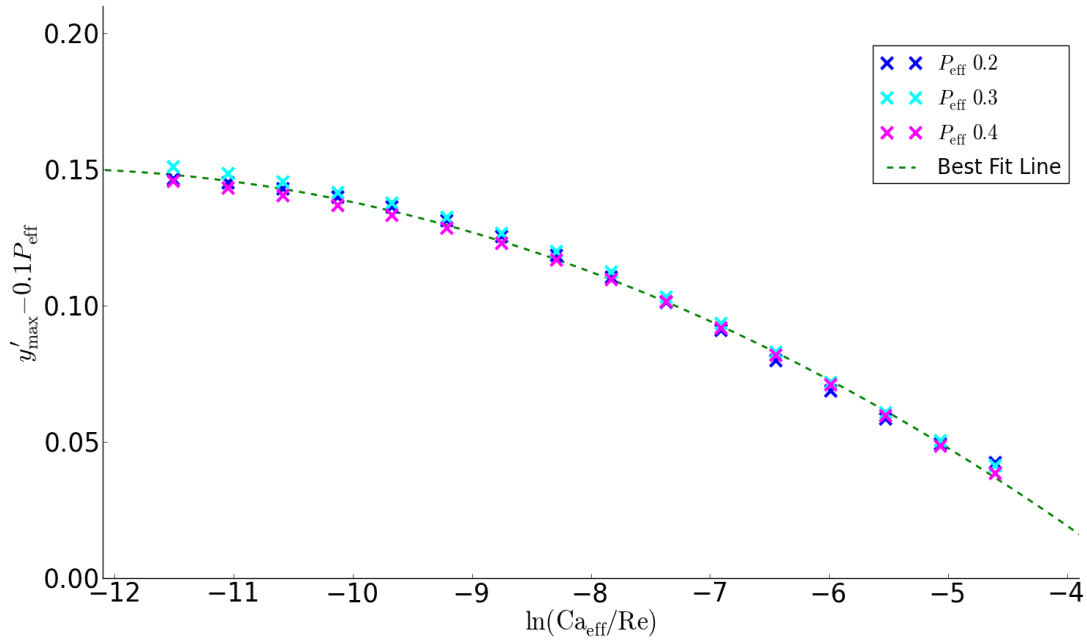

Figure 6.6 Maximum vertical displacement $y'_{\max} - 0.1P_{\text{eff}}$ results quadratic best fit line for $\ln(\text{Ca}_{\text{eff}}/\text{Re})$ parameter-space tested.

Table 6.6 Parameter variations for static non-dimensional scheme sensitivity test.

P_{eff}	$\ln(\text{Ca}_{\text{eff}}/\text{Re})$	$\ln(\text{Ca}_{\text{eff}}.\text{Re})$
0.2	-10.1	-9 to 0
	-6.0	-9 to 0
0.3	-10.1	-9 to 0
	-6.0	-9 to 0
0.4	-10.1	-9 to 0
	-6.0	-9 to 0

are similar to that predicted by Equation 6.8. This data is also shown in combination with the overall $y'_{\max} - 0.1P_{\text{eff}}$ data in Figure 6.8. There is more discrepancy at $\ln(\text{Ca}_{\text{eff}}/\text{Re}) = -6.0$ than at -10.1. This reinforces the limitation that the formulation of Equation 6.8 is more suitable for large wall deformations. The $\ln(\text{Ca}_{\text{eff}}/\text{Re}) = -6$ set is already smaller than channel midline and therefore is not considered to be a large deformation. This error is considered small for the large deformation range of interest and the ommision of $\text{Ca}_{\text{eff}}/\text{Re}$ is acceptable.

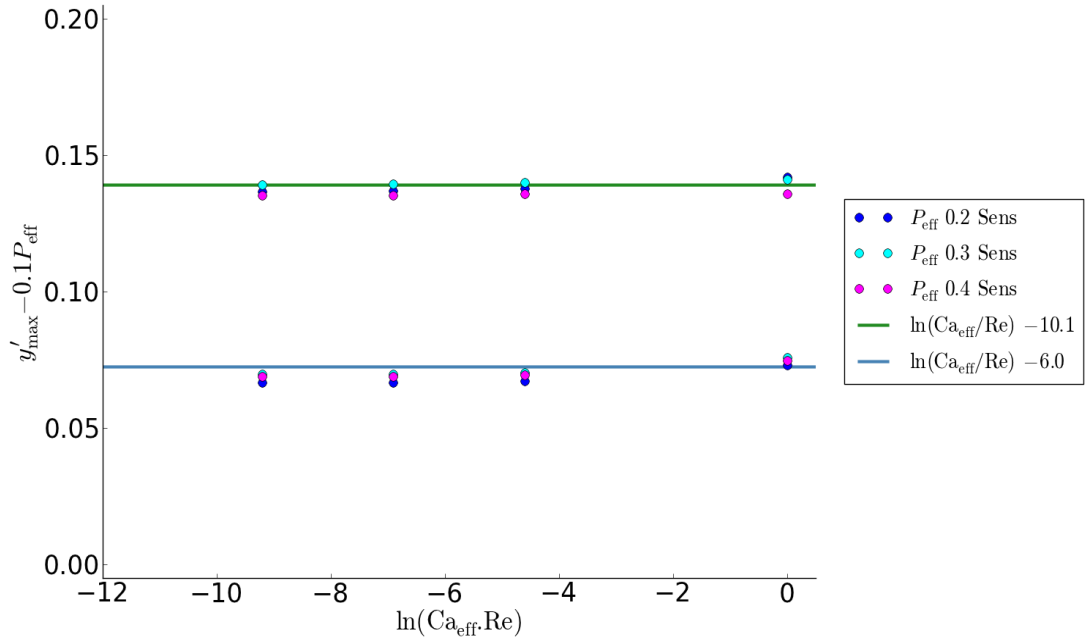

Figure 6.7 Maximum vertical displacement $y'_{max} - 0.1P_{eff}$ best fit line for ln(Ca$_{eff}$.Re) parameter space tested.

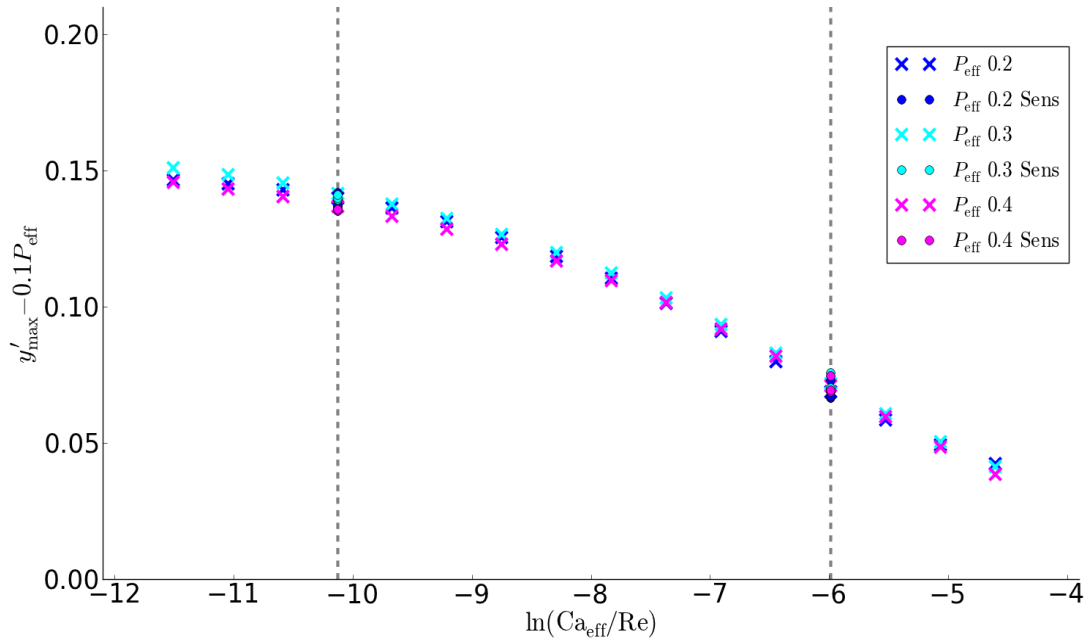

Figure 6.8 Maximum vertical displacement $y'_{max} - 0.1P_{eff}$ results with sensitivities at ln(Ca$_{eff}$/Re)=-10.1 to -6.

6.6 Summary

A non-dimensional scheme was proposed consisting of three parameters (P_{eff}, $\text{Ca}_{\text{eff}}/\text{Re}$ and $\text{Ca}_{\text{eff}}.\text{Re}$) to characterise the steady-state (static) flexible insert behaviour. Internal variations were performed of the dimensional parameters within those non-dimensional components to ensure they are suitable. Sensitivity testing was also performed on each non-dimensional component to determine their relative importance. A range of deflection types was shown to be possible with variation of these parameters. The system is sensitive to variation in P_{eff} and $\text{Ca}_{\text{eff}}/\text{Re}$ but relatively insensitive to changes in $\text{Ca}_{\text{eff}}.\text{Re}$. A simple equation was able to be formulated to predict y'_{max} in terms of just P_{eff} and $\text{Ca}_{\text{eff}}/\text{Re}$.

Chapter 7

Dynamic Single Wall Parameterisation Scheme

7.1 Dynamic Scheme Validation

Dynamic testing is performed to determine the consistency of the dynamic behaviour using the non-dimensionalisation scheme identified in Section 6.4. The work in this chapter has been previously published in Lai et al. (2016).

The non-dimensional parameters ($Ca_{eff}.Re$, Ca_{eff}/Re and P_{eff}) are again kept constant while dimensional parameters are varied within the three non-dimensional groups. The base case parameters are the same as Table 6.1 and specific variations are made as per the static variations test in Table 6.2.

Dynamic testing is performed based on the methodology discussed in Section 3.3.6. The base case behaviour of y'_{max} is plotted against the non-dimensional time t as shown in Figure 7.1. The system initally has larger amplitude oscillation and then settles into a saturated oscillation, an unstable case.

The y'_{max} variations against t for the various validation variation cases are shown in Figure 7.2. All cases are similar except for case V-3 which show slight variations in terms of having larger freqencies (shorter period) and larger A_{max} values. The A_{max} and f values and their respective variation from the base case are shown in Table 7.1 for all cases. All variations however are deemed reasonably similar to be characterised by the non-dimensional groups. This is because all cases exhibit unstable behaviour and their oscillation forms are similar. Figure 7.3 shows the flexible insert deformations over one complete oscillation for the base case, variation cases V-1 and V-3. The pressure along the flexible wall also show similar form in variation in one complete oscillation cycle in Figure 7.4. The non-dimensional scheme is considered robust since it is able to cater for changes in sensitive parameters like the wall Young's modulus E^*, flexible insert length L^*_{flex} and insert location relative to the downstream end. Therefore it is concluded

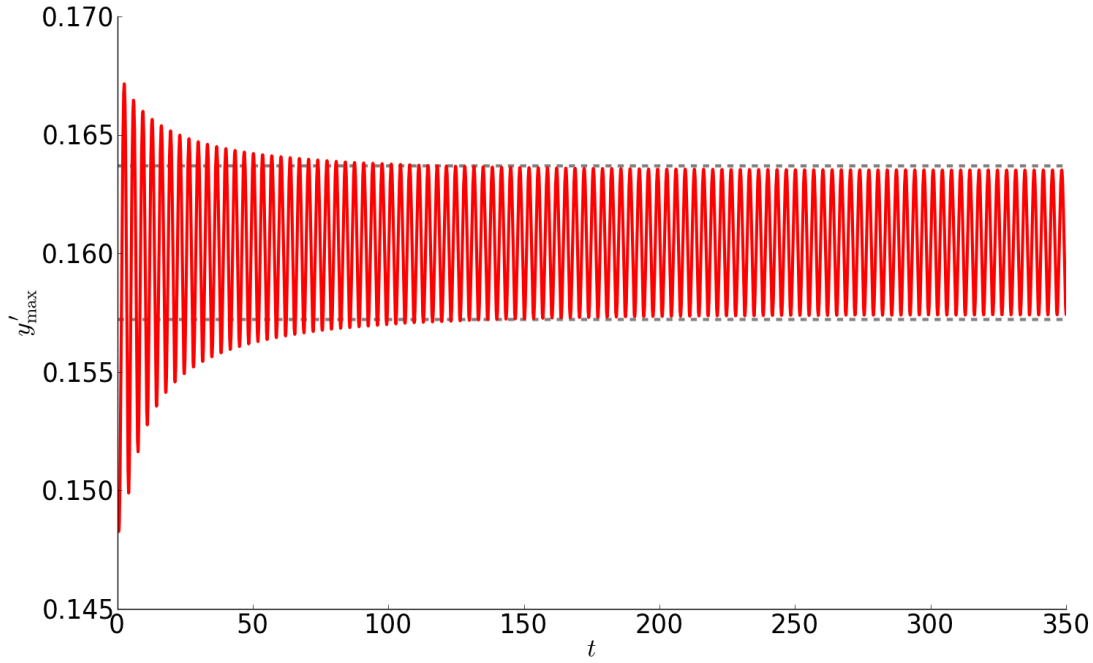

Figure 7.1 Time history for y' at the steady-state maximum deformation point from simulation start-up showing the system settling into constant oscillations.

Table 7.1 Dynamic non-dimensional scheme validation variation results.

Variation Number	f	A_{max}	f Error (%)	A_{max} Error (%)
Base case	0.295	0.0077	N/A	N/A
V-1	0.295	0.0078	0.0	1.0
V-2	0.295	0.0079	0.0	1.6
V-3	0.297	0.0088	0.6	13.7
V-4	0.295	0.0077	0.0	0.0
V-5	0.295	0.0078	0.0	0.5
V-6	0.295	0.0078	0.0	1.6

that the present non-dimensional scheme is suitable to characterise the system dynamic behaviour, as it was for characterising the flexible insert steady-state shape.

7.2 Single Flexible Insert Dynamic Parameterisation

System parameterisation is performed based on the non-dimensional parameters from the previous section. It was considered whether it is possible to simplify the non-dimensional scheme as was done in characterising the static flexible wall insert shape in Section 6.3. The static case simplification was possible by just using the P_{eff} and Ca_{eff}/Re terms to characterise y'_{max}. The system was sufficiently independent of $Ca_{eff}.Re$ for this purpose. This however does not provide a good representation of fluid behaviour and FSI system stability, which requires consideration of the $Ca_{eff}.Re$

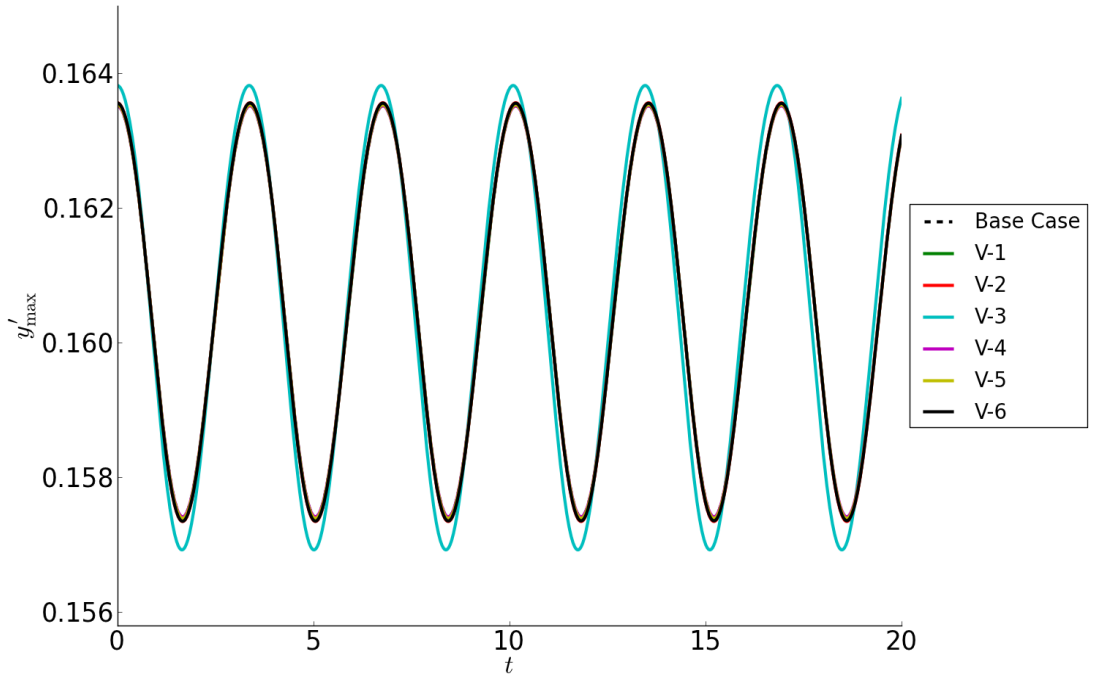

Figure 7.2 Truncated time history for the maximum vertical displacement y'_{max} for various internal parameter variation cases showing the saturated oscillation form.

Table 7.2 Dynamic non-dimensional scheme parameter test limits.

Non-Dimensional Parameter	Range
P_{eff}	0.2 to 0.4
$\ln(Ca_{eff}/Re)$	-11.5 to -7.5
$\ln(Ca_{eff}.Re)$	-8 to 10
Re	0.1 to 500

term. Therefore no simplification can be assumed due to the dynamic system sensitivity to both the flexible wall and fluid behaviour. All three non-dimensional parameters are required to characterise the dynamic stability of the system.

A parametric study is performed by varying all three non-dimensional parameters P_{eff}, Ca_{eff}/Re and $Ca_{eff}.Re$. This will provide a reference map that would show whether the system is stable or unstable. The methodology for testing is by selecting a value for P_{eff} and Ca_{eff}/Re, then increasing the $Ca_{eff}.Re$ term to see when the system transitions from a stable system to an unstable one. The limits applicable to the parametric study are listed in Table 7.2.

For P_{eff} values smaller than the lower limit (0.2), no case shows unstable behaviour for the Ca_{eff}/Re and $Ca_{eff}.Re$ range tested. For values larger than the upper limit (0.4), it is difficult to achieve system convergence.

For Ca_{eff}/Re, the limits are based on the results of the flexible wall insert shape in Figure 6.5. System parameterisation is limited to large flexible insert deformations,

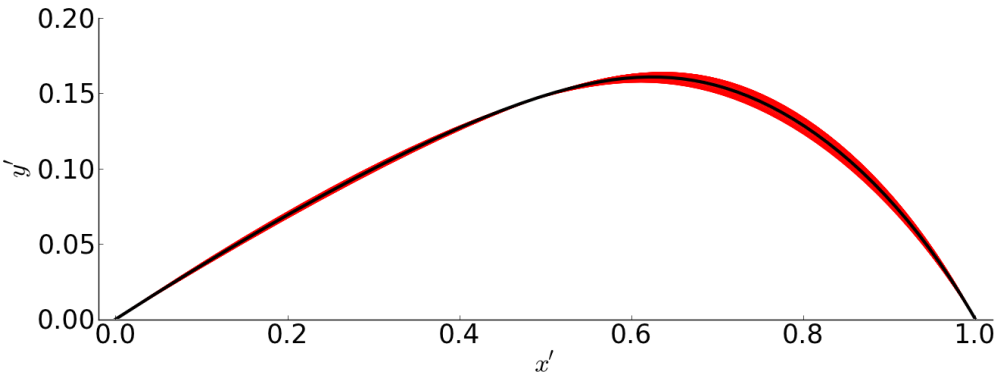

(a) Base case

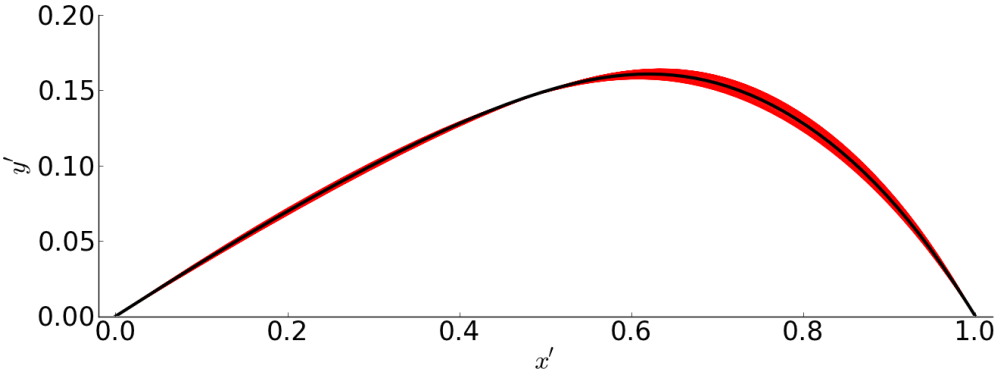

(b) Variation case V-1

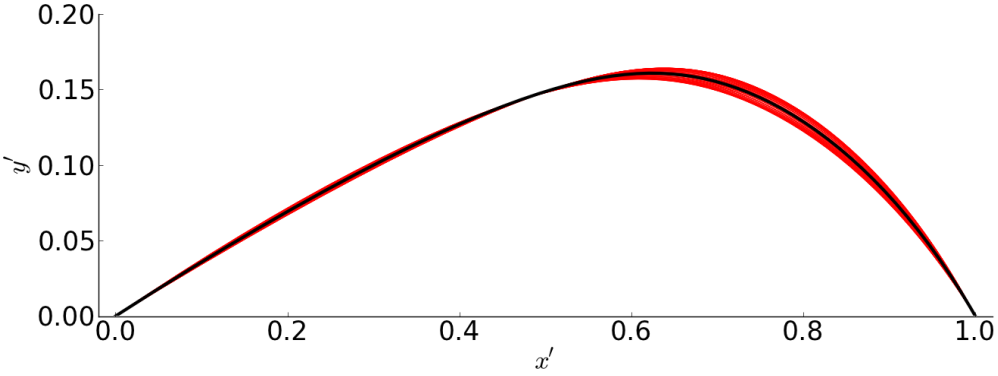

(c) Variation case V-3

Figure 7.3 Flexible insert deformation shape under steady-state conditions (black) and over one oscillation period (red).

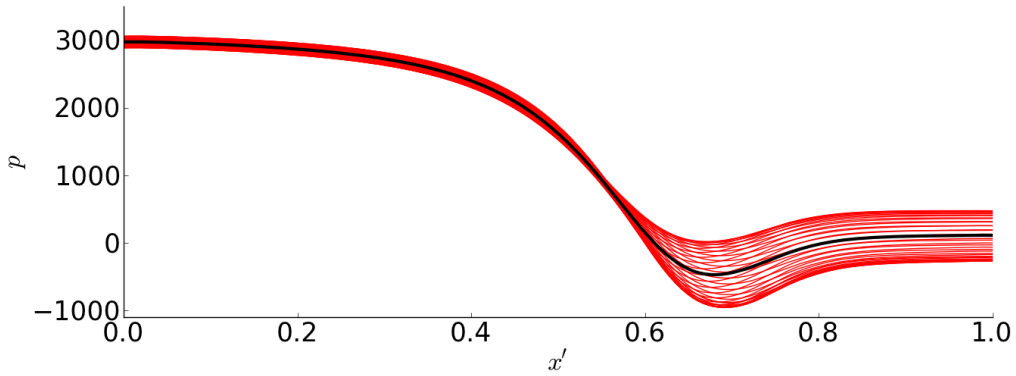

(a) Base case

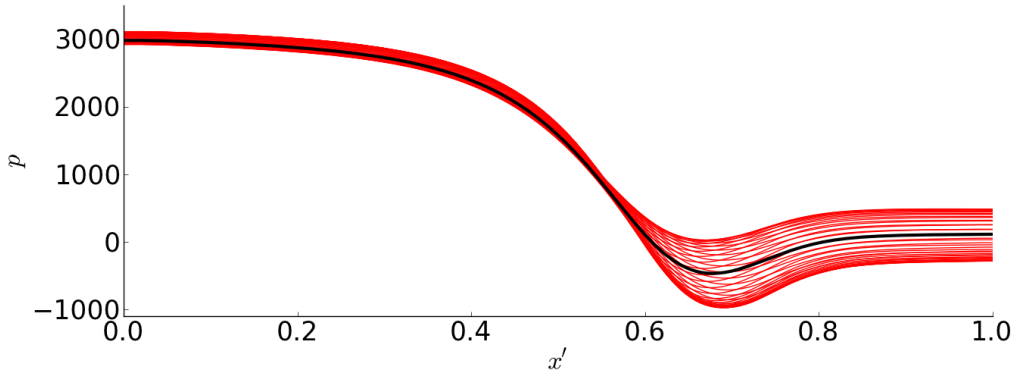

(b) Variation case V-1

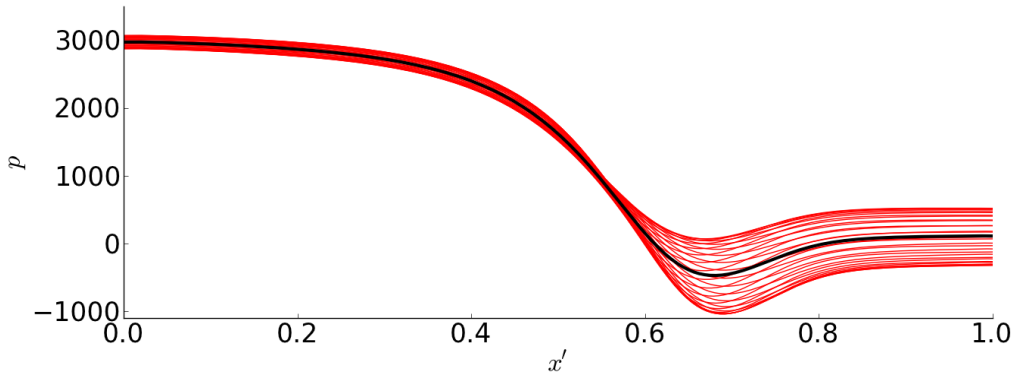

(c) Variation case V-3

Figure 7.4 Pressure p along the flexible insert under steady-state conditions (black) and over one oscillation period (red).

i.e. deformations larger than channel midline to deformations approaching the full channel height. For the $\ln(\text{Ca}_{\text{eff}}/\text{Re})$ lower limit of -11.5, this is driven by numerical issues where exceedingly large deformation cases approaching the channel bottom wall struggle to achieve numerical convergence because the mean deflection is too large.

For Ca_{eff}.Re, the absolute limits are driven by the required stability tests. The testing method sees specification of P_{eff} and $\text{Ca}_{\text{eff}}/\text{Re}$, with variation of Ca_{eff}.Re. Once a clear definition of the critical stability point can be determined no further points are then tested. Therefore it is noted that not all combinations of P_{eff} and $\text{Ca}_{\text{eff}}/\text{Re}$ are tested to the absolute Ca_{eff}.Re limits listed in Table 7.2. A general observation is that any value significantly higher (by an order of magntude) of the Ca_{eff}.Re stability point sees the system unable to achieve convergence. The specific Ca_{eff}.Re stability point is unique to each specific P_{eff} and $\text{Ca}_{\text{eff}}/\text{Re}$ combination.

The final limit is for Reynolds number Re which is limited to 0.1 - 500 because only laminar flow is considered.

The final result of this parameterisation study is a contour plot as shown in Figure 7.5 with P_{eff}, $\text{Ca}_{\text{eff}}/\text{Re}$ and Ca_{eff}.Re as the three parameters. The full set of detailed results used in generating this plot is shown in Appendix B. Values below the specified Ca_{eff}.Re results are stable (perturbation damp out to the steady-state flexible insert shape) and values above the surface are unstable (flexible insert oscillates indefinitely as seen in Figure 7.1). It can be interpreted that for a specific P_{eff} and $\text{Ca}_{\text{eff}}/\text{Re}$ combination, the required Ca_{eff}.Re needs to be met or exceeded for instability to occur. If this condition is not met, the system returns to its steady-state after the applied perturbation.

As was previously discussed in Section 6.3, the static flexible insert shape (characterised by y'_{max}) is not dependent on Ca_{eff}.Re. This graphically means based on Figure 7.5, any variation in the vertical (Ca_{eff}.Re) axis sees no change in y'_{max}. The actual y'_{max} values for specific pairings of P_{eff} and $\text{Ca}_{\text{eff}}/\text{Re}$ can be seen in Figure 7.6. Therefore, there is no relationship between system stability and y'_{max}, and y'_{max} cannot be used as an indicator of whether a system is stable or unstable. The consideration of the two plots is therefore independent with Figure 7.5 used to determine dynamic stability and Figure 7.6 as an indicator of flexible insert deflection through y'_{max}.

7.3 Dynamic Behaviour across P_{eff} Values

It is of interest to better understand the dynamic behaviour differences in the 3-d space as represented in Figure 7.5. The approach to study this is by fixing the Ca_{eff}.Re and $\text{Ca}_{\text{eff}}/\text{Re}$ values and increasing P_{eff} from 0.2 to 0.4 in 0.02 increments. The two sets of fixed Ca_{eff}.Re and $\text{Ca}_{\text{eff}}/\text{Re}$ values are listed in Table 7.3 and termed sets α and β. The stability results of this P_{eff} variation test is plotted in Figure 7.7 as a 3-d stability surface. The selection of these values are based on the criterion that for the α (blue) or

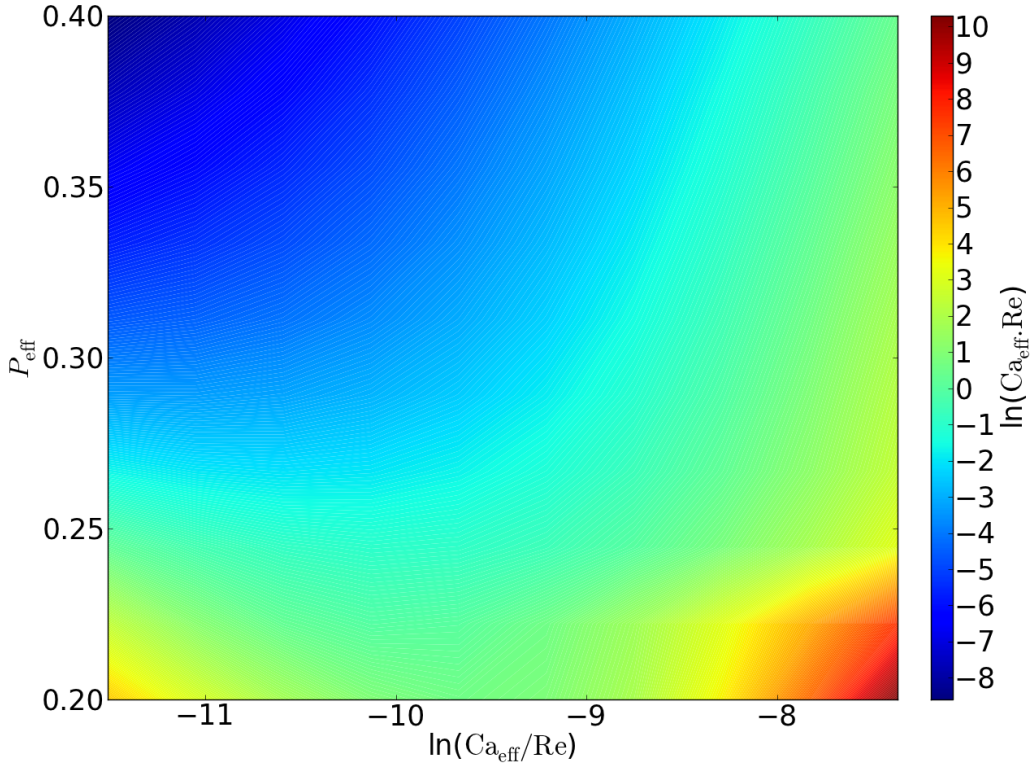

Figure 7.5 Contour plot of critical stability for the single flexible insert configuration.

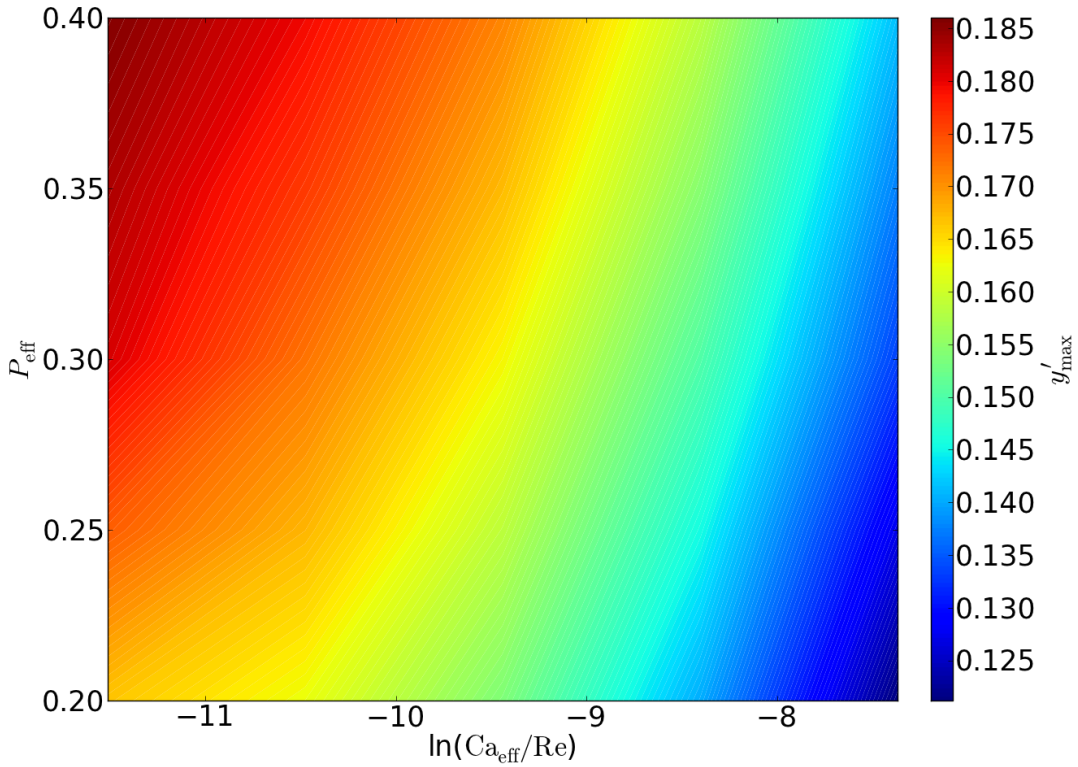

Figure 7.6 Contour plot of the single flexible insert steady-state maximum deformation.

Table 7.3 Dynamic test parameters for effective pressure P_{eff} variation.

Set	$\text{Ca}_{\text{eff}}/\text{Re}$	$\text{Ca}_{\text{eff}}.\text{Re}$
α	1×10^{-4}	1.00
β	5×10^{-4}	2.00

β (orange) set, varying P_{eff} penetrates the stability surface. The dashed line sections denote stability and the coloured solid line sections denote instability.

The y'_{max} variation with time is shown for set α in Figure 7.8. Figure 7.8a shows the transition from stability to instability as P_{eff} increases. The system is stable up to P_{eff} 0.22 and is unstable at P_{eff} 0.24. The y'_{max} value increases with P_{eff} which is to be expected as a larger external pressure results in larger mean deflection of the flexible insert.

Figure 7.8b shows unstable cases of set α. The time history has been truncated to just show the steady-state oscillations (rather than the initial start-up transient behaviour). This is to align all test points to have a y'_{max} trough point coinciding at $t = 0$. It can be seen that the oscillation forms are similar with A_{max} and f increasing with P_{eff}. This is confirmed through the increasing changes in the flexible wall shape and fluid pressure along the flexible insert over one oscillation shown in Figure 7.10 and Figure 7.11 respectively. The $P_{\text{eff}} = 0.40$ case is not shown as simulation convergence was not possible due to exceedingly large flexible-insert deformations.

Similar plots of y'_{max} variation with time are shown for set β in Figure 7.9. Figure 7.9a shows stable cases at $P_{\text{eff}} = 0.20$ and 0.30, and instability commencing with $P_{\text{eff}} = 0.36$. The unstable cases show similar trends as found for set α. The flexible wall shape and fluid pressure along the flexible insert over one oscillation are shown in Figure 7.12 and Figure 7.13 respectively. The magnitude of the flexible wall motion and fluid pressure variation along the flexible also increase as with set α.

The A_{max} and f values for sets α and β are listed in Table 7.4. This qualitatively confirms that both A_{max} and f increase with P_{eff} for both sets α and β. The only point of comparison between the α and β sets is from $P_{\text{eff}} = 0.36$ or higher where both cases are unstable. In this region, A_{max} and f values are higher for set α compared to β. This is reasonable considering set α is unstable at a lower P_{eff} compared to set β. However, the initial instability P_{eff} point sees set α having higher A_{max} and f values compared to set β. Therefore although increasing P_{eff} gives the same qualitative trend for A_{max} and f, the quantitative values are different across the sets as the instability behaviour may be dissimilar. The instability mechanism is therefore the focus of investigation in the following section.

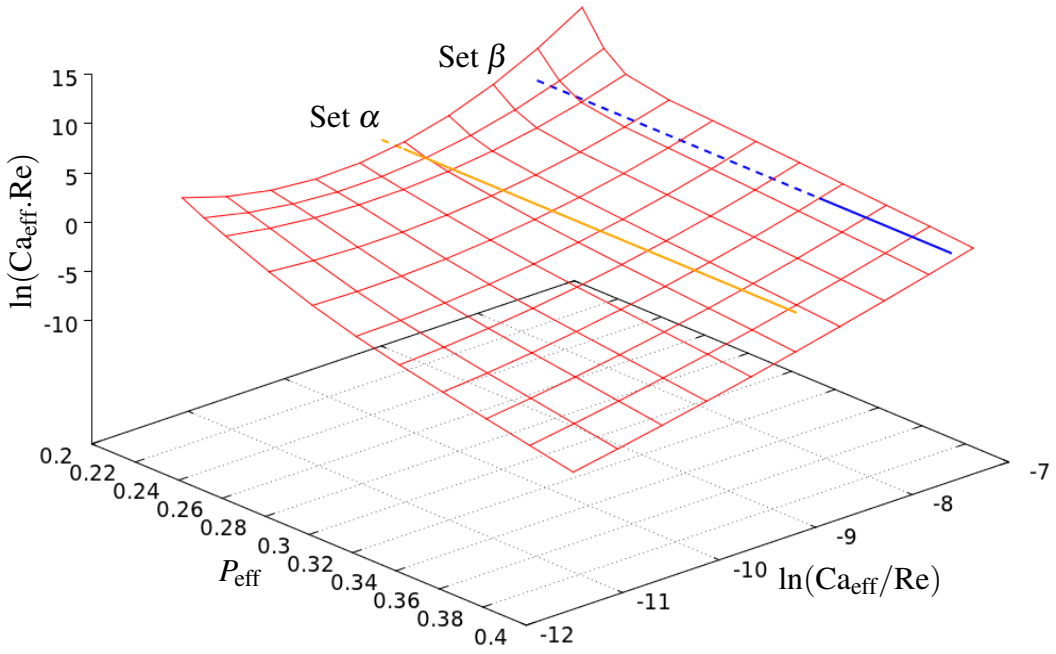

Figure 7.7 Critical stability surface with effective pressure P_{eff} variation lines. Solid lines and dashed lines denote the unstable and stable regions of the parameter-space respectively.

Table 7.4 Dynamic simulation test results for effective pressure P_{eff} variation sets α and β while keeping $\text{Ca}_{\text{eff}}/\text{Re}$ and $\text{Ca}_{\text{eff}}.\text{Re}$ constant.

Set	α		β	
P_{eff}	A_{max}	f	A_{max}	f
0.20	Stable		Stable	
0.22	Stable		Stable	
0.24	0.019	0.271	Stable	
0.26	0.030	0.276	Stable	
0.28	0.037	0.281	Stable	
0.30	0.042	0.287	Stable	
0.32	0.047	0.292	Stable	
0.34	0.062	0.299	Stable	
0.36	0.078	0.305	0.022	0.208
0.38	0.093	0.311	0.031	0.210
0.40	No Convergence		0.038	0.212

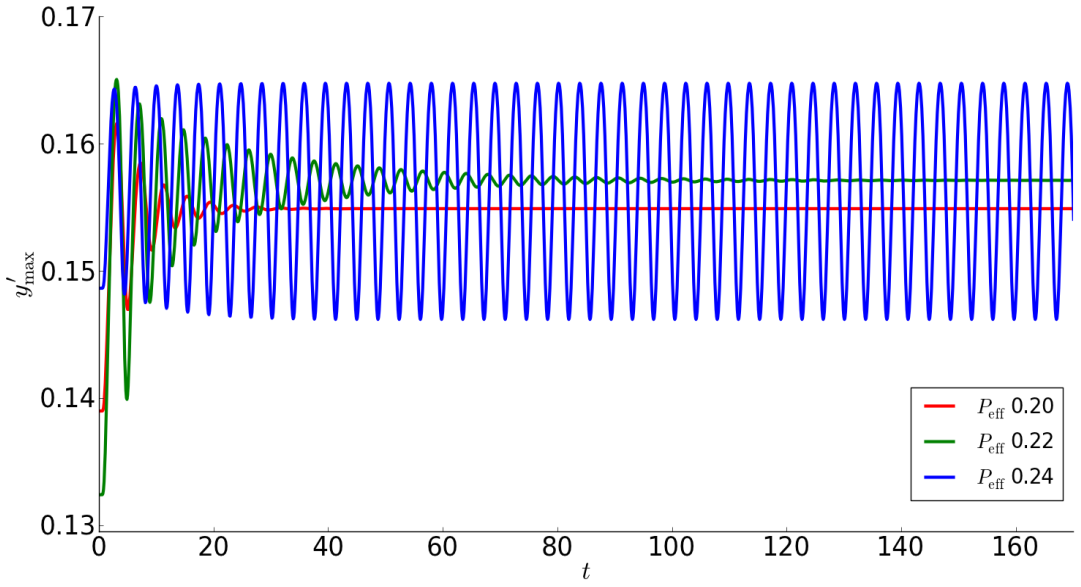

(a) Time history from simulation start-up showing P_{eff} transition from stability to instability.

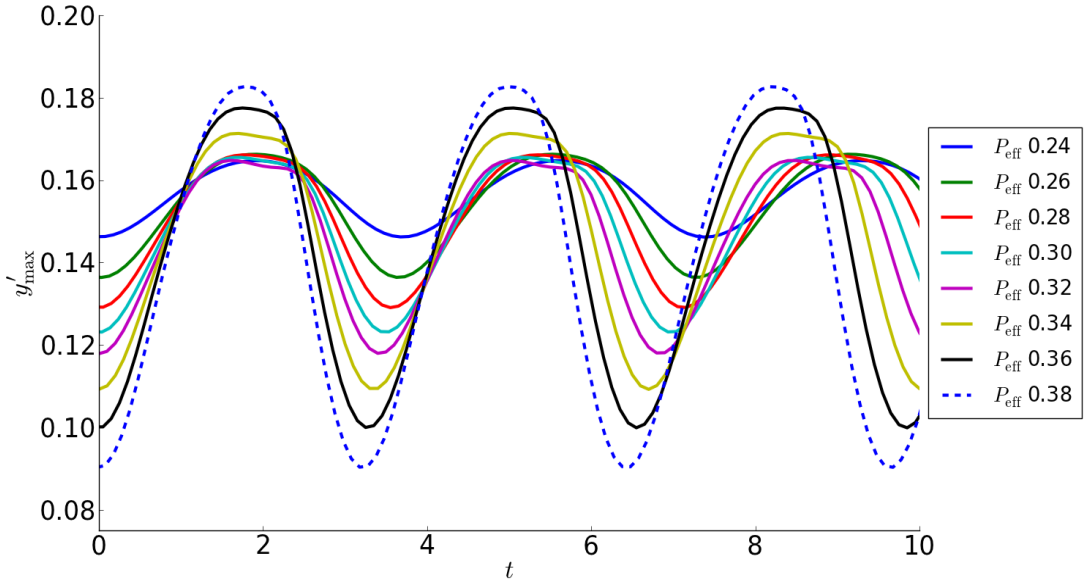

(b) Truncated time history for unstable cases showing different oscillation patterns with P_{eff} variation.

Figure 7.8 Maximum vertical displacement $y'_{\max}$ time history for set α effective pressure P_{eff} variation tests.

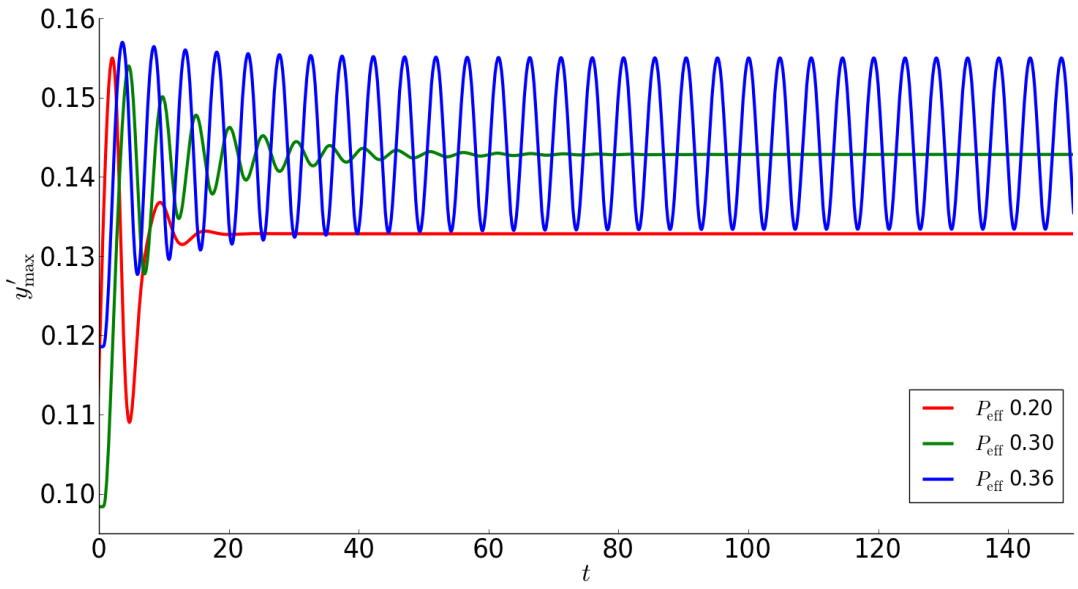

(a) Time history from simulation start-up showing P_{eff} transition from stability to instability.

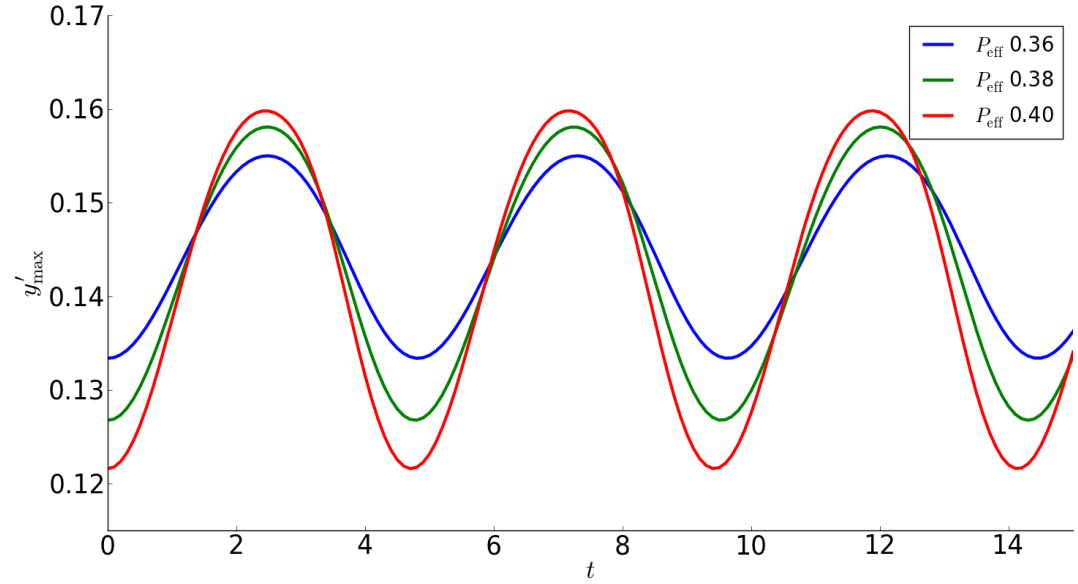

(b) Truncated time history for unstable cases showing different oscillation patterns with P_{eff} variation.

Figure 7.9 Maximum vertical displacement $y'_{\max}$ time history for set β effective pressure P_{eff} variation tests.

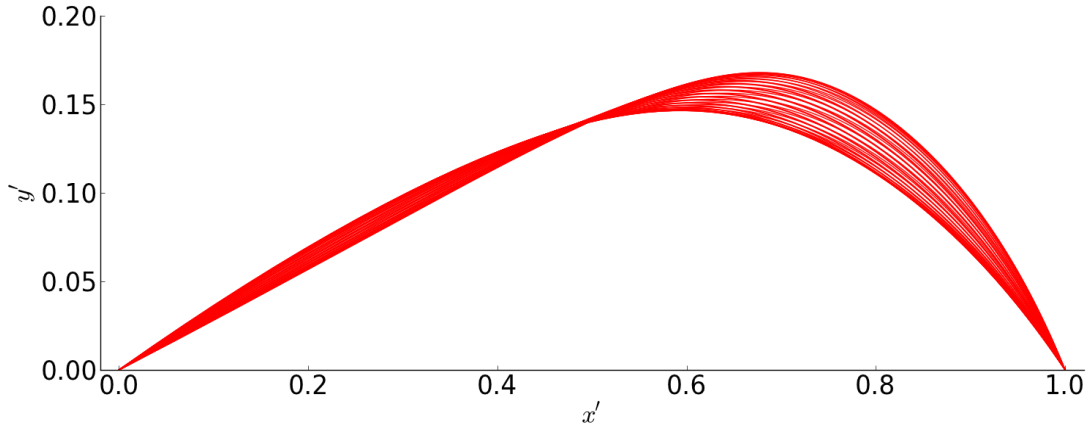

(a) P_{eff} 0.24

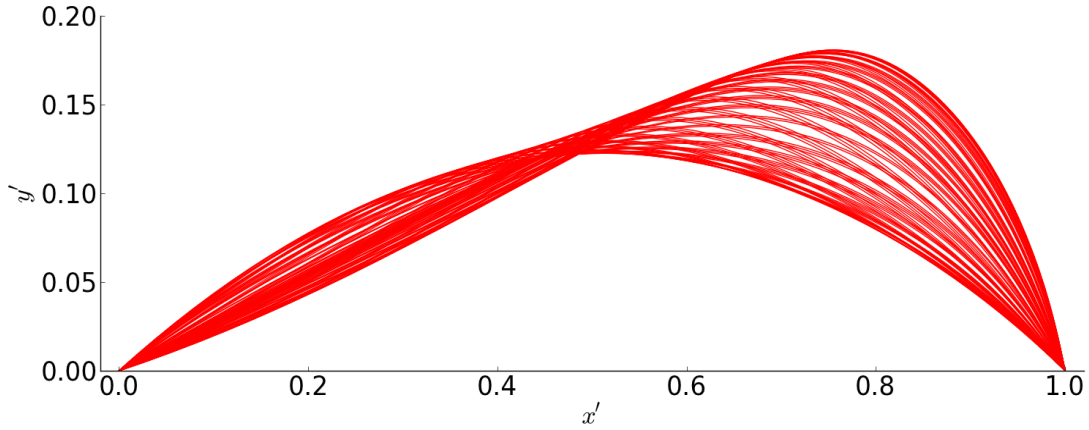

(b) P_{eff} 0.32

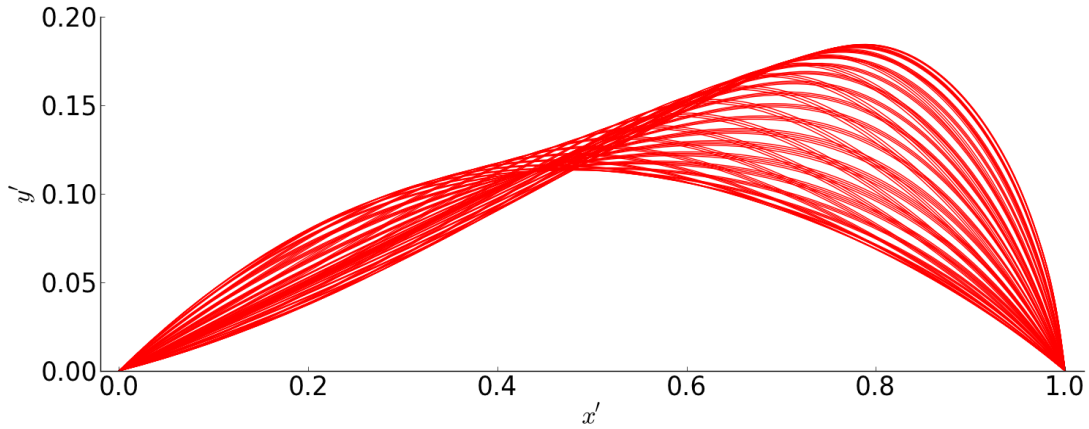

(c) P_{eff} 0.38

Figure 7.10 Flexible insert shape over one oscillation for effective pressure P_{eff} variation set α.

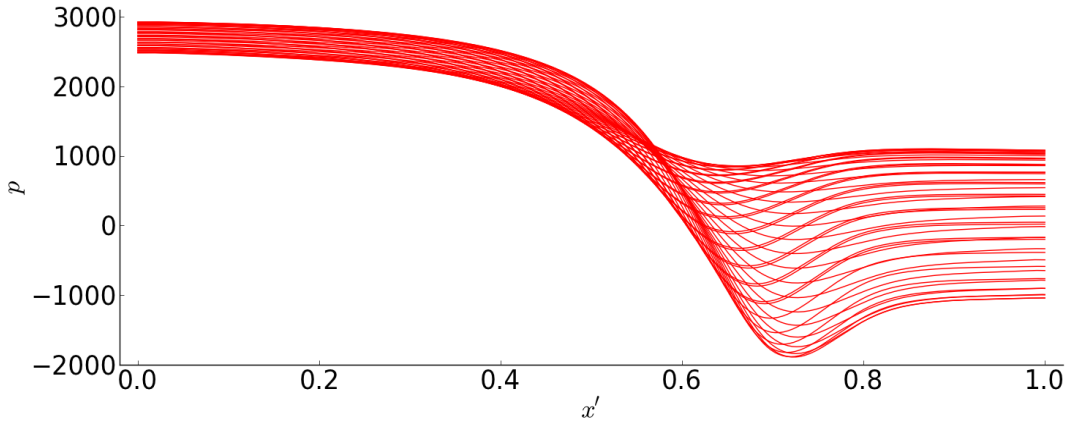

(a) P_{eff} 0.24

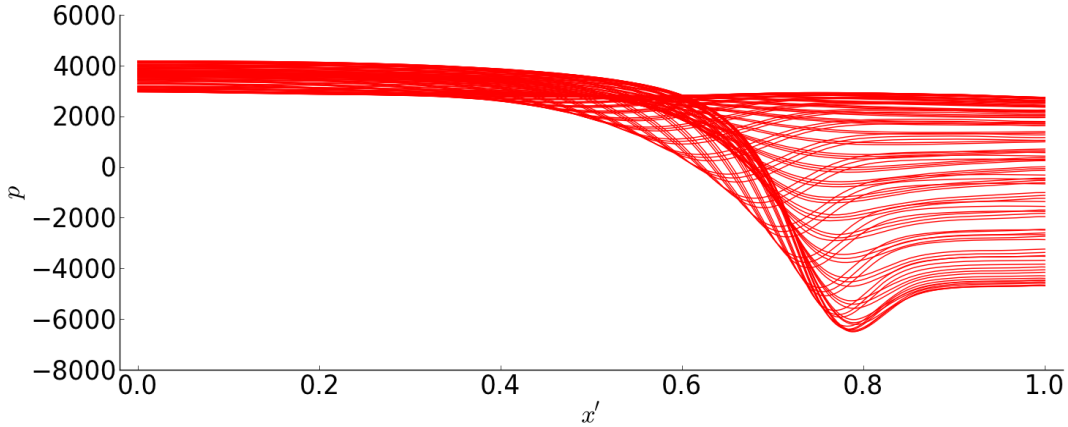

(b) P_{eff} 0.32

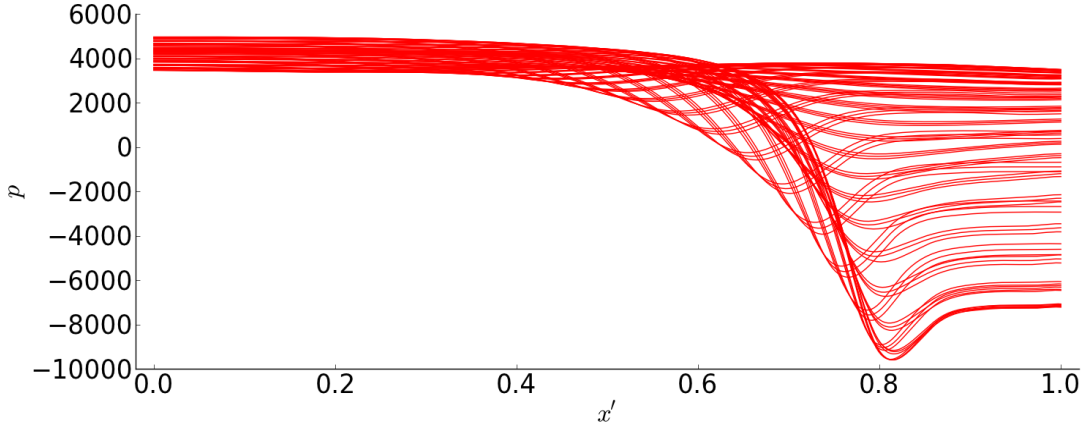

(c) P_{eff} 0.38

Figure 7.11 Fluid pressure p along flexible insert over one oscillation for effective pressure P_{eff} variation set α.

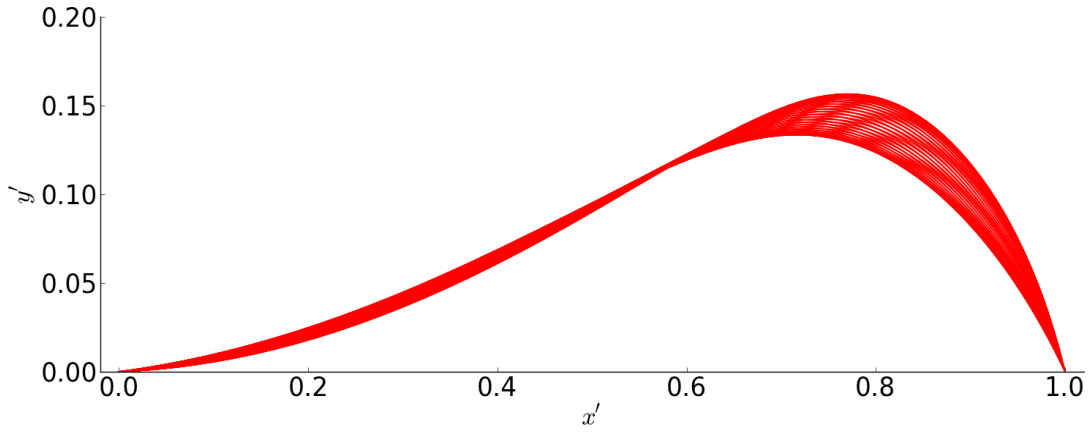

(a) P_{eff} 0.36

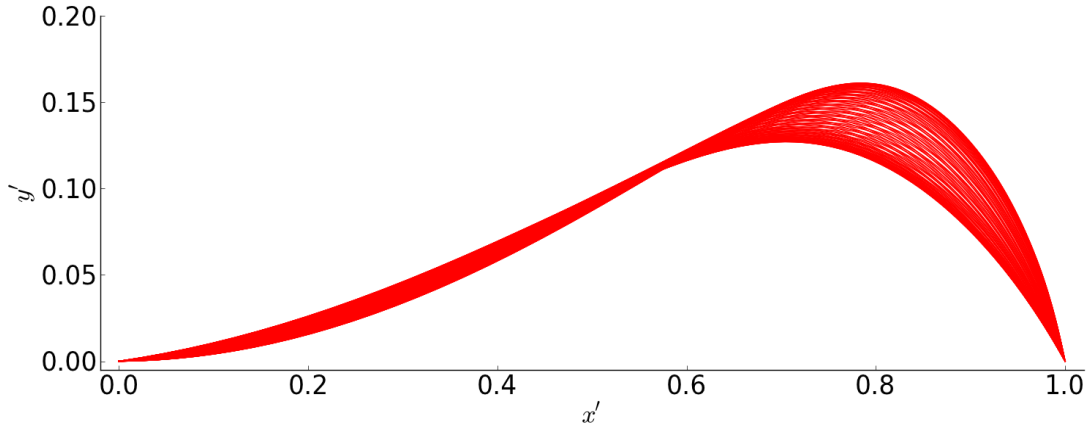

(b) P_{eff} 0.38

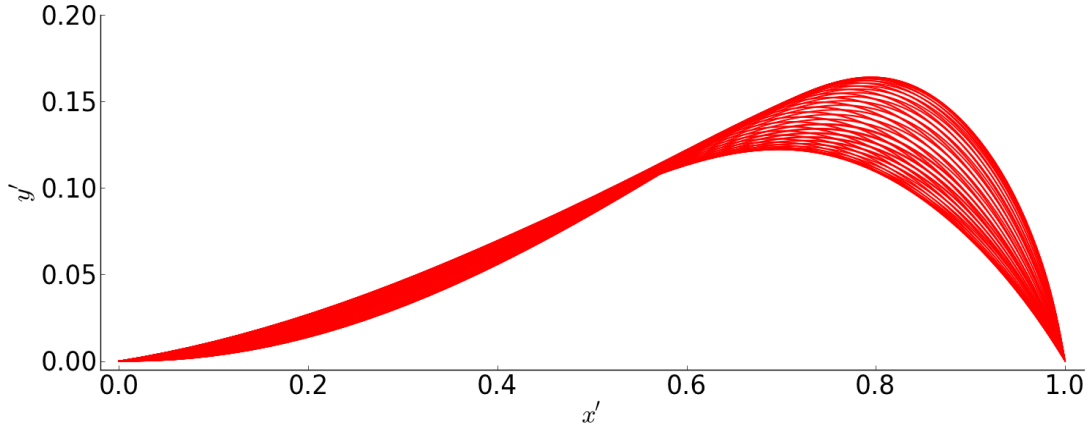

(c) P_{eff} 0.40

Figure 7.12 Flexible insert shape over one oscillation for effective pressure P_{eff} variation set β.

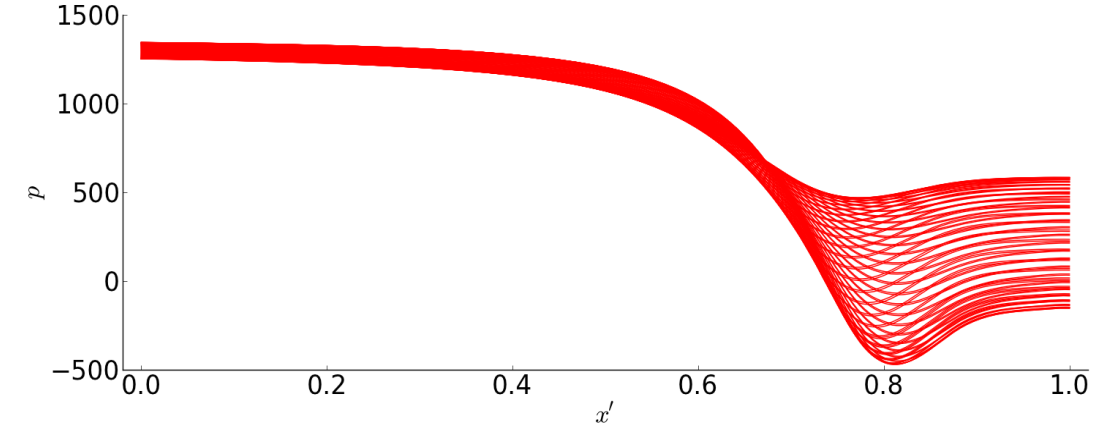

(a) P_{eff} 0.36

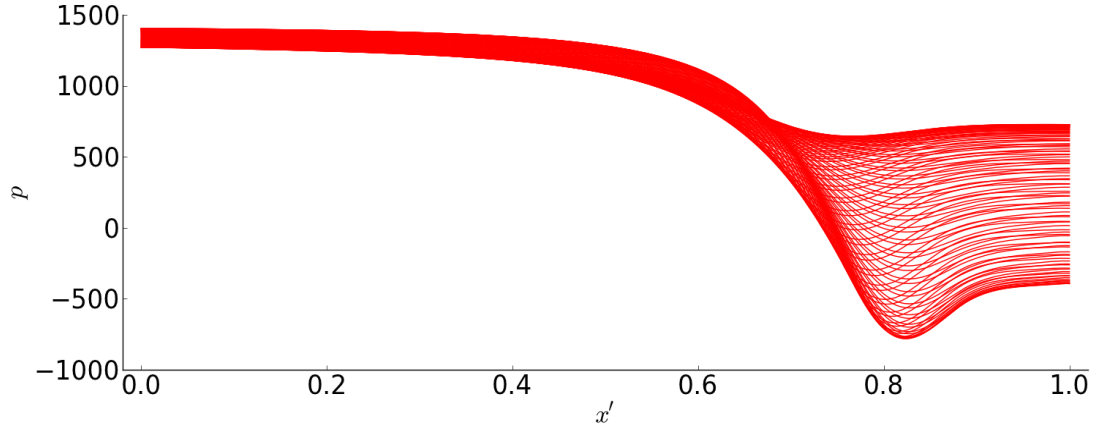

(b) P_{eff} 0.38

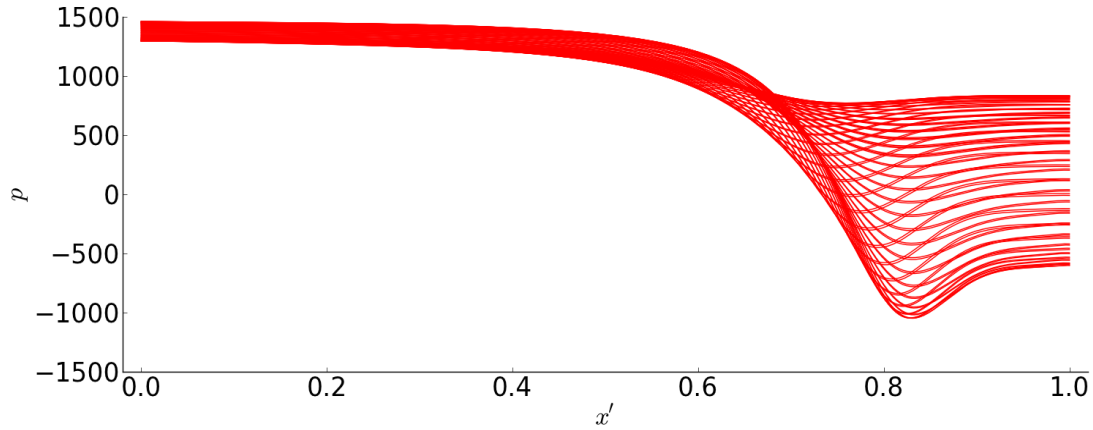

(c) P_{eff} 0.40

Figure 7.13 Fluid pressure p along flexible insert over one oscillation for effective pressure P_{eff} variation set β.

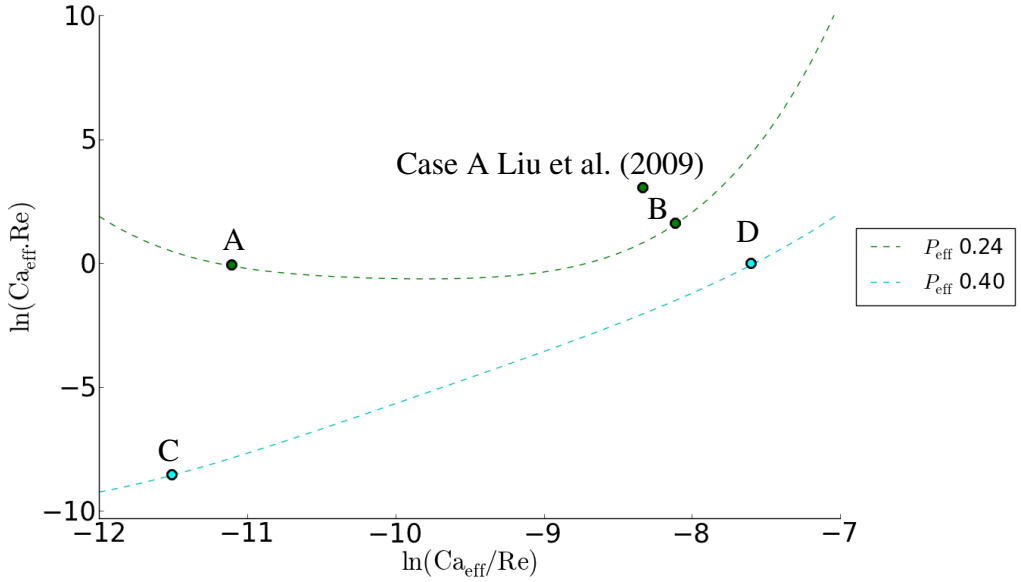

Figure 7.14 Dynamic critical stability lines for test points A to D and Case A of Liu et al. (2009) from Chapter 5.

7.4 Stability Surface Dynamic Behaviour Analysis

The stability surface of Figure 7.5 shows a non-uniform surface profile across the P_{eff} range. Figure 7.14 show the critical stability surface slices or lines (at $P_{\text{eff}} = 0.24, 0.40$). At the lower $P_{\text{eff}} = 0.24$ value the critical stability surface has a parabolic shape, whereas at the higher $P_{\text{eff}} = 0.40$ value the stability surface transitions to a linear relationship with increasing $\ln(\text{Ca}_{\text{eff}}/\text{Re})$ and $\ln(\text{Ca}_{\text{eff}}.\text{Re})$. This suggests that there are different instability mechanisms at work in the parameter space explored. Therefore the parameter sets at each of the four corners (denoted test points A to D) of the stability surface is considered for further analysis.

The points selected are listed in Table 7.5 and are plotted on the critical stability lines as shown in Figure 7.14. These points lie just above the critical stability lines (as denoted by 'Critical $\text{Ca}_{\text{eff}}.\text{Re}$') in Table 7.5. The tested Case A of Liu et al. (2009) from Chapter 5 is also listed in Table 7.5 and shown in Figure 7.14 to provide perspective of its location on the stability surface with respect to the current points A to D. The Case A of Liu et al. (2009) has parameters most closely relating to the current test point B.

The flexible insert shape variation over one oscillation period is shown in Figure 7.15. Points A and C, and B and D have similar oscillation forms which can be attributed to their $\text{Ca}_{\text{eff}}/\text{Re}$ values. Points A and C have smaller $\text{Ca}_{\text{eff}}/\text{Re}$ values, meaning the flow stiffness and fluid viscous force is smaller compared to the flexible wall stiffness and fluid inertial force. Consequently the uniform external pressure P_{ext} has a larger effect resulting in the flexible insert having a more parabolic form. The surface deflection at point C is greater than point A because the P_{eff} is larger for point C (0.40) compared to point A (0.24). It is also noted the movement of the flexible insert is much smaller in

Table 7.5 Detailed dynamic analysis test point non-dimensional parameters.

Non-Dimensional Parameters	Test Point A	B	C	D	Case A of Liu et al. (2009)
P_{eff}	0.24	0.24	0.40	0.40	0.24
Re	252	129	5	45	300
$\text{Ca}_{\text{eff}}/\text{Re}$ $(\times 10^{-5})$	1.5	30.0	1.0	50.0	24.0
$\text{Ca}_{\text{eff}}.\text{Re}$	0.95	5.00	2.00×10^{-4}	1.00	21.6
Critical $\text{Ca}_{\text{eff}}.\text{Re}$	0.90	3.79	1.86×10^{-4}	0.84	2.24

test point A compared to point C. Furthermore the movement for point A is along the entire flexible insert while the movement for point C is focussed on the downstream half of the flexible insert.

Points B and D have larger $\text{Ca}_{\text{eff}}/\text{Re}$ values. A larger $\text{Ca}_{\text{eff}}/\text{Re}$ value means the flow stiffness and fluid viscous force effects are dominant over the flexible wall stiffness and fluid inertial force. Therefore the uneven fluid pressure distribution and viscous shear stresses causes the flexible insert shape to be skewed more to the right (downstream). Both cases have larger movement in the second half (downstream) of the flexible insert with the movement in point D larger than in point B.

The steady-state position and movement over one oscillation period of the flexible insert maximum deformation point is shown in Figure 7.16. The aspect ratio is 7:20 for y' to x' and this is maintained for all plots in this thesis. All four points show orbital movements about the steady-state position. The movement is counter-clockwise for test points A, B and D while for point C the movement is clockwise. This is a characteristic that indicates that point C has a different instability mechanism.

The fluid pressure along the flexible insert over one oscillation period is shown in Figure 7.17. Test points A and C have larger non-dimensional pressure values (compared to points B and D). The point where the fluid pressure switches from positive to negative is further upstream at approximately $x' = 0.6$, consistent with their maximum deformation location. However, the pressure distribution along the flexible insert differ for points A and C. There is a 'dip' in pressure and recovery for point A whereas for point C there is no 'dip'. This 'dip' is due to flow separation occurring where there is a recirculation vortex present at the downstream end of the flexible insert. This is shown and dicussed later in Figures 7.19 to 7.22 for points A to D.

Points B and D have smaller pressure variations along the length of the flexible insert. The point where fluid pressure switches from positive to negative is further downstream, consistent with the flexible insert deformation profile at points B and D which is skewed further right. It is noted therefore the location where this inflection point is relates to the flexible wall shape. Test points B, C and D also feature a pressure variation downstream that oscillates between positive and negative values. For point

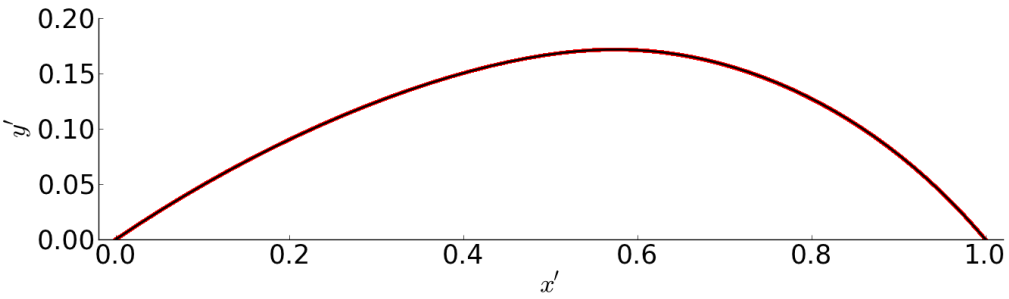

(a) Point A

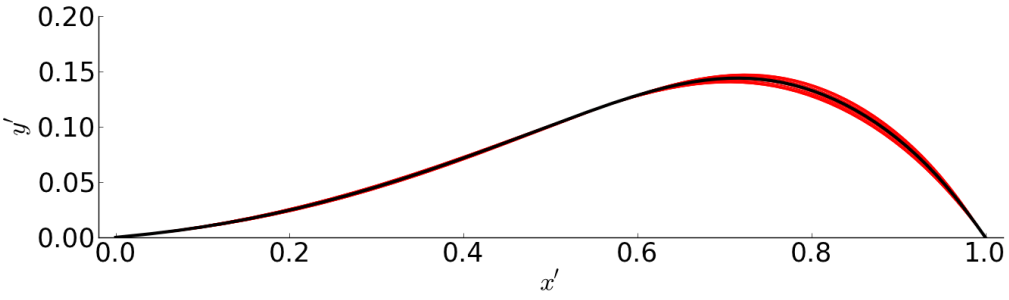

(b) Point B

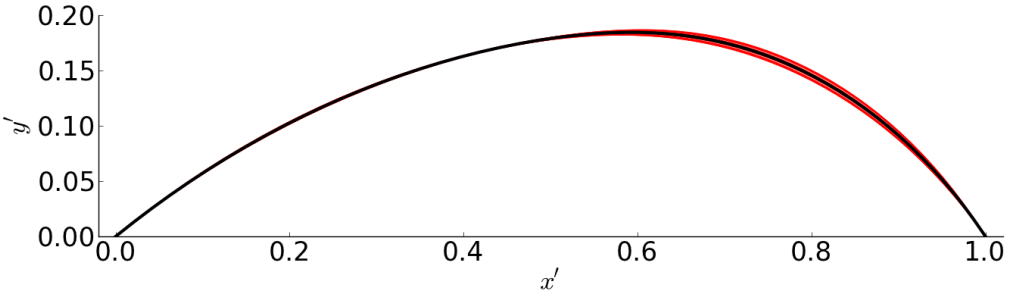

(c) Point C

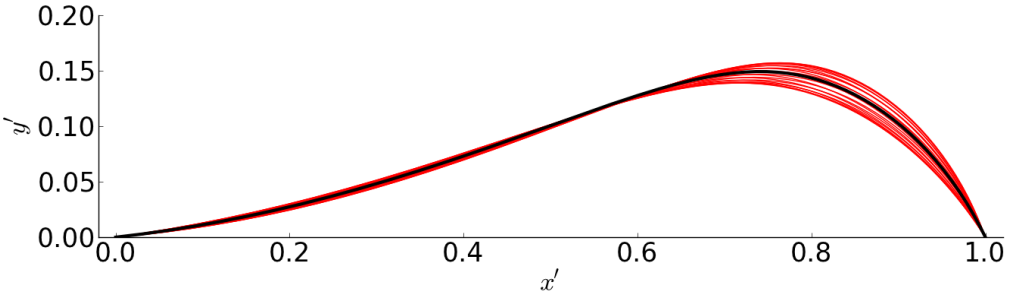

(d) Point D

Figure 7.15 Flexible insert deformation shape in steady-state (black) and over one saturated oscillation period (red) for critical stability test points A to D.

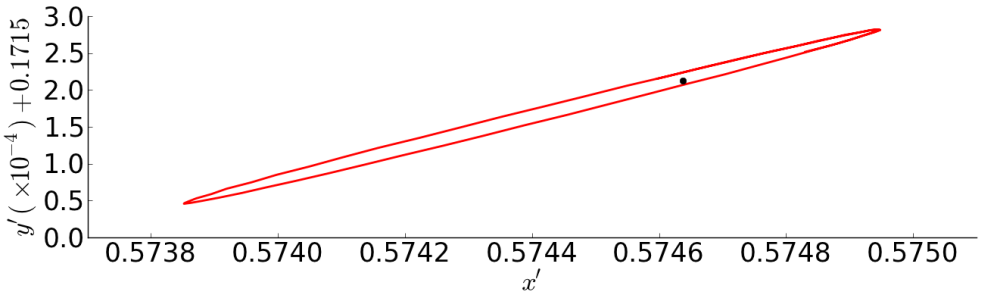

(a) Point A (counter-clockwise movement)

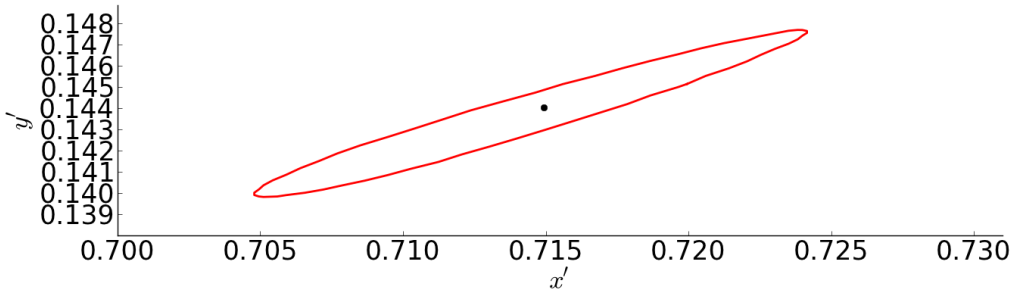

(b) Point B (counter-clockwise movement)

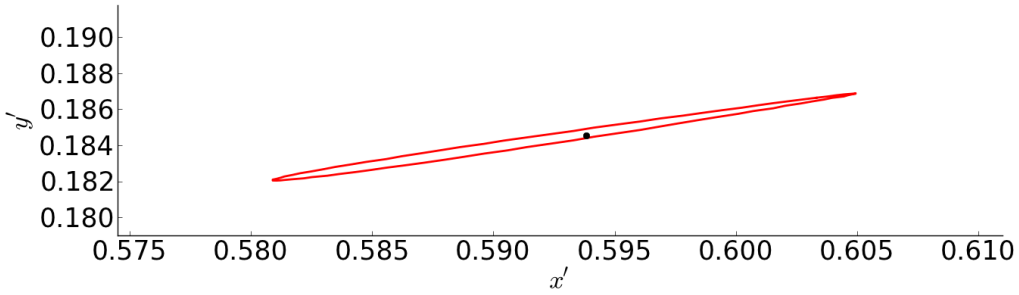

(c) Point C (clockwise movement)

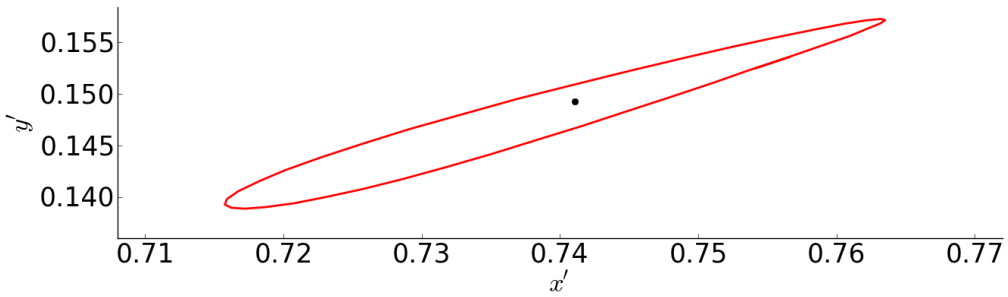

(d) Point D (counter-clockwise movement)

Figure 7.16 Flexible insert maximum deformation point location in steady-state (black) and over one saturated oscillation period (red) for critical stability test points A to D.

Table 7.6 Detailed dynamic analysis oscillation results for test points A to D.

Non-Dimensional Result	Test Case A	B	C	D	Case A of Liu et al. (2009)
$A_{max}(\times 10^{-2})$	0.039	0.83	0.45	1.76	4.1
f	0.38	0.17	3.85	0.25	0.13

A however, there is no variation between positive and negative. There is also very little pressure variation for point A, consistent with the minor wall motions of point A compared to the other points.

The flexible wall y'_{max} variation with t is shown in Figure 7.18. The time history has been truncated to show just the steady-state oscillations to align all test points so as to have the y'_{max} minimum point coinciding at $t = 0$. The y'_{max} oscillation peak-to-peak amplitude A_{max} and frequency f are shown in Table 7.6. The test points in order of increasing A_{max} size values are point A, C, B and D. This matches the pressure variations in Figure 7.17. In terms of the oscillation frequency, it is increasing from points B, D, A and C. Test points A, B and D have similar order of magnitude f whereas point C has a significantly higher f. It is noted test point B and Case A from Liu et al. (2009) (see Chapter 5) have similar f. The A_{max} value is however much larger for the previous study than point B. This is due to the previous study case located at a much higher Ca_{eff}.Re with respect to the stability surface as shown in Figure 7.14.

To better understand the different instabilities, the fluid domain behaviour is analysed for points A to D as shown in Figures 7.19 to 7.22. These plots are scaled 1:5 from channel length to height. The flexible insert maximum vertical displacement y'_{max} variation with time t is provided with cross marks for each time step at which the fluid domain plots are captured over one oscillation cycle. Consistent over the four test points, $t = 0$ has been adjusted to coincide with the start of a single flexible wall insert with y'_{max} at its minimum point. In each fluid domain plot the streamlines (white), vorticity contours (black) and non-dimensional pressure (colour) contours are shown.

Point A shown in Figure 7.19 exhibits the largest recirculation zone downstream of the flexible wall. However, it is noted this case has very small flexible oscillation amplitude with the recirculation zones remaining relatively stationary. There is only vortex shedding occurring further downstream.

For point B shown in Figure 7.20 at $t = 0$ there exists a recirculation zone behind the flexible wall which has drifted slightly downstream through to $t = 3.0$. This culminates in the largest wall deformation (y'_{max}) at $t = 3.0$. Throughout this time there is also a small recirculation zone at the bottom channel wall. This vortex grows is at its largest extent at $t = 0.0$. It continues to move downstream and dissipate until $t = 3.0$ until it disappears. A new vortex has formed at the bottom wall at this time as well. By $t = 4.4$

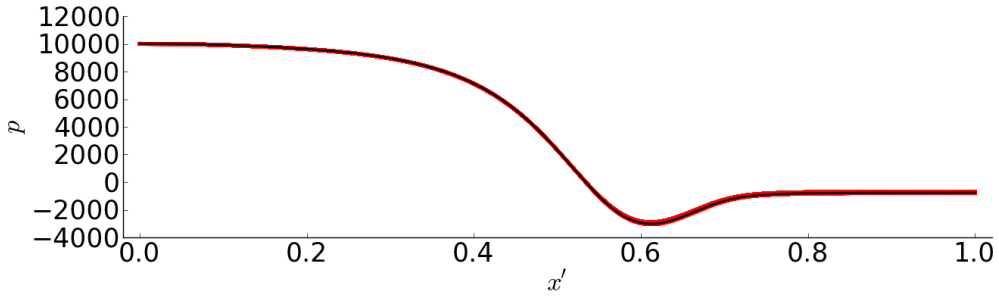

(a) Point A

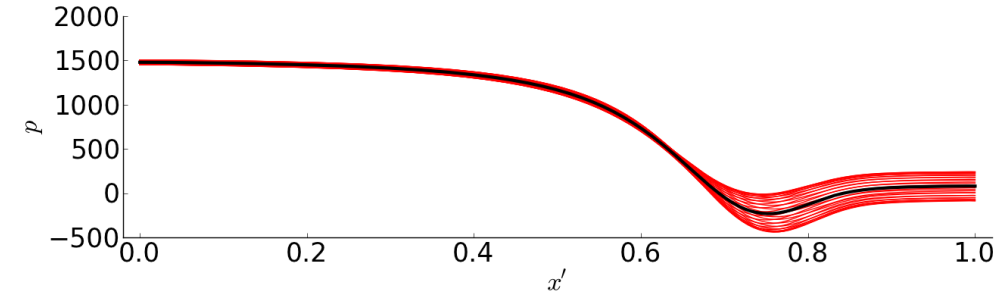

(b) Point B

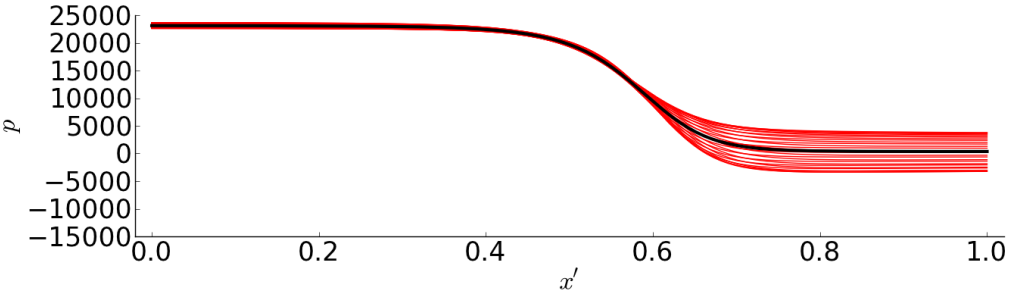

(c) Point C

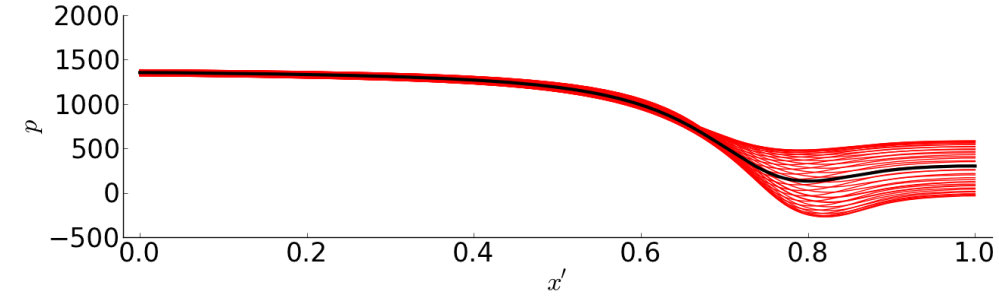

(d) Point D

Figure 7.17 Pressure p along the flexible insert in steady-state (black) and over one saturated oscillation period (red) for critical stability test points A to D.

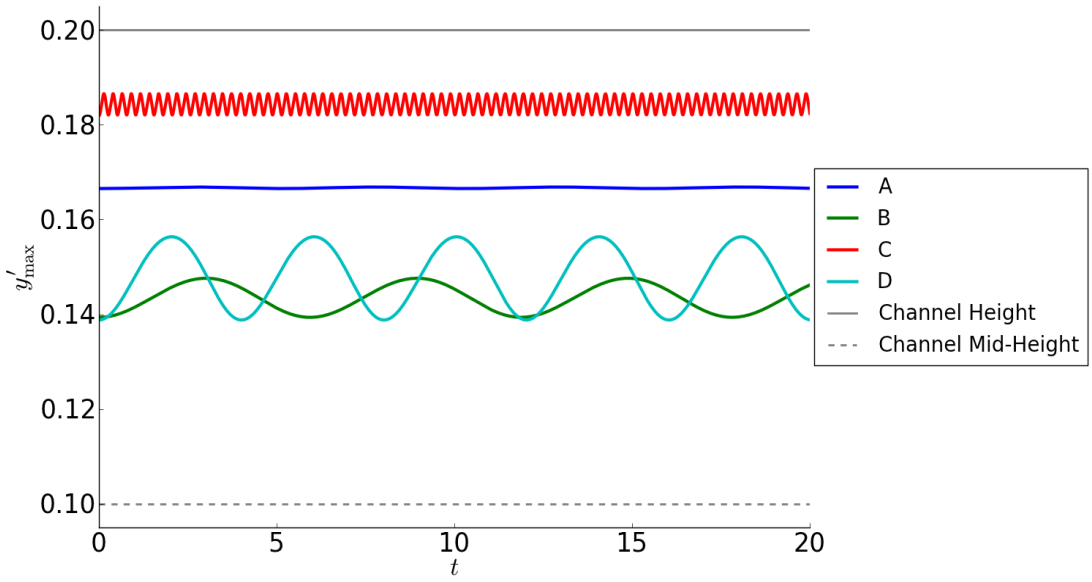

Figure 7.18 Truncated time history of maximum vertical displacement y'_{max} at the steady-state maximum deformation point for critical stability test points A to D.

the recirculation vortex at the bottom wall has grown again and moving downstream. At $t = 5.9$ the oscillation cycle is complete.

The fluid flow exhibits less unsteady recirculation vortices in test point B compared to point A. However there are similarities in the vortex-forming mechanism although this happens further downstream for point A (after the large recirculation zone pair). This may account for point A having very small oscillations because the 'similar' instability is occuring further downstream where its effect on A_{max} is diminished. This also explains the reason there is no positive and negative variation of pressure for point A in Figure 7.17a. This similar mechanism is also confirmed with both points having similar magnitude oscillation f. The main difference therefore is in the location where the vortex shedding occurs.

It is also worth pointing out the similarity of test point B with the point A from Liu et al. (2009) (see Chapter 5). The instability mechanism is similar in terms of the areas of recirculation vortex growth, shedding and decay. This is quantitatively confirmed through the similarity in A_{max} and f of both points. The level of streamline activity in Case A from Liu et al. (2009) is higher than the current test point B. This confirms the relationship that the higher Ca_{eff}.Re is above the stability surface (see Figure 7.14), the higher the levels of instability.

Point C is shown in Figure 7.21. At $t = 0$, the flexible insert is at its smallest deformation. There are also no disturbances in the streamlines. The flexible insert deformation increases through $t = 0.116$ where a recirculation zone can be see at the intersection between the flexible insert downstream end and the start of the rigid wall. A vortex can also be seen forming at the corresponding bottom wall. The deformation is largest at $t = 0.128$ where the vortex is still growing. These vortices start to shed

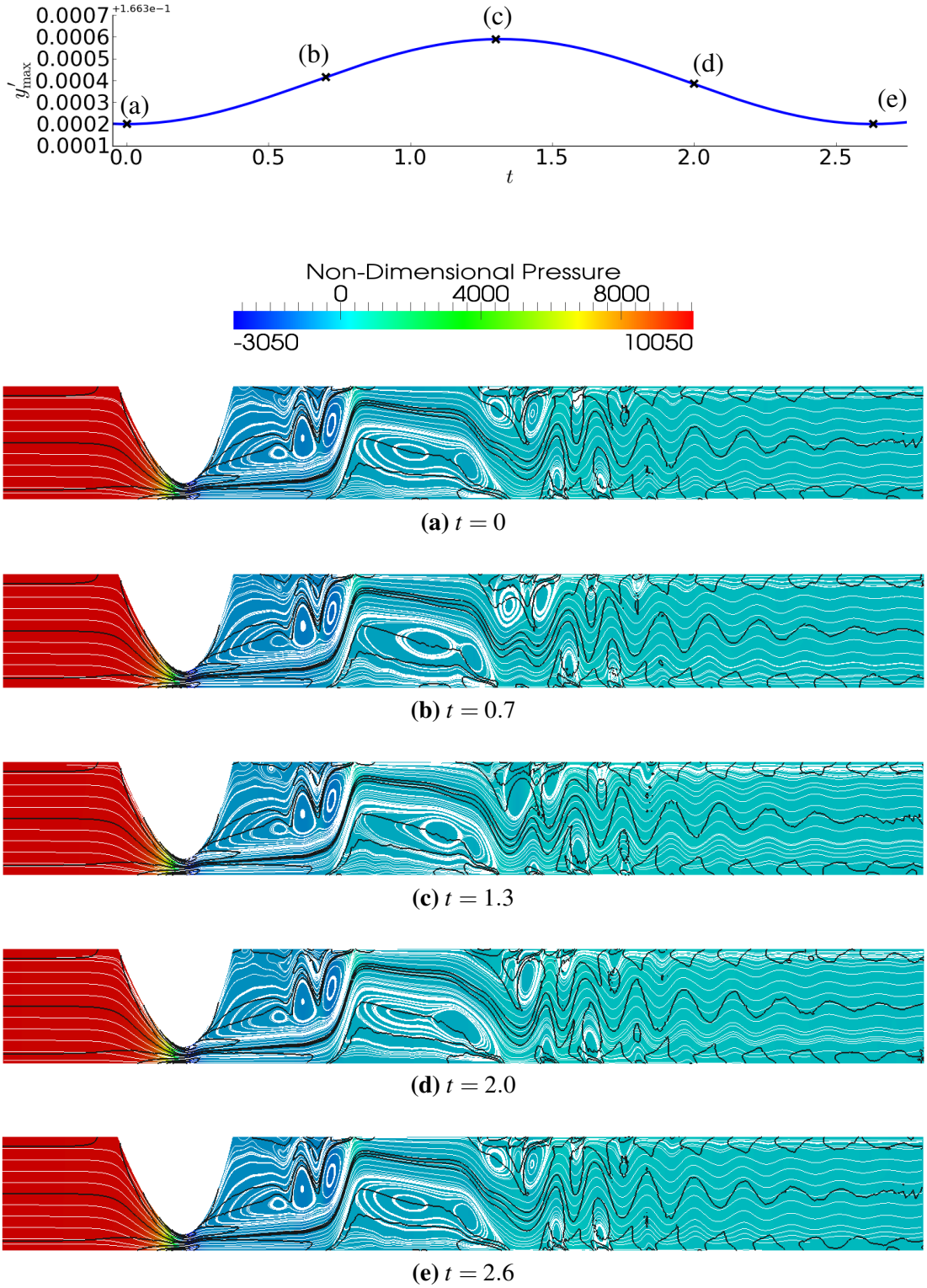

(a) $t = 0$

(b) $t = 0.7$

(c) $t = 1.3$

(d) $t = 2.0$

(e) $t = 2.6$

Figure 7.19 Maximum vertical displacement y'_{max} time history over one saturated oscillation cycle with corresponding streamlines (white), vorticity contours (black) and non-dimensional pressure (colour) contours at various timesteps for critical stability test point A. The fluid domain is scaled with a ratio of 1:5 (channel length to height).

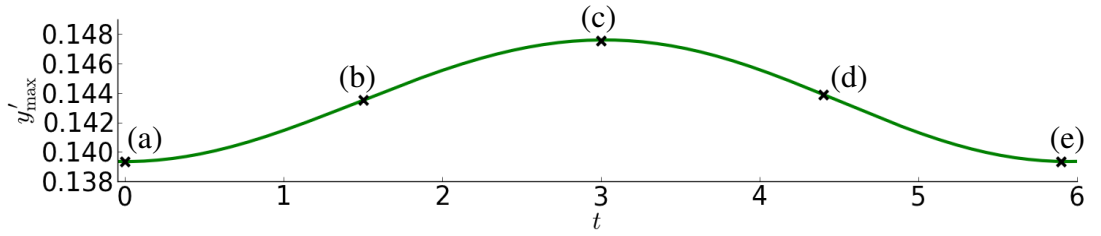

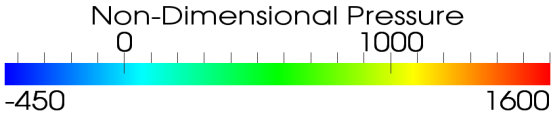

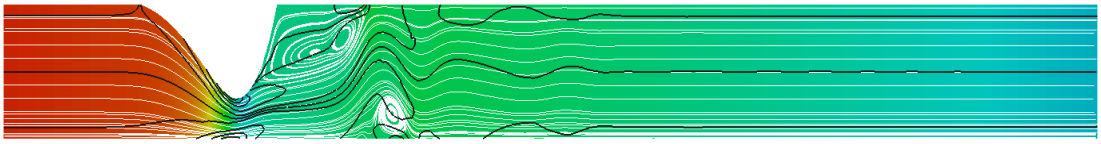

(a) $t = 0$

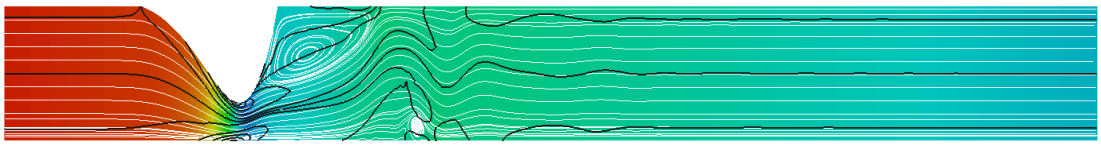

(b) $t = 1.5$

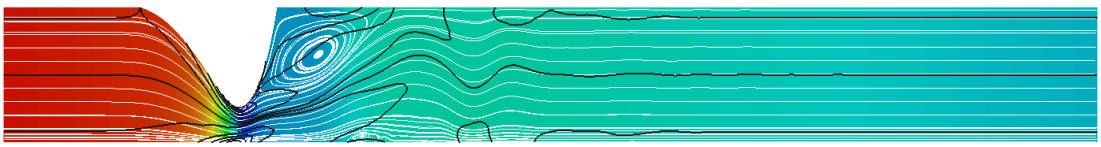

(c) $t = 3.0$

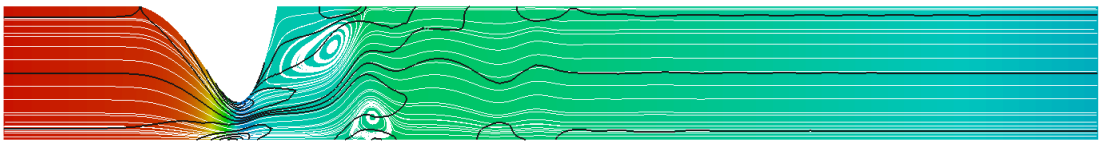

(d) $t = 4.4$

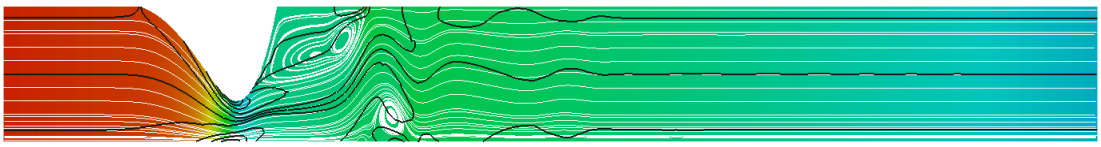

(e) $t = 5.9$

Figure 7.20 Maximum vertical displacement y'_{max} time history over one saturated oscillation cycle with corresponding streamlines (white), vorticity contours (black) and non-dimensional pressure (colour) contours at various timesteps for critical stability test point B. The fluid domain is scaled with a ratio of 1:5 (channel length to height).

at $t = 0.147$ at which point wall deformation is decreasing. This shedding continues to $t = 0.169$ where the recirculation zones have grown to a bigger size. At $t = 0.203$, the vortices collapse and form smooth streamlines again at $t = 0.260$. The instability mechanism for point C is due to the large flexible insert deformation. This causes small recirculation vortices to form periodically at the top and bottom walls downstream of the flexible insert. In essence, the first half of the oscillation cycle sees the the flexible insert trying to find an equilibrium position and forming a recirculation vortex as a result. The second half of the cycle sees growing recirculation vortices shedding downstream.

Test points A and B have ever-present recirculation zones whereas half the oscillation cycle in point C sees no recirculation vortex formation. The Reynolds number $\mathrm{Re} = 5$ for this point C is low compared to the other points (see Table 7.5). In this case, fluid experiences the Coandă effect with creeping fluid flow that is attached to the flexible wall (Sobey 2000). The flexible wall deformation is larger than the other points with the flexible insert being significantly stretched.

Test point D is shown in Figure 7.22. At $t = 0$, there is a recirculation zone directly behind (downstream) of the flexible insert. At this time, the flexible insert deformation and vortex are at their smallest. After this point the vortex grows and pushes the wall upstream at $t = 1.0$. At $t = 2.0$ the vortex and flexible deformation are at their largest. Following this, the vortex reduces in size while shifting downstream. This shift downstream also pulls the flexible insert very slightly to the right. This can be seen as time progresses through $t = 3.0$. At $t = 4.0$, the oscillation cycle is complete and the recirculation vortex and wall deformation is again at their smallest. There are similarities between points B and D in the movement of the recirculation zone behind the flexible wall. No vortex shedding occurs in this case from either the upper or lower wall. Therefore this instability mechanism is driven purely by the interaction between the flexible wall and the growth and decline of the recirculation zone behind it.

The instability mechanisms have been described looking at the channel flow streamlines and relating it with the flexible insert shape and fluid pressure along the flexible insert. There are two mechanisms idenfified. In the first, there are growth, decay and shedding of recirculation zones behind the flexible wall, as seen in test points A, B and D. In the second mechanism (test point C), the creeping flow remains attached to the oscillating flexible wall and flow recirculation occurs closer to the flat rigid lower wall. This second instability mechanism appears to be characterised by larger average deformation of the flexible wall and higher oscillation frequency.

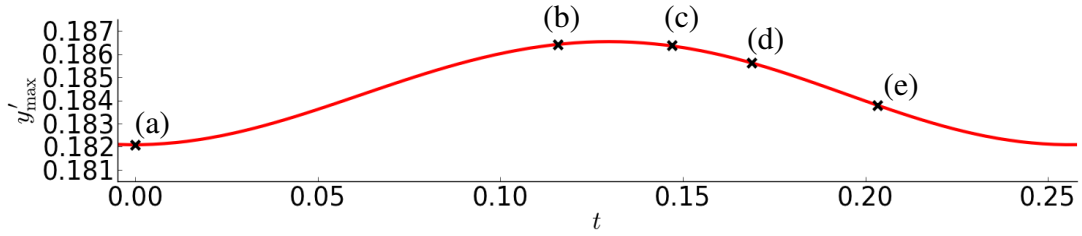

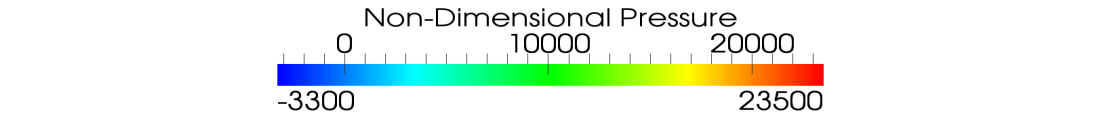

(a) $t = 0$

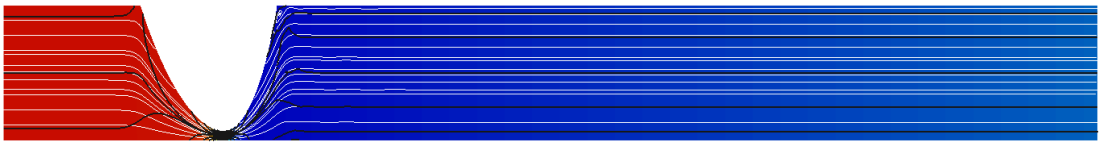

(b) $t = 0.116$

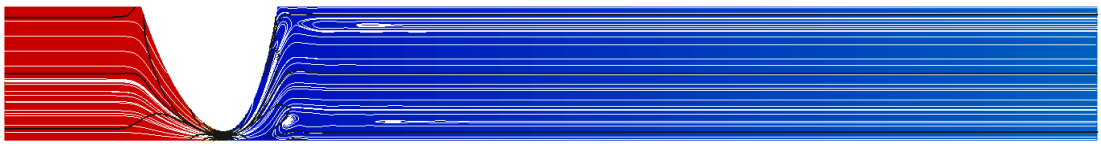

(c) $t = 0.147$

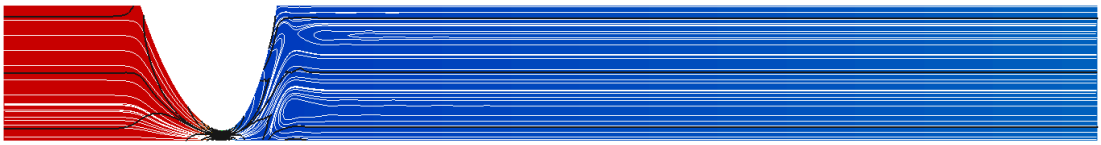

(d) $t = 0.169$

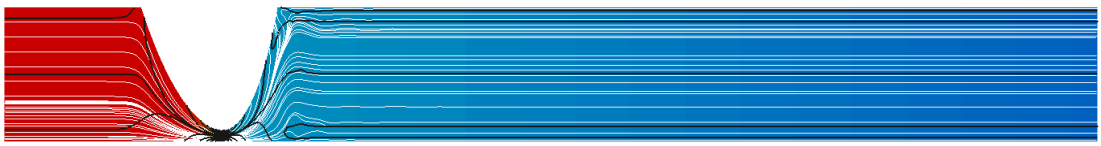

(e) $t = 0.203$

Figure 7.21 Maximum vertical displacement y'_{max} time history over one saturated oscillation cycle with corresponding streamlines (white), vorticity contours (black) and non-dimensional pressure (colour) contours at various timesteps for critical stability test point C. The fluid domain is scaled with a ratio of 1:5 (channel length to height).

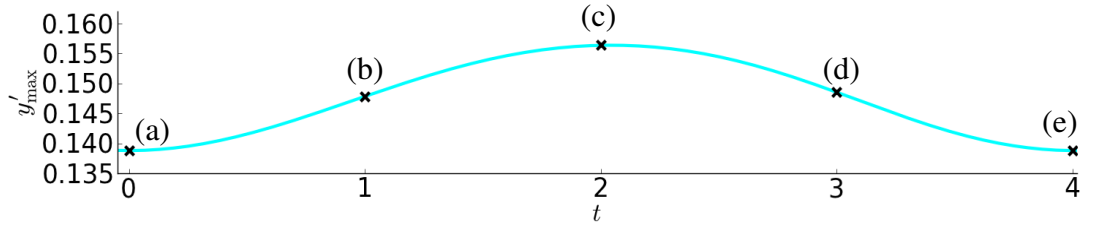

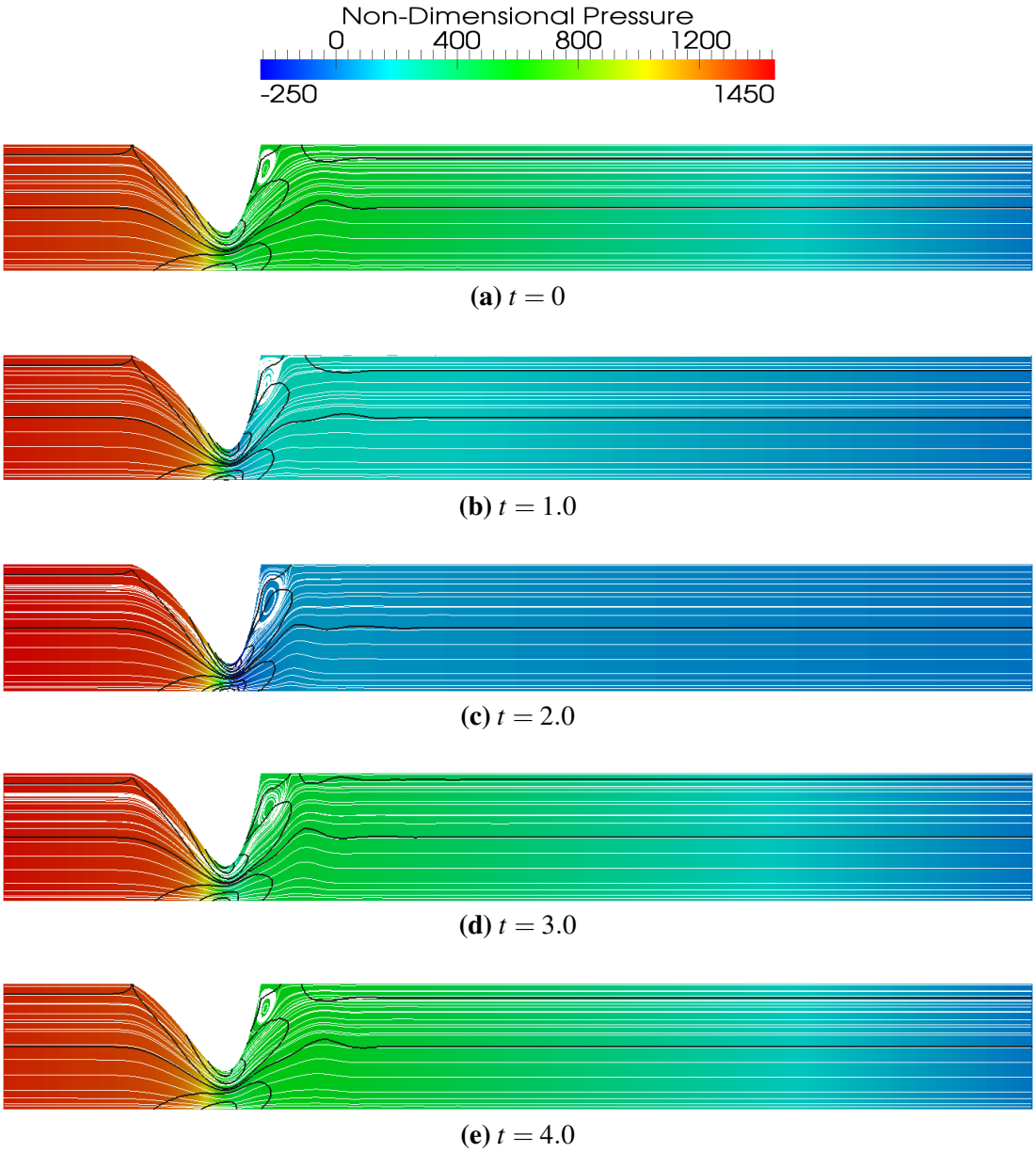

(a) $t = 0$

(b) $t = 1.0$

(c) $t = 2.0$

(d) $t = 3.0$

(e) $t = 4.0$

Figure 7.22 Maximum vertical displacement y'_{max} time history over one saturated oscillation cycle with corresponding streamlines (white), vorticity contours (black) and non-dimensional pressure (colour) contours at various timesteps for critical stability test point D. The fluid domain is scaled with a ratio of 1:5 (channel length to height).

7.5 Stability Surface Energy Budget Analysis

The energy budget is characterised in terms of the rate of energy and work occuring in the system over the saturated oscillation cycles. The four test points (A to D) as defined in Section 7.4 are analysed to determine the difference in energy budget of various regions of the parameter space studied. Figure 7.23 to Figure 7.26 show the overall and individual components of rate of work and energy for the fluid domain. Figure 7.27 to Figure 7.30 show the overall flexible insert rates of work and energy as well as its individual components for the four test points. The plots for points A to D show truncated time histories of the saturated oscillations. All cases show the driving mechanism to be $\dot{W}_{\mathrm{IO}}$ and the main loss in the system is from $\dot{D}_{\mathrm{fluid}}$. The magnitudes for rates of work and energy for points A, B and D are similar. In all instances, $\dot{PE}_{\mathrm{axial}}$ is the main contributor in the flexible insert energy budget balanced by $\dot{W}_{\mathrm{wall}} + \dot{W}_{\mathrm{Pext}}$.

Test point C is driven by a different instability mechanism and experiences significantly different rates of work and energy, in the order of $> 10^3$ rather than $< 10^1$ (as was the case for points A, B and D). It is confirmed that the large wall deformation plays an important role for point C instability. This is the largest deformation point out of the four. $\dot{W}_{\mathrm{wall}}$ which is relatively small compared to the other energy quantities in other cases is large in point C as seen in Figure 7.25b. The large external pressure results in the counter-acting $\dot{PE}$ being large as well as shown in Figure 7.29a. The large $\dot{PE}$ actually drives the instability. This different mechanism therefore drives the different orbital direction of the flexible wall maximum deformation point seen in Figure 7.16c.

The system average rate of work and energy for the overall channel fluid and flexible insert is shown in Table 7.7. The magnitudes of points A, B and D are comparable but the magnitude of point C being significantly larger for $\overline{\dot{W}}_{\mathrm{IO}}$ and $\overline{\dot{D}}_{\mathrm{fluid}}$. This is also true for $\overline{\dot{PE}}_{\mathrm{axial}}$ which is two orders of magnitude larger for point C compared to the other cases, looking at the rate of potential energy in Table 7.8. The $\overline{\dot{W}}_{\mathrm{wall}}$ traction components are also several orders of magnitudes larger in Table 7.9. This confirms the significant contribution of the wall in the instability occuring for point C.

From this it is deduced the instability mechanism for test points A, B and D are the same as they result in similar rates of energy and work, driven by the fluid inertia and flow recirculation zone growth, decay and shedding. The point C instability is driven by the highly stretched flexible insert only allowing a small pathway for fluid flow that results in the intermittent formation and dissipation of recirculation vortices.

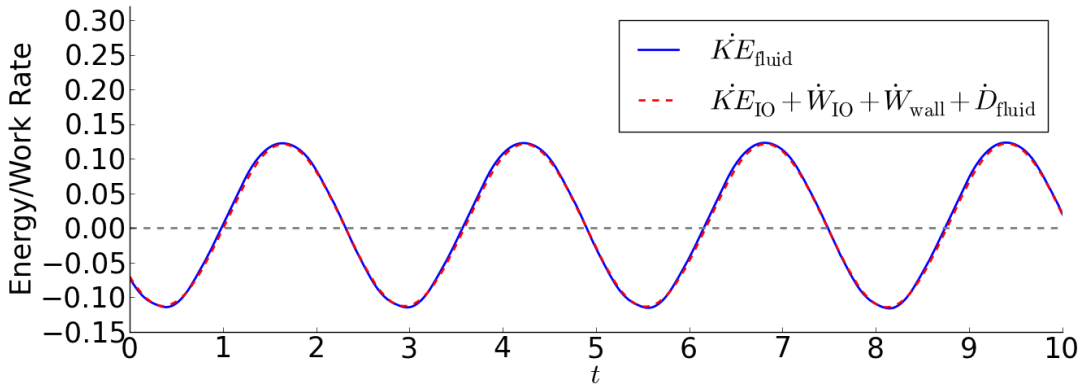

(a) Overall fluid domain energy budget balance.

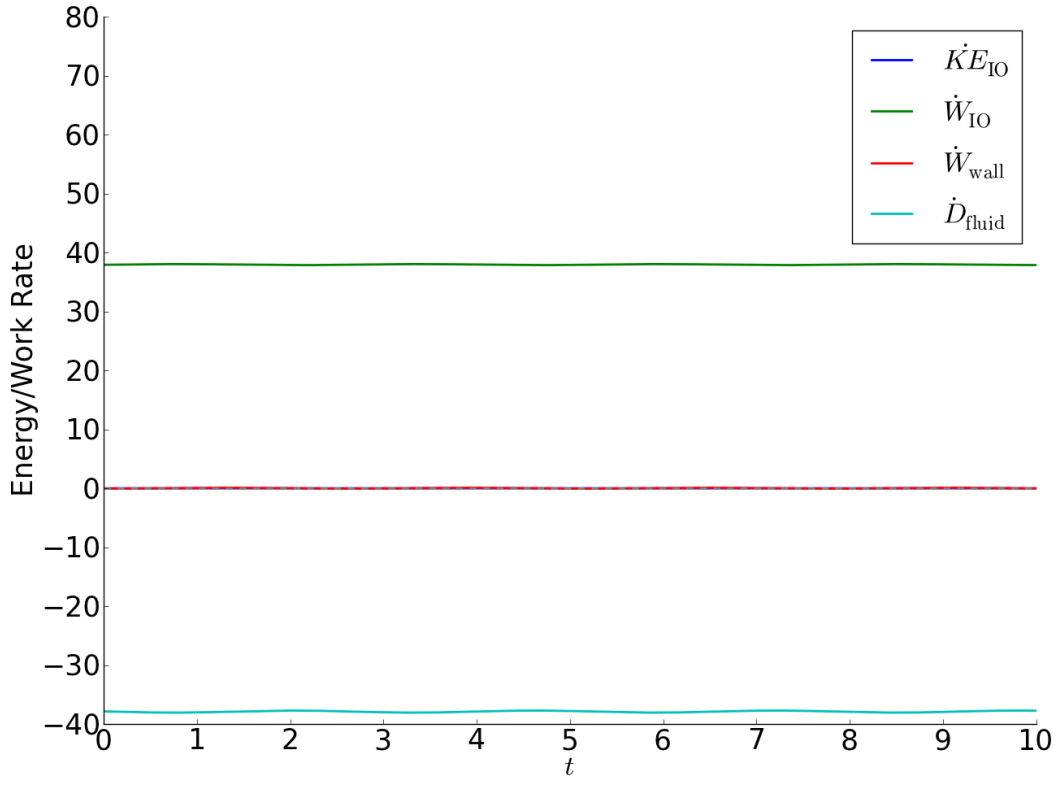

(b) Channel fluid components rate of work and energy.

Figure 7.23 Test point A rate of work/energy plots for the channel fluid domain and its individual components.

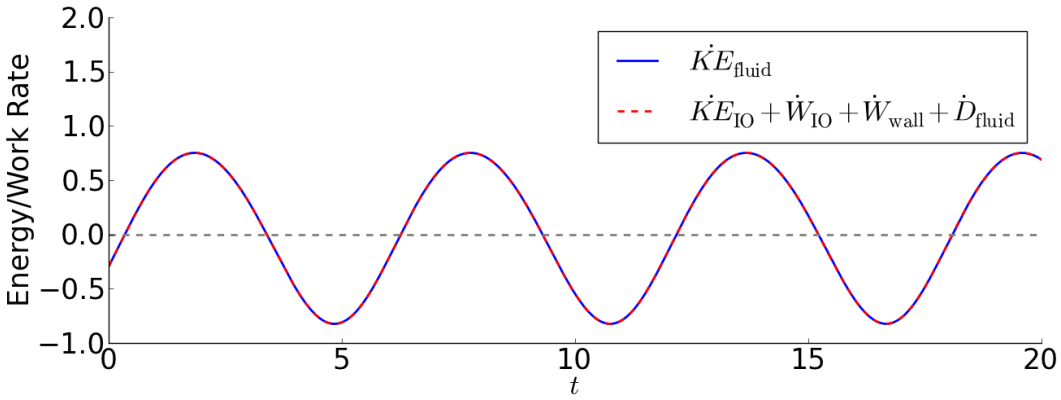

(a) Overall fluid domain energy budget balance.

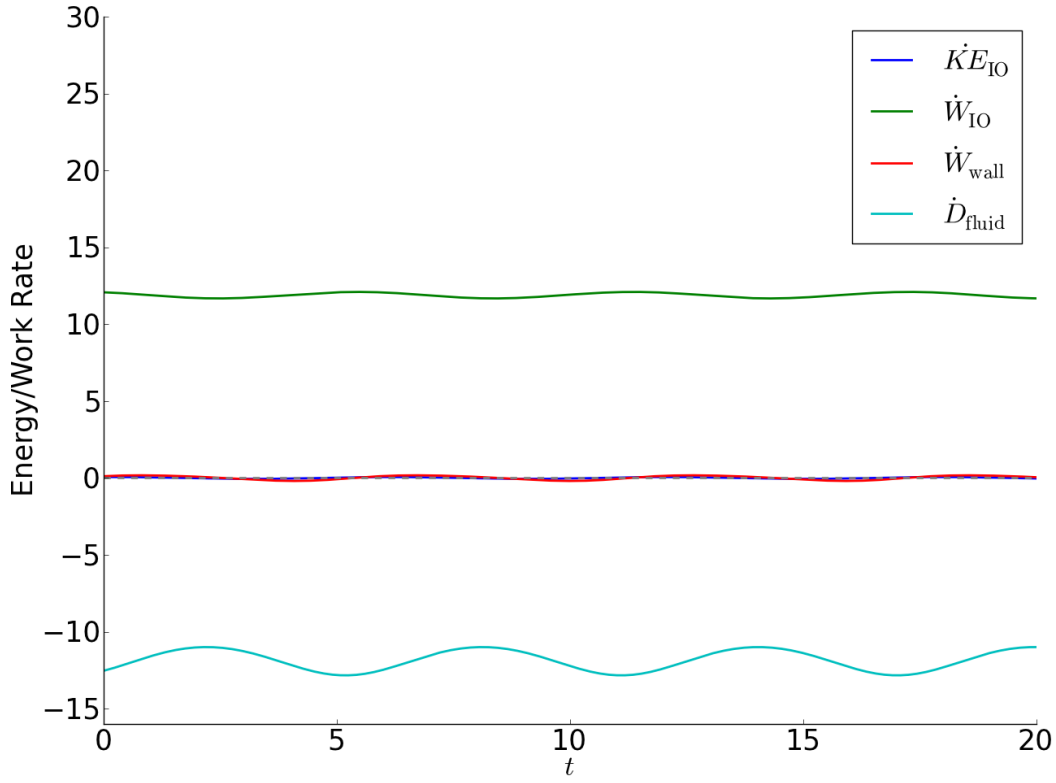

(b) Channel fluid components rate of work and energy.

Figure 7.24 Test point B rate of work/energy plots for the channel fluid domain and its individual components.

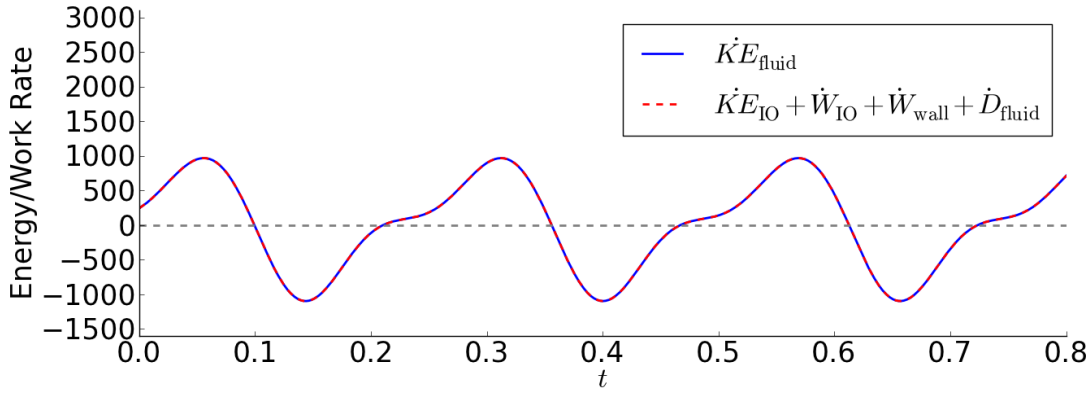

(a) Overall fluid domain energy budget balance.

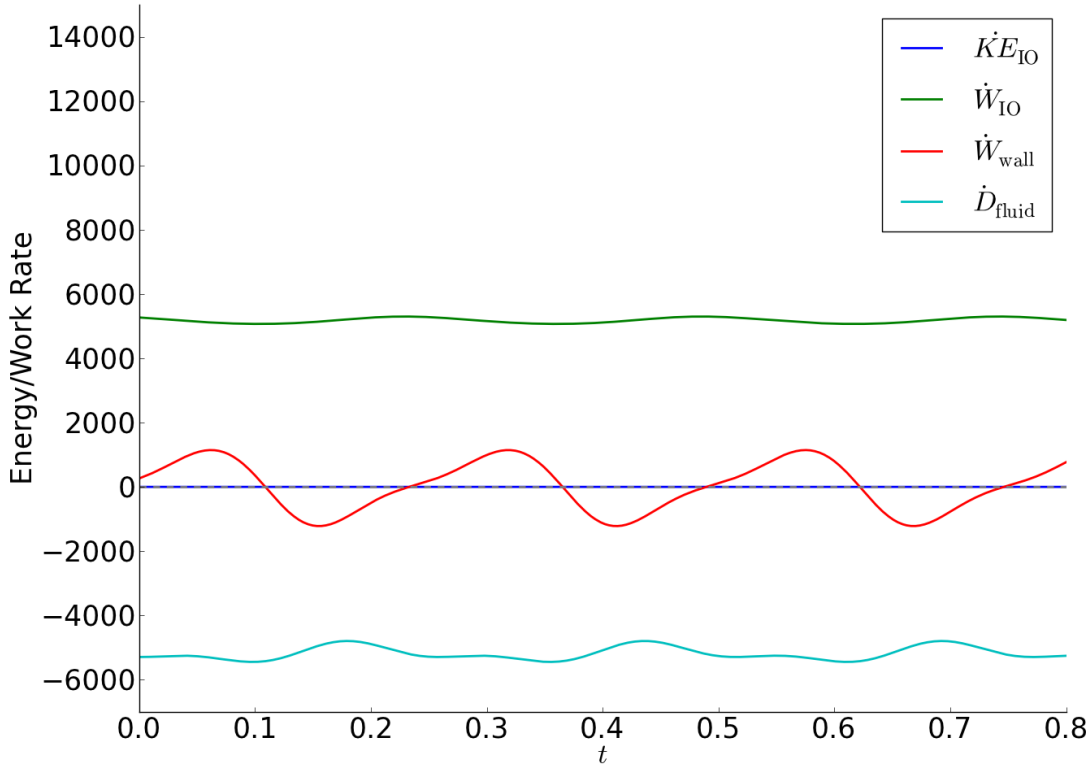

(b) Channel fluid components rate of work and energy.

Figure 7.25 Test point C rate of work/energy plots for the channel fluid domain and its individual components.

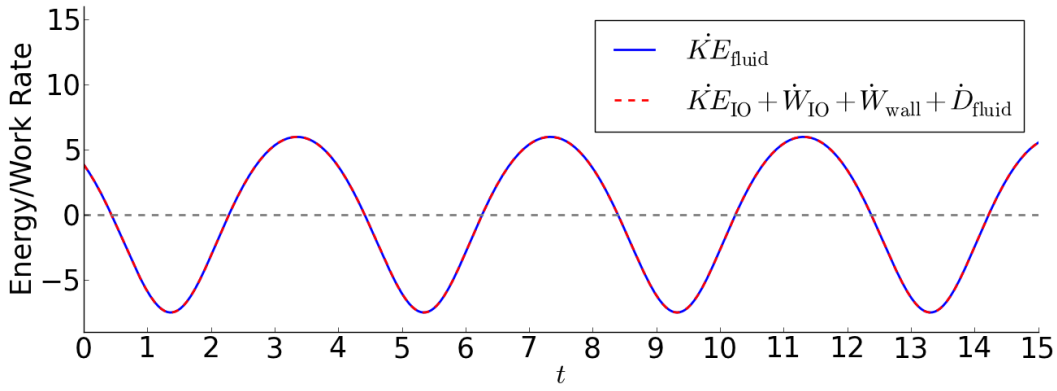

(a) Overall fluid domain energy budget balance.

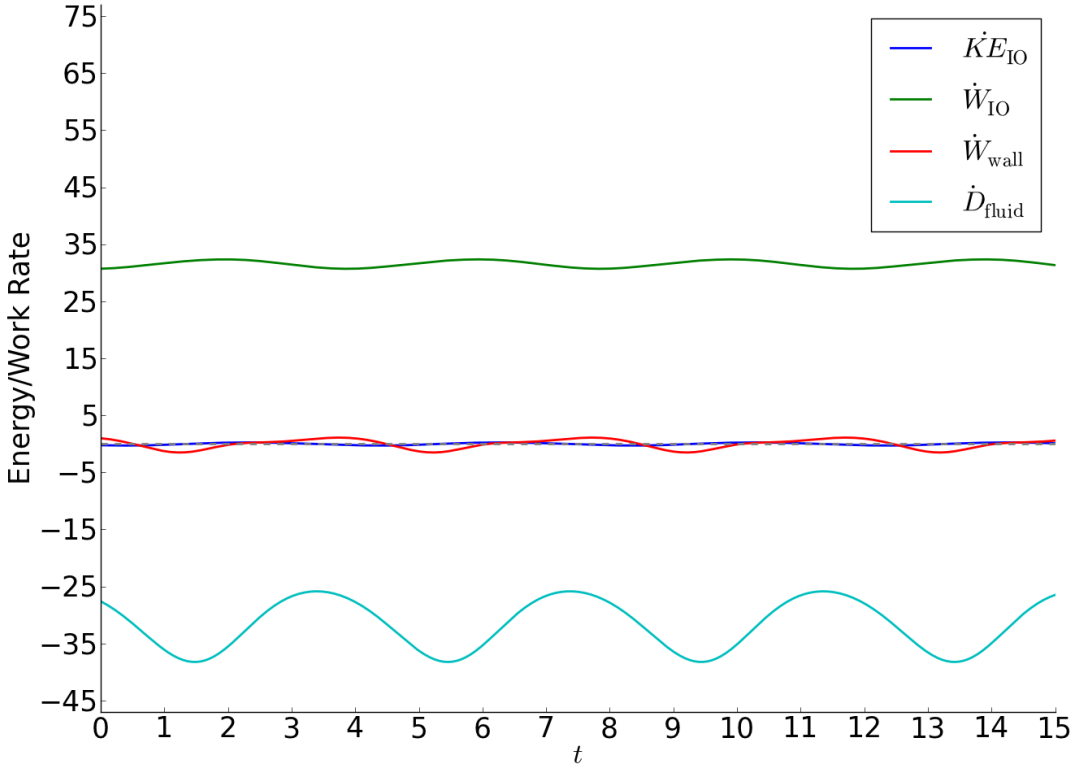

(b) Channel fluid components rate of work and energy.

Figure 7.26 Test point D rate of work/energy plots for the channel fluid domain and its individual components.

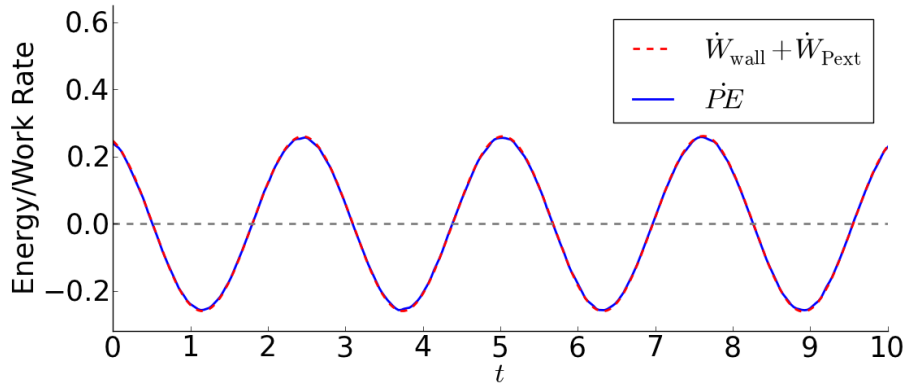

(a) Flexible wall overall rate of work.

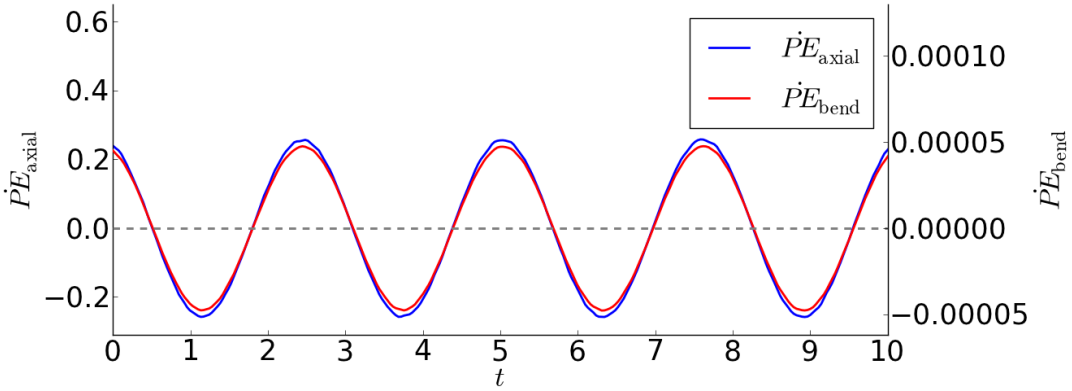

(b) Flexible wall rate of potential energy components.

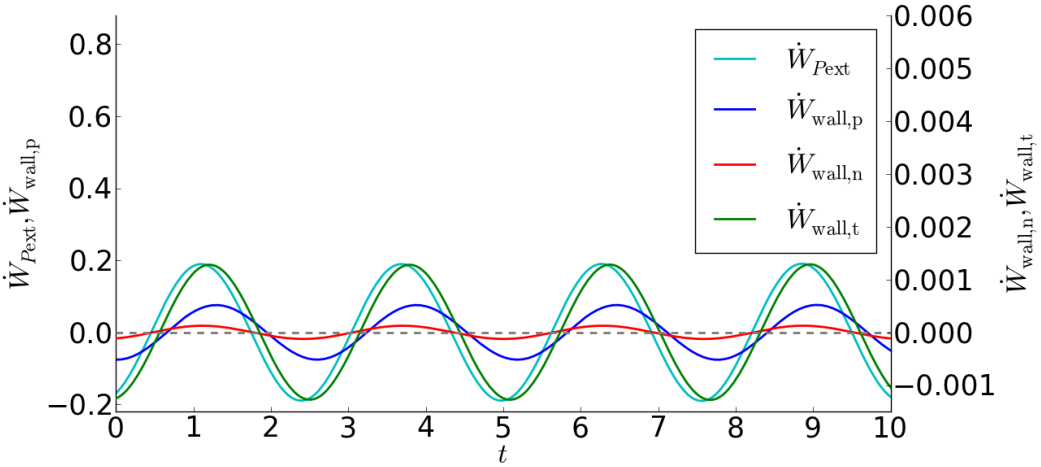

(c) Flexible wall rate of external work categorised into the pressure, and normal and tangential traction components.

Figure 7.27 Test point A rate of work/energy plots for the flexible insert and its individual components.

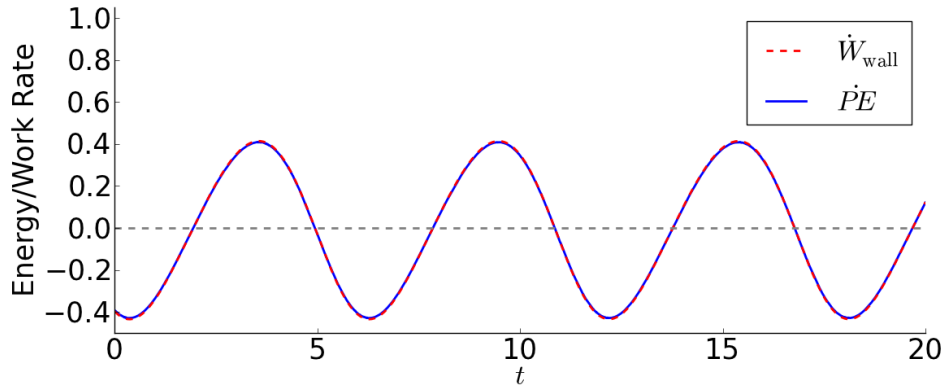

(a) Flexible wall overall rate of work.

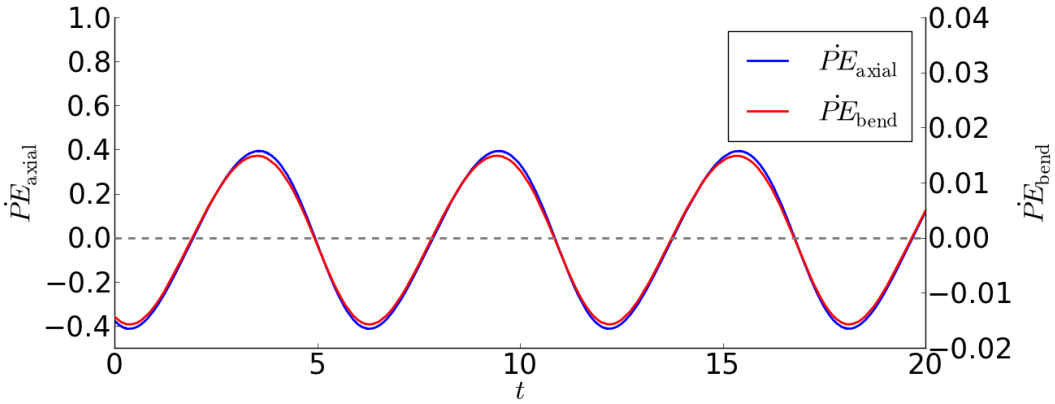

(b) Flexible wall rate of potential energy components.

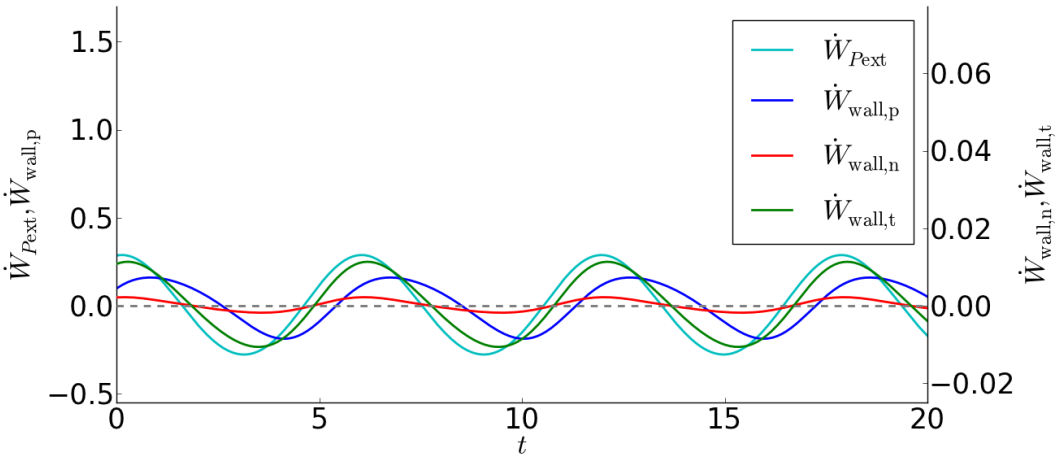

(c) Flexible wall rate of external work categorised into the pressure, and normal and tangential traction components.

Figure 7.28 Test point B rate of work/energy plots for the flexible insert and its individual components.

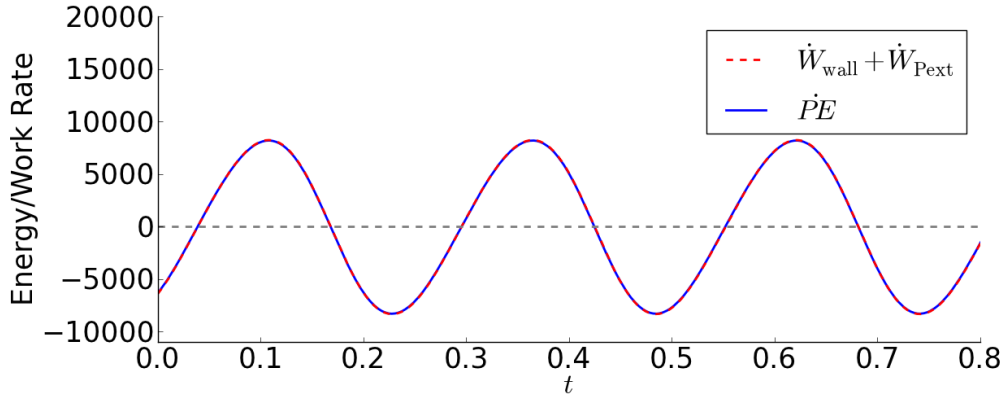

(a) Flexible wall overall rate of work.

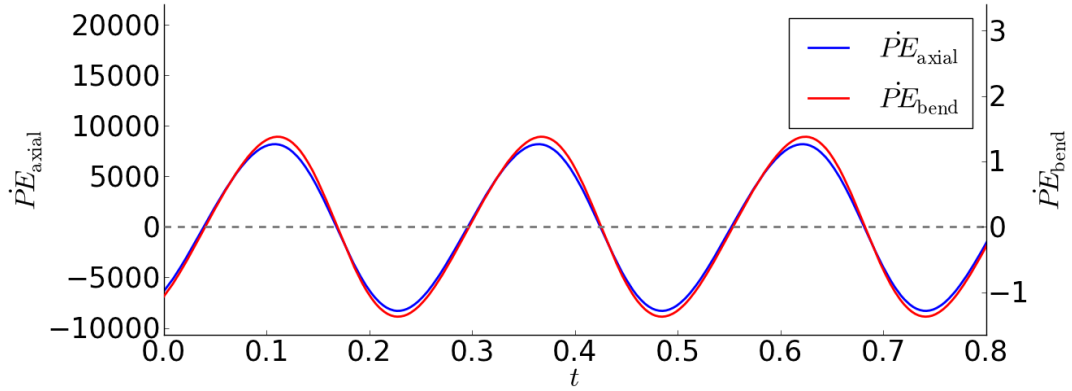

(b) Flexible wall rate of potential energy components.

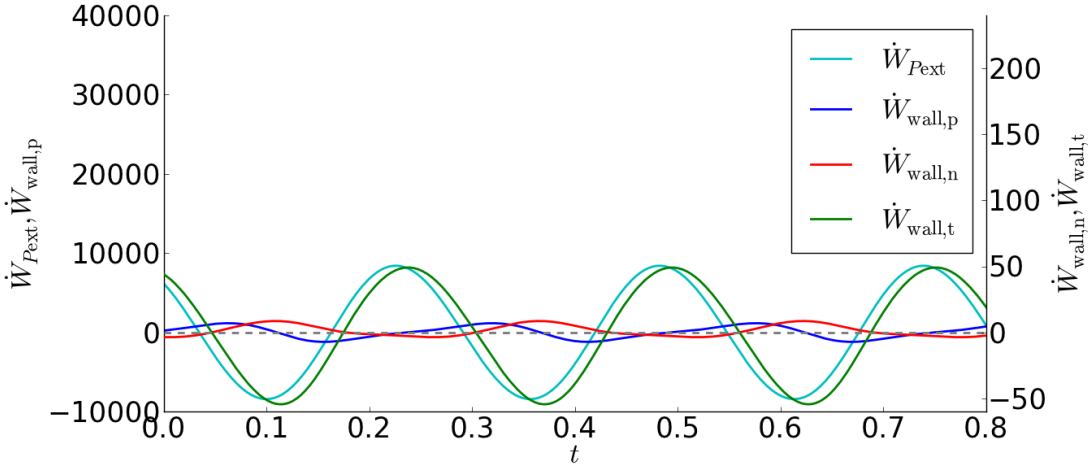

(c) Flexible wall rate of external work categorised into the pressure, and normal and tangential traction components.

Figure 7.29 Test point C rate of work/energy plots for the flexible insert and its individual components.

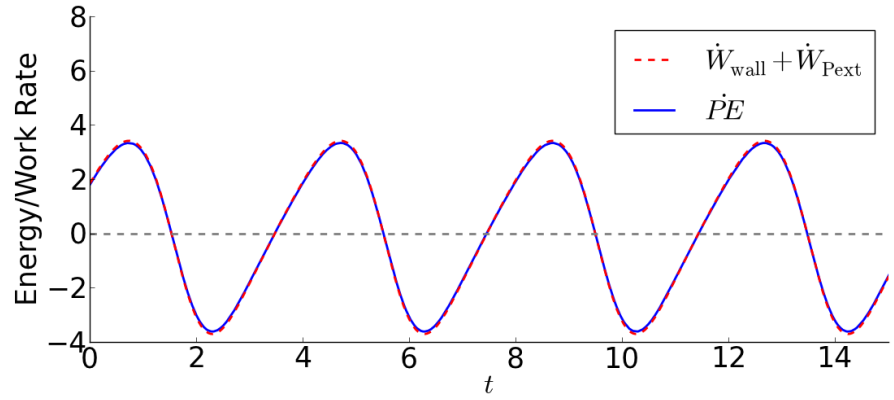

(a) Flexible wall overall rate of work.

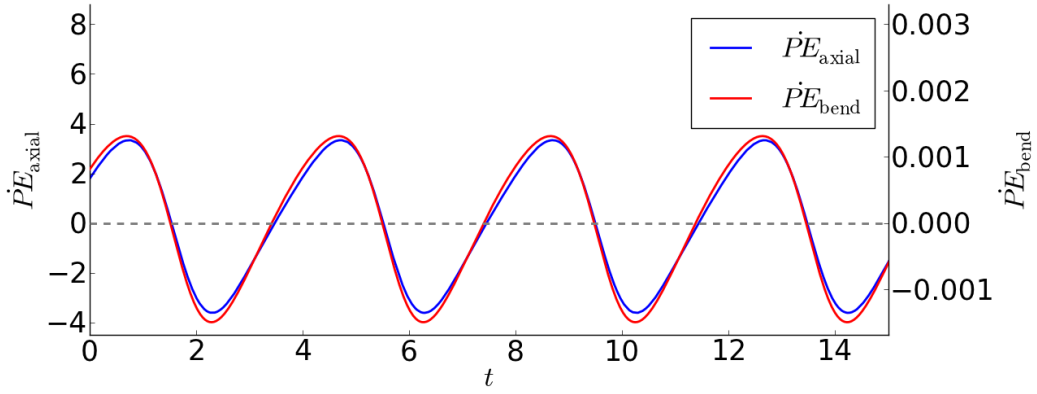

(b) Flexible wall rate of potential energy components.

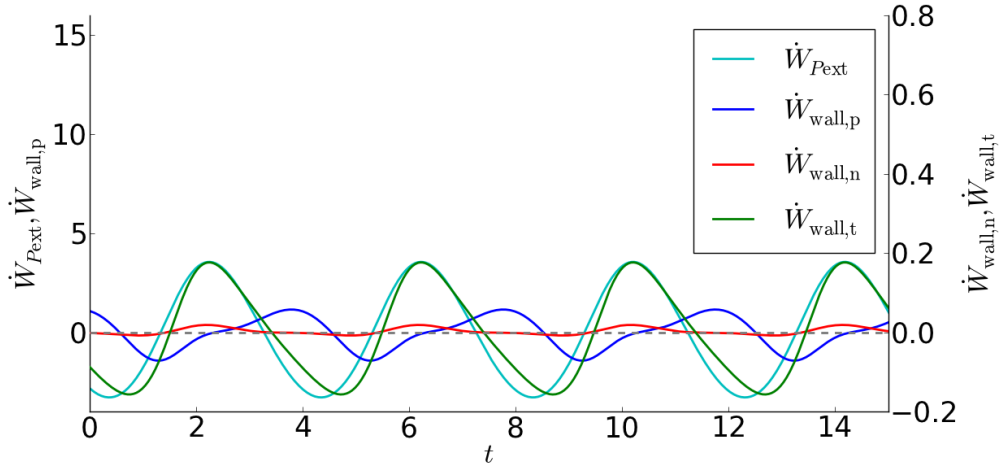

(c) Flexible wall rate of external work categorised into the pressure, and normal and tangential traction components.

Figure 7.30 Test point D rate of work/energy plots for the flexible insert and its individual components.

Table 7.7 Average rates of work and energy for overall flexible insert and channel fluid for test points A to D.

Test point	$\overline{\dot{KE}}_{\text{fluid}}$	$\overline{\dot{KE}}_{\text{IO}}$	$\overline{\dot{W}}_{\text{IO}}$	$\overline{\dot{W}}_{\text{wall}}$	$\overline{\dot{D}}_{\text{fluid}}$
A	3.88×10^{-2}	-1.34×10^{-2}	37.93	-8.10×10^{-4}	-37.90
B	4.94×10^{-5}	-8.46×10^{-4}	11.89	9.17×10^{-5}	-1.89
C	3.43×10^{-2}	-0.848	5177.9	-6.35×10^{-2}	-5176.9
D	-3.86×10^{-5}	-1.66×10^{-2}	31.54	1.80×10^{-5}	-31.52

Table 7.8 Average rates of potential energy for flexible insert for test points A to D.

Test point	$\overline{\dot{PE}}_{\text{axial}}$	$\overline{\dot{PE}}_{\text{bend}}$
A	-5.43×10^{-4}	1.81×10^{-7}
B	-2.22×10^{-4}	8.50×10^{-6}
C	5.46×10^{-2}	9.51×10^{-6}
D	3.64×10^{-4}	1.54×10^{-7}

Table 7.9 Average rates of work for flexible insert for test points A to D.

Test point	$\overline{\dot{W}}_{\text{wall,p}}$	$\overline{\dot{W}}_{\text{wall,n}}$	$\overline{\dot{W}}_{\text{wall,t}}$	$\overline{\dot{W}}_{P\text{ext}}$
A	2.70×10^{-5}	2.98×10^{-6}	2.15×10^{-6}	5.17×10^{-4}
B	3.60×10^{-6}	9.12×10^{-5}	7.30×10^{-6}	1.52×10^{-4}
C	-0.383	1.46	-1.16	6.75×10^{-3}
D	-2.94×10^{-3}	3.01×10^{-3}	-5.51×10^{-5}	-8.88×10^{-5}

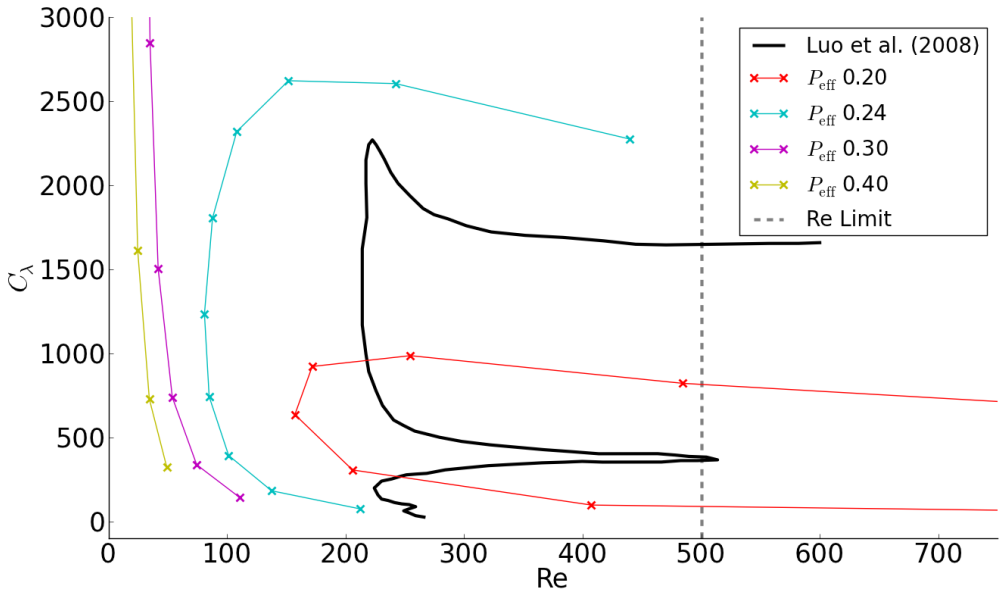

Figure 7.31 Alternative formulation for critical stability lines using C_λ and Re based on the approach by Luo et al. (2008).

7.6 Alternative Non-Dimensional Formulation

An alternative representation of the dynamic non-dimensionalisation scheme is using the C_λ and Re form introduced by Luo et al. (2008). The critical stability lines produced from this approach are shown in Figure 7.31. Values within the loops (to the right) are unstable and outside the loops (to the left) are stable. The grey vertical line is the Re limit of 500. To the the right of the Re limit are data points derived from predictions extrapolated based on the base non-dimensional scheme parameterisation. All actual tested data points are below to the left of the Re limit.

Similarities can be seen between Figure 7.31 and the stability cascade structure by Luo et al. (2008), with a loop-form. This indicates the approaches and findings are likely consistent. The current study results use P_{eff} to characterise the contribution system pressure whereas the cascade stability line by Luo et al. (2008) uses the definition $P'_{\text{ext}} = P^*_{\text{ext}}/(\rho^*_{\text{f}} U^*_{\text{mean}})$. The definition of P_{eff} involves terms considering L^*_{flex} and the insert position. The current results which consider different P_{ext} therefore result in multiple stability lines (for various P_{eff}) which differ in shape from Luo's stability data for a single P_{ext}. In addition, the previous work is confined to a fixed position of the flexible insert along the channel and a fixed length for L^*_{flex} whereas the present work has tested variations and sensitivities for both.

The P_{eff}, $\text{Ca}_{\text{eff}}/\text{Re}$ and Ca_{eff}.Re form was selected because it was deemed with this representation system stability is more easy to interpret, particularly with multiple P_{eff} values analysed. It also 'unfolds' the cascade structure to a critical stability surface

where Ca_{eff}.Re values below this surface is stable and above which is unstable. The current non-dimensional formulation was also particularly beneficial for simplifying the flexible insert shape characterisation (Section 6.4) to two parameters (P_{eff} and Ca_{eff}/Re). This would not have been possible with the alternative (P_{eff}, Ca_{eff} and Re) form.

Comparison with the same range parameter range tested experimentally showed absolute stability is achieved at Re < 260 (Bertram and Elliott 2001). For the current work, there is consistency with the trend of having a finite lower bound Re where the system achieves absolute stability. However this Re threshold varies where higher P_{eff} values results in a lower Re stability threshold. It can be be seen that with higher P_{eff} the Re threshold for absolute stability is increasing and will likely approach the Re = 200 threshold for $P_{eff} < 0.20$. Quantitative differences with experimental work may be attributed to the inherent 2-d modelling approach as well as the assumption that the modeled flexible insert being massless and very thin.

7.7 Experimental Comparison

It is of interest to compare the current study results with past experimental work to ensure the current numerical scheme is representative of the physical system. Two published experimental studies discussed in Section 2.1 are selected for comparison with the current work; Bertram (1986) and Bertram and Tscherry (2006). Table 7.10 lists the parameters and formulation into the current non-dimensional scheme for these experimental studies. A range of values were tested in these studies with the values listed being for the critical stability points that exhibit dynamic (oscillatory) instability. Both experiment specifications have not listed the downstream lengths for the experimental apparatus, but downstream pressure is measured following the trailing edge of the flexible tube section. For comparison with the current numerical scheme, this downstream pressure is calculated to an equivalent downstream length L_{down} based on the idealised case of linear pressure drop for a rigid circular pipe using the equation (White 2011)

$$\frac{p_{down} H^2}{32 \mu U} \tag{7.1}$$

This is important for the calculation of P_{mean} which is contained in the non-dimensional parameter P_{eff} as described in Section 6.1.

Current study non-dimensional parameter ranges are listed in Table 7.2 for comparison with Table 7.10. The Bertram (1986) study has Re=13300 and is higher than any Re tested in the current work (Re < 500) and is also in the turbulent flow regime. The Bertram and Tscherry (2006) study is more relevant because Re = 290 is in the laminar range due to the conscious effort given by the authors to replicate parameter ranges typical of numerical studies.

Table 7.10 Dimensional and non-dimensional parameters for experimental studies showing oscillatory instability onset.

Parameter	Values	
Experimental Study	Bertram (1986)	Bertram and Tscherry (2006)
L^*_{flex} (mm)	239	186
H^* (mm)	13.3	12.0
h^* (mm)	2.4	1.0
ρ^*_{f} ($\times 10^3$ kg.m^{-3})	1	1
μ^* ($\times 10^{-3}$ Pa.s)	1	1.5
U^* (m.s^{-1})	1	0.56
E^*_{eff} ($\times 10^5$ Pa)	500	500
P^*_{ext} ($\times 10^3$ Pa)	100	40
P^*_{down} $\times 10^3$ (Pa)	100	20
Re	13300	290
ln(Ca_{eff}/Re)	-15.02	-11.75
ln(Ca_{eff}.Re)	3.97	-0.41
P_{eff}	0.25	0.23

Comparison of the current work parameter ranges and experimental studies is more clearly seen by characterising in terms of the three non-dimensional parameters in Figure 7.32 where the current work critical stability surface is shown with red lines and the experimental studies shown as blue dots. The experimental study Ca_{eff}.Re and P_{eff} values are within current study ranges for both studies. The Ca_{eff}/Re is beyond the current study (ln(Ca_{eff}/Re) < -11.5), with the case of Bertram and Tscherry (2006) just slightly lower than tested ranges.

The proximity of these experimental points relative to the stability surface can be seen more clearly in Figure 7.33 where both experimental study points being plotted and numerical stability line for P_{eff} = 0.23 and 0.25 lines shown. The stability lines have been extrapolated to be in better proximity of the experimental points. A vertical dotted line shows the actual current study tested range for Ca_{eff}/Re. In both instances the experimental case instabilities are seen to occur at lower Ca_{eff}.Re values for a given Ca_{eff}/Re and P_{eff} set. Although the values for critical stability do not closely match between the experimental and current numerical study, they are still within a reasonable range. Furthermore, the trend of critical instability occuring at larger Ca_{eff}.Re values with lower Ca_{eff}/Re is consistent with the trend of the parabolic critical instability curve at these P_{eff} ranges. Therefore qualitative similarities can be seen even though quantitatively there are some differences.

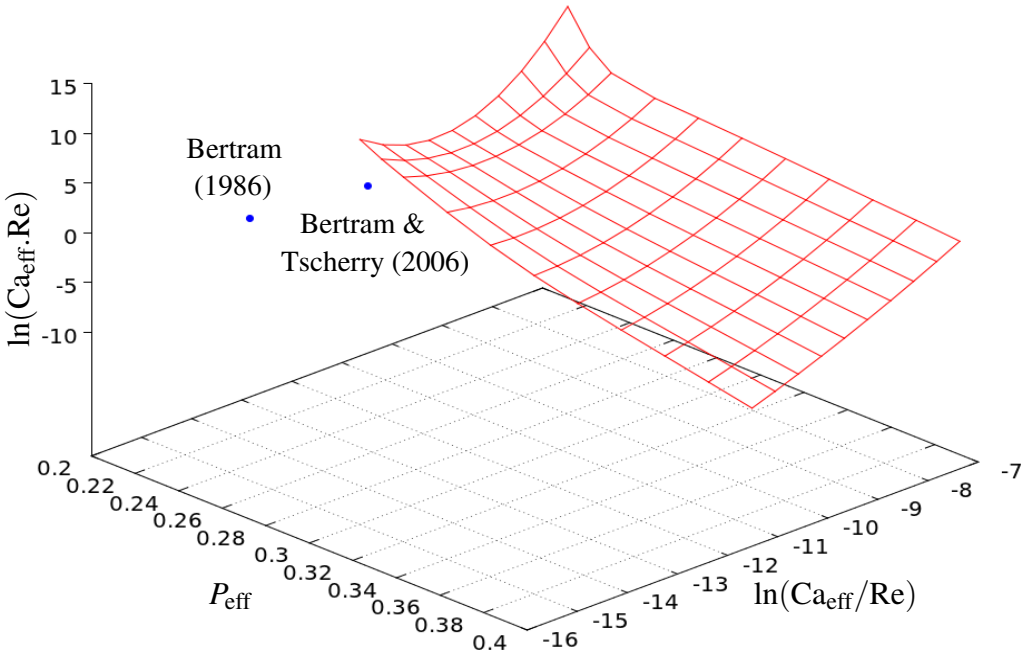

Figure 7.32 Current numerical study critical stability surface (red lines) and experimental data points denoting unstable cases (blue dots).

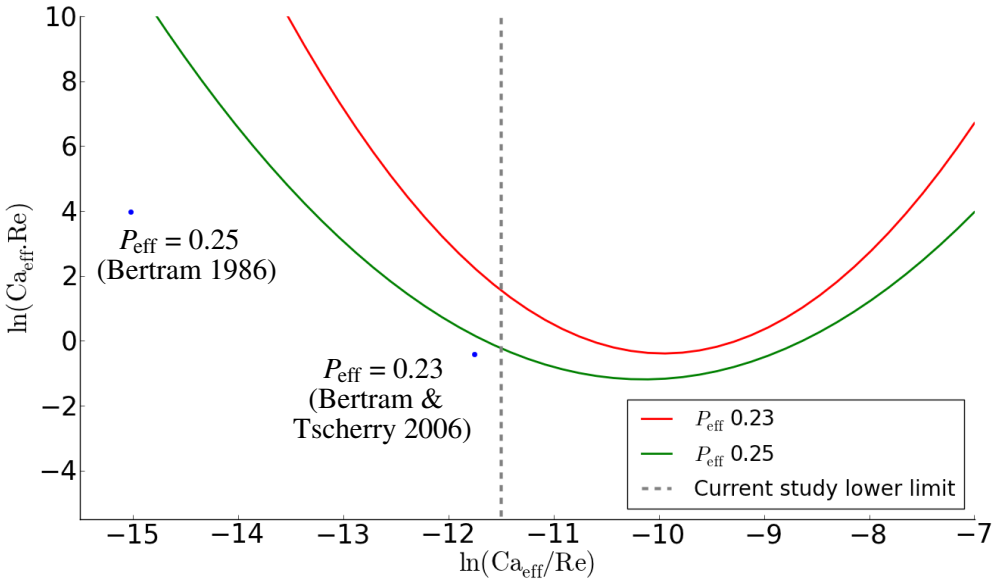

Figure 7.33 Experimental data points denoting unstable cases (blue dots) and dynamic critical stability lines for $P_{\text{eff}} = 0.23$ & 0.25. The P_{eff} lines are shown to compare with the respective experimental case points.

7.8 Summary

The non-dimensional scheme based on the three parameters of P_{eff}, $\text{Ca}_{\text{eff}}/\text{Re}$ and $\text{Ca}_{\text{eff}}.\text{Re}$ was tested on whether it was suitable to characterise the flexible channel dynamic behaviour. Variation of internal dimensional parameters within each of the non-dimensional parameters was performed and it was found they were robust to these changes. On this basis, a parametric study is performed by varying the three parameters. The result is the creation of a colour contour representation of the stability surface where stability can be predicted. It is noted there is no direct relationship between wall deformation magnitude and instability onset. Four test points (A to D) on the stability surface was also selected for further analysis to highlight the different instability mechanisms possible depending on the combination of the non-dimensional parameters. It was found instability was mainly driven by the growth, decay and shedding of recirculation zones downstream of the flexible insert. However, there are situations where the large flexible deformation drives the instability (point C). This type of instability has the characteristic of having significantly higher oscillation frequencies, in the order of $f = 10^0$ compared to $f = 10^{-1}$ for all other points (A, B and D). This formulation of the stability surface was also compared with the alternative C_λ and Re representation. Compared with the alternative formulation, the current stability plot has the ability to more clearly represent stability of various P_{eff} that considers L_{flex} and flexible wall locations. A comparison with previously published experimental work was also performed. Instability is seen to occur at lower $\text{Ca}_{\text{eff}}.\text{Re}$ values for given $\text{Ca}_{\text{eff}}/\text{Re}$ and P_{eff} sets, though the critical instability line trend is consistent between experimental and numerical works. The proposed non-dimensional scheme is therefore considered suitable.

Chapter 8

Dual Flexible Insert Configuration Study

8.1 General

A new configuration of dual flexible insert configuration is introduced as was shown in Figure 1.1b. This configuration consists of flexible inserts on opposing sides of the channel with the same length and material properties. First a stability study is performed to determine whether the same instability mechanisms are still possible with this configuration. The possible relationships are analysed between the single and dual-wall systems in terms of the flexible insert shape and fluid flow behaviour during instability. The non-dimensional parameters (static and dynamic) scheme proposed is also assessed on whether the single flexible insert configuration findings still prove to be useful for the dual-flexible insert configuration.

8.2 Instability Study

A sample case is selected to test whether it is possible for the dual wall system to become unstable. A set of standard (base case) parameters are selected with the dimensional and non-dimensional properties listed in Table 8.1, similar to Table 6.1 used in the single wall dynamic testing in Section 7.1. The effective pressure P_{eff} is varied by changing the external pressure P_{ext} as the means to test when the system becomes unstable. Note that P_{eff} is the effective pressure applied inwards of the channel. The corresponding P_{ext} therefore also acts inwards of the channel (downwards for upper wall and upwards for lower wall) and normal to the flexible wall surfaces.

P_{eff} variations are shown in Table 8.2 along with the stability outcomes. Instability is shown to occur at $P_{\text{eff}} = 0.05$. The $P_{\text{eff}} = 0.05$ case and its instability mechanism is analysed using the same diagnostic tools as for the single wall case.

Table 8.1 Base case dimensional and non-dimensional validation parameters for dual flexible wall system stability testing.

Parameter	Value	Description
L^*_{up} (mm)	50	Upstream length of channel
L^*_{flex} (mm)	50	Collapsible length of channel
L^*_{down} (mm)	300	Downstream length of channel
H^* (mm)	10	Height of channel
h^* (mm)	0.1251	Thickness of flexible insert
$\rho^*_f (\times 10^2$ (kg.m^{-3})	7.993605	Density of fluid
μ^* ($\times 10^{-3}$ Pa.s)	1	Dynamic viscosity of fluid
ν	0.5	Poisson's ratio of solid
$\rho^*_s h^*$	0	Mass per unit area of solid
$B^* (\times 10^{-9}$ N.m)	1.6315	Flexural rigidity of flexible insert
$E^*_{eff} (\times 10^6$ Pa)	0.01	Young's modulus of flexible insert
$U^*_{mean} (\times 10^{-2}$ m/s)	1.251	Inlet mean velocity
Ca_{eff}	0.01	Effective Cauchy number Ca_{eff}
Re	100	Reynolds number Re
Ca_{eff}.Re	1.0	FSI strength
Ca_{eff}/Re ($\times 10^{-4}$)	1.0	FSI ratio

Table 8.2 Dual wall dynamic stability test results with variation of effective pressure P_{eff} and external pressure P^*_{ext}.

P_{eff}	P^*_{ext} (Pa)	Stability
0.02	0.73809	Stable
0.03	0.86319	Stable
0.04	0.98829	Stable
0.05	1.11339	Unstable

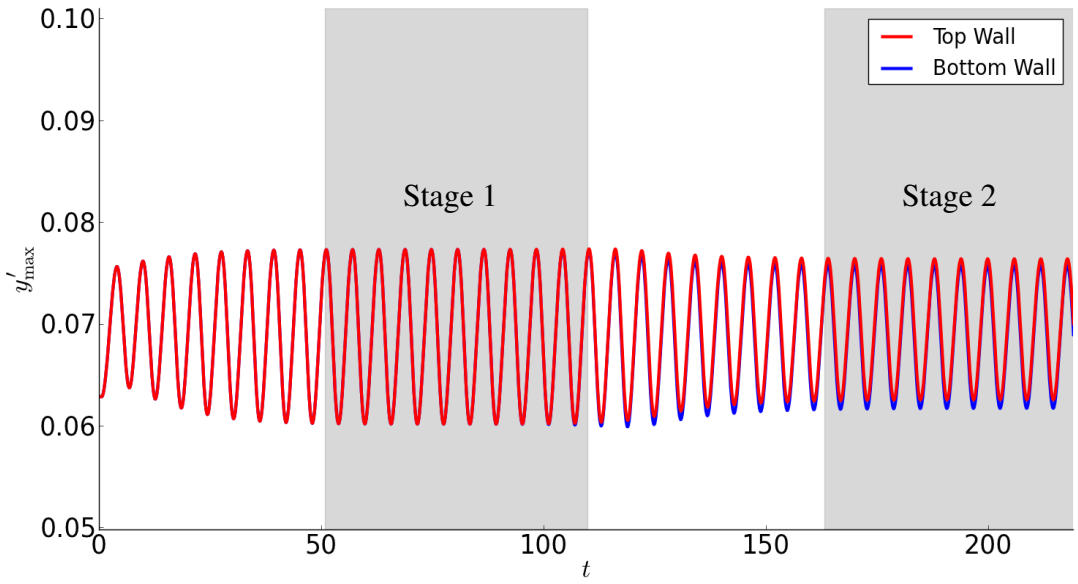

Figure 8.1 Flexible insert y'_{max} vs. time t for the top and bottom flexible insert showing two stages of saturated oscillation states.

Figure 8.1 shows the full maximum vertical displacement y'_{max} variation with time t for the upper and lower wall. Transient oscillations occur at the start following removal of P_{pturb}. The system then settles into the first saturated oscillation state with both flexible walls moving with the same form (the lower and upper wall y'_{max} lines overlay each other for $t = 50 - 110$). This is defined as the first stage of the symmetric oscillation state. This state however is not sustainable because any numerical imbalance in the fluid domain causes the flexble wall motion to transition to a second saturated oscillation state. At $t = 165$ onwards, the top wall has a slightly larger y'_{max} than the lower wall. This second state is termed the non-symmetric oscillation state and is the final state of the system.

It was also tested whether other instability forms are possible by varying the perturbation pressure P_{pturb} configurations with two additional initiation setups considered. The first configuration is with perturbation applied on one wall (perturbation applied on the top wall only with no perturbation applied on the bottom wall). The second configuration is with the same perturbation direction. The top wall perturbation is applied outward and the bottom wall perturbation applied inward. Both these configurations resulted in the same outcome of the system settling directly into the non-symmetric oscillation state. This is because the system was set up with unbalanced conditions and therefore does not transition through a symmetric state. This also shows that the final solution is robust and independent of the perturbation configuration.

The first instability state that is symmetrical along the channel mid-height is analysed in further detail. The upper flexible wall behaviour is shown in Figure 8.2. The lower flexible wall behaviour is not shown because it is simply a mirror image of the upper

wall throughout this stage. The black line is the steady-state behaviour and the red lines are the variation with time during one unstable oscillation cycle. The flexible wall shape is shown in Figure 8.2a. The flexible wall profile is skewed to the right (downstream). This is more clearly characterised with the maximum deformation location shown in Figure 8.2b with an aspect ratio of 7:20 for y' to x'. The steady-state location is at $x' = 0.765$, $y' = 0.071$. During an unstable oscillation cycle, there is both vertical and lateral movement of the flexible insert revolving counter-clockwise around the steady-state location. This movement as well as the flexible wall shape is mainly due to the interaction between the flexible insert's axial stiffness, fluid pressure (see Figure 8.2c) and viscous forces. From the pressure plot, it can also be seen the downstream section (right of $y'_{\max}$) sees the change between positive and negative pressure values. The flexible insert oscillations are pulled and pushed corresponding to the negative and positive pressure respectively.

For stage two, the top and bottom wall are no longer symmetrical with the flexible wall behaviour shown in Figure 8.3. The upper and lower flexible wall behaviour during this stage are shown in Figure 8.3a and Figure 8.3b respectively. There are only slight differences between the overall top and bottom flexible wall motion. The difference can be more clearly seen with the maximum deformation location shown in Figure 8.3c with an aspect ratio of 7:20 for y' to x'. There is both vertical and lateral movement of the flexible insert revolving counter-clockwise around the steady-state location. Both points follow roughly the same path, although the bottom wall has its maximum deformation point tending more to the right with slightly larger deformation compared to the top wall.

The pressure along the flexible insert of the top and bottom wall are shown in Figure 8.4. Corresponding to the flexible wall deformations, there are only minor differences in the pressure variations with a slightly larger variation in the bottom wall compared to the top wall. This matches with the larger motion of the bottom wall compared to the top wall.

The fluid flow behaviour over one oscillation cycle are shown in Figure 8.5 and 8.6 for the symmetric and non-symmetric stages respectively. The figures show the streamlines (white), vorticity contour lines (black) and non-dimensional pressure colour contours with a 1:5 scaling of the channel length to height dimensions. The time steps are adjusted to have $t = 0$ coincide with the minimum $y'_{\max}$ point. One oscillation cycle takes approximately $\delta t = 5.9$ for the symmetric state and $\delta t = 6.0$ for the non-symmetric state. There is an ever-present recirculation zone behind each of the flexible insert for both stages.

For the symmetric stage at $t = 0$, the vortices behind the flexible inserts are at their smallest. Through $t = 1.6$, the wall deformation grows along with the recirculation vortex. Maximum wall deformation occurs at $t = 3.2$. The recirculation vortex size however does not reduce but continues to grow and elongate at $t = 4.6$ with decreasing

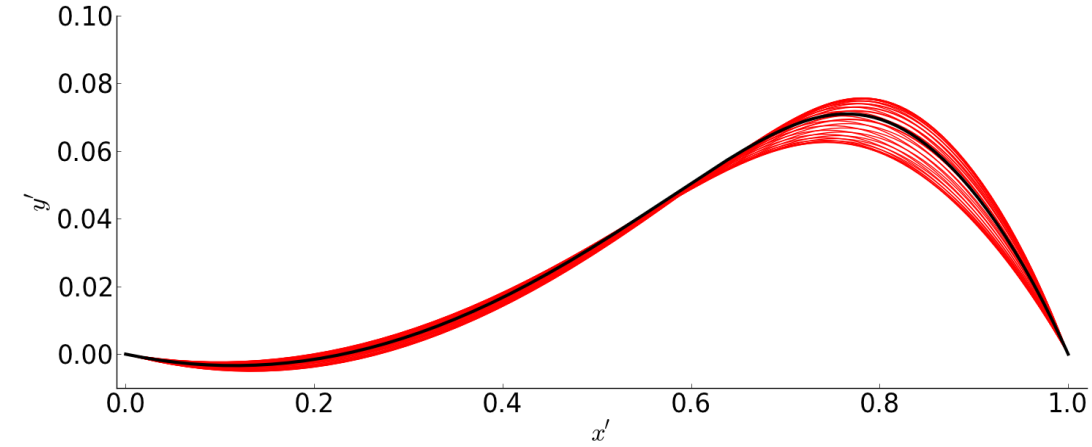

(a) Flexible insert deformation.

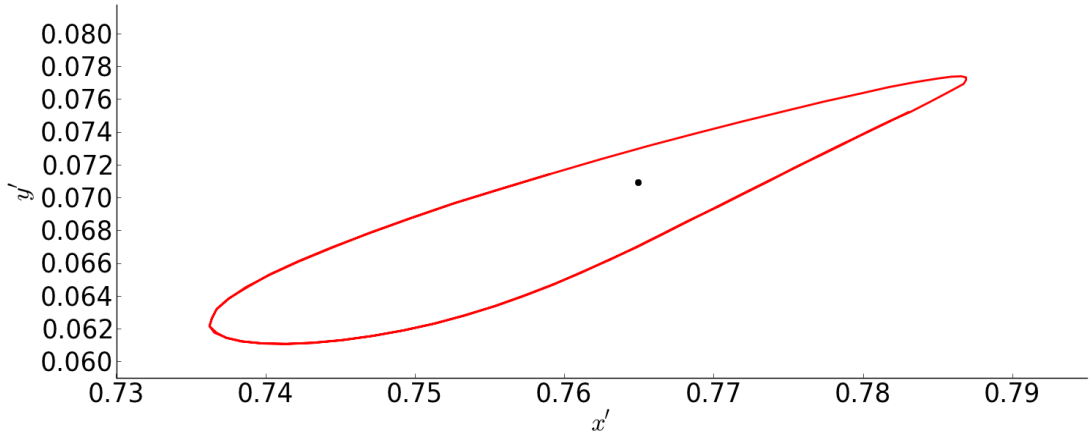

(b) Maximum deformation point.

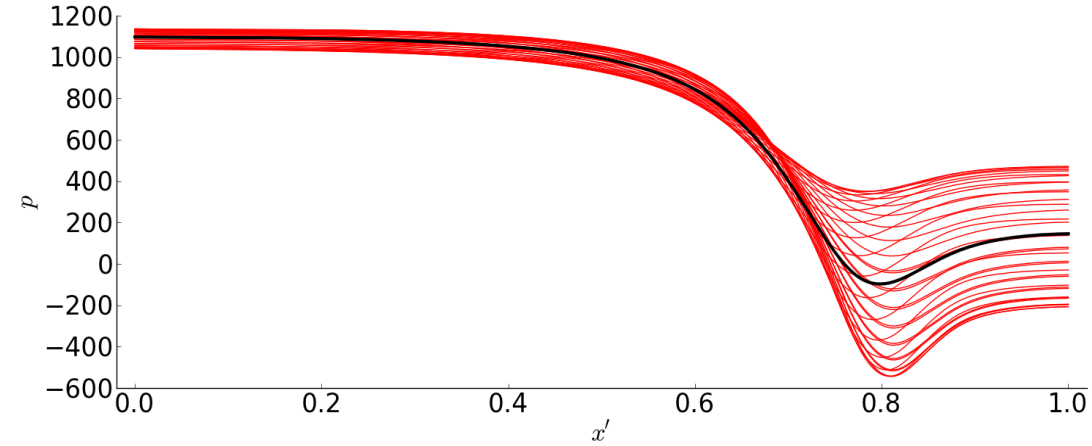

(c) Fluid pressure along flexible insert.

Figure 8.2 Stage 1 (symmetric state) top flexible insert behaviour under steady-state conditions (black line) and over one unstable oscillation cycle (red lines) for a dual flexible wall configuration unstable case at $\mathrm{Ca}_{\mathrm{eff}}.\mathrm{Re} = 1.0$, $\mathrm{Ca}_{\mathrm{eff}}/\mathrm{Re} = 10^{-4}$ and $P_{\mathrm{eff}} = 0.05$.

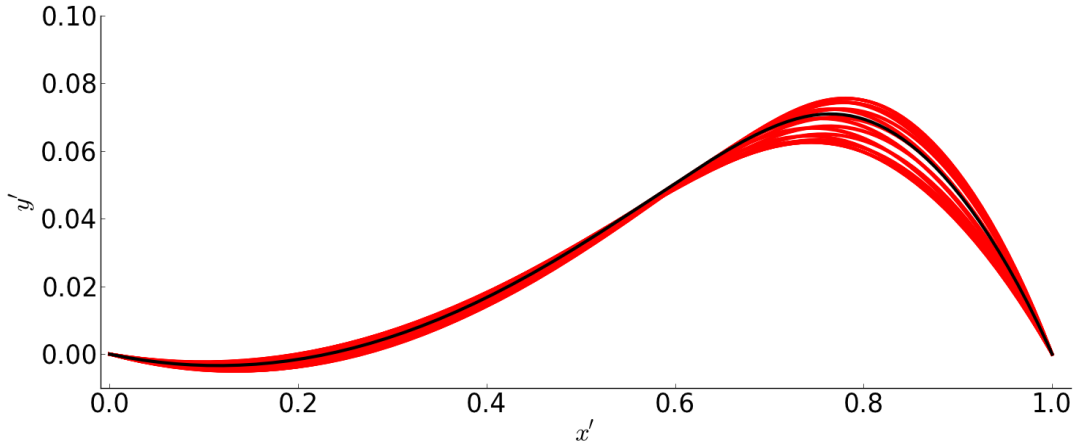

(a) Top wall deformation shape.

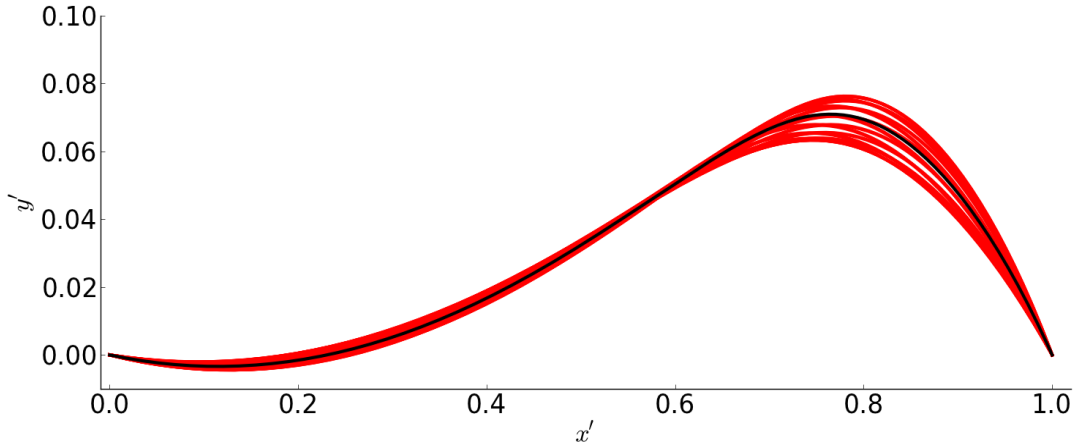

(b) Bottom wall deformation shape.

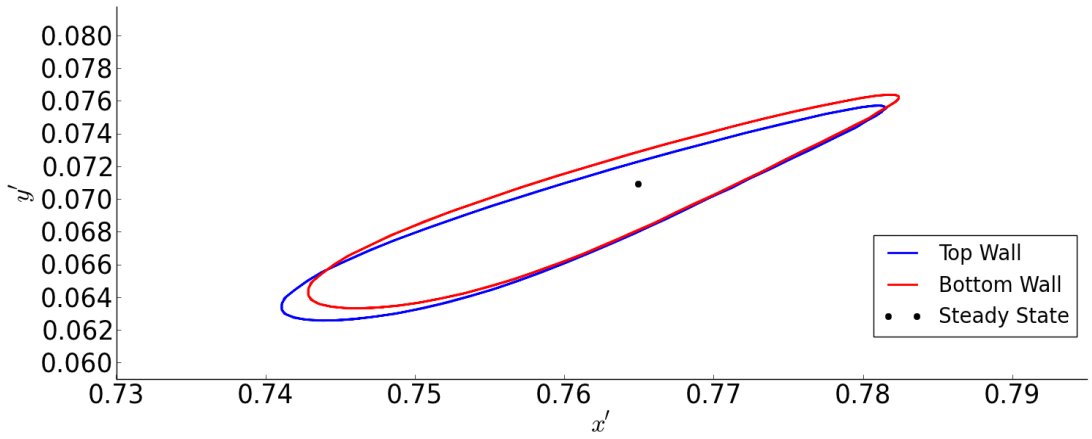

(c) Maximum deformation point of top and bottom wall.

Figure 8.3 Stage 2 (non-symmetric state) flexible wall comparison between the top and bottom wall. The steady-state conditions (black line) and over one unstable oscillation cycle (red lines) for a dual flexible wall configuration unstable case at $\mathrm{Ca}_{\mathrm{eff}}.\mathrm{Re} = 1.0$, $\mathrm{Ca}_{\mathrm{eff}}/\mathrm{Re} = 10^{-4}$ and $P_{\mathrm{eff}} = 0.05$.

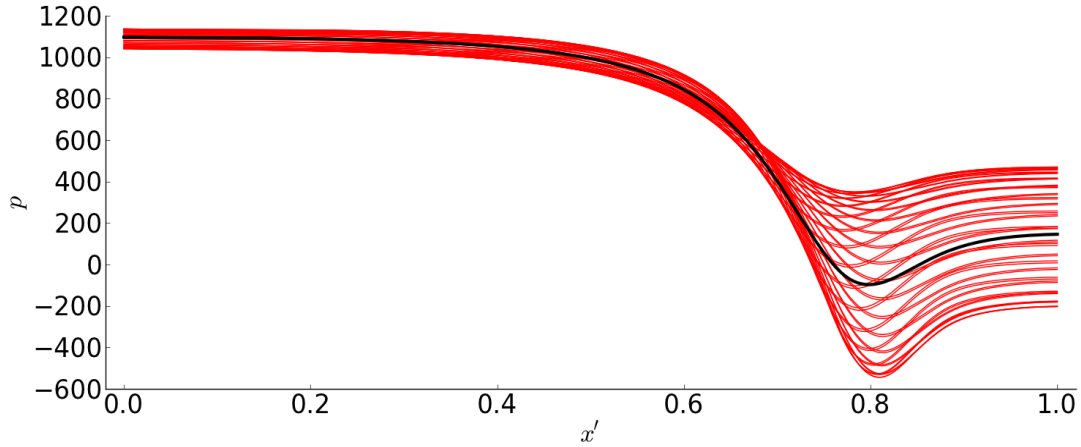

(a) Top wall deformation shape.

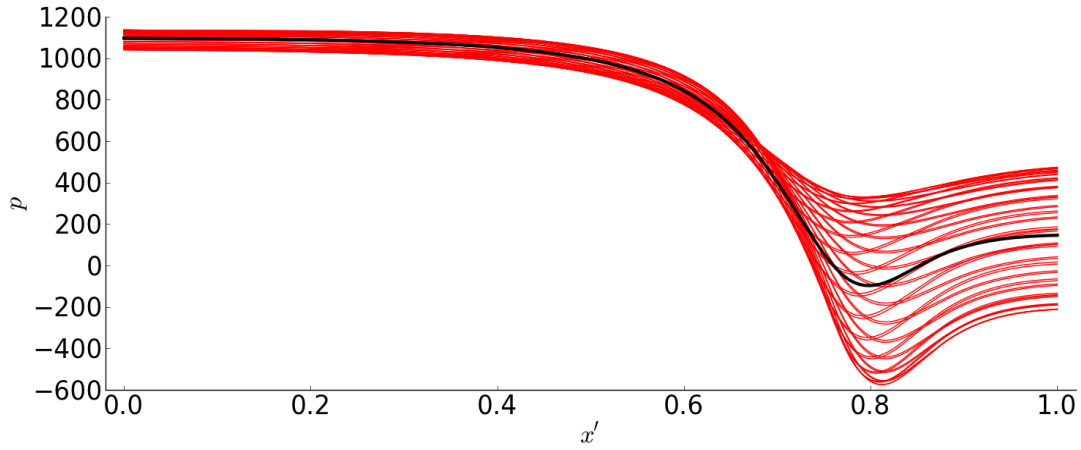

(b) Bottom wall deformation shape.

Figure 8.4 Stage 2 (non-symmetric state) pressure along the flexible inserts comparison between the top and bottom wall. The steady-state conditions (black line) and over one unstable oscillation cycle (red lines) for a dual flexible wall configuration unstable case at $\mathrm{Ca}_{\mathrm{eff}}.\mathrm{Re} = 1.0$, $\mathrm{Ca}_{\mathrm{eff}}/\mathrm{Re} = 10^{-4}$ and $P_{\mathrm{eff}} = 0.05$.

flexible wall deformation. The recirculation zone then quickly reduces at $t = 5.9$ with the minimum flexible wall deformation occuring again, completing the oscillation cycle. This form is similar to the streamline behaviour of test point D shown in Figure 7.22. The parameters for the single wall test point D are not comparable with this dual wall case. Although both cases have the same $\mathrm{Ca}_{\mathrm{eff}}$.Re, the values for $\mathrm{Ca}_{\mathrm{eff}}/\mathrm{Re}$ and P_{eff} are significantly different. In fact there was no instability observed for any combination of $\mathrm{Ca}_{\mathrm{eff}}$.Re and $\mathrm{Ca}_{\mathrm{eff}}/\mathrm{Re}$ for $P_{\mathrm{eff}} = 0.05$ of the single wall case.

For the non-symmetric stage, the vortices downstream of the top and bottom walls are different. In general, the bottom wall has a larger recirculation zone than the top wall. However, the general evolution of recirculation vortex growth and decay are similar to the symmetric state. At $t = 0$, the vortex downstream of the top wall is small with some vortex shedding further downstream. For the bottom wall, the recirculation vortex has split into two smaller vortices. At this point, both walls are at their smallest deformation. From $t = 1.5$ through to $t = 3.1$ the vortices have grown with the flexible wall deformations to their largest. This condition is unstable and the recirculation vortices begins to collapse and shed at $t = 4.5$. The oscillation cycle is complete at $t = 6.0$ with the vortex collapsed and shed. The difference in wall shape and maximum deformation point movement shown in Figure 8.3 can be attributed to the larger recirculation zone behind the bottom wall pulling the flexible insert inward and downstream compared to the smaller recirculation zone of the top wall.

8.3 Energy Budget

The dual wall dynamic behaviour is further analysed in terms of its energy budget. Figure 8.7 shows the energy budget balance for the channel fluid domain during the symmetric stage. The overall energy budget for the channel fluid and the flexible insert is shown in Figure 8.7a. The magnitudes for rate of fluid kinetic energy $\dot{KE}_{\mathrm{fluid}}$ is similar to the sum of the rates of work and energy at the domain interfaces ($\dot{KE}_{\mathrm{IO}}, \dot{W}_{\mathrm{IO}}, \dot{W}_{\mathrm{wall}}$) and the internal fluid dissipation rate $\dot{D}_{\mathrm{fluid}}$. The summation of fluid terms ($\dot{KE}_{\mathrm{IO}}$+$\dot{W}_{\mathrm{IO}}$+2$\dot{W}_{\mathrm{wall}}$+$\dot{D}_{\mathrm{fluid}}$) has been inverted to show its good match with $\dot{KE}_{\mathrm{fluid}}$. Also note that in this energy budget $\dot{W}_{\mathrm{wall}}$ is mutiplied by two due to the same contributions from the top and bottom flexible inserts. The energy component sizes as well as magnitudes are within similar ranges as the single wall case which shows the instability energy budgets are comparable. It is most similar in magnitude and form to the single wall test point D in Figure 7.26.

The individual energy components are shown in Figure 8.7b. The contributions from $\dot{KE}_{\mathrm{IO}}$ and $\dot{W}_{\mathrm{wall}}$ are small compared to $\dot{W}_{\mathrm{IO}}$ and $\dot{D}_{\mathrm{fluid}}$. This is quantitatively shown through the rate of work and energy averages (denoted by an overbar) for the fluid domain in Table 8.3. $\overline{\dot{KE}}_{\mathrm{fluid}}$ and $\overline{\dot{KE}}_{\mathrm{IO}}$ should approximate 0. The difference is attributed to numerical error. The large proportion of energy entering the system is

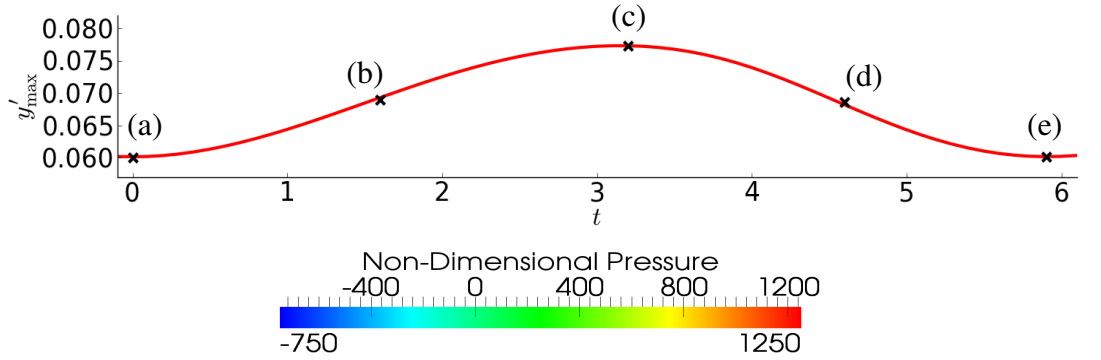

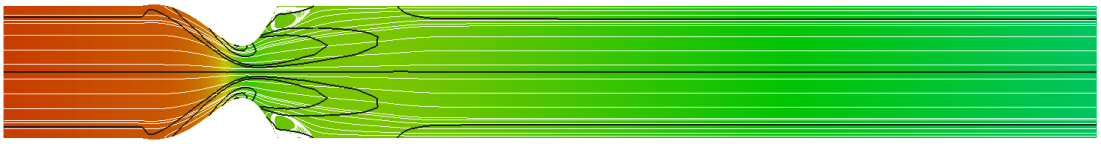

(a) $t = 0$

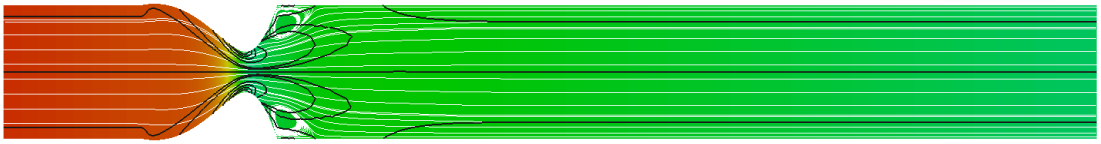

(b) $t = 1.6$

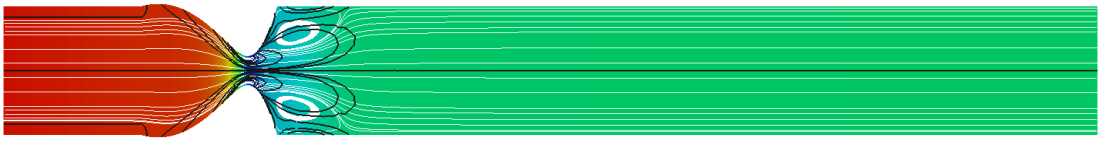

(c) $t = 3.2$

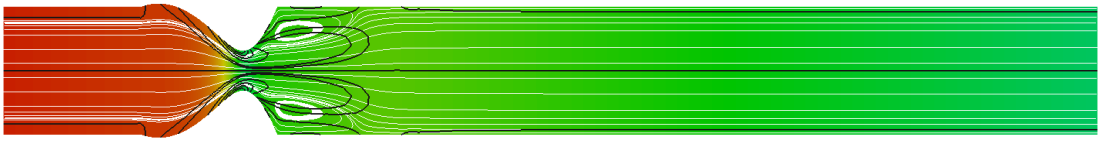

(d) $t = 4.6$

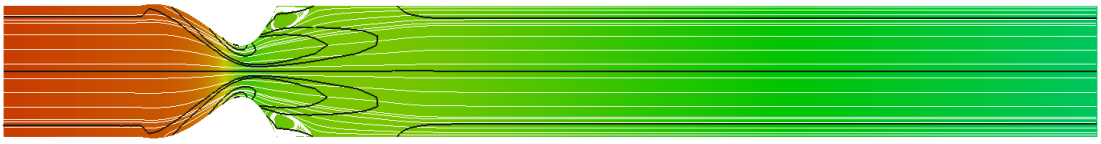

(e) $t = 5.9$

Figure 8.5 Stage 1 (symmetric state) bottom wall variation of the maximum vertical displacement y'_{max} over one unstable oscillation cycle at effective pressure $P_{eff} = 0.05$. Marked with crosses 'x' are the time steps when snapshots of the fluid domain are shown with the streamlines (white), vorticity contour (black) lines and the non-dimensional pressure (colour) contours. The fluid domain is scaled with a ratio of 1:5 (channel length to height).

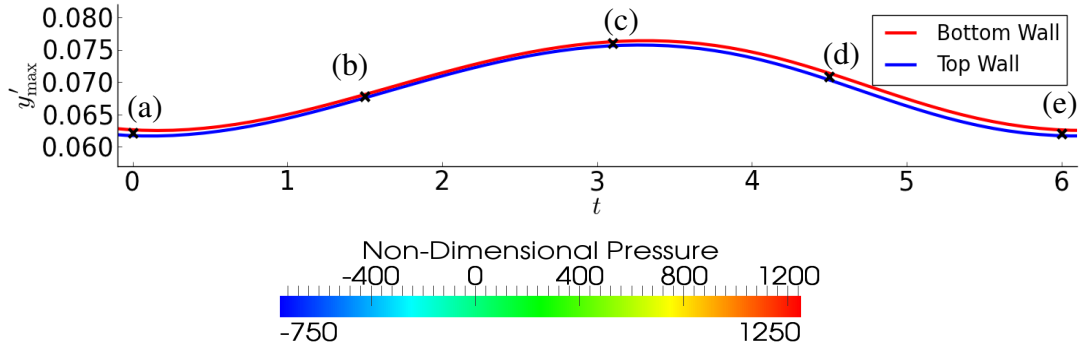

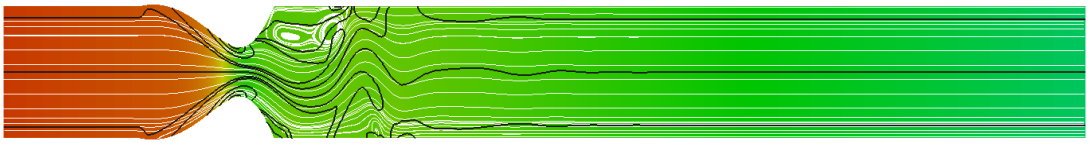

(a) $t = 0$

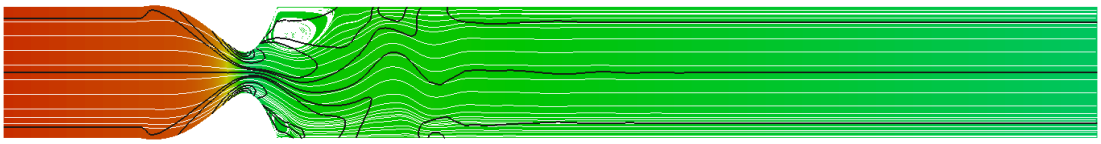

(b) $t = 1.5$

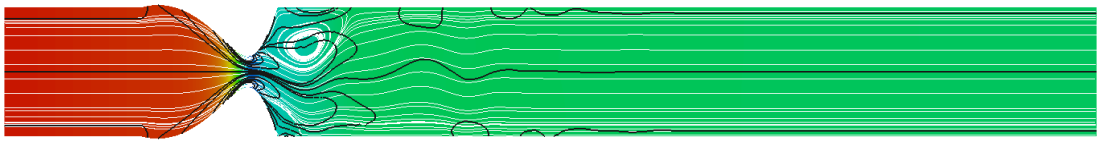

(c) $t = 3.1$

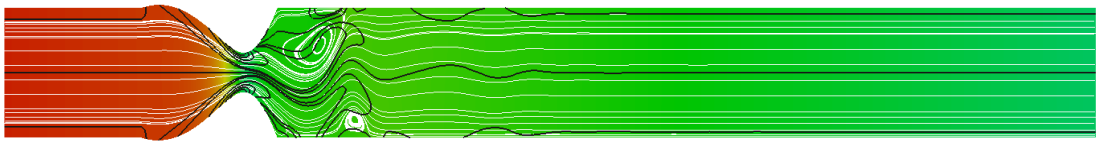

(d) $t = 4.5$

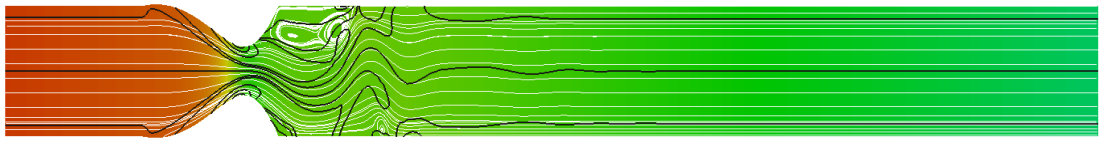

(e) $t = 6.0$

Figure 8.6 Stage 2 (non-symmetric state) upper and lower wall variation of y' over one unstable oscillation cycle for the steady-state maximum deformation point at $P_{\text{eff}} = 0.05$. Marked with crosses 'x' are the time steps when snapshots of the fluid domain are shown with the streamlines (white), vorticity contour (black) lines and the non-dimensional pressure (colour) contours. The fluid domain is scaled with a ratio of 1:5 (channel length to height).

Table 8.3 Average rates of work and energy for the overall flexible insert and channel fluid for the symmetric and non-symmetric unstable oscillation stages.

Stage	$\overline{\dot{KE}}_{\text{fluid}}$	$\overline{\dot{KE}}_{\text{IO}}$	$\overline{\dot{W}}_{\text{IO}}$	$\overline{\dot{W}}_{\text{wall,top}}$	$\overline{\dot{W}}_{\text{wall,bottom}}$	$\overline{\dot{D}}_{\text{fluid}}$
Symmetric	5.07×10^{-4}	-6.35×10^{-3}	11.5	4.85×10^{-3}	4.85×10^{-3}	-11.5
Non-Symmetric	6.10×10^{-4}	-6.77×10^{-3}	11.5	5.37×10^{-3}	5.37×10^{-3}	-11.5

through $\overline{\dot{W}}_{\text{IO}}$ and energy loss is mainly through $\overline{\dot{D}}_{\text{fluid}}$ with minor losses at $\overline{\dot{KE}}_{\text{IO}}$ and $\overline{\dot{W}}_{\text{wall}}$.

There are negligible differences in energy budget results for the overall fluid domain between the second non-symmetric stage compared to the first symmetric stage shown in Figure 8.7. Only the average energy results are shown in Table 8.3 which also do not show any significant difference compared to the symmetric stage results.

The energy balance for the flexible insert is shown in Figure 8.8 for the symmetric stage. Figure 8.8a shows the rate of energy balance between the flexible insert potential energy and rate of work on the flexible insert (inverted). The plot shown is for the top wall only as the bottom wall gives similar results. Figure 8.8b shows the individual rates of potential energy components $\dot{PE}_{\text{axial}}$ and $\dot{PE}_{\text{bend}}$. The $\dot{PE}$ contribution is dominated by $\dot{PE}_{\text{axial}}$ due to the large flexible deformation and low bending stiffness compared to axial stiffness. Figure 8.8c presents the external rates of work acting on the flexible insert that includes the external pressure $\dot{W}_{P\text{ext}}$, fluid pressure $\dot{W}_{\text{wall,p}}$, normal $\dot{W}_{\text{wall,n}}$ and tangential $\dot{W}_{\text{wall,t}}$ traction components. The major contributors are $\dot{W}_{P\text{ext}}$ and $\dot{W}_{\text{wall,p}}$ with minor contributions from $\dot{W}_{\text{wall,n}}$ and $\dot{W}_{\text{wall,t}}$. The averages of the flexible insert rates of work and energy are listed in Table 8.4 and Table 8.5. The overall largest contributors for the wall are $\dot{PE}_{P\text{axial}}$ and $\dot{W}_{P\text{ext}}$ showing the system driven by the wall stretch and the external pressure applied on the flexible insert.

The detailed non-symmetric stage results are not shown for the flexible insert energy budget as they are very similar to the results for the symmetric stage shown in Figure 8.8. This is shown through Figure 8.9 with $W_{\text{wall,top}}$ and $W_{\text{wall,bottom}}$ giving similar results during the non-symmetric stage. The average rates of work and energy are shown in Table 8.4 and Table 8.5. They are similar to the symmetric stage values with the bottom wall value generally larger and the top wall value smaller compared to the symmetric stage values. This may be attributed to the magnitude of flexible wall motion with a larger recirculation zone at the bottom wall and therefore its associated energy components are larger as well.

With the system transitioning from the symmetric to non-symmetric stage, there are some differences in the flexible wall motion and most noticeably in the streamlines. However the energy budget is very similar and it is difficult to discern any significant energy difference between the two stages. This shows the main instability mechanisms

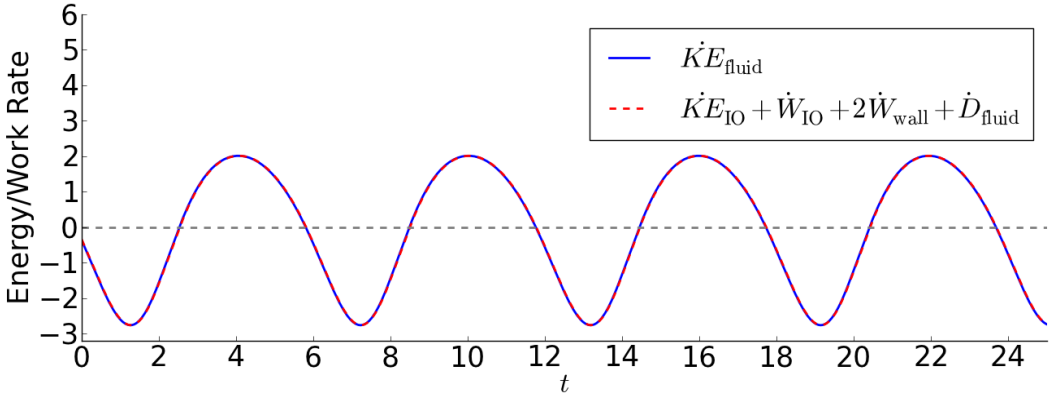

(a) Channel fluid domain kinetic energy rate KE_{fluid} matching with sum of other constituent components.

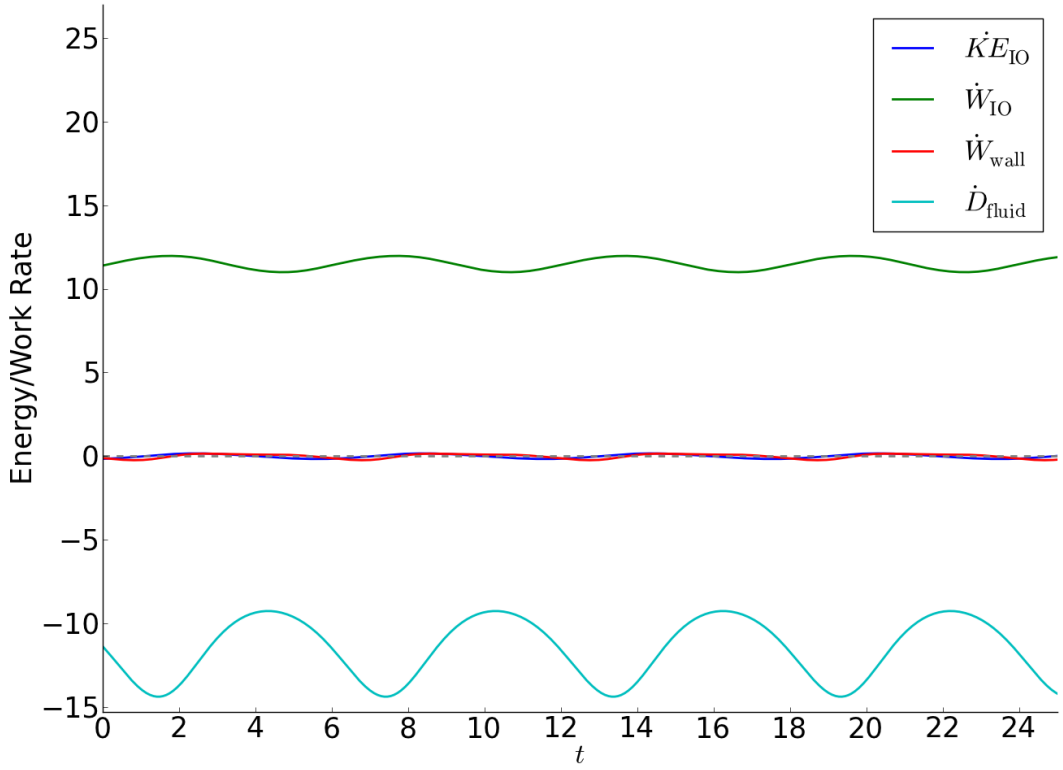

(b) Channel fluid components rate of energy vs. time

Figure 8.7 `oomph-lib` rate of work/energy plots for the channel fluid domain and its individual components.

are still the same but with a non-symmetric distribution of the bottom wall experiencing larger motions than the top wall.

Table 8.4 Average rates of potential energy for the dual flexible inserts.

Stage	$\overline{\dot{PE}}_{\text{axial}}$	$\overline{\dot{PE}}_{\text{bend}}$
Symmetric	-1.45×10^{-2}	-2.93×10^{-5}
Non-Symmetric Top Wall	-9.37×10^{-3}	-1.60×10^{-5}
Non-Symmetric Bottom Wall	-9.93×10^{-3}	-1.70×10^{-5}

8.4 Dual Flexible Insert Non-Dimensional Scheme

Instability was shown to occur for the dual wall configuration with $P_{\text{eff}} = 0.05$, $\text{Ca}_{\text{eff}}/\text{Re} = 1.0 \times 10^{-4}$ and $\text{Ca}_{\text{eff}}.\text{Re} = 1.0$. It was also shown that the instability behaviour most closely resemble test point D of the single wall which has significantly different non-dimensional values as listed in Table 7.5. Therefore no relationship can be established between the single and dual wall configurations in terms of the specific non-dimensional values in predicting system stability based on single wall data. However, the non-dimensional scheme created for the single wall case proves to be suitable for characterising the steady-state and dynamic behaviour. Further testing is performed to verify whether it is possible to extend the same non-dimensionalisation scheme and system parameterisation for the dual wall system. Two stages of verification are performed, considering the static steady-state system and dynamic system oscillations of an unstable case. These are explained in the following sub-sections.

8.4.1 Dual Flexible Insert Static Non-Dimensional Verification

The non-dimensional scheme consists of three parameters; P_{eff}, $\text{Ca}_{\text{eff}}.\text{Re}$ and $\text{Ca}_{\text{eff}}/\text{Re}$. The verification method is the same as for the single flexible insert case described in Section 6.2. The three non-dimensional parameters are kept constant and the dimensional terms within them are varied. The test case dimensional and non-dimensional

Table 8.5 Average rates of work and energy for the dual flexible inserts.

Stage	$\overline{\dot{W}}_{\text{wall,p}}$	$\overline{\dot{W}}_{\text{wall,n}}$	$\overline{\dot{W}}_{\text{wall,t}}$	$\overline{\dot{W}}_{P\text{ext}}$
Symmetric	4.18×10^{-3}	1.92×10^{-4}	4.85×10^{-4}	1.02×10^{-2}
Non-Symmetric Top Wall	4.91×10^{-3}	1.51×10^{-4}	3.04×10^{-4}	2.44×10^{-2}
Non-Symmetric Bottom Wall	6.29×10^{-3}	1.99×10^{-4}	2.53×10^{-4}	4.45×10^{-2}

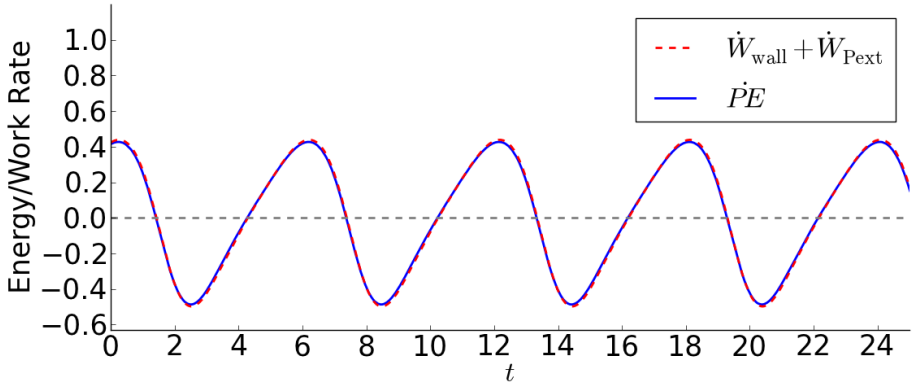

(a) Flexible wall overall rate of work.

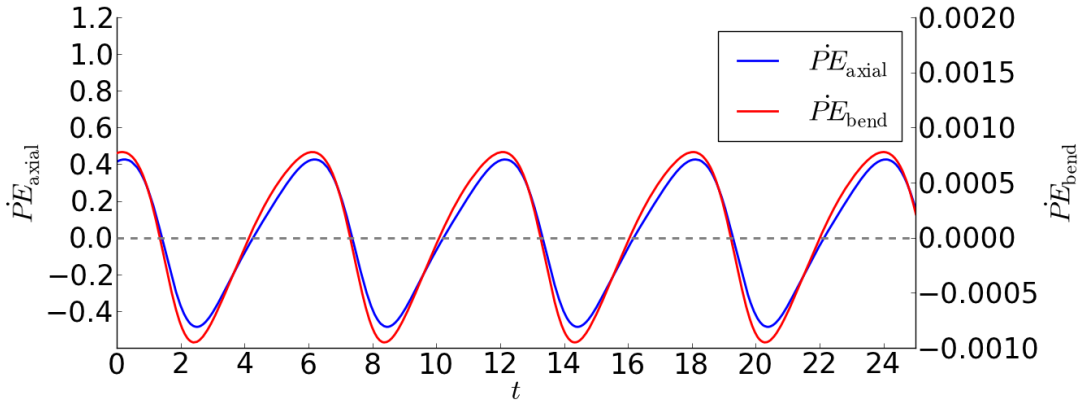

(b) Flexible wall rate of potential energy components.

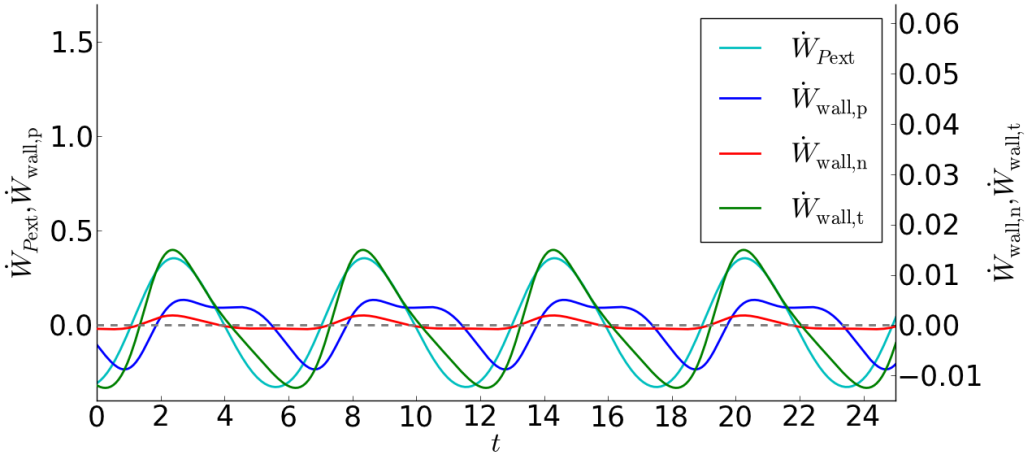

(c) Flexible wall rate of external work categorised into the pressure, and normal and tangential traction components.

Figure 8.8 Rate of work/energy plots for the dual flexible insert and its individual components.

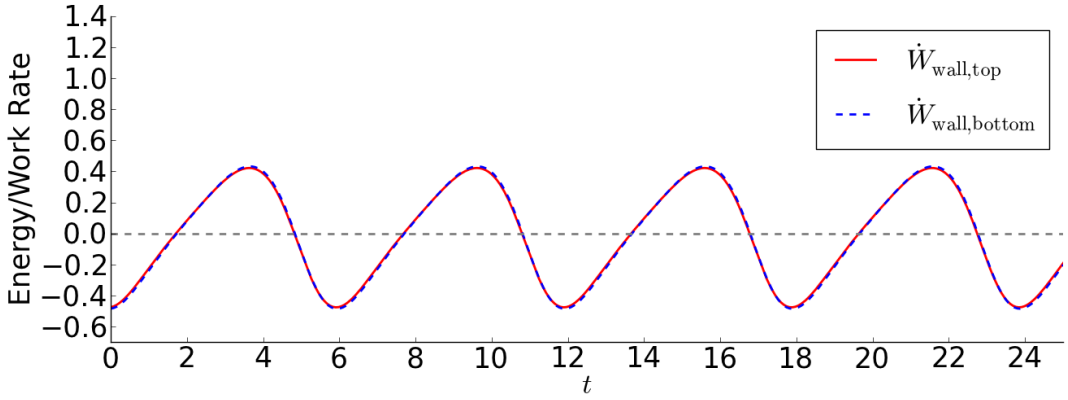

Figure 8.9 Flexible insert rate of work comparison between top and bottom wall.

Table 8.6 Dual wall configuration non-dimensional scheme validation variations.

Variation Number	Dimensional Parameters							
	$L^*_{\text{flex}} + L^*_{\text{down}}$ (m)	H^* (m)	h^* (m)	ρ^* (kg/m^3)	μ^* (Pa.s)	E^* (MPa)	U^* (m/s)	P^*_{ext} (Pa)
V-1	-	-	0.1	-	-	100	-	-
V-2	-	-	-	10	-	1	0.1	0.1
V-3	-	-	-	100	10	-	0.1	-
V-4	5	5	-	0.2	-	-	-	0.2
V-5	2	2	-	0.125	-	40	4	2
V-6	2	-	-	-	20	2	-	-

parameters are the same as in Table 8.1 and $P_{\text{eff}} = 0.05$ with the internal variations as listed in Table 8.6.

The static flexible wall shape is shown in Figure 8.10 for variations V-1 to V-6. Only the bottom wall shape is shown as the top wall has the same profile. The flexible wall shapes are very similar in all variations of internal dimensional parameter instances. The y'_{max} and associated x'_{max} of Figure 8.10 are listed in Table 8.7. The maximum difference for y'_{max} and x'_{max} are 0.006% and 0.001% respectively. The y'_{max} difference is larger than x'_{max} as there is little variation along the horizontal direction and large wall deformation in the vertical direction. Overall, these differences are deemed small enough to be treated insignificant and the non-dimensional scheme is considered suitable to characterise a unique static flexible insert shape.

Sample steady-state fluid domain plots for the base case and sensitivity cases V-3 and V-6 are shown in Figure 8.11. It can be seen all three cases show similar fluid flow behaviour. Therefore it is considered suitable to characterise the steady-state large deformation dual wall flexible insert channel flow system using the three non-dimensional parameters; $\text{Ca}_{\text{eff}}.\text{Re}$, $\text{Ca}_{\text{eff}}/\text{Re}$ and P_{eff}.

It is also worthwhile to analyse the effects of each of the non-dimensional parameters on the system. Sensitivity testing is performed on these non-dimensional parameters

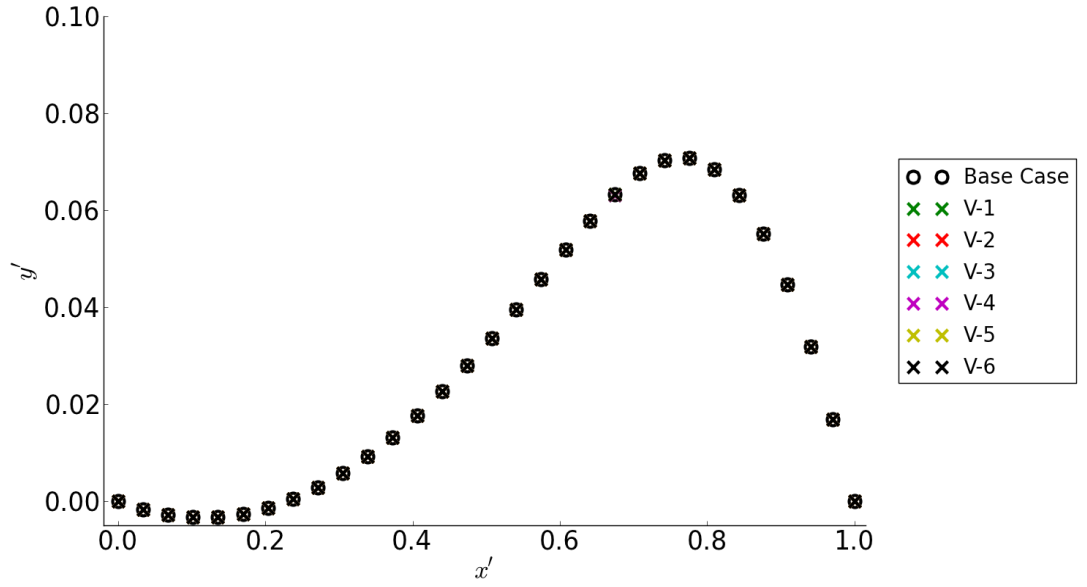

(a) Flexible insert deformation.

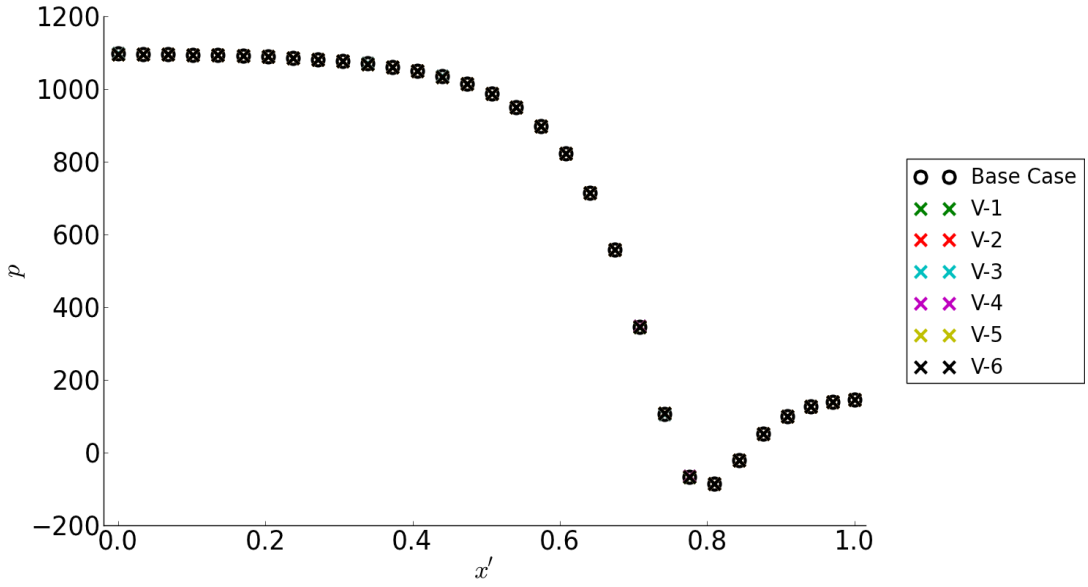

(b) Fluid pressure along flexible insert.

Figure 8.10 Flexible insert behaviour for non-dimensional scheme verification keeping parameters $\mathrm{Ca}_{\mathrm{eff}}.\mathrm{Re} = 1.0$, $\mathrm{Ca}_{\mathrm{eff}}/\mathrm{Re} = 10^{-4}$ and $P_{\mathrm{eff}} = 0.05$ constant while varying internal dimensional parameters. The base case and variations V-1 to V-6 are overlaid on each other.

Table 8.7 Maximum deformation and percentage difference results for dual wall configuration static non-dimensional scheme verification.

Variation Number	y'_{max}	x'_{max}	Difference (y'_{max}, x'_{max})
Base case	0.070827	0.74211	N/A
V-1	0.070832	0.74212	0.006%, 0.001%
V-2	0.070827	0.74211	0.000%, 0.000%
V-3	0.070827	0.74211	0.000%, 0.000%
V-4	0.070832	0.74212	0.006%, 0.001%
V-5	0.070830	0.74212	0.005%, 0.001%
V-6	0.070831	0.74212	0.005%, 0.001%

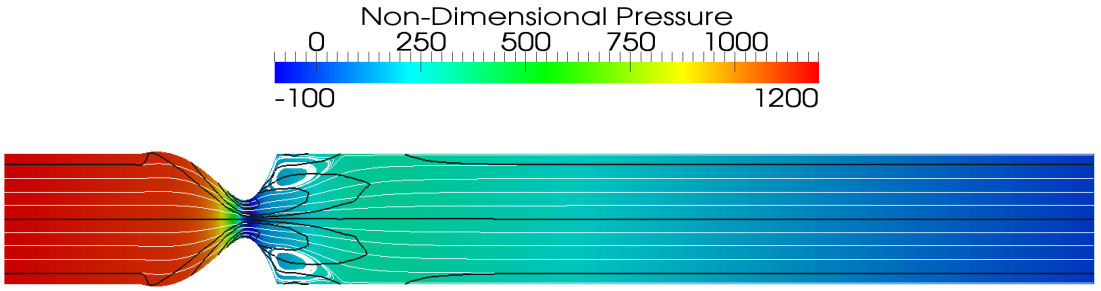

(a) Base case

(b) V-3

(c) V-6

Figure 8.11 Dual wall flexible insert channel fluid streamlines (white) and vorticity contour (black) lines and non-dimensional pressure colour contours for steady-state (static) non-dimensional scheme verification comparing the base case and variation test cases V-3 and V-6. The fluid domain is scaled with a ratio of 1:5 (channel length to height).

Table 8.8 Non-dimensional scheme sensitivity variations for the dual wall configuration.

Sensitivity Number	Parameter Tested	Dimensional Parameter Ratio ($\times$ Base case)					
		$L^*_{flex}+L^*_{down}$ (m)	H^* (m)	ρ^* (kg/m^3)	E^* (MPa)	U^* (m/s)	P^*_{ext} (Pa)
S-1	$0.5P_{eff}$	0.5	-	-	5	-	0.5
S-2	$2P_{eff}$	2	-	-	20	-	2
S-3	$0.5Ca_{eff}/Re$	2	-	$\sqrt{2}$	40	-	2
S-4	$2Ca_{eff}/Re$	0.5	-	$\sqrt{0.5}$	2.5	-	0.5
S-5	$0.5Ca_{eff}.Re$	2	2	$\sqrt{128}$	40	4	2
S-6	$2Ca_{eff}.Re$	2	2	$\sqrt{32}$	40	4	2
S-7	$0.2Ca_{eff}.Re$	2	2	$\sqrt{320}$	40	4	2
S-8	$5Ca_{eff}.Re$	2	2	$\sqrt{3.2}$	40	4	2

to determine the relative importance between all three terms. For each instance, two parameters are kept constant and the third altered to determine its effect on the system. The variable parameters are doubled and halved in the first test. If no significant changes occur, they are multiplied and divided by a factor of five. The specific test parameters are listed in Table 8.8.

Results of the P_{eff} and Ca_{eff}/Re parameter sensitivity tests are shown in Figure 8.12. There is significant difference in wall shape between the base case and the $0.5P_{eff}$ and $2P_{eff}$ (cases S-1 and S-2 respectively) as well as for the Ca_{eff}/Re sensitivities (cases S-3 and S-4). The pairings of cases S-1 and S-4, and cases S-2 and S-3 exhibit similar flexible deformation shapes even though they are varying different parameters because they cause the same change in ratio of flexible insert stiffness and external pressure relative to fluid pressure. It is also noted all these sensitivity cases give different flexible wall shapes and pressure profiles along the flexible insert as compared with the base case as seen in Figure 8.12. Therefore, these parameters are unique and need to be treated separately.

The Ca_{eff}/Re sensitivity test in Figure 8.13 shows that the flexible wall shape is similar for 0.5 and 2.0 times Ca_{eff}/Re as well as when 0.2 and 5 Ca_{eff}/Re is tested. This is quantified by determining the maximum deflection point as listed in Table 8.9. It is deemed that the difference in Ca_{eff}/Re is small enough to simply collapse all Ca_{eff}/Re values into a single representative data point. This may be extended to produce a single 2-D plot with variation of P_{eff} and $Ca_{eff}.Re$ to characterise the two flexible wall system as was done for the single flexible wall in Section 6.3. The trends for these sensitivities are similar to those of the sensitivity tests of the single wall in Section 6.3.

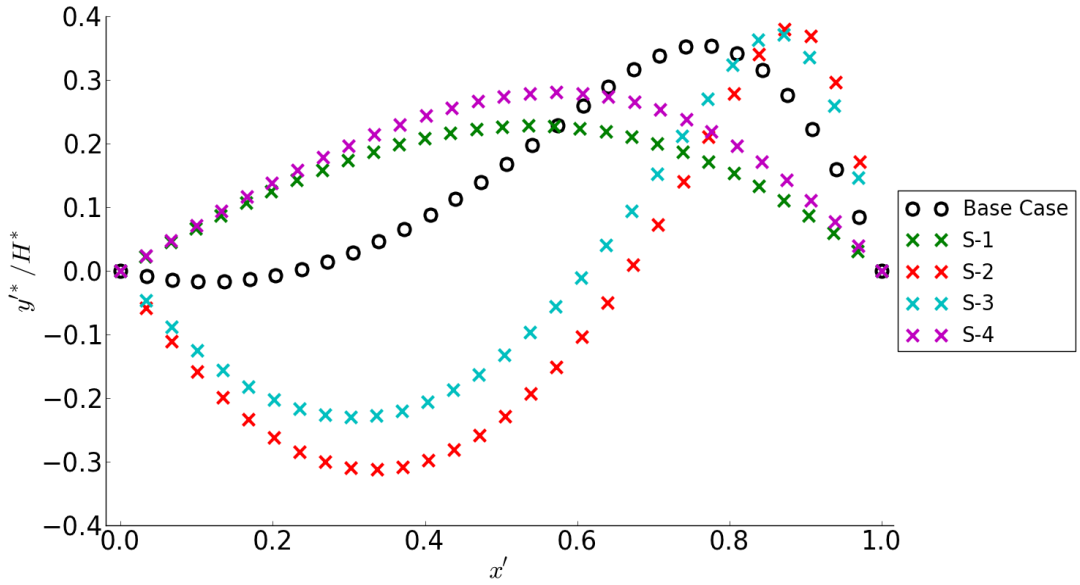

(a) Flexible insert steady-state shapes with y' (H^*-normalised).

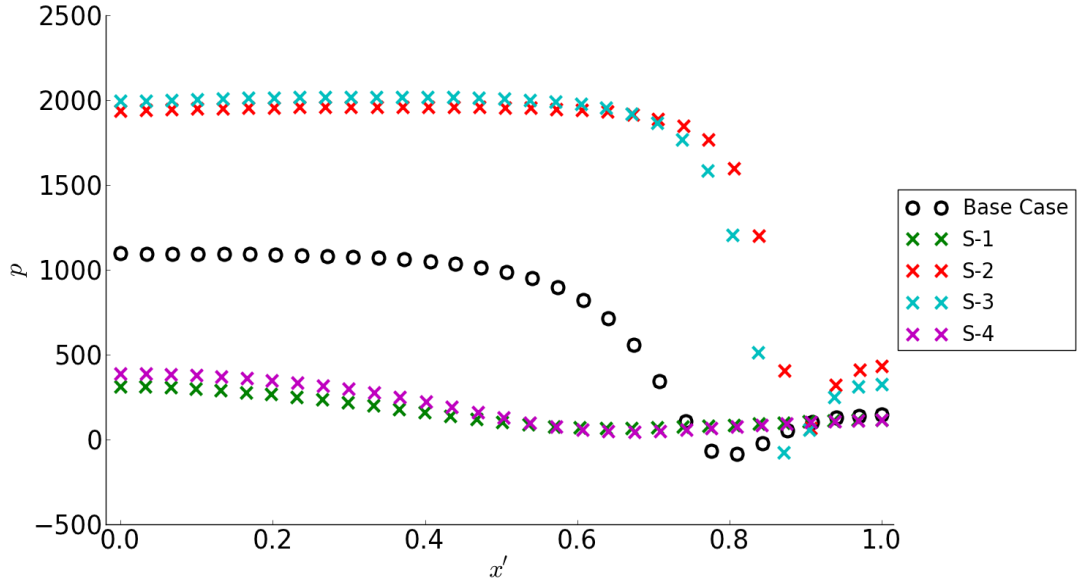

(b) Fluid pressure along flexible insert.

Figure 8.12 Flexible insert deformation and pressure behaviour for non-dimensional scheme sensitivity test cases S-1 to S-4 comparison with base case.

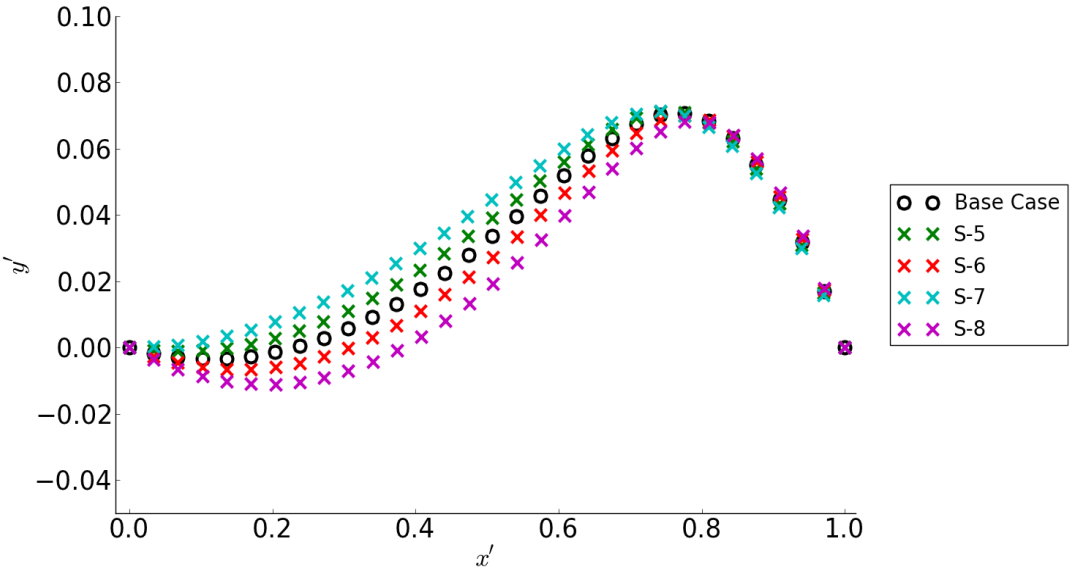

(a) Flexible insert steady-state shapes.

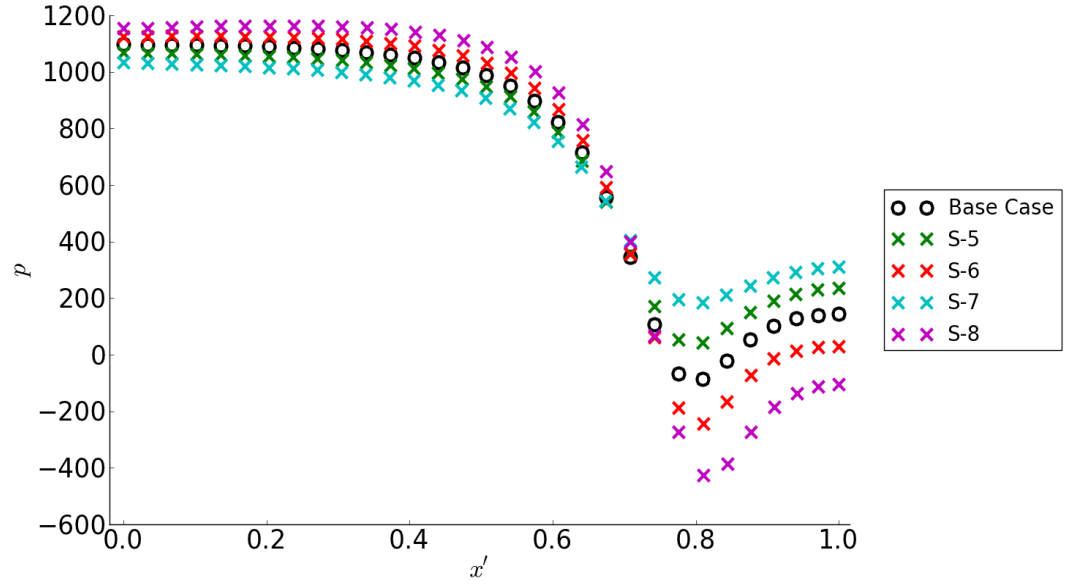

(b) Fluid pressure along flexible insert.

Figure 8.13 Flexible insert deformation and pressure behaviour for non-dimensional scheme sensitivity test cases S-5 to S-8 comparison with base case.

Table 8.9 Non-dimensional scheme sensitivity results for the dual wall configuration.

Variation Number	y'_{max}	x'_{max}	y'_{max} Error (%)	x'_{max} Error (%)
Base case	0.070827	0.74211	N/A	N/A
S-5	0.071301	0.74199	0.67	0.02
S-6	0.070110	0.77612	1.01	4.58
S-7	0.071305	0.74172	0.68	0.05
S-8	0.068141	0.77607	3.79	4.58

Table 8.10 Dual wall dynamic non-dimensional scheme validation results.

Variation Number	f	A_{max}	f Error (%)	A_{max} Error (%)
Base case	0.16728	0.01394	N/A	N/A
V-1	0.16725	0.01370	0.02	1.7
V-2	0.16736	0.01391	0.04	0.2
V-3	0.16724	0.01401	0.03	0.5
V-4	0.16732	0.01372	0.02	1.6
V-5	0.16734	0.01378	0.03	1.2
V-6	0.16721	0.01378	0.04	1.2

8.4.2 Dual Flexible Insert Dynamic Non-Dimensional Verification

The non-dimensional scheme is assessed for its suitability in describing the system dynamic behaviour and ensuring consistency in predicting unstable behaviour. The non-dimensional parameters (Ca_{eff}.Re, Ca_{eff}/Re and P_{eff}) are again kept constant while (dimensional) variations are performed internally within the three non-dimensional parameters. Dynamic simulations are performed to check for the peak-to-peak amplitude A_{max} and oscillation frequencies f. Specific dimensional and non-dimensional parameters are the same as the initial dual wall stability test in Table 8.1 with $P_{eff} = 0.05$ for an unstable case. Internal dimensional parameter variations are given in Table 8.6; *i.e.* the same as for the static non-dimensional scheme verification.

The maximum vertical displacement y'_{max} time history is shown in Figure 8.14 for the top wall during the second non-symmetric stage. All variations show similar oscillation forms and periods with the base case. The time history results are adjusted to have the fully developed instability y'_{max} trough coincide at $t = 0$. The transient period is neglected for easier comparison between the various variation cases. The quantitative comparison for instability is listed in Table 8.10. The f and A_{max} results are similar with the base case with a maximum difference of just 0.04% and 1.6% respectively.

More detail of the dynamic system comparison can be obtained by observing the system changes over one instability oscillation cycle in terms of the flexible wall deformation in Figure 8.15 and pressure along the flexible insert in Figure 8.16. The

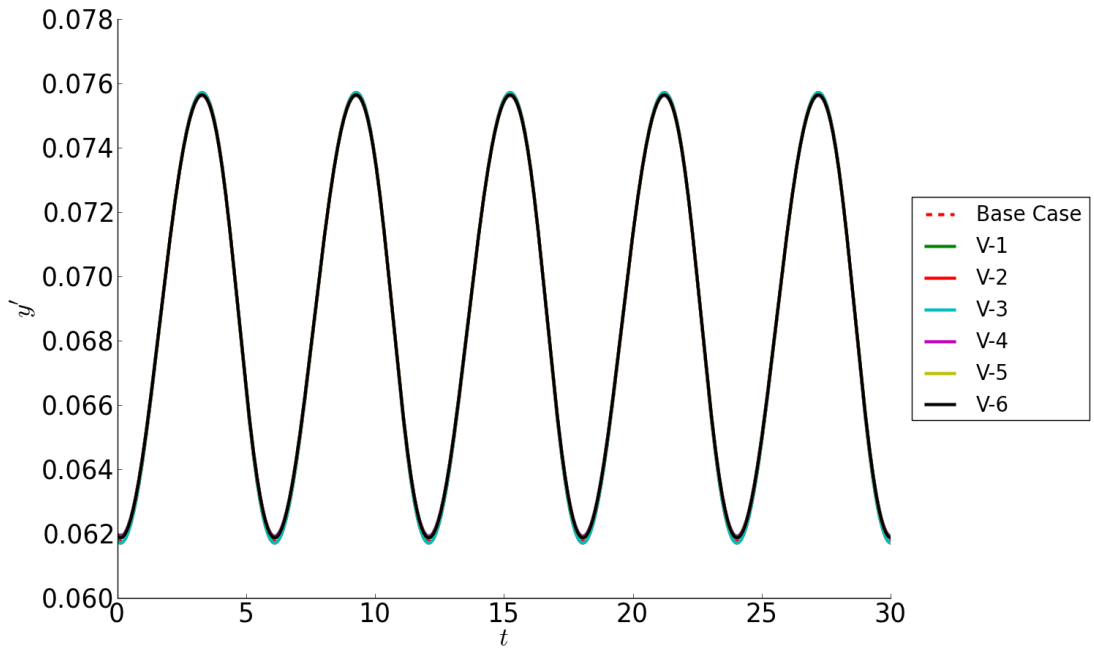

Figure 8.14 Flexible insert top wall maximum vertical displacement y'_{max} time history for non-dimensional scheme verification keeping parameters $\text{Ca}_{\text{eff}}.\text{Re} = 1.0$, $\text{Ca}_{\text{eff}}/\text{Re} = 10^{-4}$ and effective prssure $P_{\text{eff}} = 0.05$ constant while varying internal dimensional parameters. The base case and variation cases V-1 to V-6 are overlaid on each other.

black line denotes the system steady-state condition and the red lines the variation over one oscillation period. Comparing the base case and sample variation cases V-3 and V-6, the differences in terms of flexible insert shape and pressure along the flexible insert are not easily distinguishable. The dynamic behaviour is therefore deemed similar and the non-dimensional scheme is suitable for characterising the dual wall dynamic instability behaviour.

Sensitivity tests performed on the static configuration showed the flexible insert deformation to be dependent on P_{eff} and $\text{Ca}_{\text{eff}}/\text{Re}$. It was however insensitive to $\text{Ca}_{\text{eff}}.\text{Re}$ variations. It is therefore of interest to determine the difference in dynamic behaviour due to changes in $\text{Ca}_{\text{eff}}.\text{Re}$. The sensitivity cases S-7 and S-8 applied varying $\text{Ca}_{\text{eff}}.\text{Re}$ by factors of 0.2 and 5 respectively. Figure 8.17 shows the y'_{max} time history showing the system from start-up. Case S-7 is actually stable and settles into its static shape. The base case and case S-8 settle into the unstable saturated oscillation states. The different dynamic oscillation behaviour over one period are shown in terms of the flexible wall deformation and pressure along the flexible insert in Figures 8.18 and 8.19 respectively. Both the oscillation magnitude and pressure variation can be seen to be larger in case S-8 compared to the base case.

The dynamic differences are quantified in Table 8.11 between the base case and case S-8. The differences in A_{max} and f are 25.7% and 60.0% respectively. Therefore

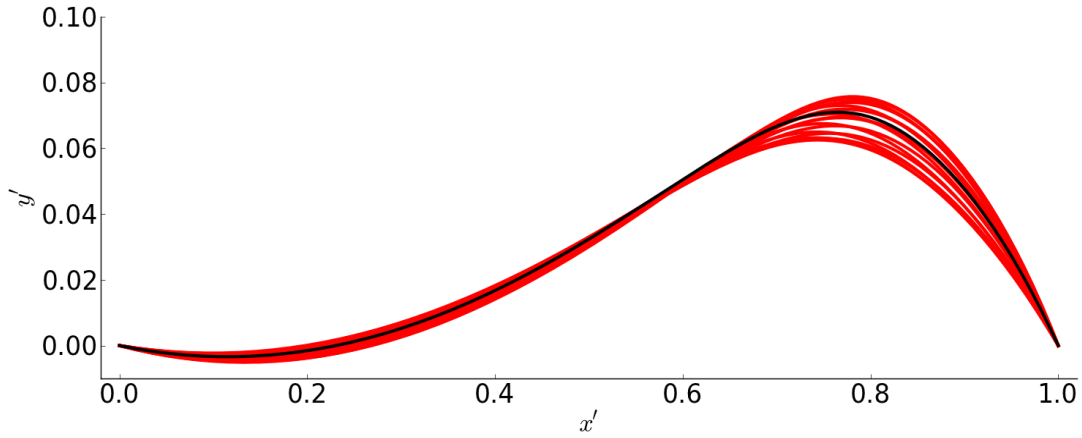

(a) Base case

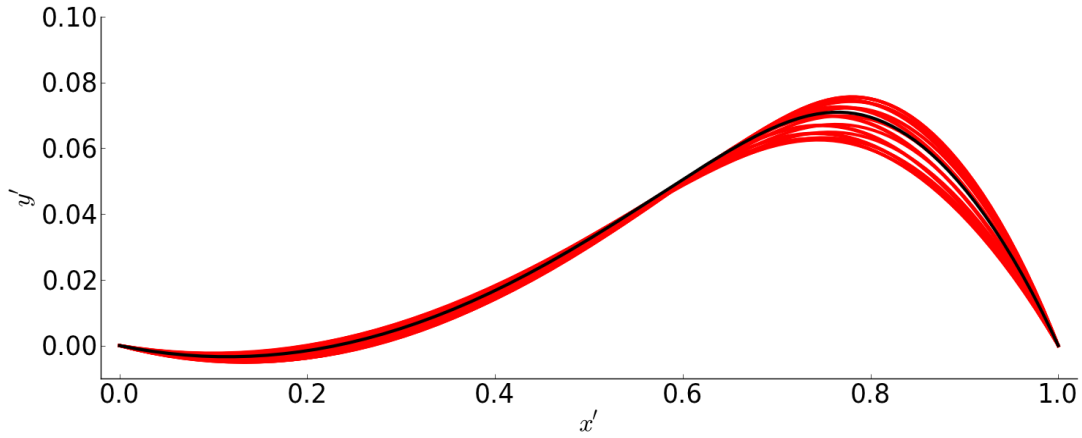

(b) V-3

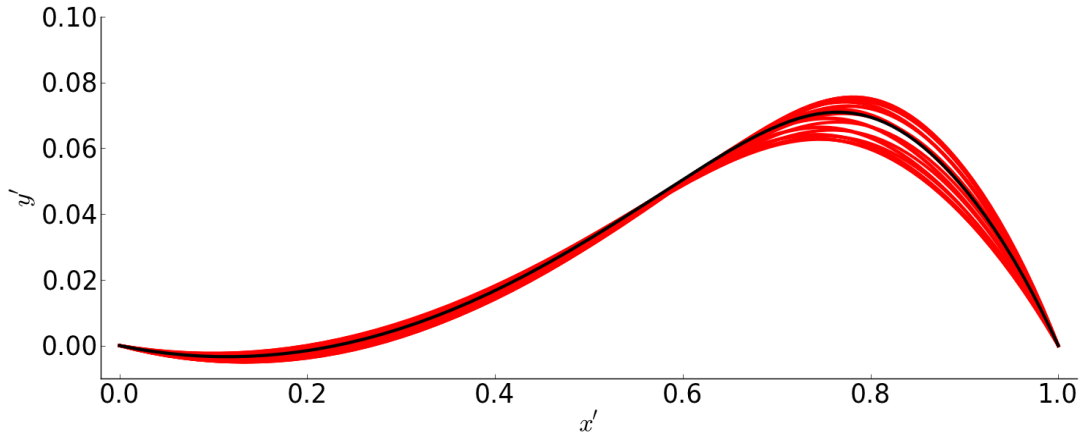

(c) V-6

Figure 8.15 Dual wall flexible insert deformation shape during steady-state (black line) and dynamic instability over one oscillation period (red lines) comparing the base case and sample variation test cases V-3 and V-6.

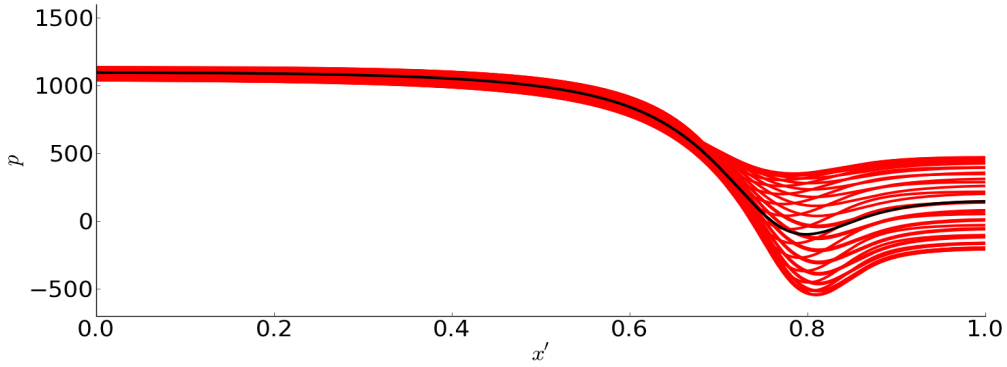

(a) Base case

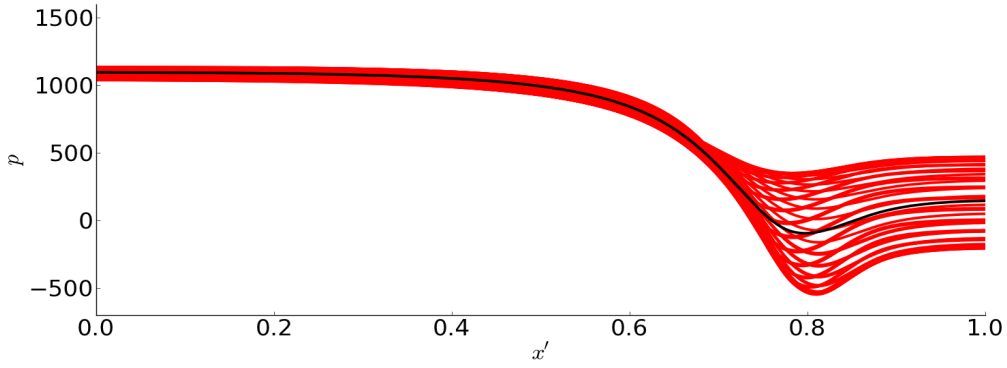

(b) V-3

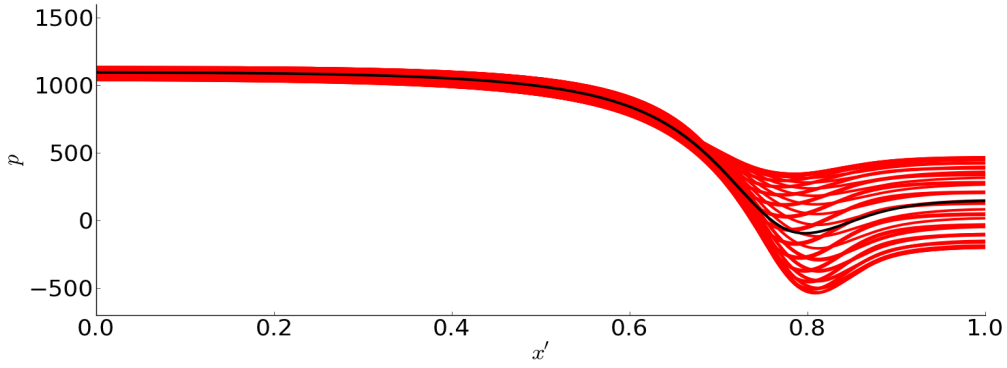

(c) V-6

Figure 8.16 Pressure p along the dual wall flexible insert during steady-state (black line) and dynamic instability over one oscillation period (red lines) comparing the base case and sample variation test cases V-3 and V-6.

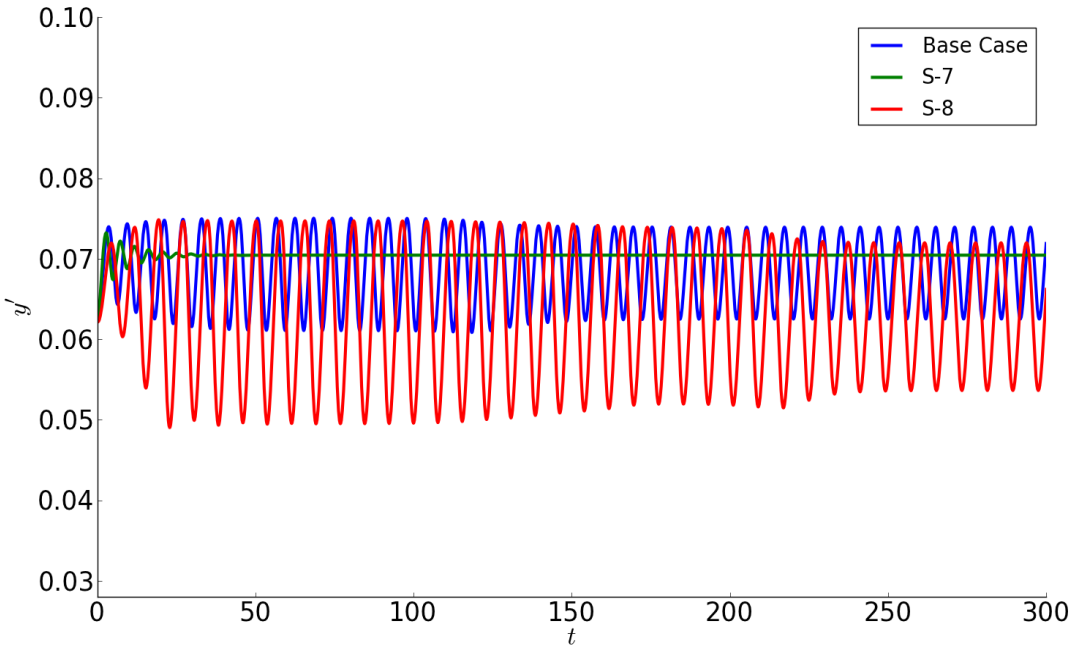

Figure 8.17 Transient oscillations of the flexible insert maximum vertical displacement y'_{max} vs. time t for the base case (unstable) and cases S-7 (stable) and S-8 (unstable).

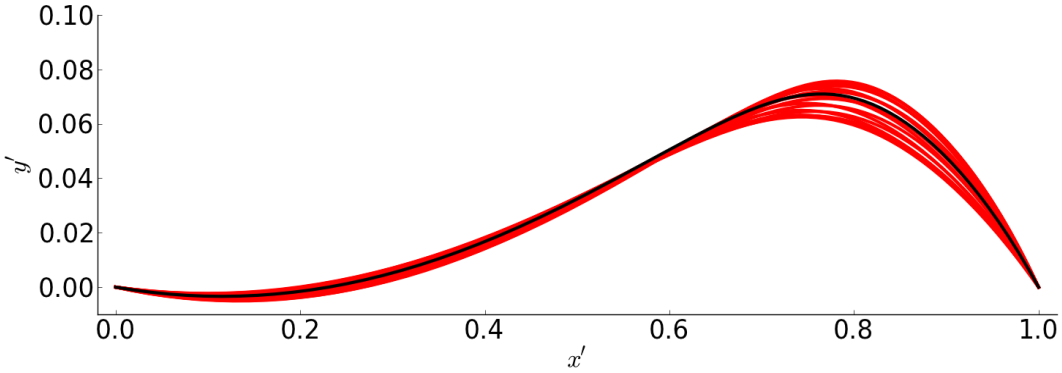

(a) Base case

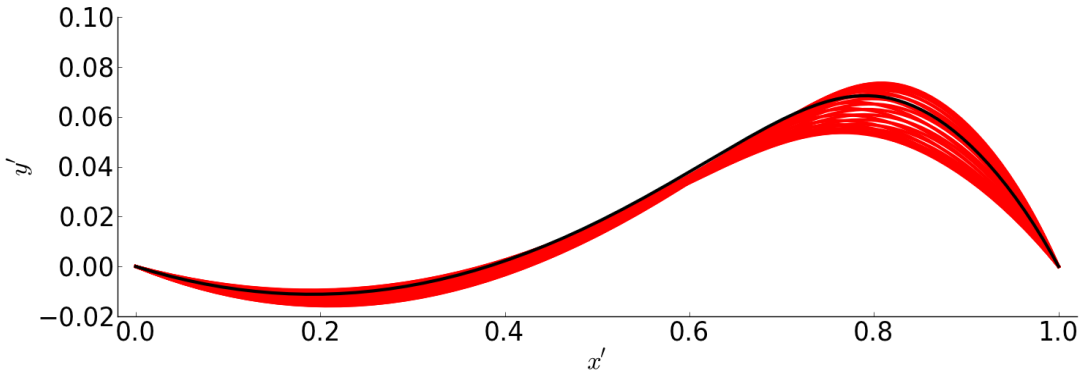

(b) Case S-8

Figure 8.18 Dual wall flexible insert deformation shape during steady-state (black line) and dynamic instability over one oscillation period (red lines) comparing the base case and unstable sensitivity test case S-8.

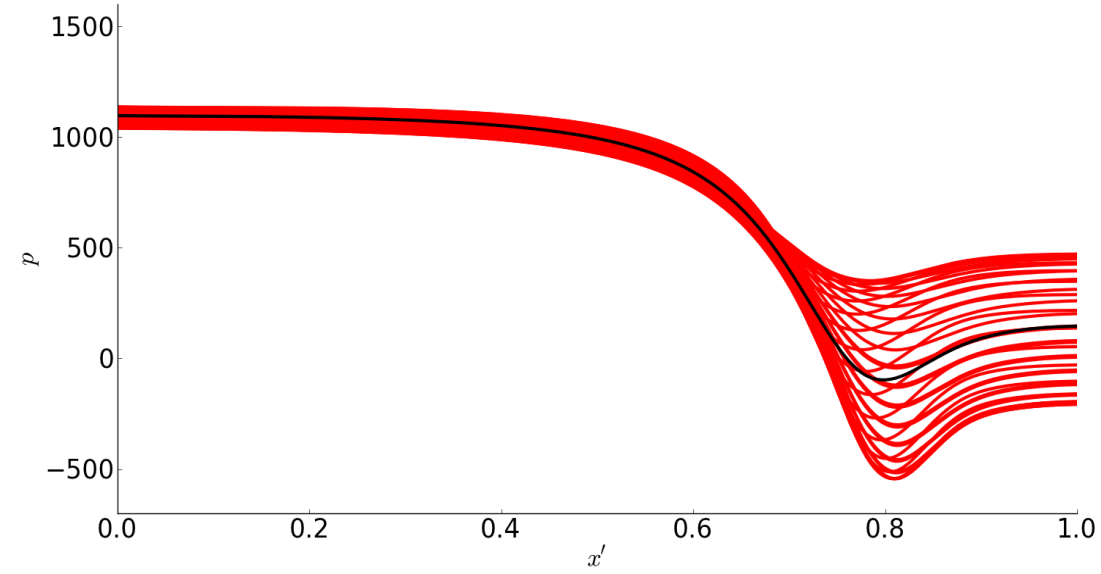

(a) Base case

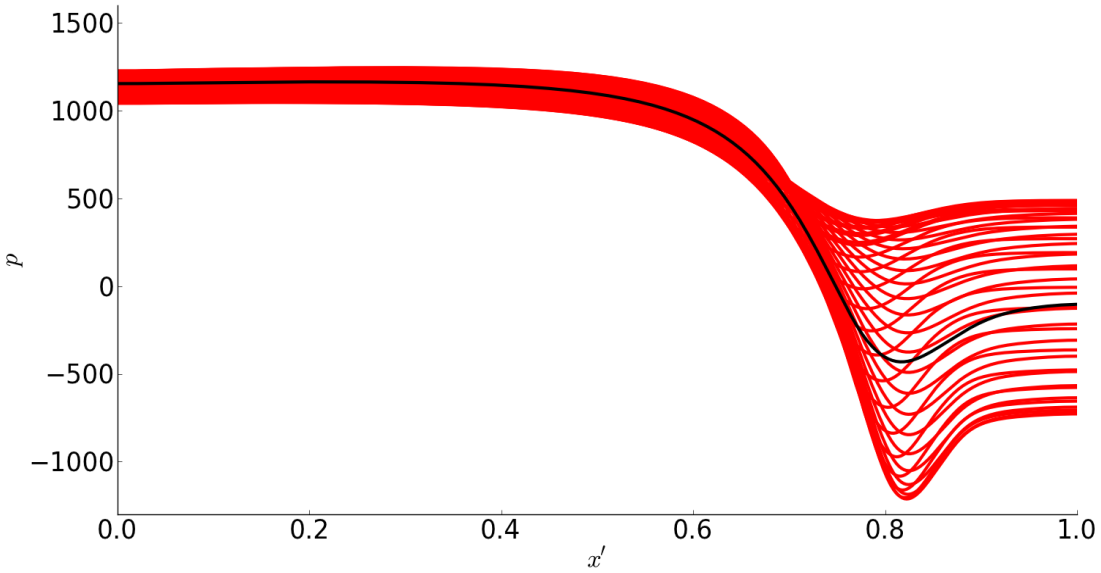

(b) Case S-8

Figure 8.19 Pressure p along the dual wall flexible insert during steady-state (black and dynamic instability over one oscillation period (red lines) comparing the base case and unstable sensitivity test case S-8.

Table 8.11 Dual wall configuration dynamic behaviour results for Ca_{eff}.Re sensitivity.

Variation Number	f	A_{max}	f Error (%)	A_{max} Error (%)
Base case	0.167	N/A	0.01143	N/A
S-8	0.124	25.7	0.01834	60.0

all three non-dimensional parameters including Ca_{eff}.Re have to be considered when characterising the dynamics of the system.

These dynamic verification tests show the suitability of using the non-dimensional parameters Ca_{eff}.Re and Ca_{eff}/Re and P_{eff} to characterise stability as was done for the single wall configuration. The importance and sensitivity effects of these parameters on stability are also similar. These similarities mean a full parametric study could be performed on this dual wall configuration to generate a relationship that enables prediction of stability behaviour.

8.5 Summary

Instability of the dual wall flexible insert configuration has been investigated. The test case selected was with $Ca_{eff}.Re = 1.0$ and $Ca_{eff}/Re = 10^{-4}$ and varying P_{eff}. It was found that this particular system was unstable at $P_{eff} = 0.05$. This unstable case was studied further in terms of the flexible insert shape, pressure along the flexible insert and fluid behaviour both during steady-state and its saturated instability oscillation cycle. The rate of work and energy budget was also analysed.

It was found that the similar behaviour of the single wall case occur at significantly different non-dimensional parameters. This showed that no quantitative relationship could be established both in terms of the steady-state and dynamic behaviour. This is due to differences in FSI behaviour. The single flexible wall reacts to a rigid wall, whereas the dual flexible inserts react with each other. Therefore the dual wall case is more unstable, *i.e.* requiring a smaller P_{eff} (but applied over double the number of sides) before becoming unstable. Ultimately this means that no relationship could be established between the single and dual wall cases to determine system stability.

Although no stability prediction could be made between the two configurations, it was still worthwhile to determine whether the non-dimensional scheme created for the single wall configuration was still applicable for the dual wall case. To test this, internal dimensional parameter variations were performed whilst keeping the three non-dimensional parameters the same. It was found that statically the FSI system behaviours were similar. The static tests were then extended to determine the system sensitivity to each of the non-dimensional parameters. It was found the maximum wall deformation y'_{max} was sensitive to variations in P_{eff} and Ca_{eff}/Re, and not sensitive to variations in

Ca_{eff}.Re. Therefore the static flexible insert deformation can be characterised using just two non-dimensional parameters.

Dynamic system testing show that the three non-dimensional parameters developed in the single-insert study were suitable as the instability behaviour characterised in terms of A_{max} and f showed similar results. All three non-dimensional parameters are required to predict stability and dynamic behaviour because the system is sensitive to all FSI changes and not just the maximum wall deformation.

The non-dimensional scheme is therefore suitable to characterise the flexible wall shape (using two parameters) and the dynamic/stability behaviour (using three parameters). Further comprehensive system testing is required to define this relationship which has not been performed as part of the current work.

Chapter 9

Conclusions

9.1 General

The aim of this work was to better understand the FSI behaviour of a 2-d channel with internal fluid flow and flexible insert sections with large deformation. For this configuration, the onset of self-excited oscillation instabilities have been observed in experiments using the Starling resistor. The increasing capacity of computational power has enabled significant developments in the understanding of this problem using numerical approaches. For this work, the software package `oomph-lib` is used. Particular focus was given to understanding the instability mechanism and determining the system's control parameters. This system is of interest because it relates to many applications in industrial and biomechanical engineering. A summary of the original contributions and findings are listed in the following sections. The limitations of the current work and future research direction are also listed.

9.2 Original Contributions

The original contributions from the current work extend the understanding of the flexible insert channel flow system studied. These are listed below:

- Creation of a non-dimensional scheme to characterise the system with consideration of flexible insert stiffness, length and location along the channel. Previous investigations typically lack the consideration of flexible insert length and location.
- Development of an analysis template to study the FSI behavior in terms of the flexible insert static and dynamic deformation and fluid flow behaviour. Analysis of the system energy balance and quantifying of the major energy components was also performed. This provided a common framework for characterising FSI behaviour, enabling simpler comparison for any given parameter set in terms of identifying similar or unique instability mechanisms.

- A comprehensive parametric study was performed for the single flexible wall configuration to develop plots for mapping steady-state and dynamic instability behavior which can serve as predictive tools. For the static flexible insert case, a lookup plot and curve-fit equation was generated for determining the flexible insert maximum deformation. For dynamic cases, a lookup plot is generated to determine system stability.

- Analysis of the configuration of two geometrically independent and opposite flexible inserts. This resulted in the finding that no direct quantitative relationship can be derived from the single and dual flexible wall equivalent parameter systems in terms of the FSI behaviour. It was however found the non-dimensional scheme created for the single flexible insert was also suitable for the dual flexible insert configuration.

9.3 Single Wall Study

A validation effort was undertaken to compare the current `oomph-lib` model with previous independent numerical studies. This included comparison against steady-state and transient simulations of small and large flexible wall deformation cases. In all instances, the steady-state systems matched well with the `oomph-lib` model. However for the dynamic systems, the `oomph-lib` model results only matched well with certain numerical approaches in terms of the actual flexible wall oscillatory motion. In other instances there were differences due to the inherent differences in the modelling assumptions. However, all models showed consistency in terms of whether instability occurred.

The validated `oomph-lib` model was then used to investigate the system instability mechanism in detail. A set of diagnostic tools were developed to characterise the system in terms of the flexible wall mean deformation, dynamic motion, fluid flow streamlines and energy budget. A comprehensive parametric study was performed to determine the parameters required for instability to occur and the characteristics of the different instability types possible. For the majority of cases, it was found that instability was driven by the combination of large wall deformations and recirculation vortices forming behind the flexible insert. These cases analysed had adverse pressure gradients along the flexible insert section which resulted in the periodic growth, decay and shedding of vortices. The level of flexible wall movement is affected by the downstream location and magnitude of the vortex shedding. However, when flexible wall deformations are very large and approaching the opposing wall, an alternative instability mechanism was also discovered where there is still recirculation vortices formation and dissipation but this is not ever-present during the oscillation cycle. The instability driver in this instance

is the flexible wall stretched to a very taut and unstable state reacting to any disturbance in the fluid flow.

These instability types are categorised in the parameter-space using a non-dimensional scheme consisting of three parameters: $Ca_{eff}.Re$, Ca_{eff}/Re and P_{eff}. This non-dimensional scheme was extensively tested to ensure it satisfied variations of its internal dimensional parameters. The sensitivity of each of the non-dimensional parameters was also tested. The mean flexible wall deformation was found to be strongly linked to Ca_{eff}/Re and P_{eff} but only has a weak relationship to $Ca_{eff}.Re$. Therefore development of a single quadratic equation was possible to characterise the flexible wall maximum deformation as a function of Ca_{eff}/Re and P_{eff}. In terms of determining dynamic instability however, all three non-dimensional parameters are important and a stability contour map is generated.

9.4 Dual Wall Study

A limited study of channel flow with dual geometrically independent flexible inserts was performed. This system was analysed using the same diagnostic tools as for the single wall case and it was found that similar instability mechanisms exist in this configuration. With similar startup conditions for both top and bottom flexible walls, both flexible walls oscillate with the same motion and the vortex shedding pattern are also symmetric about the channel centreline. However, the system is not able to maintain this symmetric state indefinitely. Numerical imbalance or different initial perturbation magnitudes on the upper and lower walls see the recirculation vortex dominating on one of the flexible inserts. This in turn creates slightly different saturated flexible wall motions for the two walls. This non-symmetric state is the final state where the unstable system oscillates indefinitely.

It was shown that the same non-dimensional scheme proposed for the single wall case can be used for the dual wall configuration. However, a new parametric study is required to establish the quantitative plots for predicting maximum wall deformation and system stability of the dual wall configuration that is distinct from the single wall data set.

9.5 Limitations

A comprehensive investigation of insert stability has been performed. However, it is recognised there are limitations to the methodology employed in the current work which are as follows:

- Fluid flow was limited to Newtonian fluid in the laminar flow region with the range of $Re < 500$.

- The flexible insert was treated as massless (fluid inertia dominates over flexible insert inertia) and thin (axial strain dominates over bending strain).
- The work is bounded to two-dimensions spatially. Effects in the third dimension are not captured in this work.
- Only constant, uniform external pressures are applied to the flexible insert. No variation in time and pressure profile along the flexible insert is considered.
- For the dual flexible insert case, both flexible inserts are constrained to have the same material properties as well as the same external loading profile and magnitude.

9.6 Future Research Direction

There are several possible avenues where the current work can be extended for further investigation. These include

- Consideration of flexible walls of finite thickness and having mass (inertia) or pre-tension that could change the stability behaviour.
- Extending to higher Reynolds numbers than $\mathrm{Re} = 500$ which may result in the discovery of other instability mechanisms.
- Consideration of non-Newtonian fluids as was done by Chakraborty et al. (2010, 2015) in extending the study to three viscoelastic fluids (Oldroyd-B, FENE-P, Owens blood models).
- Different external pressure types can be investigated including time-varying magnitudes and non-uniform pressures along the flexible insert. This will change the temporal and spatial response of the flexible insert and therefore the stability response.
- A full, comprehensive parametric study can be performed for the dual wall configuration. From this, non-dimensional plots for predicting maximum wall deformation and system stability can be established.
- For dual wall configurations, the study can be extended to having the top and bottom flexible walls with different lengths, locations along the channel, material properties and loading types.
- Creation of a tubular model that is a fully-coupled three dimensional system enables the system to be more representative of the Starling Resistor experimental setup.

- A different configuration can be investigated where a single flexible insert is separated between two separate channel flows.
- Physical experiments can be performed on the simulated test points of the current work for real-world comparison.

References

1. M. Amabili, F. Pellicano, and M. P. Païdoussis. Non-linear dynamics and stability of circular cylindrical shells containing flowing fluid. part i: stability. *Journal of sound and Vibration*, 225(4):655–699, 1999a.

2. M. Amabili, F. Pellicano, and M. P. Païdoussis. Non-linear dynamics and stability of circular cylindrical shells containing flowing fluid, part ii: large-amplitude vibrations without flow. *Journal of Sound and Vibration*, 228(5): 1103–1124, 1999b.

3. M. Amabili, F. Pellicano, and M. P. Païdoussis. Non-linear dynamics and stability of circular cylindrical shells containing flowing fluid. part iii: truncation effect without flow and experiments. *Journal of Sound and Vibration*, 237(4): 617–640, 2000a.

4. M. Amabili, F. Pellicano, and M. P. Païdoussis. Non-linear dynamics and stability of circular cylindrical shells containing flowing fluid. part iv: large-amplitude vibrations with flow. *Journal of Sound and vibration*, 237(4):641–666, 2000b.

5. Y. Bai and Q. Bai. *Subsea engineering handbook*. Gulf Professional Publishing, 1st edition edition, 2012.

6. K.-J. Bathe. *Finite element procedures*. Prentice Hall, 2006.

7. C. D. Bertram. Two modes of instability in a thick-walled collapsible tube conveying a flow. *Journal of Biomechanics*, 15(3):223–224, 1982.

8. C. D. Bertram. Unstable equilibrium behaviour in collapsible tubes. *Journal of Biomechanics*, 19(1):61–69, 1986.

9. C. D. Bertram. Fluid flow in distensible vessels. *Clinical and Experimental Pharmacology and Physiology*, 36:206–216, 2009.

10. C. D. Bertram and R. J. Castles. Flow limitation in uniform thick-walled collapsible tubes. *Journal of Fluids and Structures*, 13(3):399–418, 1999.

11. C. D. Bertram and N. S. J. Elliott. Aqueous flow limitation in uniform collapsible tubes: multiple flow-limited flow-rates at the same pressure drop and upstream transmural pressure. *ASME-PUBLICATIONS-BED*, 50:383–384, 2001.

12. C. D. Bertram and N. S. J. Elliott. Flow-rate limitation in a uniform thin-walled collapsible tube, with comparison to a uniform thick-walled tube and a tube of tapering thickness. *Journal of Fluids and Structures*, 17:541–559, 2003.

13. C. D. Bertram and T. J. Pedley. A mathematical model of unsteady collapsible tube behaviour. *Journal of Biomechanics*, 15(1):39–50, 1982.

14. C. D. Bertram and J. Tscherry. The onset of flow-rate limitation and flow-induced oscillations in collapsible tubes. *Journal of Fluids and Structures*, 22 (8):1029–1045, 2006.

15. C. D. Bertram, C. J. Raymond, and T. J. Pedley. Mapping of instabilities for flow through collapsed tubes of differing length. *Journal of Fluids and Structures*, 4(2):125–153, 1990.

16. F. Bonsignori and M. Salvini. Unidimensional steady flow in collapsible tubes with applications to blood vessels. *Il Nuovo Cimento D*, 6(4):317–333, 1985.

17. D. Braess. *Finite elements: Theory, fast solvers, and applications in solid mechanics*. Cambridge University Press, 2007.

18. B. S. Brook and T. J. Pedley. A model for time-dependent flow in (giraffe jugular) veins: uniform tube properties. *Journal of biomechanics*, 35(1):95–107, 2002.

19. B. S. Brook, S. A. E. G. Falle, and T. J. Pedley. Numerical solutions for unsteady gravity-driven flows in collapsible tubes: evolution and roll-wave instability of a steady state. *Journal of Fluid Mechanics*, 396:223–256, 1999.

20. R. L. Burden and J. G. Faires. Numerical analysis. 1993.

21. C. Cancelli and T. J. Pedley. A separated-flow model for collapsible-tube oscillations. *Journal of Fluid Mechanics*, 157:375–404, 1985.

22. E. Carrera, G. Giunta, and M. Petrolo. *Beam structures: classical and advanced theories*. John Wiley & Sons, 2011.

23. D. Chakraborty and J. R. Prakash. Viscoelastic fluid flow in a 2d channel bounded above by a deformable finite-thickness elastic wall. *Journal of Non-Newtonian Fluid Mechanics*, 218:83–98, 2015.

24. D. Chakraborty, M. Bajaj, L. Yeo, J. Friend, M. Pasquali, and J. R. Prakash. Viscoelastic flow in a two-dimensional collapsible channel. *Journal of Non-Newtonian Fluid Mechanics*, 165(19):1204–1218, 2010.

25. W. A. Conrad. Pressure-flow relationships in collapsible tubes. *Biomedical Engineering, IEEE Transactions on*, BME-16(4):284–295, 1969.

26. C. Davies and P. W. Carpenter. Instabilities in a plane channel flow between compliant walls. *Journal of Fluid Mechanics*, 352:205–243, 1997.

27. V. D. Djordjevic and M. Vukobratovic. On a steady, viscous flow in two-dimensional collapsible channels. *Acta mechanica*, 163(3-4):189–205, 2003.

28. H. L. Jr. Dodds and H. L. Runyan. Effect of high-velocity fluid flow on the bending vibrations and static divergence of a simply supported pipe. *NASA Technical Note*, NASA TN D-2870, 1965.

29. N. S. J. Elliott, A. D. Lucey, and M. Heil. Large-amplitude oscillations of a finite-thickness cantilevered flexible plate in viscous channel flow. In *Proc. ASME FEDSIM-ICNMM2010-30438*, Montreal, Canada, 1–5 Aug 2010.

30. A. M. N. Gardner, M. J. Turner, C. C. Wilmshurst, and D. J. Griffiths. Hydrodynamics of blood flow through the inferior vena cava. *Medical and Biological Engineering and Computing*, 15(3):248–253, 1977.

31. N. Gavriely, T. R. Shee, D. W. Cugell, and J. B. Grotberg. Flutter in flow-limited collapsible tubes: a mechanism for generation of wheezes. *Journal of Applied Physiology*, 66(5):2251–2261, 1989.

32. M. H. Ghayesh, M. P. Païdoussis, and M. Amabili. Nonlinear dynamics of cantilevered extensible pipes conveying fluid. *Journal of Sound and Vibration*, 332(24):6405–6418, 2013.

33. S. Ghomeshi. Numerical simulation and stability of flow in a collapsible channel. Master's thesis, Institute for Aerospace Studies, University of Toronto, 2003.

34. J. H. Ginsberg. The dynamic stability of a pipe conveying a pulsatile flow. *Journal of Sound and Vibration*, 11:1013–1024, 1973a.

35. J. H. Ginsberg. Large amplitude forced vibrations of simply supported thin cylindrical shells. *Journal of Applied Mechanics*, 40(2):471–477, 1973b.

36. J. H. Ginsberg. Nonlinear axisymmetric free vibration in simply supported cylindrical shells. *Journal of Applied Mechanics*, 41(1):310–312, 1974.

37. D. J. Griffiths. The velocity of the urine stream during female micturition. *Medical and biological engineering*, 7(5):527–531, 1969a.

38. D. J. Griffiths. Urethral elasticity and micturition hydrodynamics in females. *Medical and biological engineering*, 7(2):201–215, 1969b.

39. D. J. Griffiths. Hydrodynamics of male micturition—i theory of steady flow through elastic-walled tubes. *Medical and Biological Engineering*, 9(6):581–588, 1971a.

40. D. J. Griffiths. Hydrodynamics of male micturition—ii measurements of stream parameters and urethral elasticity. *Medical and biological engineering*, 9(6): 589–596, 1971b.

41. D. J. Griffiths. Steady fluid flow through veins and collapsible tubes. *Medical and biological engineering*, 9(6):597–602, 1971c.

42. J. B. Grotberg and O. E. Jensen. Biofluid mechanics in flexible tubes. *Annual Review of Fluid Mechanics*, 36(1):121, 2004.

43. J. C. Guneratne. *High Reynolds number flow in a collapsible channel.* PhD thesis, University of Cambridge, 1999.

44. J. C. Guneratne and T. J. Pedley. High-reynolds-number steady flow in a collapsible channel. *Journal of Fluid Mechanics*, 569:151–184, 2006.

45. A. L. Hazel and M. Heil. Steady finite-reynolds-number flows in three-dimensional collapsible tubes. *Journal of Fluid Mechanics*, 486:79–103, 2003.

46. M. Heil and J. Boyle. Self-excited oscillations in three-dimensional collapsible tubes: simulating their onset and large-amplitude oscillations. *Journal of Fluid Mechanics*, 652:405–426, 2010.

47. M. Heil and A. L. Hazel. Oomph-lib – an object-oriented multi-physics finite-element library. *Fluid-Structure Interaction*, pages 19–49, 2006.

48. M. Heil and A. L. Hazel. Fluid-structure interaction in internal physiological flows. *Annual Review of Fluid Mechanics*, 43:141–162, 2011.

49. M. Heil and O. E. Jensen. Flows in deformable tubes and channels theoretical models and biological applications. *Fluid Mechanics and Its Applications*, 72: 15–50, 2003.

50. M. Heil and S. L. Waters. How rapidly oscillating collapsible tubes extract energy from a viscous mean flow. *Journal of Fluid Mechanics*, 601:199–227, 2008.

51. Keith D Hjelmstad. *Fundamentals of structural mechanics*. Springer Science & Business Media, 2007.

52. L. Hollaway. *Polymer composites for civil and structural engineering*. Springer, 1st edition edition, 1993.

53. P. J. Holmes. Pipes supported at both ends cannot flutter. *Journal of Applied Mechanics*, 45(3):619–622, 1978.

54. L. Huang. Viscous flutter of a finite elastic membrane in poiseuille flow. *Journal of Fluid and Structures*, 15(7):1061–1088, 2001.

55. O. Jensen. Instabilities of flows through deformable tubes and channels. *Springer Netherlands*, pages 101–116, 2013.

56. O. E. Jensen. Instabilities of flow in a collapsed tube. *Journal of Fluid Mechanics*, 220:623–659, 1990.

57. K. Karagiozis, M. Amabili, and M. P. Païdoussis. Nonlinear dynamics of harmonically excited circular cylindrical shells containing fluid flow. *Journal of Sound and Vibration*, 329(18):3813–3834, 2010.

58. A. I. Katz, Y. Chen, and A. H. Moreno. Flow through a collapsible tube: experimental analysis and mathematical model. *Biophysical Journal*, 9(10): 1261, 1969.

59. I. Kececioglu, M. E. Mcclurken, R. D. Kamm, and A. H. Shapiro. Steady, supercritical flow in collapsible tubes. part 1. experimental observations. *Journal of Fluid Mechanics*, 109:367–389, 1981.

60. S. K. Khaitan and A. Gupta. *High performance computing in power and energy systems*. Springer, 2013.

61. F. P. Knowlton and E. H. Starling. The influence of variations in temperature and blood-pressure on the performance of the isolated mammalian heart. *The Journal of physiology*, 44(3):206–219, 1912.

62. D. N. Ku. Blood flow in arteries. *Annual Review of Fluid Mechanics*, 29(1): 399–434, 1997.

63. R. B. Kudenatti, N. M. Bujurke, and T. J. Pedley. Stability of two-dimensional collapsible-channel flow at high reynolds number. *Journal of Fluid Mechanics*, 705:371–386, 2012.

64. L. Lai, N. S. J. Elliott, A. D. Lucey, and M. W. Pitman. Numerical two-dimensional flexible channel model fixed at both ends for flow-induced instability analysis. In *Proc. 6th Australasian Congress on Applied Mechanics*, pages 207–211, Perth, Western Australia, 2010. Engineers Australia. ISBN 978-0-8582-5941-6.

65. L. Lai, A. D. Lucey, N. S. J. Elliott, and M. W. Pitman. Computational modelling of a fluid-conveying flexible channel using oomph-lib. In *Proc. 19th International Congress on Modelling and Simulation*, 2011.

66. L. S. H. Lai, A. D. Lucey, and N. S. J. Elliott. Computational stability analysis of a channel flow with a large deformation compliant insert. In *The 18th Australasian Fluid Mechanics Conference, Launceston, Australia: Australasian Fluid Mechanics Society*, 2012.

67. L. S. H. Lai, A. D. Lucey, and Novak S. J. Elliott. Flow-induced deformations of a compliant insert in channel flow: from small to large amplitudes. In *ASME 2012 International Design Engineering Technical Conferences and Computers and Information in Engineering Conference*, pages 31–40. American Society of Mechanical Engineers, 2012.

68. LSH Lai, J Cisonni, and AD Lucey. Stability of flexible inserts in laminar channel flow. In *The 20th Australasian Fluid Mechanics Conference, Perth, Australia: Australasian Fluid Mechanics Society*, 2016.

69. H. P. Langtangen. *Computational partial differential equations: numerical methods and diffpack programming*, volume 2. Springer Science & Business Media, 2013.

70. X. Li, J. Bai, S. Cui, and S. Wang. Simulation study of the cardiovascular functional status in hypertensive situation. *Computers in Biology and Medicine*, 32(5):345–362, 2002.

71. H. F. Liu, X. Y. Luo, Z. X. Cai, and T. J. Pedley. Sensitivity of unsteady collapsible channel flows to modelling assumptions. *Communications in Numerical Methods in Engineering*, 25(5):483–504, 2009.

72. H. F. Liu, X. Y. Luo, and Z. X. Cai. Stability and energy budget of pressure-driven collapsible channel flows. *Journal of Fluid Mechanics*, 705:348–370, 2012.

73. T. W. Lowe and T. J. Pedley. Computation of stokes flow in a channel with a collapsible segment. *Journal of Fluids and Structures*, 9(8):885–905, 1995b.

74. X. Y. Luo and T. J. Pedley. A numerical simulation of steady flow in a 2-d collapsible channel. *Journal of Fluids and Structures*, 9(2):149–174, 1995a.

75. X. Y. Luo and T. J. Pedley. The effects of wall inertia on flow in a two-dimensional collapsible channel. *Journal of Fluid Mechanics*, 363:253–280, 1998b.

76. X. Y. Luo and T. J. Pedley. Multiple solutions and flow limitation in collapsible channel flows. *Journal of Fluid Mechanics*, 420:301–324, 2000.

77. X. Y. Luo, Z. X. Cai, W. G. Li, and T. J. Pedley. The cascade structure of linear instability in collapsible channel flows. *Journal of Fluid Mechanics*, 600:45–76, 2008.

78. A. Marzo, X. Y. Luo, and C. D. Bertram. Three-dimensional collapse and steady flow in thick-walled flexible tubes. *Journal of Fluids and Structures*, 20 (6):817–835, 2005.

79. M. E. Mcclurken, I. Kececioglu, R. D. Kamm, and A. H. Shapiro. Steady, supercritical flow in collapsible tubes. part 2. theoretical studies. *Journal of Fluid Mechanics*, 109:391–415, 1981.

80. Y. Modarres-Sadeghi, C. Semler, M. Wadham-Gagnon, and M. P. Païdoussis. Dynamics of cantilevered pipes conveying fluid. part 3: Three-dimensional dynamics in the presence of an end-mass. *Journal of Fluids and Structures*, 23 (4):589–603, 2007c.

81. M. Molati and F. M. Mahomed. Symmetry classification of collapsible tube model incorporating tension. *Communications in Nonlinear Science and Numerical Simulation*, 17(1):93–99, 2012.

82. oomph-lib. Flow in a 2d collapsible channel revisited – enabling adaptivity in fsi problems, 2016. URL www.oomph-lib.maths.man.ac.uk.

83. M. P. Païdoussis and J.-P. Denise. Flutter of thin cylindrical shells conveying fluid. *Journal of Sound and Vibration*, 20(1):9–26, 1972.

84. M. P. Païdoussis, C. Semler, M. Wadham-Gagnon, and S. Saaid. Dynamics of cantilevered pipes conveying fluid. part 2: dynamics of the system with intermediate spring support. *Journal of Fluids and Structures*, 23(4):569–587, 2007b.

85. T. J. Pedley. Longitudinal tension variation in collapsible channels: A mechanism for the breakdown of steady flow. *ASME Journal of Biomechanical Engineering*, 114(1):60–67, 1992.

86. T. J. Pedley and X. Y. Luo. Modelling flow and oscillations in collapsible tubes. *Theoretical and Computational Fluid Dynamics*, 10(1-4):277–294, 1998a.

87. T. J. Pedley and D. Pihler-Puzović. Flow and oscillations in collapsible tubes: Physiological applications and low-dimensional models. *Sadhana*, 40(3):891–909, 2015.

88. G. Pedrizzetti. Unsteady tube flow over an expansion. *Journal of Fluid Mechanics*, 310:89–111, 1996.

89. G. Pedrizzetti. Fluid flow in a tube with an elastic membrane insertion. *Journal of Fluid Mechanics*, 375:39–64, 1998.

90. M. P. Rast. Simultaneous solution of the navier-stokes and elastic membrane equations by a finite element method. *International Journal for Numerical Methods in Fluids*, 19(12):1115–1135, 1994.

91. J. N. Reddy and D. K. Gartling. *The finite element method in heat transfer and fluid dynamics*. CRC press, 2010.

92. M. E. Rosar. *A three-dimensional computer model for fluid flow through a collapsible tube*. PhD thesis, New York University, 1994.

93. A. P. Rothmayer. The viscous flow through symmetric collapsible channels. *Mathematika*, 36(01):153–181, 1989.

94. R. A. Scroggs, S. B. M. Beck, and E. A. Patterson. An integrated approach to modelling the fluid-structure interaction of a collapsible tube. *JSME International Journal Series B Fluids and Thermal Engineering*, 47(1):20–28, 2004.

95. L. F. Shampine. *Numerical solution of ordinary differential equations*, volume 4. CRC Press, 1994.

96. A. H. Shapiro. Physiologic and medical aspects of flow in collapsible tubes. In *Proc. Sixth Canadian Congress of Applied Mechanics*, pages 883–906, 1977.

97. E. B. Shim and R. D. Kamm. Numerical simulation of steady flow in a compliant tube or channel with tapered wall thickness. *Journal of Fluids and Structures*, 16(8):1009–1027, 2002.

98. E. B. Shim, J. Y. Sah, and C. H. Youn. Mathematical modeling of cardiovascular system dynamics using a lumped parameter method. *The Japanese Journal of Physiology*, 54(6):545–553, 2004.

99. I. J. Sobey. *Introduction to interactive boundary layer theory*, volume 3. Oxford University Press on Demand, 2000.

100. P. S. Stewart, S. L. Waters, and O. E. Jensen. Local and global instabilities of flow in a flexible-walled channel. *European Journal of Mechanics-B/Fluids*, 28 (4):541–557, 2009.

101. B. Szabó and I. Babuška. *Introduction to finite element analysis: formulation, verification and validation*, volume 35. John Wiley & Sons, 2011.

102. C. Tang, L. Zhu, G. Akingba, and X. Lu. Viscous flow past a collapsible channel as a model for self-excited oscillation of blood vessels. *Journal of Biomechanics*, 48(10):1922–1929, 2015.

103. E. C. Ting and A. Hosseinipour. A numerical approach for flow-induced vibration of pipe structures. *Journal of Sound and Vibration*, 88(3):289–298, 1983.

104. N. K. Truong and C. D. Bertram. The flow-field downstream of a collapsible tube during oscillation onset. *Communications in Numerical Methods in Engineering*, 25(5):405–428, 2009.

105. M. Wadham-Gagnon, M. P. Païdoussis, and C. Semler. Dynamics of cantilevered pipes conveying fluid. part 1: Nonlinear equations of three-dimensional motion. *Journal of Fluids and Structures*, 23(4):545–567, 2007a.

106. J. W. Wang, Y. T. Chew, and H. T. Low. Effects of downstream system on self-excited oscillations in collapsible tubes. *Communications in Numerical Methods in Engineering*, 25(5):429–445, 2009.

107. Frank M White. *Fluid Mechanics, in SI Units*. McGraw-Hill, 2011.

108. N. S. Wijeratne and K. A. Hoo. An analytical approach to identify fluid flow separation and re-attachment in a collapsible channel. *Computers & Chemical Engineering*, 31(4):346–360, 2007.

109. D. M. Wootton and D. N. Ku. Fluid mechanics of vascular systems, diseases, and thrombosis. *Annual Review of Biomedical Engineering*, 1(1):299–329, 1999.

110. F. Xu, J. Billingham, and O. E. Jensen. Divergence-driven oscillations in a flexible-channel flow with fixed upstream flux. *Journal of Fluid Mechanics*, 723:706–733, 2013.

111. F. Xu, J. Billingham, and O. E. Jensen. Resonance-driven oscillations in a flexible-channel flow with fixed upstream flux and a long downstream rigid segment. *Journal of Fluid Mechanics*, 746:368–404, 2014.

112. Y. Zhu, X. Y. Luo, H. M. Wang, R. W. Ogden, and C. Berry. Three-dimensional non-linear buckling of thick-walled elastic tubes under pressure. *International Journal of Non-Linear Mechanics*, 48:1–14, 2013.

Appendix A

Fluid Domain Streamlines with No Dimensional Scaling

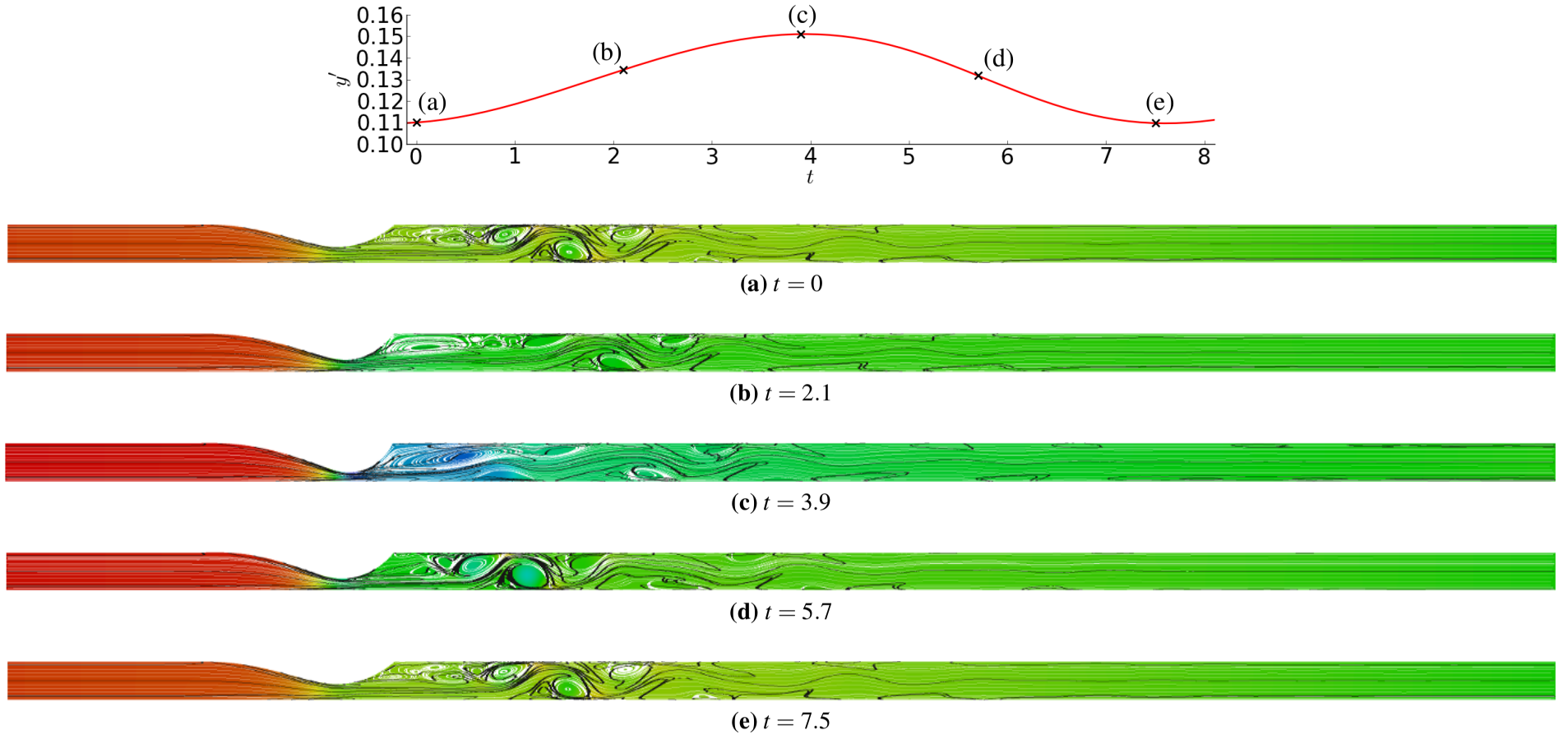

Figure A.1 Time history of the flexible insert maximum vertical displacement y'_{max} with corresponding fluid streamlines (white lines), vorticity lines (black lines) and pressure contours over one instability oscillation cycle based on Case A from the study by Liu et al. (2009) with no scaling of the fluid domain dimensions.

Appendix B

Dynamic Flexible Insert Parameterisation Detailed Study

This section explains in detail the steps performed in the parameterisation of the dynamic flexible insert. Dynamic simulations are performed for various effective pressure P_{eff} values (0.20, 0.22, 0.24, 0.30, 0.40). The results of this is shown in Figures B.1 to B.4. The 'x' markers in each plot signify a dynamic simulation case, with blue markers being stable cases and red markers unstable ones. Best estimate 'o' points are created, separating the stable and unstable region of the plots. These are labelled the critical stability lines for each P_{eff}. There is less result resolution at $P_{\text{eff}} = 0.20$ as computational time is high. On a computer with Intel i7 processors and 8GB of RAM, computation of a single dynamic case can take several hours to several weeks of continuous CPU time. Resolution for cases between $P_{\text{eff}} = 0.24 - 0.40$ is better as simulation time is typically shorter; between several hours to several days per dynamic simulation case. The seemingly lack of a methodical selection of dynamic simulation cases selected is due to the iterative process of creating the non-dimensional scheme. This resulted in running of more dynamic cases that was necessary at the time for the final scheme being defined. Regardless, all dynamic simulation cases have been included for completeness.

The critical stability lines from Figures B.1 to B.4 are collated into a single plot in Figure B.5. Any point below this line is deemed to be stable and points above this line is predicted to be unstable. Best fit lines have been created using third and fourth order polynomials as listed in Table B.1. The term A is $\ln(\text{Ca}_{\text{eff}}.\text{Re})$ and term B is $\ln(\text{Ca}_{\text{eff}}/\text{Re})$. These lines are used for the creation of the critical stability surface in Figure 7.5.

Table B.1 Critical stability line formulae for various effective pressure P_{eff} values.

P_{eff}	Best Fit Line Formulae
0.20	$A = 0.1849B^3 + 6.799B^2 + 79.54B + 301.2$
0.24	$A = 0.1041B^4 + 4.201B^3 + 63.77B^2 + 431.7B + 1098$
0.30	$A = 0.02994B^4 + 1.225B^3 + 18.96B^2 + 132.5B + 351.7$
0.40	$A = 0.0204B^4 + 0.8005B^3 + 11.8B^2 + 79.55B + 206.2$

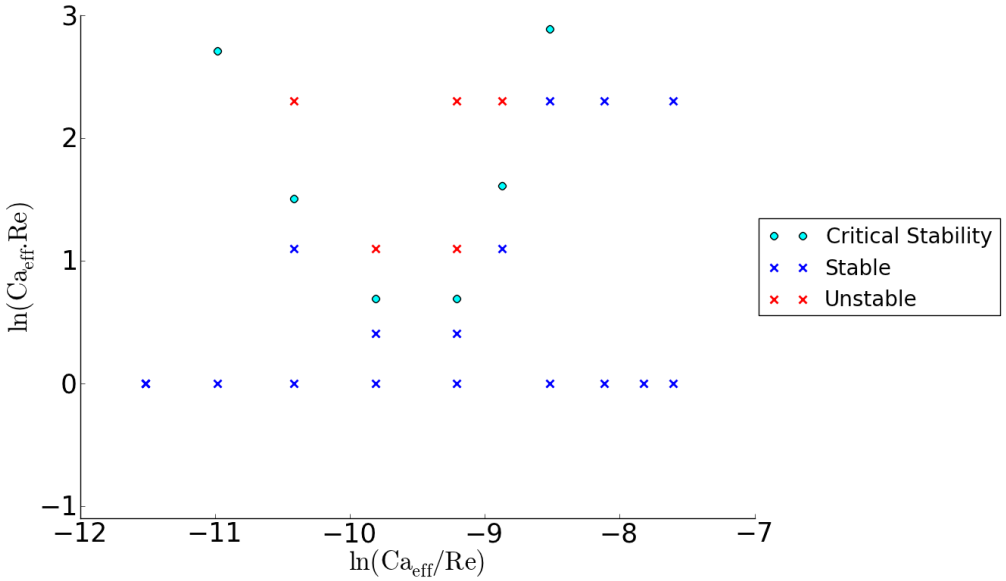

Figure B.1 Dynamic single flexible insert stability at effective pressure $P_{\text{eff}} = 0.20$.

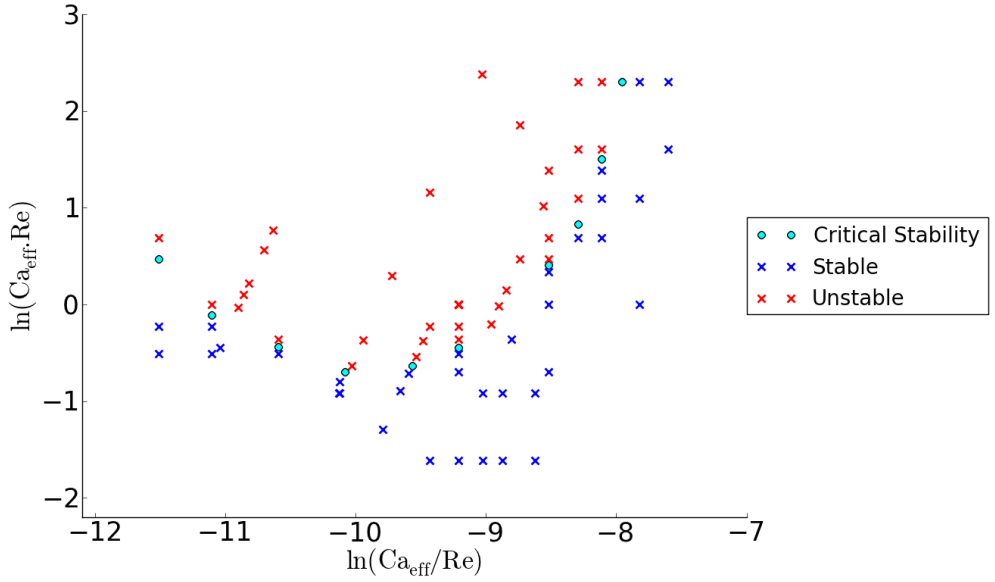

Figure B.2 Dynamic single flexible insert stability at effective pressure $P_{\text{eff}} = 0.24$.

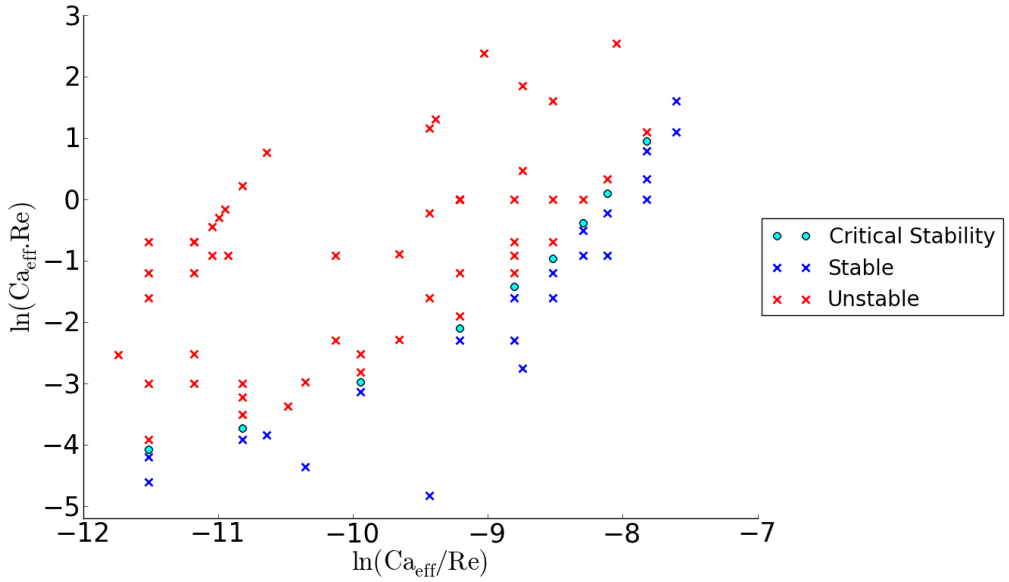

Figure B.3 Dynamic single flexible insert stability at effective pressure $P_{\text{eff}} = 0.30$.

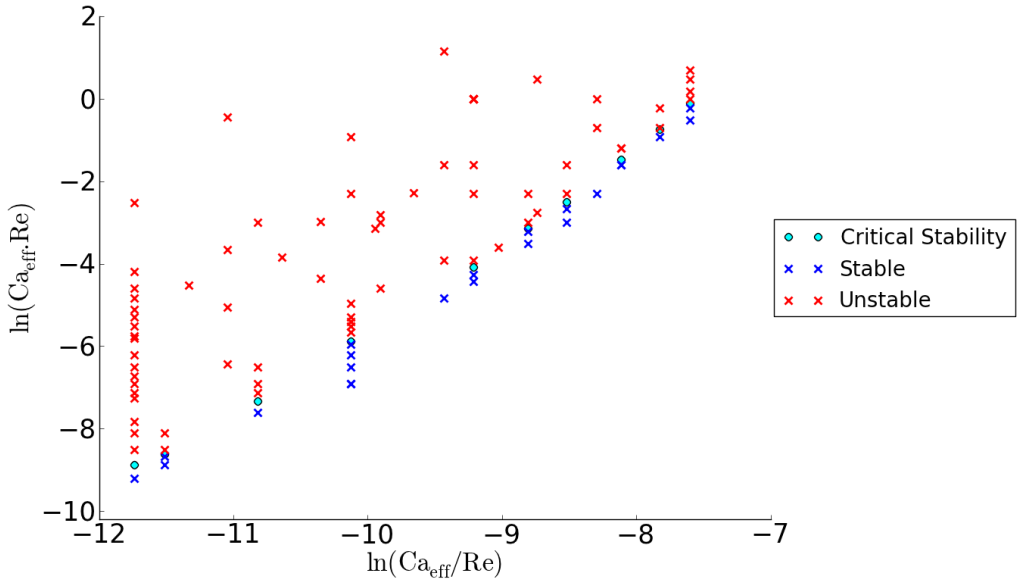

Figure B.4 Dynamic single flexible insert stability at effective pressure $P_{\text{eff}} = 0.40$.

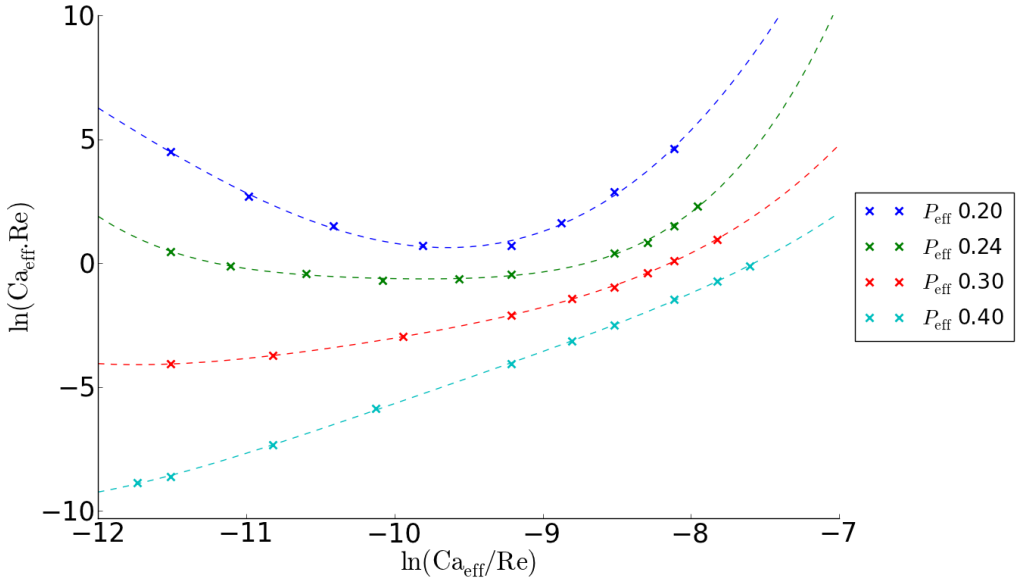

Figure B.5 Dynamic critical stability lines.

Appendix C

Mesh and Time Independence Study

Discussed in this section is the mesh and time independence study performed to show the mesh selected is suitably refined and timestep sufficiently small to capture the FSI behaviour. Case A of Liu et al. (2009) is selected as the study case because it was extensively validated with the published FBM and ADINA model results. Case A is also a good example of a dynamic system experiencing unsteady FSI behaviour as opposed to Cases B and C in Liu et al. (2009) which were stable cases. The Case A input parameters are listed in Table 4.5.

C.1 Mesh Independence

The mesh independence study was performed by varying mesh densities in the upstream, flexible insert and downstream sections of the channel. Three cases were analysed; a base case, as well as coarser and finer mesh cases. The number of cells along the length parameters are listed in Table C.1 and the undeformed channel representation shown in Figure C.1. The flexible wall section has the highest cell density, followed by the upstream and downstream sections based on the predicted areas of dynamic behaviour. The mesh is also specified to be finer approaching the walls (rigid and flexible walls) to capture the near-wall boundary effects. Note that all three cases use the adaptive mesh approach to apply mesh refinement during the simulation.

Table C.1 Mesh density (number of cells) along channel length dimensions for various mesh densities.

Case	Number of cells along length dimensions			
	L_{up}	L_{flex}	L_{down}	H
Base case	60	120	140	48
Coarse mesh	40	80	96	32
Fine mesh	120	240	280	96

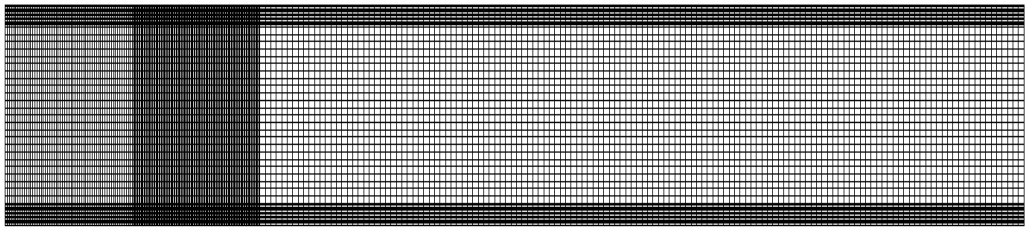

(a) Base case mesh

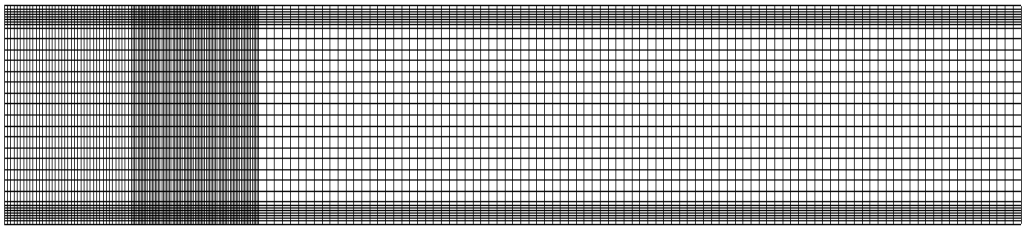

(b) Coarser mesh.

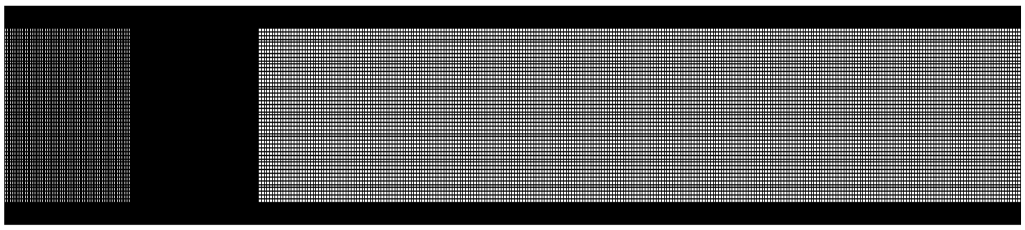

(c) Finer mesh.

Figure C.1 Undeformed channel with various levels of mesh densities for testing mesh independence. The fluid domain is scaled with a ratio of 1:5 (channel length to height) for visualisation purposes.

The steady-state analysis is performed (no perturbation applied on flexible insert) and the fluid domain mesh is shown in Figure C.2 with velocity vector colour contours. The adaptive scheme has refined the mesh around regions of significant FSI behaviour; at the large deformed flexible insert and areas of high vorticity at the flexible insert wake. It can be seen the flexible insert shape and fluid velocity behaviour are similar across the three cases. The coarser mesh case however shows lower maximum velocity (red colour) than the base and finer mesh cases.

A quantitative comparison can be seen in Figure C.3 showing the flexible insert deformation shape and pressure profile. The flexible insert shape is similar for all three cases with no perceptible difference. The non-dimensional pressure overall profile is also similar for all three cases. However, the minimum pressure is better captured in the base case and finer mesh case compared to the coarser mesh case ($p = -840, -809, -770$ respectively). In comparison with the finer mesh case, the differences for the base case and coarser mesh case are 0.38% and -4.8% respectively. The difference for the base case is deemed acceptable. For the coarser mesh case, the difference in absolute minimum non-dimensional pressure value is due to this case not having a data point closer to the pressure minima point, with its other data points consistent with the pressure profile form of the base case and finer mesh case. It can be seen the overall FSI behaviour is consistent across the three mesh cases, with the coarser mesh case having the deficiency of not capturing the pressure minima point for this test case.

Dynamic analysis is then performed with the application of a perturbation on the flexibile insert. The ensuing flexible wall dynamic motion can be deduced through the flexible insert maximum vertical displacement y'_{max} time history as seen in Figure C.4. It can be seen in Figure C.4a the mesh is sufficiently refined to generate similar flexible insert dynamic motion for the whole time history from the initial transient instability to its ultimate saturated oscillation state, which can be more clearly seen in Figure C.4b. Therefore the selection of this base case mesh density specifications is suitable.

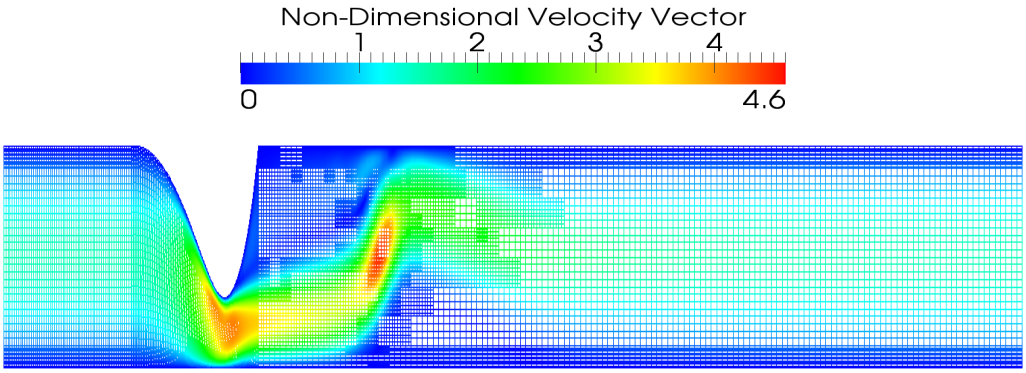

(a) Base case mesh

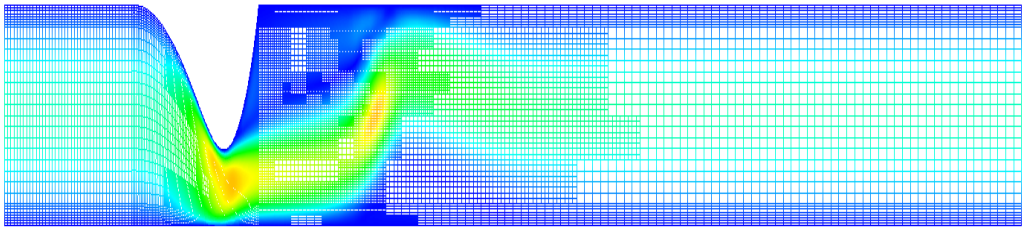

(b) Coarser mesh.

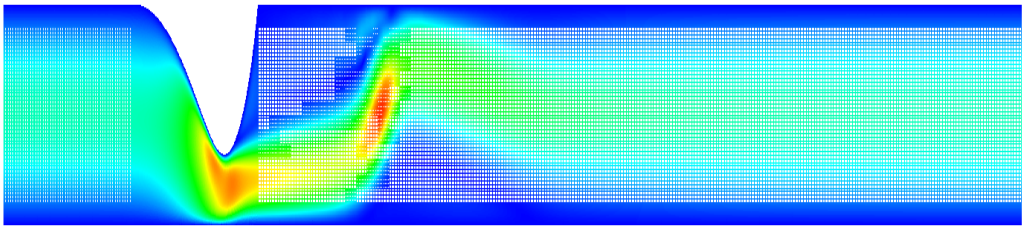

(c) Finer mesh.

Figure C.2 Steady-state deformed channel with velocity vector colour contours with various levels of mesh densities for testing mesh independence. The fluid domain is scaled with a ratio of 1:5 (channel length to height).

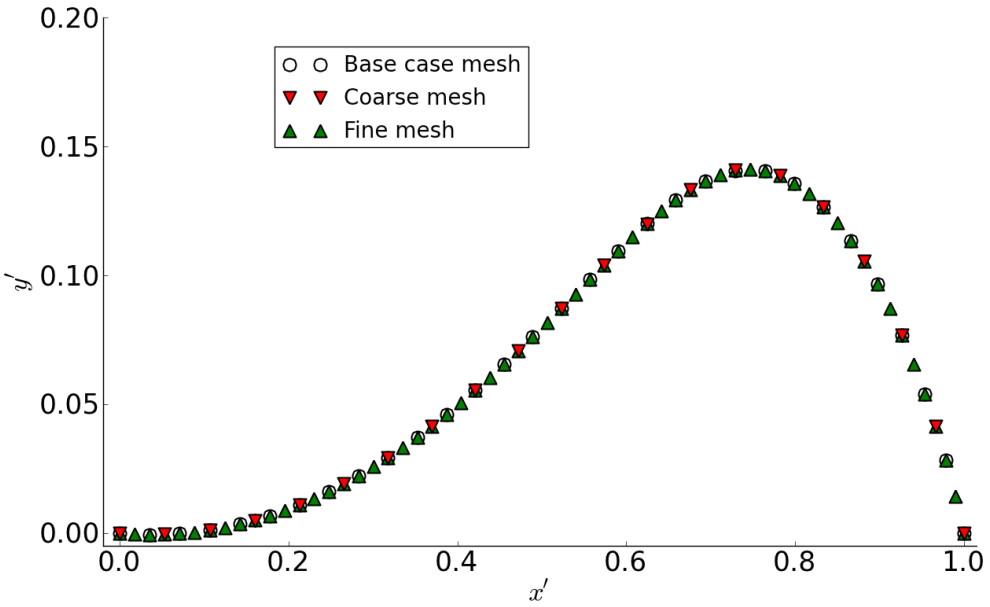

(a) Flexible insert deformation shape.

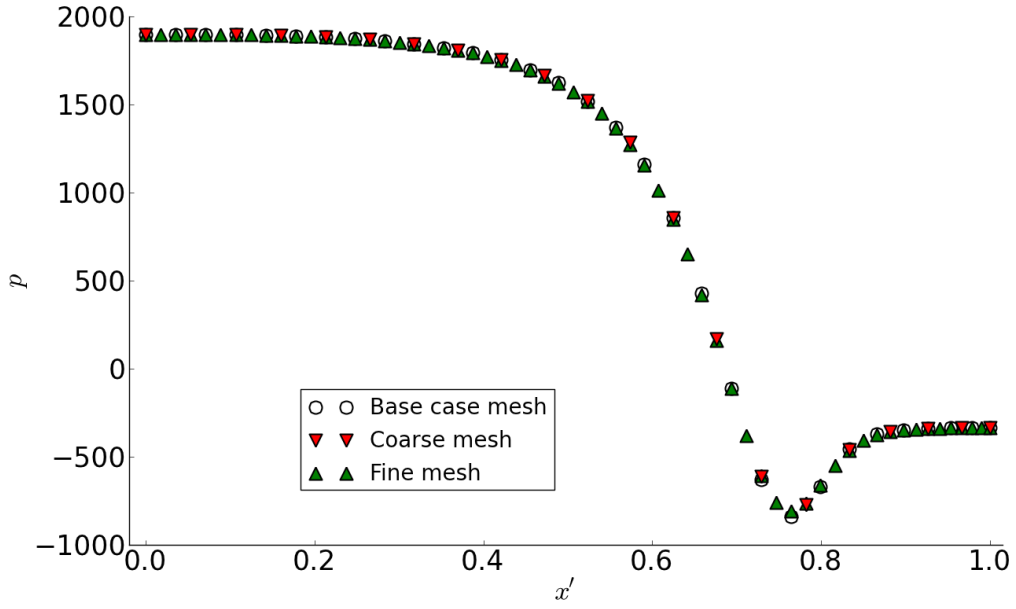

(b) Pressure along flexible insert.

Figure C.3 Flexible insert results under steady-state conditions comparison for different mesh densities.

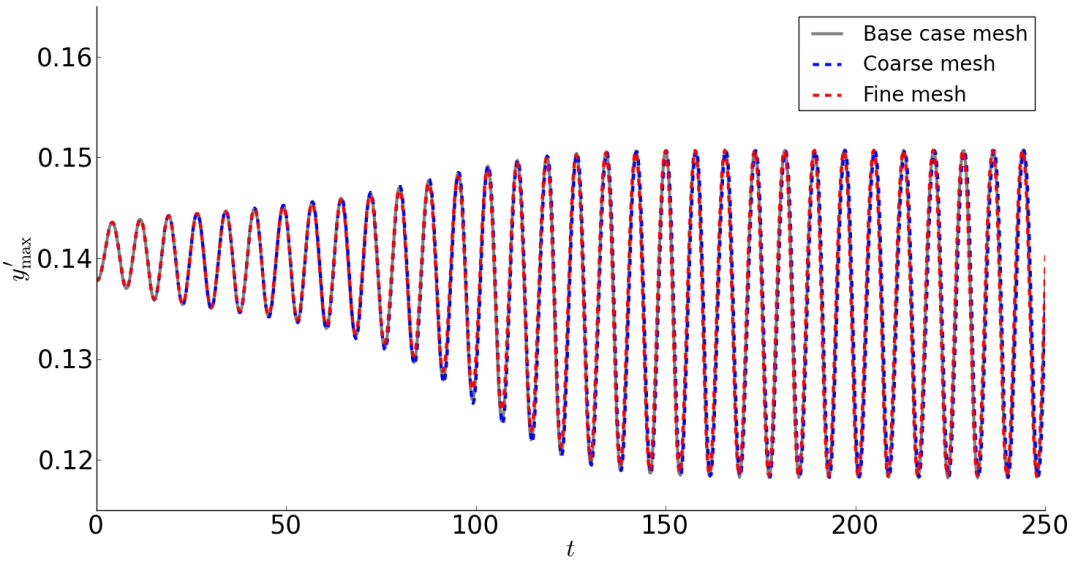

(a) Complete time history.

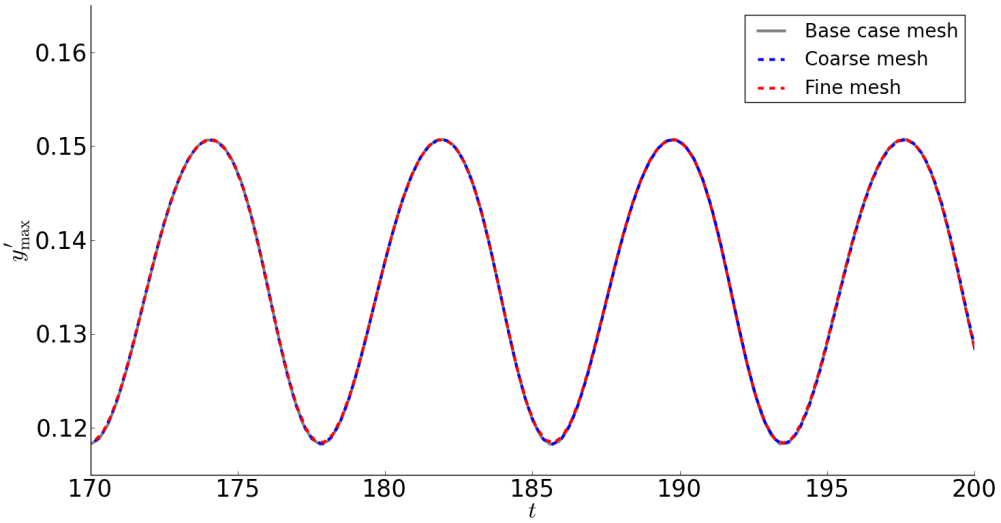

(b) Saturated oscillation state truncated time history.

Figure C.4 Maximum vertical displacement point $y'_{\max}$ time history based on Case A of Liu et al. (2009) for the mesh independence study.

C.2 Time Independence

The time independence study is performed by using the same base case as the previous section and varying the timesteps. The base case has a time step of $\Delta t = 0.1$s. Two coarser (Δt =0.2s, 0.5s) and finer timestep (Δt =0.05s, 0.02s) cases are tested to determine if the base case is temporally independent in generating consistent dynamic FSI behaviour. Figure C.5 shows the flexible insert maximum vertical displacement y'_{max} time history for the different timestep cases. Figure C.5a is the complete time history to show the initial transient oscillation behaviour. Figure C.5b is the truncated time history with the times slightly shifted to ensure the y'_{max} troughs are aligned for easier comparison.

The timestep Δt =0.5s case resulted in incorrect FSI behaviour with the flexible insert settling back into the steady-state. The Δt =0.2s case settles into saturated oscillation behaviour but with significantly smaller A_{peak} compared to the other finer timestep cases, though the oscillation frequency is similar. The other three finer timestep cases also arrive at the final state of saturated oscillations with similar oscillation frequencies. However, the base case trough y'_{max} value is larger than for the finer timestep cases (which are similar). The different percentage values are listed in Table C.2 with the Δt =0.02s case used as the comparison basis. The base case A_{peak} is approximately -6% different compared to the Δt =0.02s case, although the f difference is only -0.9%. The specific wall shape and pressure profile is seen in Figure C.6, showing that the base case and finer time step cases have similar wall and pressure profiles, and the Δt =0.2s case having completely different profiles. It is deduced the overall dynamic FSI behaviour is similar for the base case and two finer timestep cases with the measured differences within an acceptable range, thus the selection of the base case timestep is suitable.

Table C.2 Dynamic simulation results comparison based on y'_{max} for testing sensitivity of different timestep sizes.

Timestep case	Difference (%)			
Δt (s)	y'_{max} peak	y'_{max} trough	A_{peak}	f
0.5	N/A, stable case			
0.2	-4.7	16.4	-78.9	-0.7
0.1 (Base case)	-0.1	1.5	-5.8	-0.9
0.05	0.05	-0.1	0.7	-0.1
0.02	N/A, comparison based on this case			

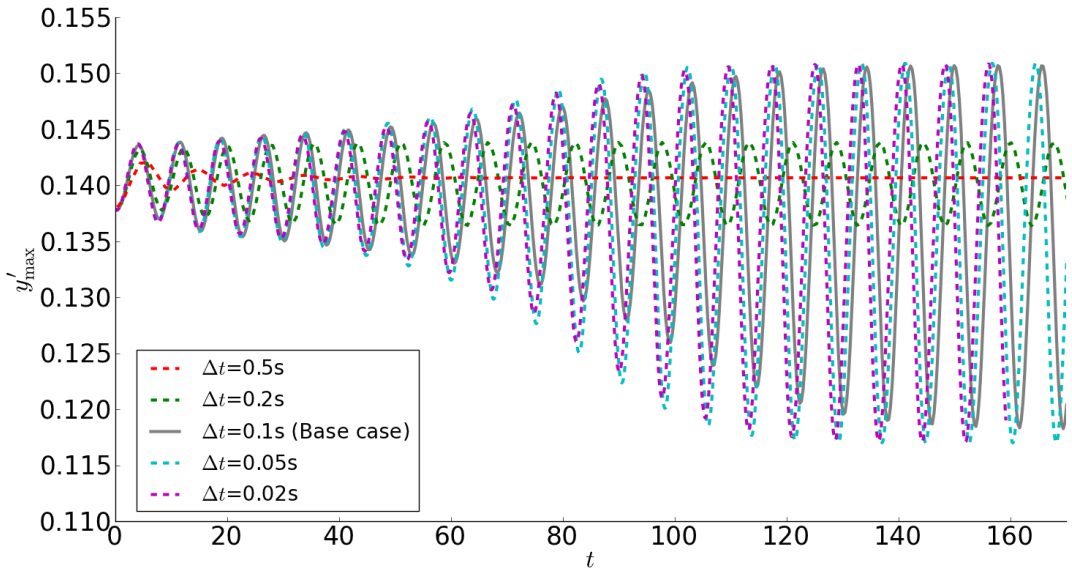

(a) Complete time history.

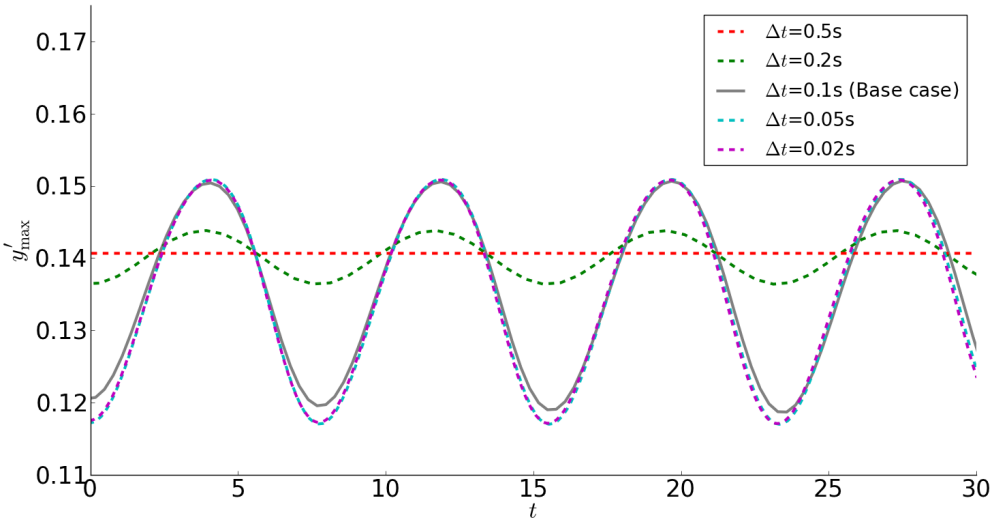

(b) Saturated oscillation state truncated time history. The start time has been shifted to ensure the y'_{max} trough is aligned for easier case comparison.

Figure C.5 Dynamic simulation results for different timestep sizes based on the y'_{max} time history of Case A from Liu et al. (2009) for the time independence study.

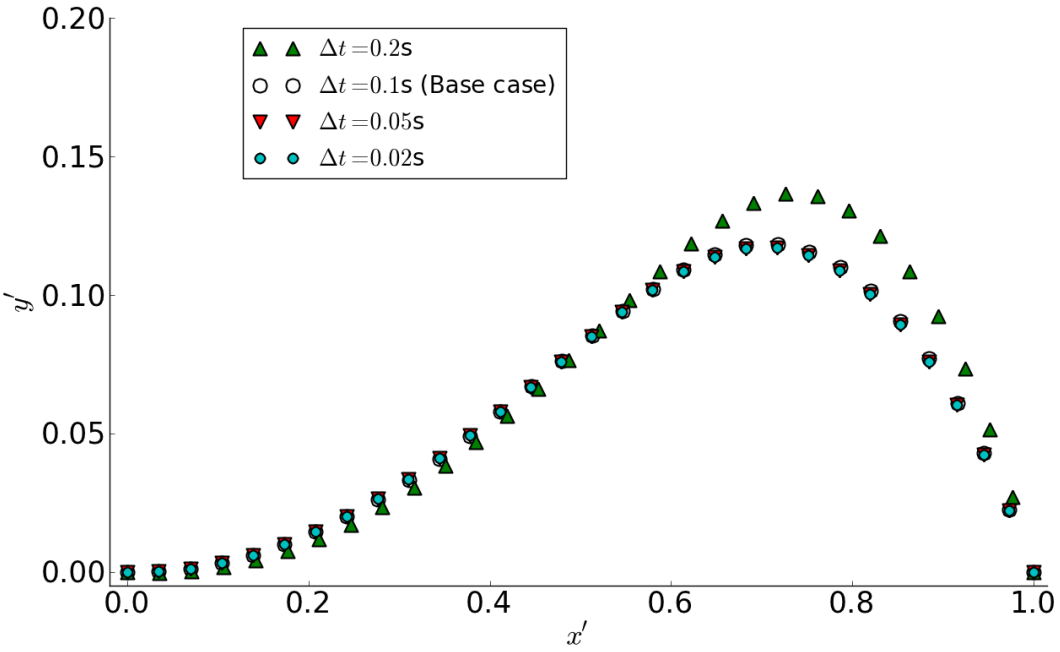

(a) Flexible insert deformation shape.

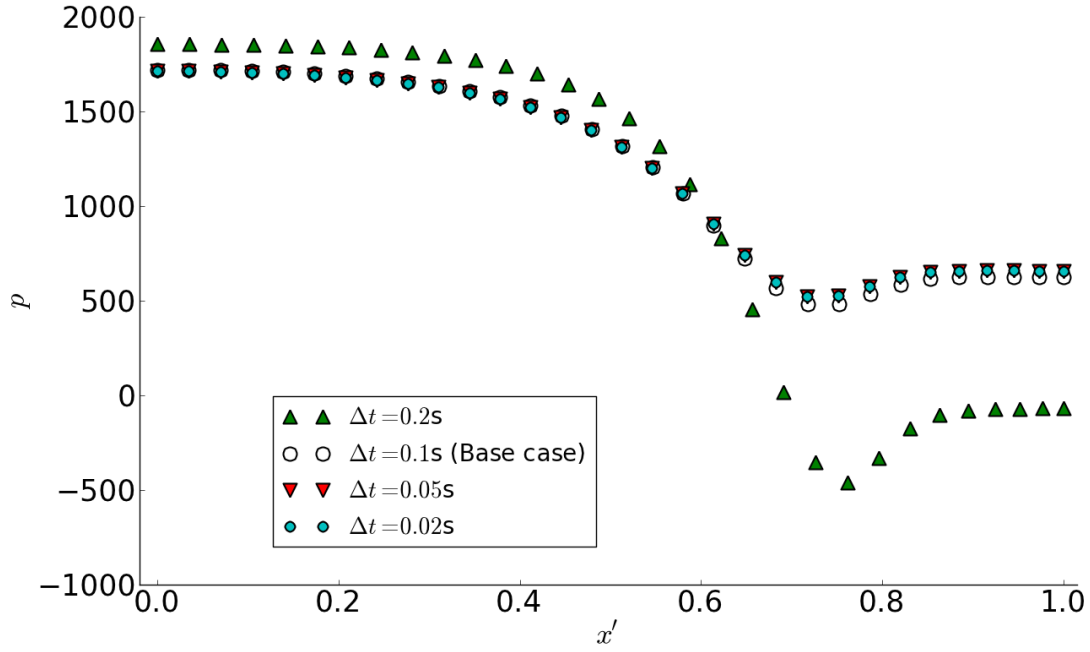

(b) Pressure along flexible insert.

Figure C.6 Dynamic simulation flexible insert results at the minimum (trough) y'_{max} position for different analysis timestep sizes.